Title
Physical Interpretations and Electrode Design Guidelines for Electrochemical Capacitors

Author
Bingang, Mei

Publication Date
2018

Peer reviewed|Thesis/dissertation

UNIVERSITY OF CALIFORNIA

Los Angeles

Physical Interpretations and Electrode Design Guidelines for Electrochemical Capacitors

A dissertation submitted in partial satisfaction
of the requirements for the degree
Doctor of Philosophy in Mechanical Engineering

by

Bing-Ang Mei

2018

ABSTRACT OF THE DISSERTATION

Physical Interpretations and Electrode Design Guidelines for Electrochemical Capacitors

by

Bing-Ang Mei
Doctor of Philosophy in Mechanical Engineering
University of California, Los Angeles, 2018
Professor Laurent G. Pilon, Chair

Electrochemical capacitors (ECs) serve as promising electrical energy storage systems due to their potential to achieve both high energy and high power densities. They can be classified as either electric double layer capacitors (EDLCs) or pseudocapacitors depending on the charge storage mechanism. EDLCs store charge in the electric double layer (EDL) forming at the electrode/electrolyte interface. Pseudocapacitors store energy both in the EDL and in the redox reactions occurring at or near the electrode surface along with ion intercalation into the electrodes. However, the interpretations of experimental results and the electrode optimization of such systems are made difficult by the coupling effect of EDL formation, redox reactions, and ion intercalation in the multidimensional porous electrode structures. This dissertation presents rigorous physical interpretations of conventional experimental characterization methods and provides design rules for EC electrodes using a multidimensional physicochemical model.

First, electrochemical impedance spectroscopy (EIS) measurements (Nyquist plots) of planar EDLC electrodes and devices were reproduced numerically for different electrode conductivity and thickness, electrolyte domain thickness, as well as ion diameter, diffusion coefficient, and concentrations. The electrode resistance, electrolyte resistance, and the equilibrium differential capacitance were identified

from Nyquist plots without relying on equivalent RC circuits. These results and interpretations were then confirmed experimentally for EDLC devices consisting of two identical activated-carbon electrodes in both aqueous and non-aqueous electrolytes. Similarly, EIS measurements of planar redox active electrodes were reproduced numerically for a wide range of electrode electrical conductivity, electrolyte thickness, redox reaction rate constant, and bias potential. The electrode, bulk electrolyte, charge transfer, and mass transfer resistances could be identified from the Nyquist plots. The results were then confirmed experimentally for $LiNi_{0.6}Co_{0.2}Mn_{0.2}O_2$ and MoS_2 electrodes in organic electrolytes.

Moreover, multidimensional simulations under cyclic voltammetry were performed for EDLC electrodes of different thicknesses consisting of spherical nanoparticles arranged in either simple cubic (SC) or face-centered cubic (FCC) packing structure. The capacitance under quasi-equilibrium (low charging/discharging rate) and rate-dependent (high charging/discharging rate) conditions were compared for different electrode nanoarchitectures and design suggestions were drawn. Moreover, multidimensional simulations were carried out for pseudocapacitive electrodes consisting of ordered conducting nanorods coated with a thin film of pseudocapacitive material. The contributions of EDL formation and redox reactions were discriminated and an optimum pseudocapacitive layer thickness that maximized total areal capacitance was identified as a function of scan rate and confirmed by scaling analysis.

Finally, commonly used methods to calculate energy and power densities of EDLC and hybrid pseudocapacitors were compared and evaluated. Energy conservation law was applied to the devices to identify the most appropriate method to calculate energy and power densities. The findings were confirmed by experimental measurements on EDLCs and hybrid pseudocapacitors.

The dissertation of Bing-Ang Mei is approved.

Chang-Jin Kim

Adrienne G. Lavine

Bruce S. Dunn

Wilbur J. Marner

Laurent G. Pilon, Committee Chair

University of California, Los Angeles

2018

This dissertation is dedicated to my beloved family.

TABLE OF CONTENT

LIST OF SYMBOLS

a	Effective ion diameter (nm)
b	power constant in $j_t = a\, v^b$
c	Ion concentration (mol/L)
c_{max}	Maximum ion concentration, $c_{max} = 1/N_A a^3$ (mol/L)
$c_{1,P,0}$	Initial concentration of intercalated Li^+ (mol/L)
$c_{1,P,max}$	Maximum concentration of intercalated Li^+ (mol/L)
C_{BET}	Areal capacitance (F/m^2)
C_g	Gravimetric capacitance (F/g)
D	Diffusion coefficient of ions in electrolyte (m^2/s)
$D_{1,P}$	Diffusion coefficient of Li^+ in electrode (m^2/s)
e	Elementary charge, $e = 1.602 \times 10^{-19}$ C
F	Faraday constant, $F = eN_A = 9.648 \times 10^4$ C mol^{-1}
f	Frequency of EIS (Hz)
H	Stern layer thickness (nm)
j	Current density (A/m^2)
j_{BET}	Magnitude of areal current density (A/m^2)
j_g	Magnitude of gravimetric current density (A/g)
$j_{F,ex}$	Exchange current density due to faradaic reactions (A/m^2)
j_{GC}	Current density imposed in galvanostatic cycling (A/m^2)
k_0	Reaction rate constant, Equation (2.7) ($m^{2.5}mol^{-0.5}s^{-1}$)
L	Half of interelectrode distance (nm)
L_C	Length of the carbon nanorod (nm)
L_D	Thickness of the diffuse layer (nm)
L_P	Total thickness of the pseudocapacitive electrode (nm)
L_r	Thickness of the pseudocapacitive layer (nm)
L_s	Thickness of the carbon current collector (nm)

m	Stoichiometric number of intercalated Li^+, $Li_mM_pO_q$
M	Molecular weight of the fully intercalated electrode (g/mol)
n	Index of refraction of the electrolyte
n_c	Cycle number
N_A	Avogadro constant, $N_A = 6.022 \times 10^{23}$ mol^{-1}
N_i	Ion flux of species i (mol m^{-2}s^{-1})
p, q	Stoichiometric numbers in the metal oxide M_pO_q
r_i	Carbon nanorod radius (nm)
r_o	Radius of MnO_2 coated carbon nanorod (nm)
r_t	Radius of region simulated (nm)
$\vec{r}$	Location in two-dimensional space (μm)
$\vec{r}_p$	Location at the pseudocapacitive layer / electrolyte interface (μm)
$\vec{r}_H$	Location at the Stern / diffuse layer interface (μm)
$\vec{r}_b$	Location at the carbon base / electrolyte interface (μm)
$\vec{r}_c$	Location at the pseudocapacitive layer / carbon interface (μm)
R	Resistance (Ω m^2)
R_{ct}	Charge transfer resistance (Ω m^2)
R_{mt}	Mass transfer resistance (Ω m^2)
R_u	Universal gas constant, $R_u = 8.314$ J mol^{-1}K^{-1}
T	Local temperature (K)
t	Time (s)
t_{cd}	Cycle period (s)
v	Scan rate of the cyclic voltammetry (V/s)
z	Ion valency

Greek symbols

α	Transfer coefficient, Equations (6.12) and (2.7)
ϵ_0	Vacuum permittivity, $\epsilon_0 = 8.854 \times 10^{-12}$ F m^{-1}
ϵ_r	Relative permittivity of electrolyte

$\Delta\psi_{eq}$	Equilibrium potential difference (V)
$\Delta\psi$	Potential drops (V)
ϕ	Phase difference between ψ_s and j_s in EIS (rad)
ϕ_D	Phase difference between ψ_s and $\Delta\psi_D$ in EIS (rad)
ϕ_F	Phase difference between ψ_s and j_F in EIS (rad)
ϕ_η	Phase difference between ψ_s and η in EIS (rad)
λ_D	Debye length (m)
η	Overpotential, $\eta = \Delta\psi_H - \Delta\psi_{eq}$ (V)
ρ	Density of the fully intercalated electrode (kg/m^3)
σ_c	Electrical conductivity of carbon electrode (S/m)
σ_P	Electrical conductivity of pseudocapacitive electrode (S/m)
ψ	Electric potential (V)
ψ_{min}, ψ_{max}	Minimum and maximum of the potential window (V)
ψ_s	Imposed cell potential (V)

Superscripts and subscripts

$*$	Refers to dimensionless variable
∞	Refers to bulk electrolyte
0	Refers to amplitude of oscillations in EIS
C	Refers to EDL contribution
D	Refers to diffuse layer
dc	Refers to frequency-independent DC contribution in EIS
eq	Refers to equilibrium conditions
F	Refers to faradaic contribution
H	Refers to Stern layer
i	Refers to ion species i
T	Refers to total value

LIST OF FIGURES

LIST OF TABLES

ACKNOWLEDGMENTS

I would like to thank my advisor, Professor Laurent Pilon, for his guidance and encouragement throughout the duration of my doctoral work. I am also grateful to Professor Bruce Dunn for his comments and guidance in the field of material science. My special thanks also go to Professor Webb Marner for his encouragement and support throughout the duration of my doctoral work. Moreover, I would like to thank Professor Adrienne Lavine and Professor Chang-Jin Kim for serving on my thesis committee. Furthermore, I would like to express my appreciation to my collaborators Dr. Hainan Wang, Dr. Anna d'Entremont, and Henri-Louis Girard for their help with my modeling skills, to my collaborators Obaidallah Munteshari, Jonathan Lau, and Ampol Likitchatchawankun for their help with the experimental work and to my collaborator Sara Vallejo-Castano for her help with my understanding in electrochemistry. I would also like to acknowledge all my lab members Dr. Alexander Thiele, Dr. Michal Marszewski, Alex Ricklefs, Louis Linden, Benjamin Young, Eylul Simsek, Tiphaine Galy, Zhenyu She, and Matevž Frajnkovič. I am also grateful to all my friends who have made my life enjoyable during my study at UCLA. Finally, I would like to thank Zezhi Zeng and my family for their endless love and support.

This material is based upon work supported, in part, by the China Scholarship Council (CSC). The computation for this study was performed on the Hoffman2 cluster hosted by the Academic Technology Services (ATS) at the University of California, Los Angeles, USA.

VITA

2010–2014	B.S. Energy and Environmental Engineering, Zhejiang University, China.
2014–present	Graduate Student Researcher, Mechanical and Aerospace Engineering Department, UCLA.

PUBLICATIONS

B. -A. Mei and L. Pilon, 2017, Three-dimensional cyclic voltammetry simulations of EDLC electrodes made of ordered carbon spheres, Electrochimica Acta 255, pp. 168-178.

B. -A. Mei, B. Li, J. Lin, and L. Pilon, 2017, Multidimensional cyclic voltammetry simulations of pseudocapacitive electrodes with a conducting nanorod scaffold, Journal of The Electrochemical Society 164 (13), pp. A3237-A3252.

B. -A. Mei, O. Munteshari, J. Lau, B. Dunn, and L. Pilon, 2017, Physical interpretations of Nyquist plots for EDLC electrodes and devices, Journal of Physical Chemistry C 122 (1), pp. 194-206.

CHAPTER 1

Introduction

1.1 Electrical energy storage

Electrical energy storage (EES) systems can be used in various applications including (i) regenerative braking in hybrid or all-electric vehicle applications, (ii) digital telecommunication, and (iii) dynamic stabilization of the utility grid [2, 7–10]. They can be classified into two major types namely (i) chemical energy storage systems including batteries, fuel cells, and pseudocapacitors and (ii) capacitive energy storage systems including electric double layer capacitors [2]. The fundamental difference is that chemical energy storage system store energy via electrochemical reactions while capacitive energy storage system store energy physically via separation of positive and negative charges [2].

Batteries store electrical energy via reversible redox reactions between ions present in an electrolyte and the electrode material [2]. Figure 1.1 shows the principle of a lithium-ion rechargeable battery system consisting of lithium cobalt oxide and carbon-based electrodes separated by an electrolyte solution containing Li^+ ions [11]. During charging, cations Li^+ are released at the cathode through a redox reaction by Li atom in the $LiCoO_2$ cathode, along with the production of electrons e^-, i.e., $2LiCoO_2 \rightarrow 2Li_{0.5}CoO_2 + Li^+ + e^-$. Then, the Li^+ ions migrate towards the anode across the electrolyte separator while the electrons migrate from the cathode to the anode via the external circuit. Finally, Li^+ react with the carbon based anode according to $6C + Li^+ + e^- \rightarrow LiC_6$ [2]. During discharging, the redox reactions at each electrode and the migration of cations and electrons occur in the opposite direction.

Moreover, the redox reactions for charge storage in a battery occur throughout the volume of the electrode material [2]. This results in a relatively high energy density. However, solid-state diffusion of Li^+ ions in the electrode is slow resulting in relatively low power density [2]. In addition, batteries feature a limited cycle lifetime due to the large changes in the crystalline structure of the electrode material caused by ion intercalation/deintercalation in the electrode along with the growth of the solid electrolyte interphase (SEI) layer during charging/discharging cycles. This results in irreversible changes in the electrode material and morphology [2].

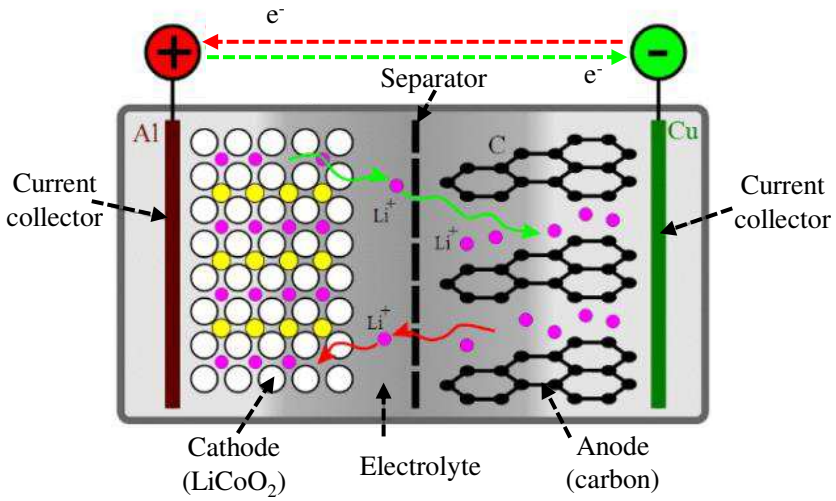

Figure 1.1: Illustration of the charge storage mechanism of a lithium-ion battery during charging and discharging (Adapted with permission under the Creative Commons Attribution-Share Alike 2.0 Germany license, Credit: Cepheiden via Wikimedia Commons).

Conventional dielectric capacitors store energy by physically separating positive and negative charges on metallic electrodes separated by an electrically insulating layer, as illustrated in Figure 1.2 [12]. Dielectric capacitors have relatively high power density but very low energy density because the electrostatic charge storage occurs only at the planar electrode surfaces [2,12]. Electrochemical capaci-

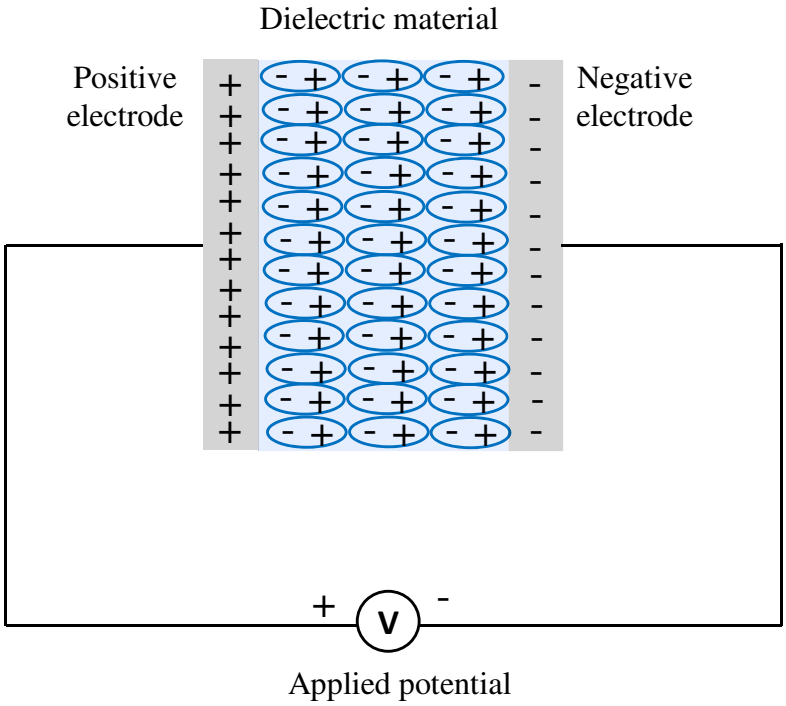

Figure 1.2: Illustration of the charge storage mechanism of a dielectric capacitor when a voltage is applied.

tors (ECs) store electrical energy via physical and/or chemical processes [2]. They consist of two electrodes separated by an ionic conducting electrolyte. In addition, ECs can be classified as either electric double layer capacitors (EDLCs) or pseudocapacitors depending on the charge storage mechanism. EDLCs store charge in the electric double layer (EDL) forming at the electrode/electrolyte interface and consisting of a layer of electronic charge in the electrode and a layer of ions with opposite charge in the electrolyte [2]. Figure 1.3 shows the Stern model for the EDL structure forming at an electrode/electrolyte interface [1]. The ions in the electrolyte can be divided into two regions: the Stern layer and the diffuse layer. The Stern layer is a compact layer of ions near the electrode/electrolyte interface with no free charge. The Stern/diffuse layer interface is the closest distance to

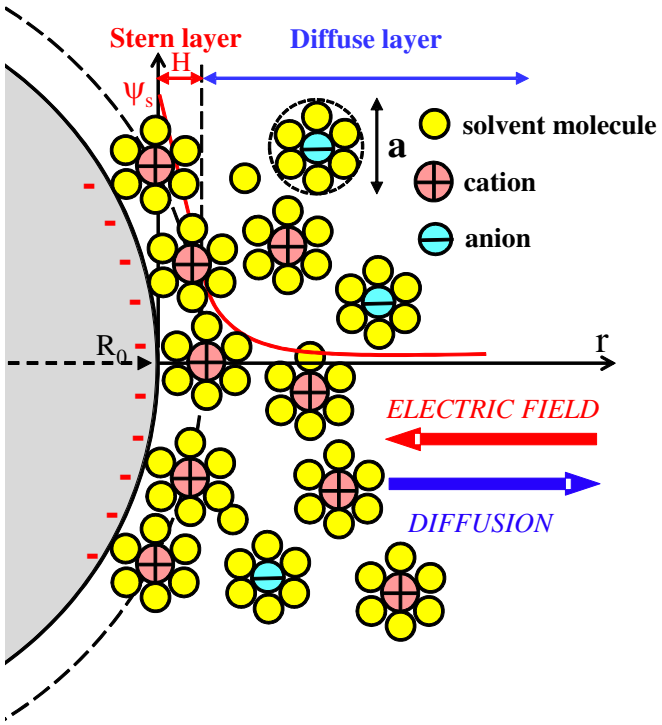

Figure 1.3: Illustration of the EDL forming at an electrode/electrolyte interface in EDLC according to the Stern model (from Ref. [1]).

the electrode surface of physically adsorbed ions. Ions in the diffuse layer are mobile under the competing effects of concentration gradients and electrostatic forces. EDLCs' energy storage capacity of EDLCs increases with increasing electrode surface area. For this reason, nanoporous carbon electrodes have been widely used in EDLCs to achieve high specific surface area (on the order of $1000-2000$ m^2/g) and low electrical resistance. This results in significantly larger energy densities for EDLCs compared with the conventional dielectric capacitors. In addition, EDLCs feature fast charging and discharging rates and thus large power density compared with batteries. Finally, unlike batteries, EDLCs also have long cycle lifetime thanks to the reversible EDL formation and dissolution.

Finally, hybrid pseudocapacitors consist of a pseudocapacitive electrode and an EDLC-like electrode separated by an electrolyte [2,12]. Besides the physical en-

ergy storage in the EDL at the electrode/electrolyte interfaces, pseudocapacitive electrodes also store energy chemically either from the reversible redox reactions occurring at the electrode/electrolyte interface or from ion intercalation into the tunnels or layers of the electrode [2, 13–15], as shown in Figure 1.4. By combining both physical and chemical mechanisms for electrical energy storage, hybrid pseudocapacitors have the potential of achieving the energy density of batteries combined with the power density of EDLCs.

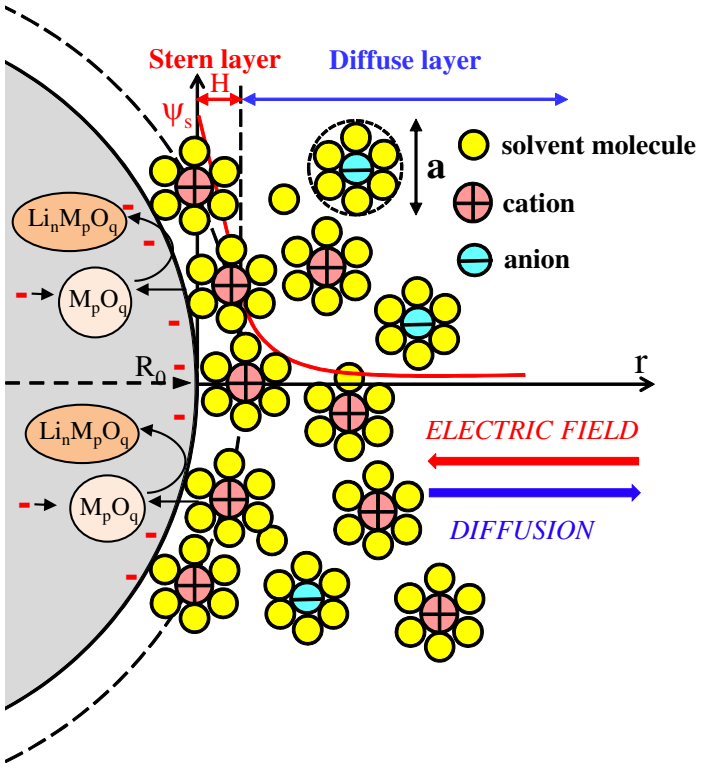

Figure 1.4: Illustration of the EDL formation and redox reation at an electrode/electrolyte interface (from Ref. [1]).

1.2 Electrochemical characterization methods

1.2.1 Cyclic voltammetry

Cyclic voltammetry consists of imposing a triangular potential $\psi_s(t)$ varying with time and measuring the resulting current j_s. The imposed potential can be expressed as [16]

$$\psi_s(t) = \begin{cases} \psi_{min} + v[t - (n_c - 1)\tau_{CV}] & \text{for } (n_c - 1)\tau_{CV} \leq t < (n_c - 1/2)\tau_{CV} \\ \psi_{max} - v[t - (n_c - 1/2)\tau_{CV}] & \text{for } (n_c - 1/2)\tau_{CV} \leq t < n_c\,\tau_{CV} \end{cases} \tag{1.1}$$

where v is the scan rate, n_c is the cycle number and τ_{CV} is the cycle period while ψ_{min} and ψ_{max} are the minimum and maximum values of the imposed potential $\psi_s(t)$, respectively. Cyclic voltammetry (CV) curves consist of plotting j_s as a function of ψ_s. Figure 1.5 shows typical CV curves at different scan rates v for (a) EDLC and (b) pseudocapacitive electrodes. The CV curves were nearly rectangle for EDLC electrodes. On the other hand, it featured a peak both during charging and during discharging for pseudocapacitive electrodes. This peak was usually linked to the presence of redox reactions [17].

1.2.2 Galvanostatic cycling

For galvanostatic cycling, the current density $j_s(t)$ at the current collector/electrode interface is imposed as

$$j_s(t) = \begin{cases} j_{GC} & \text{for } t_0 \leq t \leq t_0 + t_c \\ -j_{GC} & \text{for } t_0 + t_c < t \leq t_0 + t_c + t_d \end{cases} \tag{1.2}$$

where j_{GC} is the magnitude of the imposed current density, t_0 is the starting time, t_c is the time of charging, and t_d is the time of discharging. Then, the potential at the electrode/current collector interface is measured or computed. Figure 1.6 shows the typical potential evolution under galvanostatic cycling for different im-

(a)

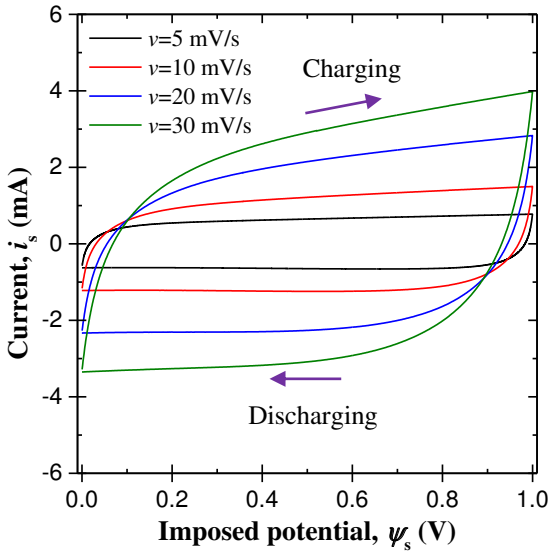

(b)

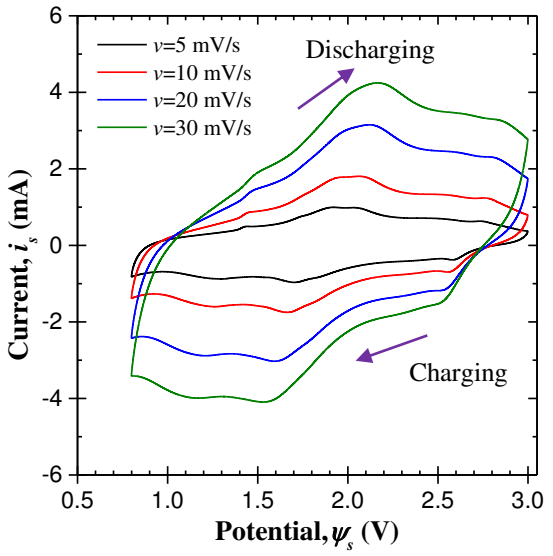

Figure 1.5: Typical CV curves for different scan rates v for (a) EDLC and (b) pseudocapacitive electrodes.

(a)

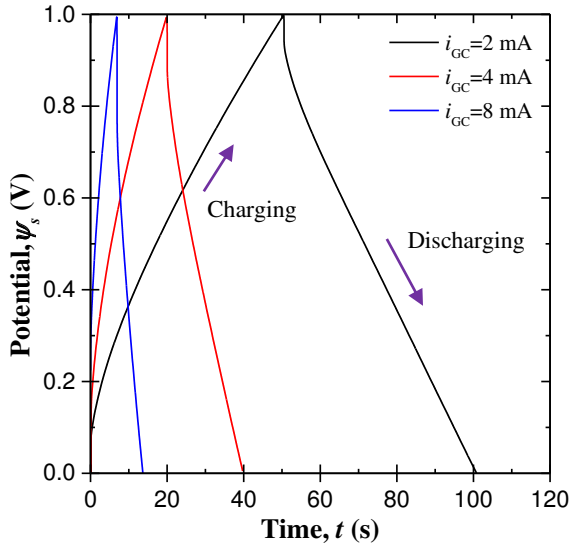

(b)

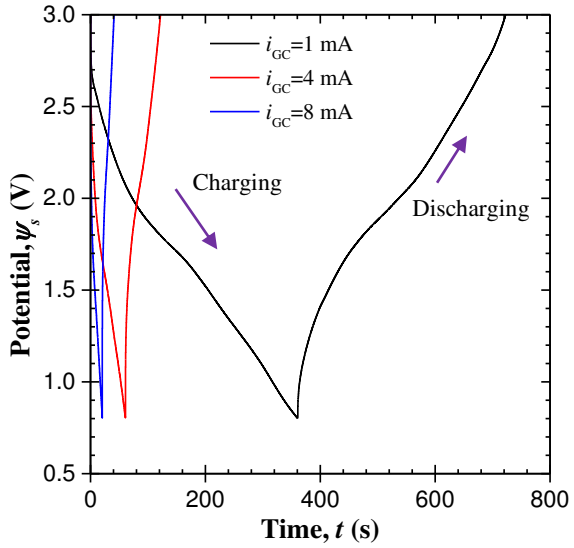

Figure 1.6: Typical potential evolution under galvanostatic cycling for different imposed current i_{GC} for (a) EDLC and (b) pseudocapacitive electrodes.

posed current i_{GC} for (a) EDLC and (b) pseudocapacitive electrodes. The potential evolution for EDLCs was symmetric during charging and discharging and nearly linear during discharging. On the other hand, the potential evolution for pseudocapacitive electrodes was asymmetric during charging and discharging and non-linear during discharging.

1.2.3 Electrochemical impedance spectroscopy (EIS)

Electrochemical impedance spectroscopy (EIS) consists of imposing a time harmonic oscillating electric potential $\psi_s(t)$ around a time-independent "DC potential" at the electrode surfaces and measuring the resulting harmonic current density $j_s(t)$ [18–20]. The amplitude of the oscillating potential is typically small and less than 10 mV. Using complex notations, the imposed electric potential $\psi_s(t)$ and the resulting current density $j_s(t)$ can be expressed as [8, 18, 21, 22],

$$\psi_s(t) = \psi_{dc} + \psi_0 e^{i2\pi ft} \quad \text{and} \quad j_s(t) = j_{s,dc} + j_{s,0} e^{i[2\pi ft - \phi(f)]} \tag{1.3}$$

where ψ_{dc} is the bias potential, ψ_0 is the amplitude of the oscillating potential at frequency f, $j_{s,dc}$ is the time-independent DC current density, $j_{s,0}$ is the amplitude of the oscillating current density, and $\phi(f)$ is the frequency-dependent phase angle between the imposed potential $\psi_s(t)$ and the current density $j_s(t)$. Then, the electrochemical impedance Z can be defined as [8, 18, 21, 22]

$$Z = \frac{\psi_s(t) - \psi_{dc}}{j_s(t) - j_{s,dc}} = \frac{\psi_0}{j_{s,0}} e^{i\phi} = Z_{re} + iZ_{im} \tag{1.4}$$

where Z_{re} and Z_{im} (expressed in Ω m^2) are the real and imaginary parts of the complex impedance, respectively. The Nyquist plot consists of plotting $-Z_{im}$ as a function of Z_{re}. Figure 1.7 shows typical Nyquist plots for (a) EDLC and (b) pseudocapacitive electrodes made of redox active material, respectively. For EDLC electrodes, it consists of a semi-circle at high frequencies between points

(a)

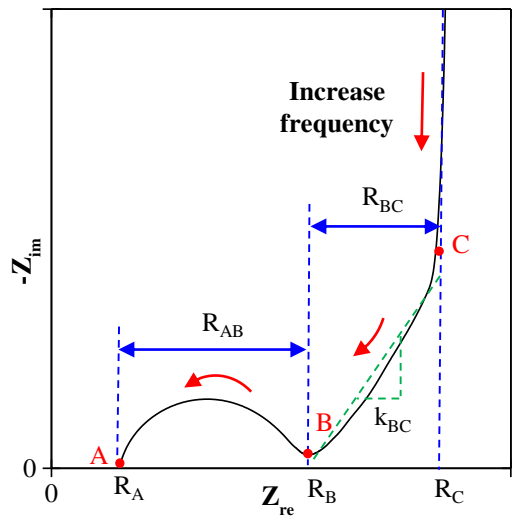

(b)

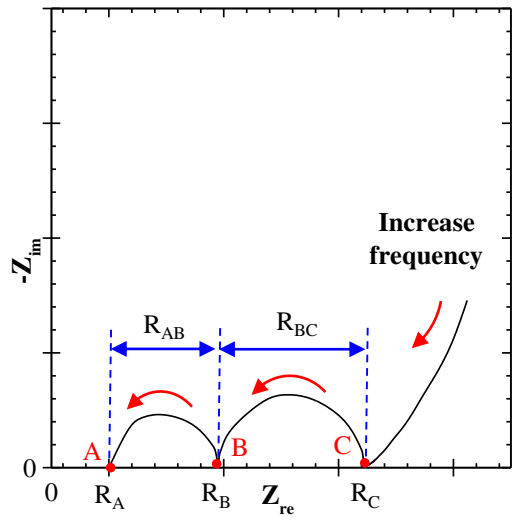

Figure 1.7: Typical Nyquist plots for (a) EDLC and (b) pseudocapacitive electrodes.

A and B, a non-vertical line at intermediate frequencies between points B and C, and a nearly vertical line with respect to the real axis at low frequencies beyond point C. For pseudocapacitive electrodes, the Nyquist plot consists of two semi-circles, i.e., a semi-circle at high frequencies between points A and B and one at intermediate frequencies between points B and C, as well as a non-vertical line with respect to the real axis at low frequencies beyond point C. Note that the non-vertical line may be absent for some electrodes [6, 23–29].

1.3 Motivation of the present study

The performance of different EC devices can be compared and assessed based on their capacitances and resistances. They can be obtained from electrochemical characterization measurements including cyclic voltammetry, galvanostatic cycling, and electrochemical impedance spectroscopy (EIS) [7]. Previous studies have established physical interpretation of cyclic voltammetry [16, 30–32] and galvanostatic cycling [33] measurements using one-dimensional numerical simulations. Still, multiple and often contradictory interpretations of experimental Nyquist plots for both EDLC and pseudocapacitive electrodes have been proposed in the literature [6, 23–29, 34–60] and clarification is needed.

In addition, the performances of ECs are greatly influenced by the electrode material as well as by the morphology of the electrodes [2,4,61–74]. Experimental synthesis have been performed on different electrode materials including (i) porous carbon electrode with ordered or disordered carbon spheres for EDLCs and (ii) pseudocapacitive electrodes made of transition metal oxides of RuO_2, MnO_2, or MoO_3 films or pseudocapacitive material coated on electrically conducting scaffold [2,4,61–74]. However, most experiments have been done by trial and error informed by physical intuition. Unfortunately, this approach is time-consuming and costly. On the other hand, most previous numerical models treated the electrode

microarchitecture as homogeneous with some effective macroscopic properties determined from effective medium approximations (EMA) and assumed transport phenomena as one-dimensional [75–86]. These models cannot account for the detailed porous electrode architecture. Therefore, multidimensional modeling tools for interfacial and transport phenomena in electrodes and electrolyte of ECs under dynamic charging/discharging cycles should be developed. This would enable one to predict and optimize the performance of electrodes with different morphology and dimensions and to develop design rules for electrodes and electrolytes. This could accelerate the development of ECs with high energy and power densities.

Finally, to compare the performance of ECs with other types of EES systems including batteries and fuel cells, energy (in J/kg) and power (in W/kg) densities are usually estimated. Ragone charts plot the energy density as a function of power density, as illustrated in Figure 1.8. To date, multiple data processing

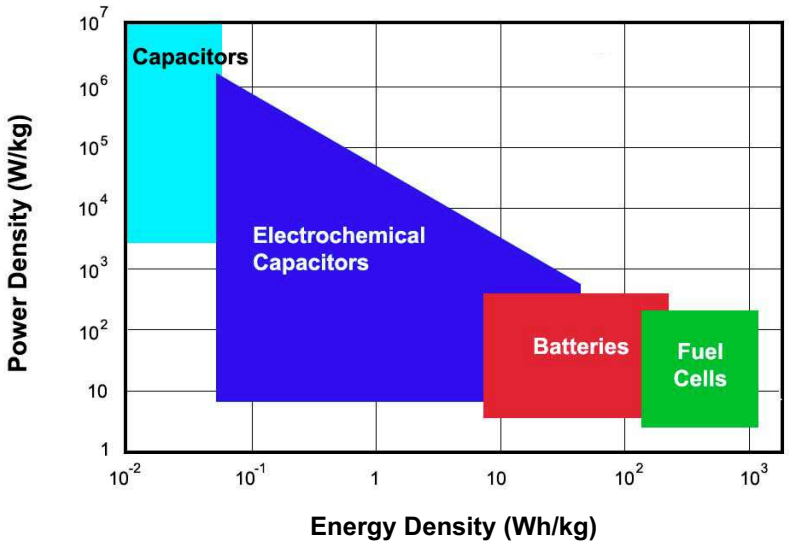

Figure 1.8: Comparison of energy and power densities of different EES systems (from Ref. [2]).

methods have been applied to generate Ragone plots of energy density versus power density for ECs [19, 35, 37, 87–114]. However, it is not clear which of these different methods is appropriate and whether they lead to the same estimation of

energy and power densities. In addition, the use of different methods makes the comparison of the performance of various ECs reported in the literature difficult. Thus, the different commonly used methods need to be compared and evaluated.

1.4 Objectives of the present study

The present study aims to (i) provide rigorous physical interpretations of EIS results for EDLC and pseudocapacitive electrodes, (ii) develop design rules for the 3D morphology of EDLC and pseudocapacitive electrodes and the associated electrolyte, and (iii) compare and evaluate the commonly used methods to estimate energy and power densities for EDLC devices and hybrid pseudocapacitors. To do so, multidimensional transient simulation tool was developed based on physical models previously derived in our group. The model accounted for (i) interfacial phenomena taking place at the electrode/electrolyte interface, (ii) multidimensional transport phenomena occurring in the electrolyte, (iii) redox reactions at the electrode surface, and (iv) intercalation of the reaction products in the pseudocapacitive electrode. The simulation tools were used to faithfully reproduce and to physically interpret experimental measurements.

1.5 Organization of the document

Chapter 2 provides background information relevant to this PhD thesis including (i) commonly used materials for electrodes and electrolytes, (ii) different electrode morphologies synthesized experimentally, and (iii) existing psysicochemical models of ECs. Chapter 3 provides rigorous physical interpretations of electrochemical impedance spectroscopy (EIS) for EDLC electrodes and devices. The electrode resistance, electrolyte resistance, and the equilibrium differential capacitance were identified from numerically-generated Nyquist plots without relying on equivalent RC circuits. Similarly, Chapter 4 provide physical interpretations of electrochem-

ical impedance spectroscopy (EIS) measurements for pseudocapacitive electrodes in three-electrode configurations. Here also, the electrode resistance, bulk electrolyte resistance, charge transfer resistance, and mass transfer resistance could be unequivocally identified from numerically-generated Nyquist plots. In both Chapters 3 and 4, effort is made to compare numerical results with experimental measurements. Chapter 5 presents a multidimensional simulation tool for porous carbon EDLC electrodes consisting of highly-ordered carbon spheres under cyclic voltammetry. The model enabled us to interpret CV curves as well as to predict the capacitance of EDLC electrodes as a function of carbon sphere diameters, overall electrode thicknesses, and packing arrangements. Then, the design rules for such EDLC electrodes under specific working conditions were discussed. Chapter 6 investigates numerically the effect of electrode morphology on the performance of pseudocapacitive electrodes consisting of a redox active material coated on an array of electrically conducting nanorods. The contribution of EDL formation and faradaic reaction to the capacitances of the electrodes were discriminated and an optimum redox layer thickness was derived. Chapter 7 compares and evaluates commonly used methods for estimating the energy and power densities of electrochemical capacitors and the associated Ragone charts. Finally, Chapter 8 summarizes the finding of this PhD thesis and provides recommendations for future research.

CHAPTER 2

Background

2.1 Material considerations for ECs

Desirable properties for EC electrodes include high specific area (on the order of $1000 - 2000$ m^2/g), low electrical resistance, good wettabilities for electrolyte to penetrate into the pores and create the necessary electrode/electrolyte interface, and low cost [7]. In addition, EDLC electrodes should not react with the electrolyte or current collector [7]. In fact, EDLC electrodes are typically made of porous carbon such as activated carbon [3,115], ordered mesoporous carbon [4, 116, 117], carbon nanotubes [118, 119], and graphene [120–122]. These carbon-based materials have the advantage of low cost and well established fabrication techniques. For example, Figure 2.1 shows the SEM images of (a) activated carbon [3] and (b) ordered carbon spheres [4].

On the other hand, pseudocapacitive materials typically consist of transition metal oxides or conductive polymers and react with cations in the electrolyte including Li^+, K^+, H^+ etc [12]. The most commonly used pseudocapacitive electrodes are made of (i) materials such as $RuO_2 \cdot xH_2O$ and MnO_2 for surface reactions or (ii) materials like Nb_2O_5 and MoS_2 for ion intercalations [12, 13, 55, 71, 72, 123–138].

Electrolyte consist of a salt (e.g., Na_2SO_4, $LiPF_6$) dissolved in a solvent (e.g., water, organic liquid). Desirable properties for the electrolytes used in ECs include (i) large relative permittivity or dielectric constant, (ii) high decomposition voltage, (iii) large ionic conductivity, as well as (iv) a wide usable temperature range [7]. They should also be environmentally friendly and inexpensive. In ad-

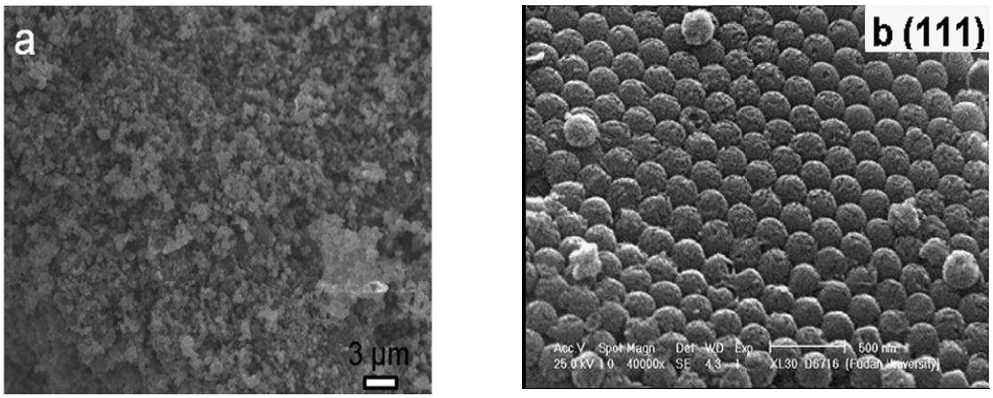

Figure 2.1: SEM images of the (a) meso-microporous activated carbon sample and (b) FCC packing monodispersed carbon sphere arrays in the view of (111) plane. (Adapted with permission from [3]. Copyright (2015) Royal Society of Chemistry. Adapted with permission from [4]. Copyright (2009) Royal Society of Chemistry.)

dition, the electrolyte should have low chemical and electrochemical activity to electrodes and current collectors for EDLCs. For pseudocapacitors, ions in the electrolyte should (i) react rapidly with the electrode material via reversible redox reactions and/or (ii) be capable of intracalating into the pseudocapacitive electrodes [7, 139]. Aqueous solutions including Na_2SO_4 or KOH offer high dielectric constant and high conductivity. However, water has a relatively low decomposition voltage of approximately 1.23 V that limits the working potential window and a relatively high freezing point that limits the working temperature range [7, 12]. Alternatively, non-aqueous solvents such as propylene carbonate (PC), ethylene carbonate (EC), dimethyl carbonate (DMC), and ethyl-methyl carbonate (EMC) offer high decomposition voltages but features relatively lower dielectric constant and ionic conductivity [7]. In addition, during the past several decades, the operating potential window of aqueous electrolyte-based ECs has been reported to be greatly increased to about 2 V by using neutral aqueous electrolytes that are electrochemically stable, i.e., lithium, sodium and potassium

sulfate solutions [139, 140]. For example, Fic et al. [140] performed experiments on EDLCs in 1 mol/L Li_2SO_4 aqueous solution and confirmed the wide potential range of 2.2 V without any significant capacitance fade during 15,000 cycles. In addition, a wide variety of new organic electrolytes with wider operating potential windows and reduced toxicity when compared to the commercial organic electrolytes have also been developed for ECs [139].

2.2 Modeling ion transport in electrochemical capacitors

2.2.1 Poisson-Nernst-Planck model

The Poisson-Nernst-Planck (PNP) model governed the spatiotemporal evolution of the electric potential $\psi(\mathbf{r}, t)$ and concentrations of the two ion species $c_i(\mathbf{r}, t)$ in the binary and symmetric electrolyte. The model treated ions as point charge with motion under the effect of diffusion, electromigration, and advection. The potential is governed by the Poisson equation according to [141–143]

$$\nabla \cdot (\epsilon_0 \epsilon_r \nabla \psi) = \begin{cases} 0 & \text{in the Stern layer} \quad (2.1a) \\ -zF(c_1 - c_2) & \text{in the diffuse layer} \quad (2.1b) \end{cases}$$

Here, $\epsilon_0 = 8.854 \times 10^{-12}$ F m^{-1} is the vacuum permittivity, ϵ_r is the field-dependent dielectric constant of the electrolyte, and $F = eN_A$ is the Faraday constant with e and N_A being the elementary charge and Avogadro number, respectively. The concentrations of ion species 1 and 2 in the electrolyte are governed by the Nernst-Planck equations and given by [142]

$$\frac{\partial c_i}{\partial t} = -\nabla \cdot \mathbf{N}_i \qquad \text{in the diffuse layer, for } i = 1, 2. \qquad (2.2)$$

Here, the mass flux vector $\mathbf{N}_i(\mathbf{r}, t)$ of ion species "i" (in mol/m^{2}s) at location $\mathbf{r}$ and time t was defined as [16]

$$\mathbf{N}_i(\mathbf{r}, t) = -D\nabla c_i - \frac{zFDc_i}{R_uT}\nabla\psi + c_i\mathbf{u} \tag{2.3}$$

where D is the diffusion coefficient of both ion species. The three terms on the right-hand side of Equation (2.3) correspond to the ion fluxes due to diffusion, electromigration, and advection, respectively [141, 144].

2.2.2 Modified Poisson-Nernst-Planck model

The modified Poisson-Nernst-Planck (MPNP) model was derived to account for Steric effects in the free energy of the electrolyte used to determine the chemical potentials and the corresponding ion fluxes. The model assumed binary and symmetric electrolyte. It used the same Poisson Equation [Equation (2.1)] and mass conservation equation [Equation (2.2)] and modified the mass flux vector as [16]

$$\mathbf{N}_i(\mathbf{r}, t) = -D\nabla c_i - \frac{zFDc_i}{R_uT}\nabla\psi - \frac{DN_Aa^3c_i}{1 - N_Aa^3(c_1 + c_2)}\nabla(c_1 + c_2) \quad \text{for } i = 1,2 \tag{2.4}$$

where D is the diffusion coefficient of both ion species. The three terms on the right-hand side of Equation (2.4) correspond to the ion fluxes due to diffusion, electromigration, and steric effects, respectively [141, 144]. This model accounts for finite ion size and is applicable to cases with large electric potential and/or electrolyte concentrations.

2.2.3 Generalized modified Poisson-Nernst-Planck model

The generalized modified Poisson-Nernst-Planck (GMPNP) model was developed by Wang et al. [16] to account for asymmetric and multi-species electrolytes with

finite ion size. The equations governing the temporal evolution of potential and ion concentrations remained the same as the modified Poisson-Nernst-Planck model while the mass flux vector $\mathbf{N}_i(\mathbf{r},t)$ of ion species "i" (in mol/m^{2}s) at location $\mathbf{r}$ and time t was generalized to account for multi-species electrolytes and defined as [16]

$$\mathbf{N}_i(\mathbf{r},t) = -D\nabla c_i - \frac{zFDc_i}{R_uT}\nabla\psi - \frac{DN_Ac_i}{1 - N_A\sum_{i=1}^{N} a_i^3 c_i}\sum_{i=1}^{N} a_i^3\nabla c_i \tag{2.5}$$

2.3 Modeling pseudocapacitance

Pseudocapacitors store energy in (i) the EDL at the electrode/electrolyte interfaces and in (ii) reversible redox reactions occurring either at the electrode surface and/or by ion intercalation into the electrode [2, 13–15]. In this study, the pseudocapacitance was modeled as a surface reaction followed by ion intercalation (diffusion) into the pseudocapacitive electrode.

The faradaic current density $j_F(\mathbf{r}_{P/E},\mathrm{t})$ caused by the redox reactions can be defined by the generalized Frumkin-Butler-Volmer model evaluated at the pseudocapacitive layer/electrolyte interface and expressed as [8]

$$j_F(\mathbf{r}_{P/E},t) = j_{F,ex}(t)\left\{\exp\left[\frac{(1-\alpha)zF\eta(\mathbf{r}_{P/E},t)}{R_uT}\right] - \exp\left[\frac{-\alpha zF\eta(\mathbf{r}_{P/E},t)}{R_uT}\right]\right\} \tag{2.6}$$

where $j_{F,ex}(t)$ is the so-called exchange current density, α is the transfer coefficient, and $\eta(\mathbf{r}_{P/E},t)$ is the surface overpotential. The exchange current density $j_{F,ex}(t)$ can be written as [145, 146]

$$j_{F,ex}(t) = zFk_0[c_1(\mathbf{r}_H,t)]^{1-\alpha}[c_{1,P,max} - c_{1,P}(\mathbf{r}_{P/E},t)]^{\alpha}[c_{1,P}(\mathbf{r}_{P/E},t)]^{\alpha} \tag{2.7}$$

where the reaction rate constant k_0 is expressed in $\mathrm{m}^{1+3\,\alpha}\mathrm{mol}^{-\alpha}\mathrm{s}^{-1}$ and $c_{1,P,max}$ is the maximum concentration of intercalated Li^+ in the pseudocapacitive layer. In

addition, the surface overpotential $\eta(\mathbf{r}_{P/E}, t)$ can be expressed as [8]

$$\eta(\mathbf{r}_{P/E}, t) = \Delta\psi_H(\mathbf{r}_{P/E}, t) - \Delta\psi_{eq}(t) \tag{2.8}$$

where $\Delta\psi_H(\mathbf{r}_{P/E})$ is the potential drop across the Stern layer at the pseudocapacitive layer/electrolyte interface and $\Delta\psi_{eq}$ is the equilibrium potential difference.

The ion intercalation into the pseudocapacitive electrode was modeled as a mass diffusion process given by [146, 147]

$$\frac{\partial c_{1,P}}{\partial t} = \frac{\partial}{\partial x}\left(D_{1,P}\frac{\partial c_{1,P}}{\partial x}\right) \quad \text{in the pseudocapacitive electrode} \tag{2.9}$$

where $D_{1,P}$ is the diffusion coefficient of intercalated lithium atoms in the pseudocapacitive electrode.

CHAPTER 3

Physical Interpretations of Nyquist Plots for EDLC Electrodes and Devices

This chapter aims to provide unequivocal physical interpretations of electrochemical impedance spectroscopy (EIS) results represented by Nyquist plots for electric double layer capacitor (EDLC) electrodes and devices. To do so, EIS measurements of (i) EDLC electrodes based on three-electrode setup and (ii) two-electrode EDLC cells were numerically reproduced for different electrode conductivity and thickness, different electrolyte domain thickness, as well as for different ion diameter, diffusion coefficient, and concentration in the electrolyte. The chapter also focuses on retrieving equilibrium differential capacitance and internal resistance from EIS simulations. Finally, it aims to validate experimentally the physical interpretations of EIS measurements developed numerically using EDLC cells consisting of two identical electrodes made of activated carbon and different aqueous and organic electrolytes.

3.1 Background

Figure 3.1 shows the schematic of a typical Nyquist plot presenting the imaginary part $-Z_{im}$ as a function of the real part Z_{re} of the complex impedance of an electric double layer capacitor (EDLC). It consists of a semi-circle at high frequencies between points A and B, a non-vertical line at intermediate frequencies between points B and C, and a nearly vertical line at low frequencies beyond point C.

Multiple and often contradictory physical interpretations of experimental Nyquist plots of EDLCs have been proposed in the literature [34–48]. For example, the

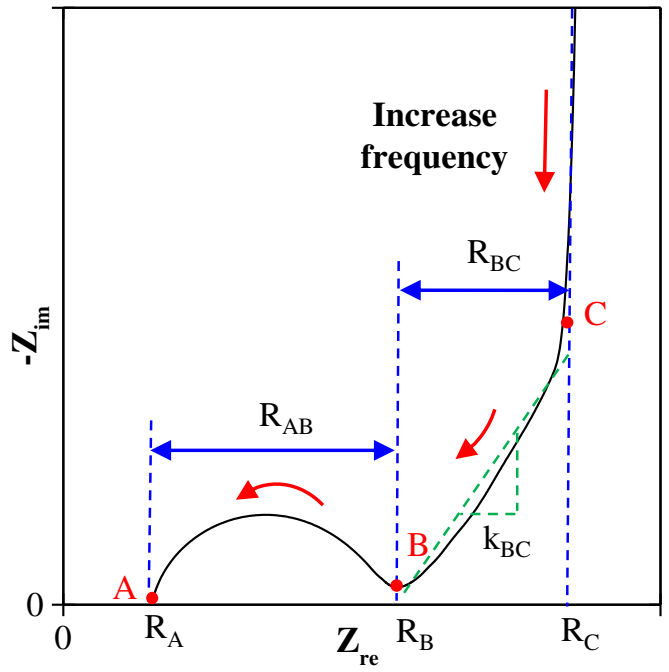

Figure 3.1: Schematic of typical Nyquist plots for EDLC electrodes or devices.

resistance R_A at point A (Figure 3.1) has been attributed to (i) the bulk electrolyte resistance [34–40] or (ii) the equivalent series resistance (ESR) also known as the internal resistance defined as the sum of the resistances of the bulk electrolyte, the electrode, and the contact resistance between the electrode and the current collector [41–45]. The diameter of the semi-circle $R_{AB} = R_B - R_A$ (Figure 3.1) has been assigned to (i) the electrolyte resistance in the pores of the electrodes [38, 41, 42], (ii) the contact resistance between electrode and current collector [46], (iii) the sum of the electrode resistance and contact resistance between the electrode and the current collector [39], or (iv) the so-called charge transfer resistance [34, 37]. For EDLC devices, the charge transfer resistance corresponds to the sum of the electrolyte resistance in the porous structure of the electrode, the electrode resistance, and the contact resistance between the elec-

trode and the current collector [37]. Based on this interpretation along with the previous interpretation of R_A as the bulk electrolyte resistance [34–40], the resistance R_B (Figure 3.1), i.e., $R_B = R_A + R_{AB}$, can be interpreted as the internal resistance, i.e., the sum of bulk electrolyte resistance and the so-called charge transfer resistance [34, 37, 39]. Furthermore, the existence of the non-vertical line BC (Figure 3.1) at intermediate frequencies has been assigned to (i) ion transport limitation in the electrolyte in porous electrode structures [34–36,39,41,44], (ii) ion transport limitation in the bulk electrolyte [40], or (iii) non-uniform pathway for ion transport from the bulk electrolyte to the porous electrode surface caused by non-uniform electrode pore size and electrode roughness [43, 45, 46]. Based on the latter interpretation, the resistance R_{BC} (Figure 3.1) was called the "equivalent distribution resistance" [45]. Finally, the vertical line at low frequencies beyond point C (Figure 3.1) was attributed to the dominant capacitive behavior of the electric double layer formed at the electrode/electrolyte interface [38,39,41,42,46]. The intersection between the vertical line and the Z_{re}-axis, corresponding to R_C, (Figure 3.1) has been termed (i) the internal resistance [37], (ii) the equivalent series resistance (ESR) [40], or (iii) the overall resistance [41] of the electrode or the device. The multiple and contradictory interpretations of the Nyquist plots are confusing and need clarification.

3.2 Analysis

3.2.1 Schematic and assumptions

Figure 3.2 shows (a) a one-dimensional (1D) simulated domain consisting of a planar current collector supporting a working electrode of thickness L_e and an electrolyte domain of thickness L corresponding to a three-electrode setup and (b) an EDLC device consisting of two identical electrodes of thickness L_e separated by an electrolyte domain of thickness $2L$. The electrolyte near each electrode

(a)

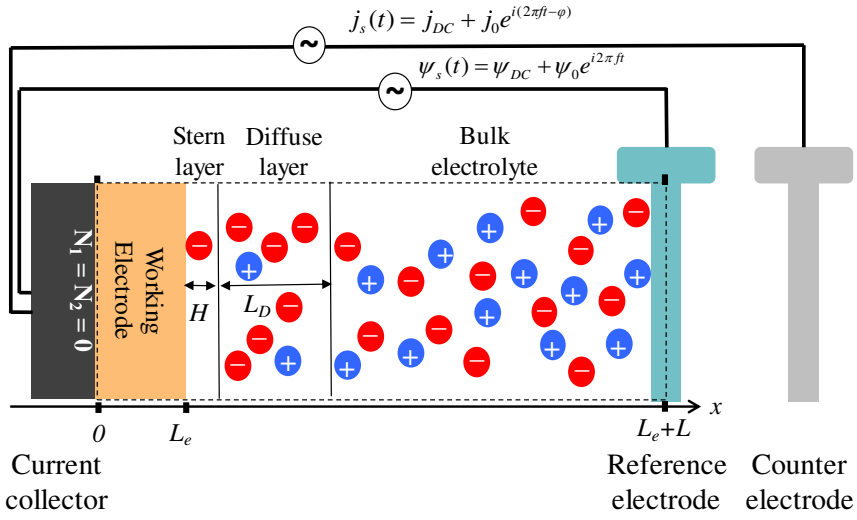

(b)

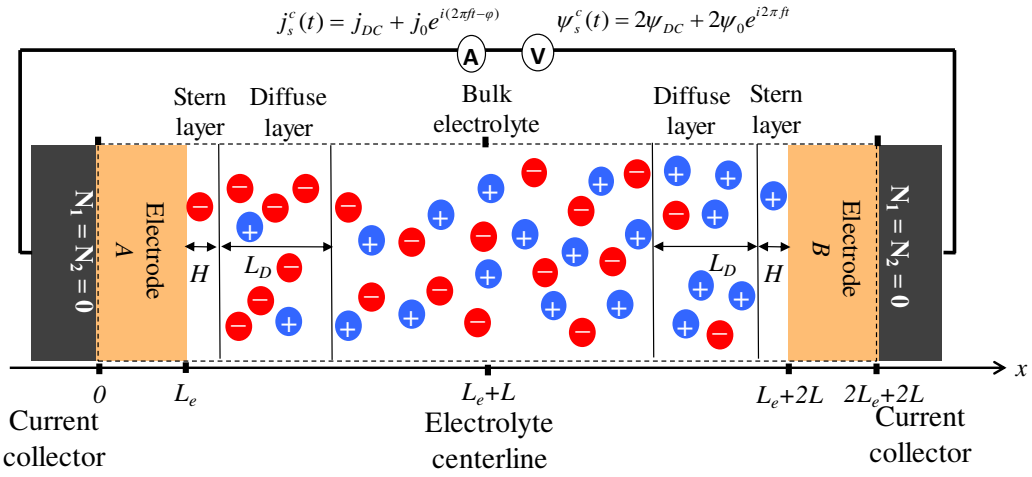

Figure 3.2: Schematics of (a) the simulated one-dimensional EDLC electrode in a three-electrode setup and (b) EDLC devices consisting of two identical electrodes. The dashed line encloses the computational domain simulated.

consisted of a Stern layer of thickness H and a diffuse layer of mobile ions of thickness L_D defined such that $[c_i(x = L_e + H + L_D, t) - c_\infty]/c_\infty \leq 5\%$, where $c_i(x = L_e+H+L_D, t)$ is the local concentration of cations ($i = 1$) or anions ($i = 2$) and c_∞ is the bulk ion concentration. Here, we considered only planar electrodes while practical EDLCs consist of porous electrodes. However, our previous work established that the simulations for planar electrodes were qualitatively comparable to experimental results, indicating that the model accounted for key physical phenomena in EDLCs [30, 148, 149]. In addition, the porous electrode can be accounted for as a curved electrode in three-dimensional simulations [150]. Following assumptions were made: (1) the electrolyte was binary and symmetric, i.e., it consisted of two ion species of opposite valency $\pm z$ ($z > 0$). The two ion species were further assumed to have identical diameter a and diffusion coefficient D. (2) The Stern layer contained no free charge and its thickness H was approximated as the radius of the ions, so that $H = a/2$ [8, 16, 151], as commonly assumed in continuum simulations of EDLCs [30, 148–150]. (3) The transport properties of the electrode and electrolyte were taken as constant. (4) Bulk motion of the electrolyte was negligible. (5) No redox reaction or ion intercalation took place at the surface or within the electrode. (6) Heat generation was ignored and the temperature was uniform and constant in the electrode and electrolyte. (7) Contact resistance between the electrode and the current collector and the electrical resistance of the current collector were negligible. (8) Self-discharge of the electrode or the device was ignored.

3.2.2 Governing equations

Simulations reported in this chapter were based on the modified Poisson-Nernst-Planck (MPNP) model for the spatiotemporal evolution of the potential $\psi(x, t)$ [Equation (2.1)] in the electrode and electrolyte as well as the ion concentrations $c_1(x, t)$ of cations and $c_2(x, t)$ of anions [Equations (2.2) and (2.4)] in the

binary and symmetric electrolyte for EDLC electrodes or devices. In addition, the boundary conditions varied depending on whether EIS or galvanostatic cycling were simulated. EIS simulations imposed potential $\psi_s(t)$ at the current collector/electrode interface or across the cell as a harmonic function of time t [Equation (1.3)]. For galvanostatic cycling, the current density $j_s(t)$ imposed at the current collector/electrode interface or across the cell was a square wave of magnitude j_{GC} with respect to the cycle period [Equation (1.2)].

3.2.2.1 Single-electrode simulations

The boundary condition at the centerline, located at $x = L_e + L$, was given by

$$\psi(L_e + L, t) = 0 \quad \text{and} \quad c_i(L_e + L, t) = c_\infty. \tag{3.1}$$

Moreover, the electric potential and current density were both continuous across the electrode/electrolyte interface, located at $x = L_e$, so that

$$\psi(L_e^-, t) = \psi(L_e^+, t) \ \text{ and } \ -\sigma_e \frac{\partial \psi}{\partial x}(L_e^-, t) = -\epsilon_0 \epsilon_r \frac{\partial^2 \psi}{\partial x \partial t}(L_e^+, t). \tag{3.2}$$

The electric potential varied linearly across the Stern layer so that the electric field at the planar Stern/diffuse layer interfaces, located at $x = L_e + H$ satisfied [1, 16]

$$\frac{\partial \psi}{\partial x}(L_e + H, t) = \frac{\psi(L_e) - \psi(L_e + H)}{H}. \tag{3.3}$$

These boundary conditions accounted for the presence of the Stern layers without explicitly simulating them in the computational domain thus reducing significantly the number of meshes [1].

Finally, based on assumption (5), no ion intercalated into the electrode. Thus, the ion mass flux vanished at the electrode/electrolyte interface, located at $x = L_e$,

such that [16]

$$N_i(L_e, t) = 0 \qquad \text{for i} = 1,\ 2, \tag{3.4}$$

3.2.2.2 Two-electrode simulations

For two-electrode simulations, the potential at one electrode was imposed as $\psi_s(t)$ [Equation (1.3)] while the other electrode was grounded, i.e.,

$$\psi(2L_e + 2L, t) = 0. \tag{3.5}$$

Moreover, by virtue of symmetry, the electric potential, current density, and ion flux at the electrode/electrolyte interface, located at $x = L_e + 2L$ were identical to the boundary conditions described in Equations (3.2)-(3.4), i.e.,

$$\begin{aligned}
\psi(L_e + 2L^-, t) &= \psi(L_e + 2L^+, t) && (3.6)\\
-\sigma_e \frac{\partial \psi}{\partial x}(L_e + 2L^+, t) &= -\epsilon_0 \epsilon_r \frac{\partial^2 \psi}{\partial x \partial t}(L_e + 2L^-, t), && (3.7)\\
\frac{\partial \psi}{\partial x}(L_e + 2L - H, t) &= \frac{\psi(L_e + 2L - H) - \psi(L_e + 2L)}{H}, && (3.8)\\
N_i(L_e + 2L, t) &= 0 \qquad \text{for i} = 1,\ 2. && (3.9)
\end{aligned}$$

3.2.3 Constitutive relationships

In order to solve the coupled transient 1D equations as well as the initial and boundary conditions, a total of 12 parameters were necessary including (i) the electrode electrical conductivity σ_e, (ii) the electrolyte properties ϵ_r, z, a, D, and c_∞, (iii) the dimensions of the simulated electrode and electrolyte domains L_e and L, along with (iv) the operating conditions ψ_{dc}, ψ_0, and f for EIS simulations and ψ_{min}, ψ_{max} and j_{GC} for galvanostatic cycling, and (v) temperature T (in K). The electrical conductivity σ_e and thickness L_e of the electrode, the electrolyte properties a, D, and c_∞, the length of the electrolyte domain L were treated as

Table 3.1: Value or range of electrode and electrolyte properties and dimensions used in the simulations reported in this study

Parameter	Symbol	Value	Unit
Electrode conductivity	σ_e	5 x 10^{-8} - 5 x 10^{-5}	S/m
Dielectric constant	ϵ_r	64.4	
Valency	z	1	
Ion diameter	a	0.33 - 1.32	nm
Diffusion coefficient	D	5 x 10^{-14} - 8 x 10^{-13}	m^2/s
Bulk ion concentration	c_∞	0.0005 - 1	mol/L
Electrode thickness	L_e	10 - 100	nm
Electrolyte thickness	L	40 - 1600	nm
DC potential	ψ_{DC}	0.3	V
Amplitude of oscillating potential	ψ_0	5	mV
Frequency	f	0.1 - 5 x 10^4	Hz
Magnitude of imposed current density	j_{GC}	10^{-3} - 0.01	mA/cm^2
Potential window	ψ_{min}	0	V
	ψ_{max}	1	V
Temperature	T	298	K

variables to achieve various resistances and capacitances. On the other hand, the temperature was set to room temperature ($T = 298$ K) and the dielectric constant was taken as that of propylene carbonate, a commonly used organic solvent, i.e., $\epsilon_r = 64.4$ [152]. The valency of the ion species was $z = 1$ [68]. Finally, in EIS simulations, the DC potential was set arbitrarily as $\psi_{dc} = 0.3$ V, the oscillating potential as $\psi_0 = 5$ mV and the frequency f varied between 0.1 and 5 x 10^6 Hz. In galvanostatic cycling, the magnitude of imposed current density j_{GC} ranged between 10^{-3} and 1 mA/cm^2 while the potential window was set as $\psi_{min} = 0$ V and $\psi_{max} = 1$ V. Table 7.1 summarizes the values or ranges of these parameters.

3.2.4 Data processing

3.2.4.1 Electrical resistances

The electrical resistance R_e (in Ω m^2) per unit surface area of the planar electrode can be expressed as

$$R_e = L_e/\sigma_e. \tag{3.10}$$

To calculate the resistance of the electrolyte, current density due to ion transport in the electrolyte needs to be considered and is given by [7]

$$j(x,t) = zF[N_1(x,t) - N_2(x,t)] \tag{3.11}$$

where z is the valency, $F = eN_A$ is the Faraday constant, $N_1(x,t)$ and $N_2(x,t)$ are the mass fluxes of cations and anions in the electrolyte (in mol/m^{2}s) expressed in Equation (2.3). Note that the local electric field $E(x,t) = -\partial\psi/\partial x$. Thus, the local ionic conductivity $\sigma(x)$ in the electrolyte, defined as $j(x,t) = \sigma(x)E(x,t)$, can be expressed as

$$\sigma(x) = zFD\frac{\partial}{\partial\psi}(c_1 - c_2) + \frac{z^2F^2D(c_1+c_2)}{R_uT} + \frac{DN_Aa^3(c_1-c_2)}{1-N_Aa^3(c_1+c_2)}\frac{\partial}{\partial\psi}(c_1+c_2) \tag{3.12}$$

where D is the diffusion coefficient, $c_1(x,t)$ and $c_2(x,t)$ are the concentrations of cations and anions at location x and time t in the electrolyte, $\psi(x,t)$ is the potential in the electrolyte, $R_u = 8.314$ J /mol K is the universal gas constant, a is the effective ion diameter, and N_A is the Avogadro's number. Here, the diffuse layer contained mobile ions with non-zero concentration gradients while the ion concentrations in the bulk electrolyte remained constant. Thus, the ionic conductivity $\sigma(x)$ varied with location in the diffuse layer and was a harmonic function of time that could be represented using complex notations. However, it remained constant and real in the bulk electrolyte. The resistance, i.e., the real part of the impedance, of the diffuse layer near one electrode can be expressed as

$$R_D = \mathrm{Re}\left[\int_{L_e}^{L_e+L_D} \frac{dx}{\sigma(x)})\right]. \tag{3.13}$$

Note that the local ion concentrations $c_1(x,t)$ and $c_2(x,t)$ in the diffuse layer as well as the diffuse layer thickness L_D were unknown and were determined

numerically. Finally, the bulk electrolyte resistance can be expressed as [7]

$$R_\infty = (L - L_D)/\sigma_\infty \qquad \text{with} \qquad \sigma_\infty = (2z^2F^2Dc_\infty)/(R_uT) \tag{3.14}$$

where σ_∞ is the electrical conductivity of the bulk electrolyte.

Moreover, for EDLC cells (referred to by superscript "c"), the resistances of the electrodes R_e^c, of the diffuse layer R_D^c, and the bulk electrolyte R_∞^c can be expressed as

$$R_e^c = 2R_e \tag{3.15}$$

$$R_D^c = \text{Re}\left[\int_{L_e}^{L_e+L_D} \frac{dx}{\sigma(x)} + \int_{L_e+2L-L_D}^{L_e+2L} \frac{dx}{\sigma(x)}\right] \tag{3.16}$$

$$R_\infty^c = 2(L - L_D)/\sigma_\infty \tag{3.17}$$

Finally, the internal resistance R_{GC} (in Ω m^2) retrieved from galvanostatic cycling for both single-electrode and device simulations can be expressed as [153, 154]

$$R_{GC}(j_{GC}) = \frac{\Delta\psi}{2j_{GC}} \tag{3.18}$$

where $\Delta\psi$ is the potential drop observed at the beginning of discharge under constant current density j_{GC}.

3.2.4.2 Equilibrium differential capacitance

The differential capacitance (in μF/cm^2) is defined as [7–9]

$$C_{diff} = \frac{\mathrm{d}q_s}{\mathrm{d}\psi_s} \tag{3.19}$$

where q_s (in C/m^2) is the surface charge density. For a given EDLC electrode under equilibrium conditions, it is denoted by $C_{diff,eq}$ and can be expressed as,

[142, 155]

$$\frac{1}{C_{diff,eq}} = \frac{1}{C^{St}_{diff,eq}} + \frac{1}{C^{D}_{diff,eq}} \tag{3.20}$$

where $C^{St}_{diff,eq}$ and $C^{D}_{diff,eq}$ are the equilibrium differential capacitances of the Stern layer and diffuse layer near the electrode, respectively. They can be expressed as [142, 155]

$$C^{St}_{diff,eq} = \frac{\epsilon_0 \epsilon_r}{H} \quad \text{and} \tag{3.21a}$$

$$C^{D}_{diff,eq} = \frac{\frac{\epsilon_0 \epsilon_r}{\lambda_D} \sinh\left(\frac{ze\psi_D}{k_B T}\right)}{\left[1 + 2\nu \sinh^2\left(\frac{ze\psi_D}{2k_B T}\right)\right] \sqrt{\frac{2}{\nu} \log\left[1 + 2\nu \sinh^2\left(\frac{ze\psi_D}{2k_B T}\right)\right]}} \tag{3.21b}$$

where $\lambda_D = [\epsilon_0 \epsilon_r k_B T/(2e^2 z^2 N_A c_\infty)]^{1/2}$ is the Debye length, e is the elementary charge, and k_B is the Boltzmann constant, respectively. The packing parameter ν is defined as $\nu = 2a^3 N_A c_\infty$. For planar electrode under equilibrium conditions, the electric potential at the Stern/diffuse layer interface, denoted by ψ_D, can be expressed as a function of the potential ψ_s imposed at the electrode/current collector interface according to [156]

$$\frac{\psi_D}{k_B T/ez} = 0.37 \left(\frac{\psi_s}{k_B T/ez}\right)^{1.16}. \tag{3.22}$$

Note that for EIS simulations, ψ_s in Equation 3.22 corresponds to the time-independent potential ψ_{dc}.

Finally, an EDLC cell with two identical electrodes can be treated as two capacitors in series. Thus, the equilibrium capacitance of the EDLC cell can be expressed as $C^{c}_{diff,eq} = C_{diff,eq}/2$.

Table 3.2: Simulation parameters and corresponding resistances R_e, R_∞, and R_D and capacitance $C_{diff,eq}$ [Equation (3.20)] and $C_{diff,eq,EIS}$ values for 25 EIS simulations for single electrodes (Cases 1-24) and an EDLC cell (Case 25)

Case number	$\boldsymbol{\sigma_e}$ **(S/m)**	$\boldsymbol{c_\infty}$ **(mol/L)**	$\boldsymbol{D}$ **(m^2/s)**	$\boldsymbol{L}$ **(nm)**	$\boldsymbol{L_e}$ **(nm)**	$\boldsymbol{a}$ **(nm)**	$\boldsymbol{\tau_D/\tau_{RC}}$	$\boldsymbol{R_e}$ **(Ω m^2)**	$\boldsymbol{R_\infty}$ **(Ω m^2)**	$\boldsymbol{R_D}$ **(Ω m^2)**	$\boldsymbol{C_{diff,eq}}$ **(μF/cm^2)**	$\boldsymbol{C_{diff,eq,EIS}}$ **(μF/cm^2)**
2	1×10^{-7}	0.001	2×10^{-13}	160	10	0.66	0.72	0.1	0.105	0.07	94.8	94.8
3	5×10^{-8}	0.001	2×10^{-13}	160	10	0.66	0.68	0.2	0.105	0.07	94.8	95.0
4	5×10^{-5}	0.01	2×10^{-13}	160	10	0.66	7.13	2×10^{-4}	0.0105	0.009	91.5	91.6
5	5×10^{-5}	0.001	2×10^{-13}	160	10	0.66	0.68	2×10^{-4}	0.105	0.07	94.8	94.6
6	5×10^{-5}	0.0005	2×10^{-13}	160	10	0.66	0.37	2×10^{-4}	0.20	0.14	92.7	94.4
7	5×10^{-5}	0.001	2×10^{-13}	80	10	0.66	0.38	2×10^{-4}	0.05	0.04	94.9	92.2
8	1×10^{-7}	0.002	2×10^{-13}	160	10	0.66	1.47	0.1	0.05	0.04	95.5	93.5
9	5×10^{-5}	0.002	5×10^{-14}	80	10	0.66	0.78	2×10^{-4}	0.105	0.09	95.6	93.7
10	5×10^{-5}	0.002	2×10^{-13}	160	10	0.33	0.62	2×10^{-4}	0.05	0.05	206.4	197.1
11	5×10^{-5}	0.0005	8×10^{-13}	320	10	0.66	0.66	2×10^{-4}	0.105	0.10	94.7	93.6
12	5×10^{-5}	0.0005	2×10^{-13}	160	10	1.32	0.91	2×10^{-4}	0.20	0.19	38.1	38.4
13	5×10^{-5}	0.001	2×10^{-13}	80	10	1.32	1.04	2×10^{-4}	0.05	0.04	37.1	36.6
14	5×10^{-5}	0.001	2×10^{-13}	320	10	0.33	0.66	2×10^{-4}	0.20	0.19	194.4	197.4
15	5×10^{-5}	0.001	2×10^{-13}	160	10	1.32	1.84	2×10^{-4}	0.105	0.10	37.1	37.1
16	5×10^{-5}	0.001	2×10^{-13}	160	10	0.33	0.33	2×10^{-4}	0.105	0.10	194.9	197.2
17	5×10^{-5}	0.001	1×10^{-13}	80	10	0.66	0.37	2×10^{-4}	0.105	0.09	94.9	93.0
18	5×10^{-5}	0.0005	1×10^{-13}	160	10	0.66	0.37	2×10^{-4}	0.41	0.40	92.7	88.3
19	5×10^{-5}	0.001	5×10^{-14}	80	10	0.66	0.37	2×10^{-4}	0.20	0.17	94.9	94.9
20	5×10^{-5}	0.001	1×10^{-13}	320	10	0.66	1.39	2×10^{-4}	0.05	0.05	92.7	94.4
21	1×10^{-7}	0.004	2×10^{-13}	160	10	0.66	3.04	0.1	0.03	0.02	95.2	93.4
22	1×10^{-7}	0.006	2×10^{-13}	160	10	0.66	4.34	0.1	0.02	0.02	94.7	93.0
23	5×10^{-5}	0.0075	2×10^{-13}	160	10	0.66	5.50	2×10^{-4}	0.01	0.01	92.3	92.2
24	5×10^{-5}	1	2×10^{-13}	1600	100	0.66	2.09×10^{4}	2×10^{-3}	1.06×10^{-3}	1.24×10^{-6}	66.5	62.0
25**	5×10^{-5}	1	2×10^{-13}	1600	100	0.66	4.18×10^{4}	4×10^{-3}	2.12×10^{-3}	2.48×10^{-6}	33.2	31.5

3.3 Results and discussion

3.3.1 Interpretation of the Nyquist plot for EDLC electrodes

Table 3.2 summarizes the different cases (Cases 1-24) considered to assess the effects of electrode and electrolyte resistances and electrode capacitance on the Nyquist plots of a single EDLC electrode.

3.3.1.1 Electrode resistance R_e

Figures 3.3(a)-3.3(c) show the Nyquist plots for EDLC electrodes of Cases 1-3 featuring electrode electrical conductivity σ_e of (a) 2 x 10^{-7} S/m, (b) 1 x 10^{-7} S/m, and (c) 5 x 10^{-8} S/m, corresponding to electrode resistance R_e [Equation (3.10)] of (a) 0.05 Ω m^2, (b) 0.1 Ω m^2, and (c) 0.2 Ω m^2, respectively. All other parameters remained the same in these three cases. First, Figures 3.3(a)-3.3(c) resembles remarkably experimental EIS measurements on single EDLC electrodes [157–159]. In addition, they indicate that changing electrode resistance led to a horizontal shift of the Nyquist plot along the Z_{re}-axis. Moreover, the high-frequency intersection of the Nyquist plot with the Z_{re}-axis (corresponding to R_A in Figure 3.1) was systematically equal to the electrode resistance R_e predicted by Equation (3.10). Note that the present simulations ignored contact resistance between the electrode and the current collector. However, it can be accounted for as a resistance in series with R_e and its sole effect on the Nyquist plot would also be to shift the plot along the Z_{re}-axis.

Furthermore, Figure 3.3(d) shows $-Z_{im}$ as a function of $Z_{re} - R_e$ for the above three cases. It indicates that the Nyquist plots for Cases 1-3 nearly collapsed on the same line regardless of changes in electrode conductivity σ_e. In other words, σ_e had no significant effects on the Nyquist plots at low and medium frequencies. In addition, it is interesting to note that the diameter of the semi-circle in Figure 3.3

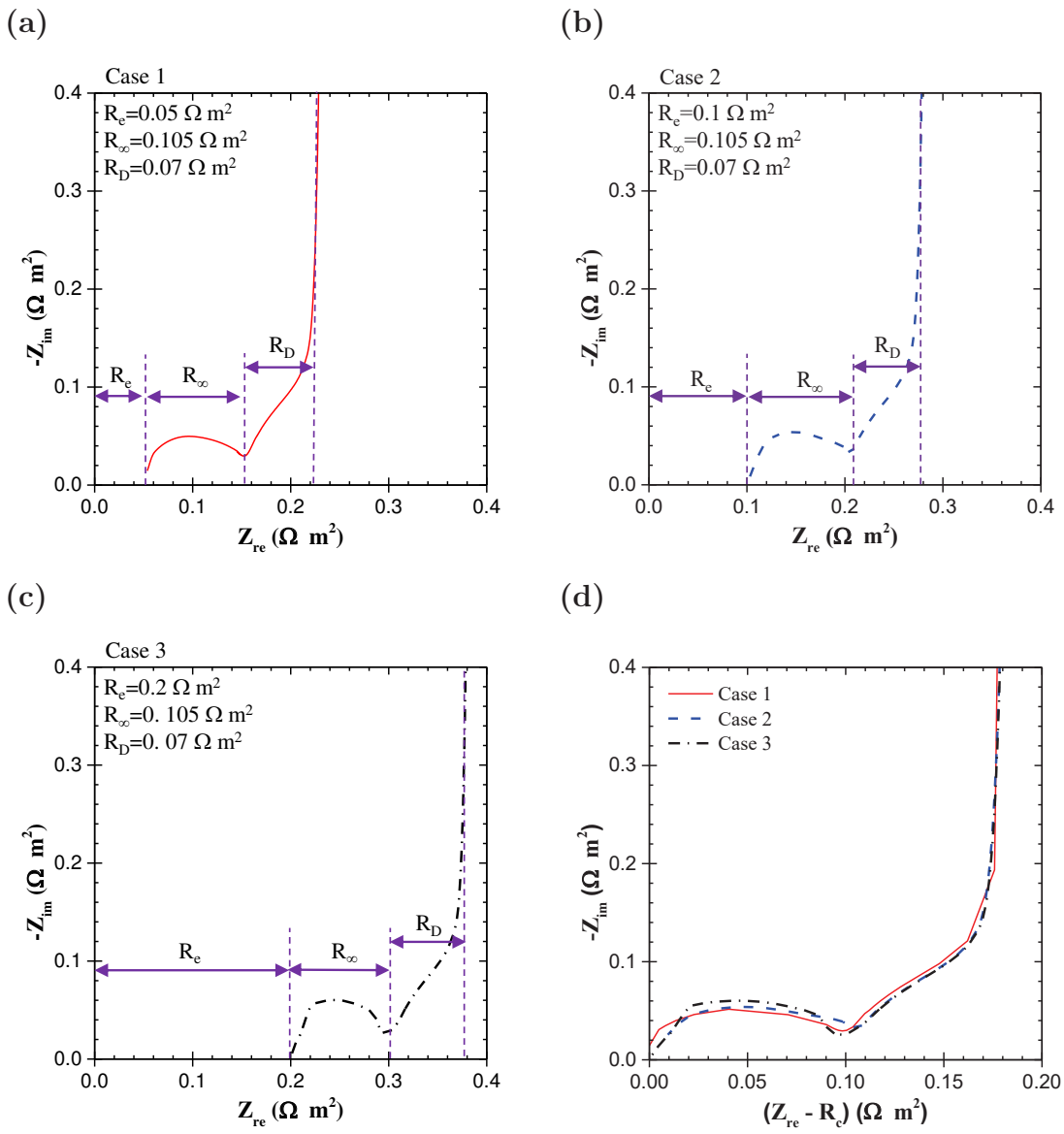

Figure 3.3: (a)-(c) Nyquist plots for EDLC electrode for Cases 1-3 (Table 3.2) featuring electrode resistance R_e of (a) 0.05 Ω m^2, (b) 0.1 Ω m^2, and (c) 0.2 Ω m^2, as predicted by Equation (3.10). (d) Modified Nyquist plots $-Z_{im}$ versus $Z_{re} - R_e$ for the three cases.

(corresponding to $R_{AB} = R_B - R_A$ in Figure 3.1) was equal to the bulk electrolyte resistance R_∞ predicted by Equation (3.14) and equal to 0.105 Ω m^2 in all three cases.

3.3.1.2 Electrolyte resistances R_∞ and R_D

To further explore the effect of electrolyte resistances R_∞ and R_D, Figures 4.5(a)-4.5(c) show the Nyquist plots for EDLC electrodes for Cases 4-6 featuring bulk ion concentration c_∞ of (a) 0.01 mol/L, (b) 0.001 mol/L, and (c) 0.0005 mol/L, corresponding to bulk electrolyte resistance R_∞ [Equation (3.14)] and diffuse layer resistance R_D [Equation (3.13)] of (a) 0.01 Ω m^2 and 0.009 Ω m^2, (b) 0.106 Ω m^2 and 0.07 Ω m^2, and (c) 0.20 Ω m^2 and 0.14 Ω m^2, respectively. All other parameters remained the same in these three cases. Figures 4.5(a)-4.5(c) establish that the diameter of the semi-circle R_{AB} (Figure 3.1) was equal to the bulk electrolyte resistance R_∞ while the resistance R_{BC} corresponded to the diffuse layer resistance R_D. In fact, the same observations could be retrospectively made in Figure 3.3. In addition, Figure 4.5(d) shows the dimensionless Nyquist plot $-Z_{im}/R_\infty$ versus $(Z_{re} - R_e)/R_\infty$ for the three cases. It indicates that, unlike σ_e, the electrolyte concentration c_∞ had a significant impact on the slope k_{BC} (Figure 3.1) corresponding to intermediate EIS frequencies.

Moreover, Figure 3.5(a) shows the dimensionless Nyquist plot -Z_{im}/R_∞ as a function of $(Z_{re} - R_e)/R_\infty$ for intermediate frequencies ranging between f_C and f_B for Cases 6, 9, and 21 in Table 3.2. The frequency f_B corresponded to the intersection between the semi-circle and the non-vertical line (point B in Figure 3.1) while frequency f_C was such that $f_C \approx f_B/20$ (point C in Figure 3.1). These three cases were chosen arbitrarily for illustration purposes. The slope k_{BC} was retrieved by least square fitting between f_B and f_C for Cases 1-23 of Table 3.2 with coefficient of determination R^2 systematically larger than 0.95. Figure 3.5(b) shows the slope k_{BC} as a function of the ratio τ_D/τ_{RC}, for the 23 cases

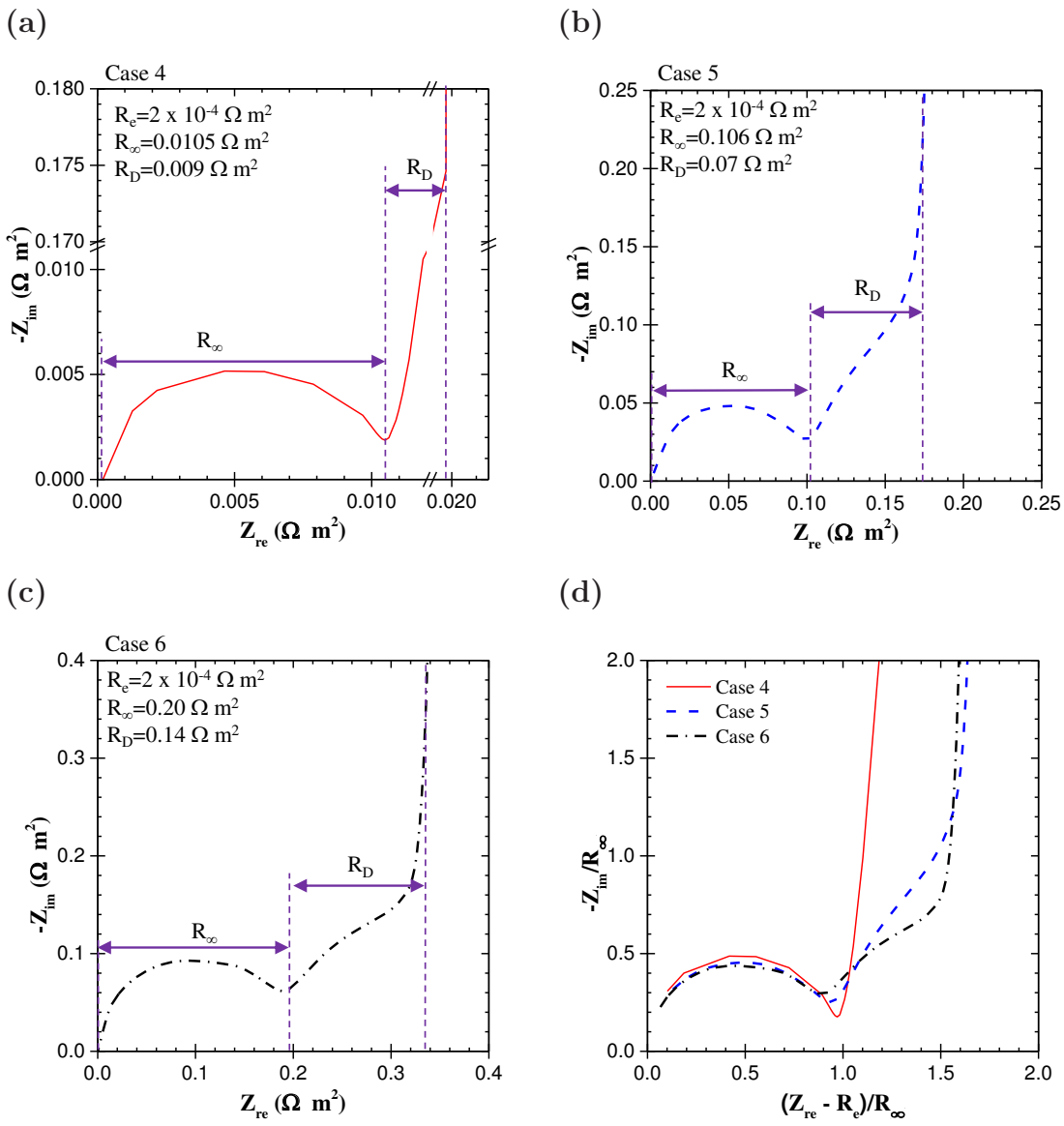

Figure 3.4: (a)-(c) Nyquist plots for EDLC electrodes for Cases 4-6 (Table 3.2) featuring bulk electrolyte resistance R_∞ of (a) 0.011 Ω m^2, (b) 0.106 Ω m^2, and (c) 0.212 Ω m^2, as predicted by Equation (3.14). (d) Dimensionless Nyquist plots $-Z_{im}/R_\infty$ versus $(Z_{re} - R_e)/R_\infty$ for the three cases.

(a)

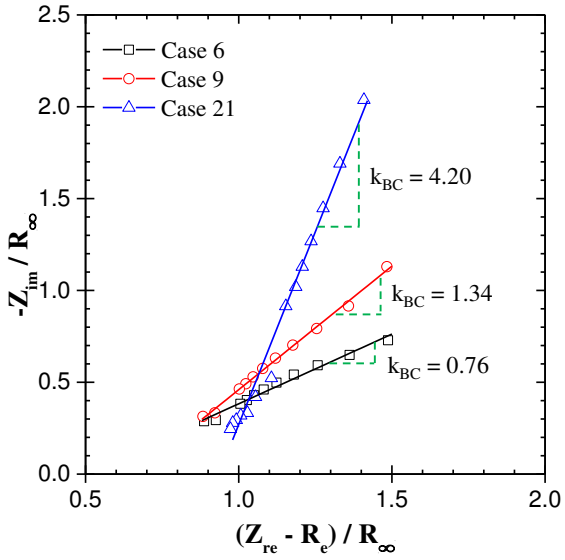

(b)

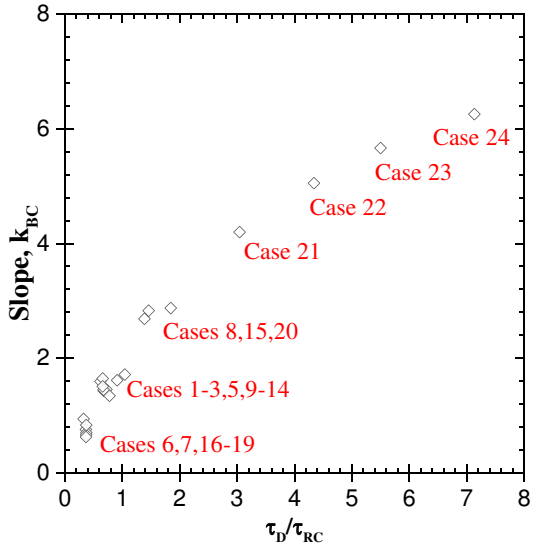

Figure 3.5: (a) Non-vertical line at intermediate frequencies for Cases 6, 9, and 21 (Table 3.2) for illustration. (b) Slope of the non-vertical line as a function of the time scale ratio τ_D/τ_{RC}.

considered. Here, $\tau_D = L^2/D$ is the time scale for ion diffusion in the electrolyte and $\tau_{RC} = (R_\infty + R_D)C_{diff,eq}$ is the RC time constant for the electrolyte domain. Here, only the electrolyte domain was considered due to the fact that σ_e or R_e did not affect the slope k_{BC} (Figure 3.3). Figure 3.5(b) indicates that the slope k_{BC} was only a function of the ratio τ_D/τ_{RC}, regardless of the different parameters considered. In addition, the slope k_{BC} increased with increasing characteristic time ratio τ_D/τ_{RC}. This can be attributed to the fact that the behavior of the electrolyte deviated from an ideal equivalent RC circuit consisting of a resistor $R_\infty + R_D$ in series with a capacitor $C_{diff,eq}$ represented by a vertical line starting from point C (Figure 3.1). Deviation from such ideal equivalent RC circuit was due to ion diffusion in the electrolyte featuring time scale of $\tau_D = L^2/D$. In other words, the slope of the non-vertical line BC (Figure 3.1) can be used to indicate whether the charging process was controlled by EDL formation (large slope) or limited by ion diffusion in the electrolyte (small slope)

3.3.1.3 Differential capacitance $C_{diff,eq}$

To retrieve the equilibrium differential capacitance from EIS simulations, one needs to first determine the low-frequency regime corresponding to the vertical line in the Nyquist plot. Figures 3.6(a) and 3.6(b) show the Nyquist plots of (a) Case 16 and (b) Case 18 (Table 3.2) for illustration purpose. Here, the vertical line indicates that the electrode can be approximated by a simplified RC circuit with a resistor in series with a capacitor. Thus, the imaginary part Z_{im} of the complex impedance Z can be expressed as $Z_{im} = -1/(2\pi C_{diff,eq,EIS} f)$ where $C_{diff,eq,EIS}$ is the equilibrium differential capacitance retrieved from EIS simulations. Figures 3.6(c) and 3.6(d) show $-Z_{im}$ as a function of $1/f$ for (c) Case 16 and (d) Case 18, respectively. They confirm that $-Z_{im}$ was proportional to $1/f$ with the coefficient of proportionality corresponding to $1/2\pi C_{diff,eq,EIS}$. Similar results were obtained for all 24 cases considered. In fact, Table 3.2 compares the

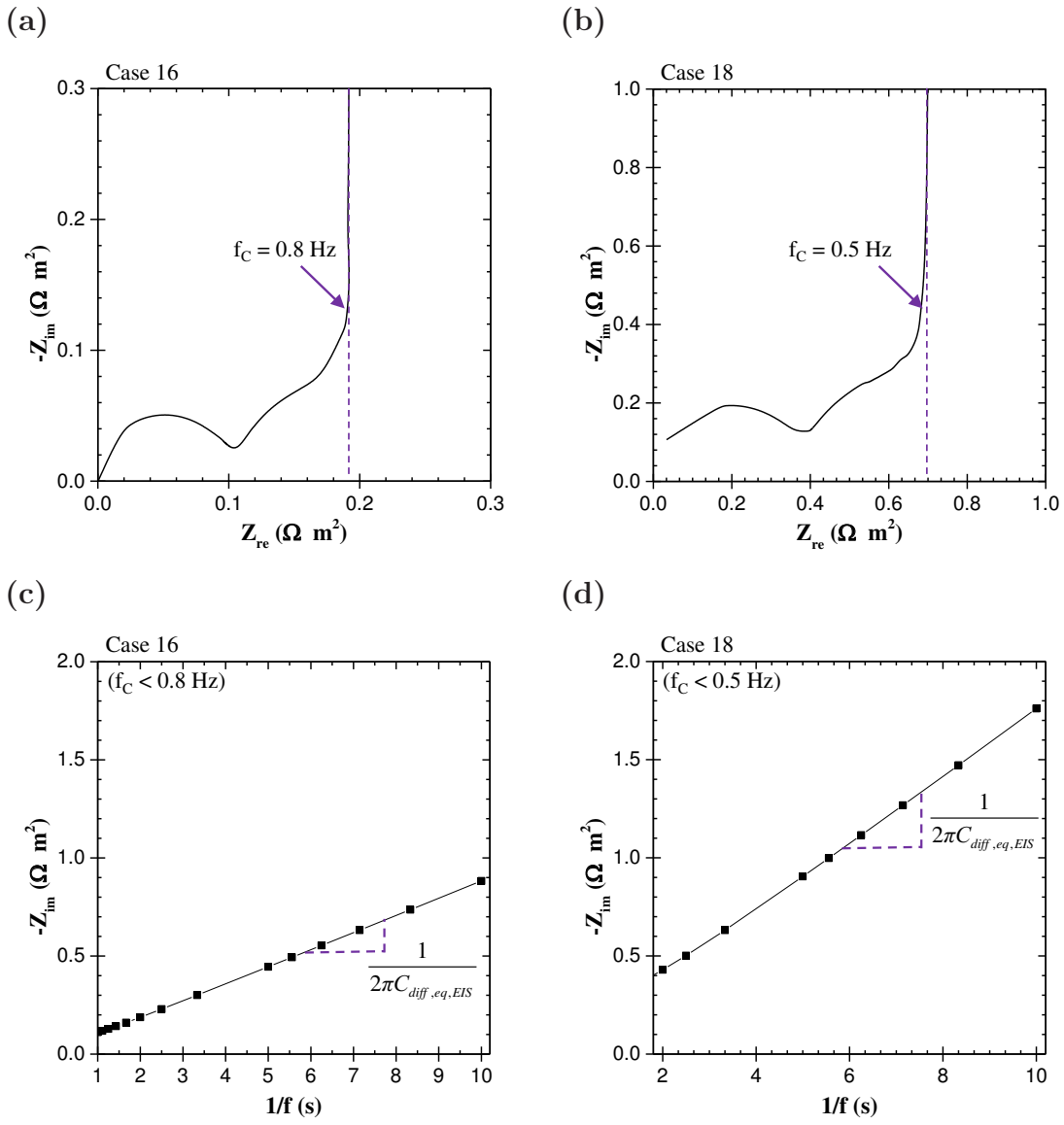

Figure 3.6: (a)(b) Nyquist plots for (a) Case 16 and (b) Case 18 (Table 3.2) and (c)(d) corresponding imaginary part of the impedance $-Z_{im}$ as a function of $1/f$ for low frequencies. Similar results were obtained for all other cases.

equilibrium differential capacitance $C_{diff,eq,EIS}$ retrieved from low frequency EIS simulations, as illustrated in Figures 3.6(c) and 3.6(d), and $C_{diff,eq}$ predicted by Equation (3.20) for all 24 cases considered. The relative difference between the two approaches $e = |C_{diff,eq,EIS} - C_{diff,eq}|/C_{diff,eq}$ was less than 5% for all cases considered, confirming the validity of the retrieval method.

3.3.1.4 Comparison between resistances from EIS and from galvanostatic cycling

Furthermore, Figures 3.7(a) and 3.7(b) show the Nyquist plots and the potential $\psi_s(t)$ as a function of time under galvanostatic cycling for $j_{GC} = 0.01$ mA/cm^2 for Cases 1, 2, 5, 8 (Table 3.2). These four cases were chosen to study the effect of R_e and R_∞ on the internal resistance such that (i) Cases 1, 2, and 5 featured the same bulk electrolyte resistance R_∞, (ii) Cases 2 and 8 had the same electrode resistance R_e, and (iii) the sum $R_e + R_\infty$ were the same for Cases 1 and 8. Moreover, Figures 3.7(c)-3.7(f) show the internal resistance R_{GC} retrieved from the "IR drop" estimated visually in galvanostatic cycling [Equation (3.18)] as well as $R_A = R_e$, $R_B = R_e + R_\infty$, and $R_C = R_e + R_\infty + R_D$ retrieved from Nyquist plot (Figure 3.1) as functions of imposed current density j_{GC} in the range of 10^{-3} - 0.01 mA/cm^2 for (c) Case 1, and (d) Case 2, (e) Case 5, and (f) Case 8. Figure 3.7 indicates that the internal resistance R_{GC} was nearly independent of the imposed current density j_{GC}. Moreover, R_{GC} agreed well with the sum of the electrode and electrolyte resistances, i.e., $R_{GC} = R_e + R_\infty$, for all four cases. The same conclusion was drawn from all 24 cases considered.

3.3.2 EDLC devices

3.3.2.1 Simulations

Figures 3.8(a) and 3.8(b) compare the Nyquist plots for (a) an EDLC electrode

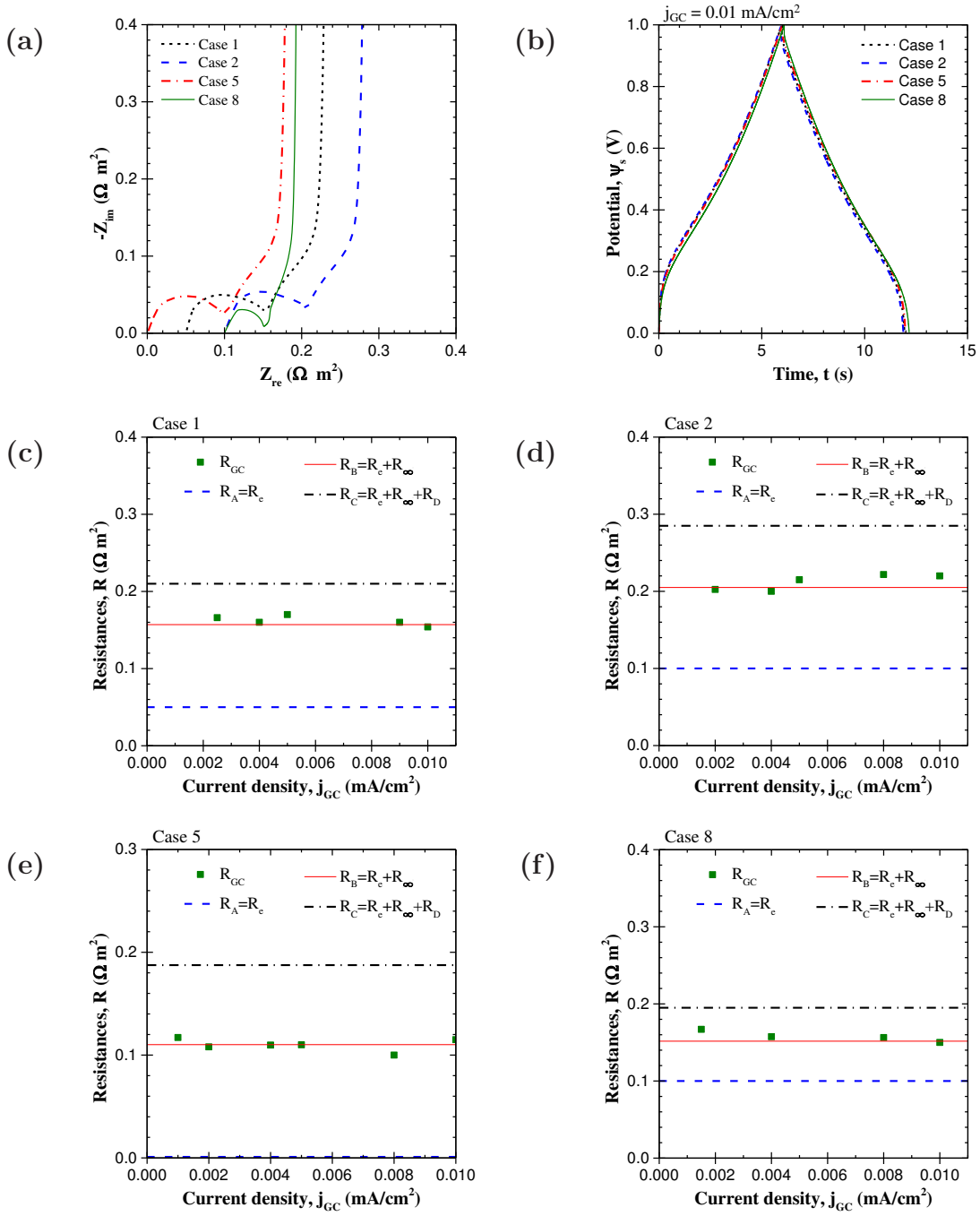

Figure 3.7: (a) Nyquist plots and (b) Potential $\psi_s(t)$ as a function of time under constant current cycling $j_{GC} = 0.01$ mA/cm^2 for Cases 1, 2, 5, and 8 summarized in Table 3.2. (c)-(f) Internal resistance R_{GC} obtained from IR drop in galvanostatic cycling as a function of current density j_{GC} and R_A, R_B, and R_C retrieved from EIS simulations for (c) Case 1, (d) Case 2, (e) Case 5, and (f) Case 8.

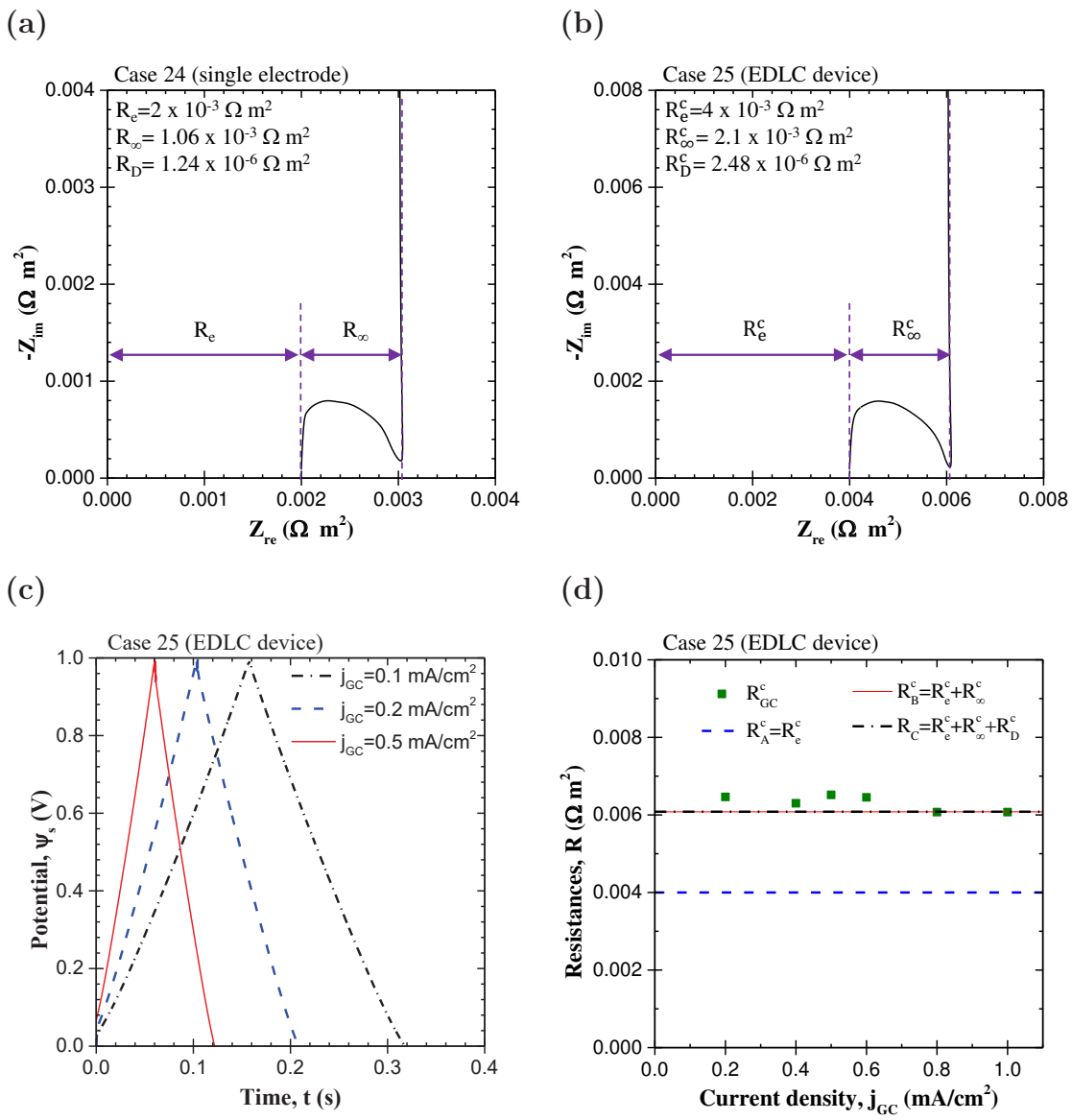

Figure 3.8: (a)(b) Nyquist plots for (a) an EDLC electrode corresponding to Case 24 (Table 3.2) and (b) an EDLC device (Case 25) consisting of two identical electrodes described in Case 24. (c)Potential $\psi_s(t)$ as a function of time for imposed current density j_{GC} of 0.1, 0.2, and 0.5 mA/cm^2 and (d) Corresponding internal resistance R^c_{GC} obtained from IR drop in galvanostatic cycling as a function of current density j_{GC} and R^c_A, R^c_B, and R^c_C retrieved from EIS simulations for Case 25.

(Case 24) and (b) an EDLC device (Case 25) consisting of two electrodes identical to that of Case 24 separated by twice the electrolyte domain thickness. All electrode and electrolyte properties were identical for both cases, as summarized in Table 3.2. The Nyquist plots for a single electrode or for the EDLC device showed the same behavior. The real and the imaginary parts of the complex impedance of the device [Figure 3.8(b)] were equal to twice the values for the individual electrode [Figure 3.8(a)], for all frequencies considered. In addition, the resistance R_A^c of the device corresponded to twice the resistance of an individual electrode, i.e., $R_A^c = R_e^c = 2R_e$. Similarly, the resistance R_{AB}^c for the device was such that $R_{AB}^c = R_\infty^c = 2R_\infty$. In addition, the overlap of points B and C in both Cases 24 and 25 was due to the small diffuse layer resistance R_D compared with R_∞. Indeed, the diffuse layer was thin compared with the relatively thick electrolyte domain due to the large ion concentration (c_∞ =1 mol/L).

Moreover, Figure 3.8 also shows (c) the potential $\psi_s(t)$ as a function of time under galvanostatic cycling for j_{GC} = 0.01 mA/cm^2, and (d) the internal resistance R_{GC} retrieved from the "IR drop" in galvanostatic cycling [Figure 3.8(c)] as well as R_A, R_B, and R_C retrieved from Nyquist plot [Figure 3.8(b)] as functions of imposed current density j_{GC} (0.1 - 1 mA/cm^2) for Case 25. Figure 3.8(d) indicates that, here also, R_{GC} was in good agreement with resistance $R_B^c = R_e^c + R_\infty^c$ for simulations of two-electrode devices. Moreover, Table 3.2 compares the equilibrium differential capacitances $C_{diff,eq,EIS}$ retrieved from EIS and $C_{diff,eq}$ predicted by Equation (3.20). The relative difference $e = |C_{diff,eq,EIS} - C_{diff,eq}|/C_{diff,eq}$ was less than 5% for both cases considered. Overall, this section confirmed that all interpretations of the Nyquist plots for single electrodes also apply to EDLC devices. In addition, the interpretations discussed previously should also be valid for EDLC devices with asymmetric electrolyte and/or non-identical electrodes. Then, the resistances R_A, R_{AB}, and R_{BC} (Figure 3.1) would correspond to (i) the sum of the resistances of the positive and negative electrodes, (ii) the bulk electrolyte

resistance, and (iii) the sum of the resistance of the two different diffuse layers near the positive and negative electrodes, respectively.

3.3.2.2 Experiments

Finally, Figure 3.9(a) shows experimental Nyquist plots for three different EDLC devices with footprint surface area of 1 cm^2 consisting of two identical electrodes made of 80 wt% activated carbon, 5 wt% TX100 as surfactant, 1.5 wt% carboxymethyl cellulose as thickening agent and binder, and 13.5 wt% styrene-butadiene rubber as binder with different electrolytes namely (i) 1 M $LiPF_6$ in EC:DMC(1:1), (ii) 1 M citric acid in DI water, and (iii) 1 M TEATFB in acetonitrile. Note that different types of binders and surfactants can affect the resistance of the electrodes by changing particle-to-particle contact of activated carbon and affect the capacitance of the electrodes by changing the available carbon surface area. Thus, surfactant and binders can affect the Nyquist plot. Details of the synthesis and characterization of the electrodes and of the EDLC devices were reported in Ref. [5] and need not be repeated. In brief, Table 3.3 summarized (i) the materials used for the electrode and electrolyte, (ii) the electrode R_e^{exp} and(iii) bulk electrolyte R_∞^{exp} resistances retrieved from the Nyquist plot based on the interpretations discussed previously, (iii) the internal resistance R_{GC} obtained from galvanostatic cycling as well as (iv) the resistances R_A^{exp}, R_B^{exp}, and R_C^{exp}, and (v) the equilibrium differential capacitance $C_{diff,eq,EIS}$ of the cell obtained from EIS measurements. The IR drop was visually estimated from the potential-time curve in galvanostatic cycling. In addition, the resistance R_C^{exp} was larger than the resistance measured at the lowest frequency due to the lack of a clear "vertical line" for low frequencies. Table 3.3 indicates that the sum of the electrode resistances R_e^{exp} was small and did not vary significantly among the three devices. This is consistent with the fact that the electrodes of all three devices were nearly identical and made of activated carbon with a CMC binder [5]. In addition, the electrode

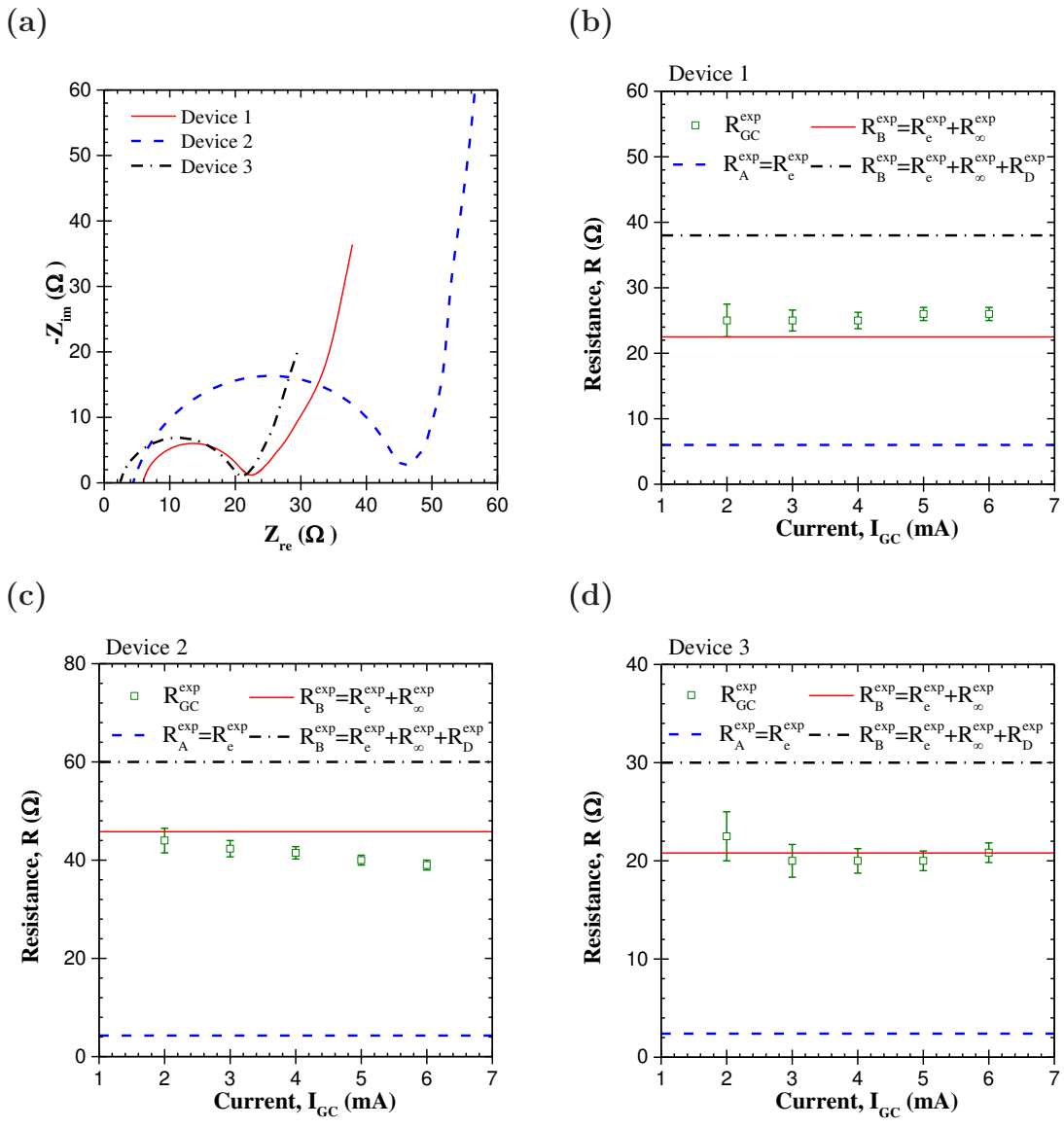

Figure 3.9: (a) Nyquist plots for the three experimental EDLC devices with activated carbon electrodes and different electrolytes (Table 3.3) [5]. (b)-(d) Internal resistance R_{GC}^{exp} obtained experimentally from galvanostatic cycling as a function of current I_{GC} and R_A^{exp}, R_B^{exp}, and R_C^{exp} obtained from EIS measurement for (b) Device 1, (c) Device 2, and (d) Device 3.

Table 3.3: Electrode materials and electrolyte species, operating conditions, resistance and capacitance values of devices in experiments [5]

Device	Electrode	Electrolyte	Potential window		Current	Resistances						Capacitance
			ψ_{min} (V)	ψ_{max} (V)	I_{GC} (mA)	R_e^{exp} (Ω)	R_∞^{exp} (Ω)	R_{GC}^{exp} (Ω)	R_A^{exp} (Ω)	R_B^{exp} (Ω)	R_C^{exp} (Ω)	$C_{diff,eq,EIS}$ (mF)
1	activated carbon	1M $LiPF_6$ in EC:DMC(1:1)	0	1	2 - 6	6.0	16.5	22.5 - 27.5	6.0	22.5	> 38.0	102.2
2	activated carbon	1M citric acid in DI water	0	1	2 - 6	4.3	41.5	38.0 - 46.5	4.3	45.8	> 60.0	117.7
3	activated carbon	1M TEATFB in Acetonitrile	0	1	2 - 6	2.4	18.4	18.3 - 25.0	2.4	20.8	> 30.0	91.4

resistance R_e^{exp} was small compared with that of the bulk electrolyte resistance R_∞^{exp}, which contributed the most to the internal resistance. Moreover, the bulk electrolyte resistance R_∞^{exp} for Device 2 was much larger than that for Devices 1 and 3. This can be attributed to the fact that citric acid is a weak electrolyte featuring low ionic conductivity [5]. Furthermore, Figures 3.9(b)-3.9(d) show the internal resistance R_{GC} retrieved from "IR drop" in galvanostatic cycling [Equation (3.18)] as a function of the imposed current I_{GC} (2 - 6 mA) as well as R_A^{exp}, R_B^{exp}, and R_C^{exp} retrieved from Nyquist plots for (b) Device 1, (c) Device 2, and (d) Device 3. Figure 3.9 indicates that here also, R_{GC} was nearly independent of the imposed current I_{GC} and in good agreement with $R_B^{exp} = R_e^{exp} + R_\infty^{exp}$. These results were consistent with numerical simulations Previously discussed.

3.4 Chapter summary

This chapter presented rigorous physical interpretations of Nyquist plots from electrochemical impedance spectroscopy (EIS) for EDLC electrodes and devices without using an equivalent RC circuit. The Nyquist plots presenting the imaginary and real parts of the complex impedance of individual EDLC electrodes and devices were numerically reproduced based on the modified Poisson-Nernst-Planck model and closely resembled experimental measurements. It established that the electrode resistance, bulk electrolyte resistance, diffuse layer resistance, and equilibrium differential capacitance can be retrieved directly from Nyquist plots. In addition, the internal resistance retrieved from the sum of electrode and bulk electrolyte resistances in EIS simulations showed good agreement with the internal resistance retrieved from the so-called "IR drop" in galvanostatic cycling. Finally, the above results and interpretations were confirmed experimentally for EDLC devices with electrodes made of activated carbon and various electrolytes.

CHAPTER 4

Physical Interpretations of Electrochemical Impedance Spectroscopy (EIS) of Pseudocapacitive Electrodes

The previous chapter provided physical interpretations of EIS results for EDLC electrodes. This chapter aims to extend the simulation tools and provide physical interpretations of EIS measurements for pseudocapacitive electrodes. To do so, EIS measurements of pseudocapacitive electrodes based on three-electrode setups were numerically reproduced for a wide range of electrode conductivity, electrolyte thickness, redox reaction rate constant, and bias potential. The chapter also aims to validate experimentally the physical interpretation of EIS measurements developed numerically.

4.1 Background

Nyquist plots present the imaginary part $-Z_{im}$ as a function of the real part Z_{re} of the complex impedance. They typically consist of one [23, 24, 49–55] or two [6, 25–29, 56–60] semi-circles at relatively high frequencies and a non-vertical line with respect to the real axis at low frequencies [49–60] for electrodes consisting of transition metal oxides or conductive polymers capable of engaging in reversible redox reactions with ions present in the electrolyte [12, 13, 55, 71, 72, 123–133, 135, 136]. Figure 4.1 shows a typical Nyquist plot for a pseudocapacitive electrode. It consists of two semi-circles, i.e., a semi-circle at high frequencies between points A and B and one at intermediate frequencies between points B and C, as well as a non-vertical line at low frequencies beyond point C. Note that the non-vertical line may be absent for some redox active electrodes [6, 23–29].

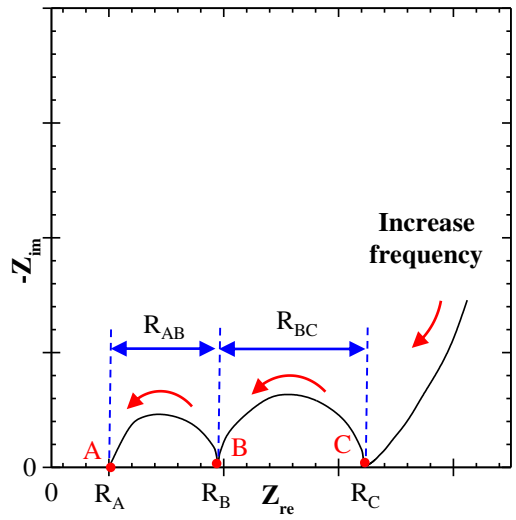

Figure 4.1: Illustration of typical Nyquist plots obtained for pseudocapacitive electrodes using three-electrode setup.

Multiple and often contradictory physical interpretations of experimental Nyquist plots have been proposed in the literature [23–27, 49–60]. For example, the resistance R_A at point A (Figure 3.1) has been attributed to (i) the bulk electrolyte resistance [23, 51, 52, 56] or to (ii) the sum of the electrode resistance, the bulk electrolyte resistance, and the contact resistance between the electrode and the current collector [24, 26, 49, 50, 54, 60]. For Nyquist plots with one semi-circle, the diameter of the semi-circle has been interpreted as (i) the so-called charge transfer resistance [23, 24, 51–54] or as (ii) the sum of the electrolyte solution and electrode resistances [55]. For Nyquist plots with two semi-circles, the diameter of the semi-circle at higher frequencies $R_{AB} = R_B - R_A$ (Figure 3.1) has been assigned to (i) the electrode resistance [56], or to (ii) the charge transfer resistance associated with pseudocapacitive charge storage including redox reactions and/or ion intercalation [25, 57, 60], or to (iii) the electrolyte resistance in the porous electrodes [26, 27, 58, 59]. The diameter of the semi-circle at lower frequencies $R_{BC} = R_C - R_B$ (Figure 3.1) has been attributed to (i) the ionic or

so-called diffusion resistance of the electrolyte [25, 60], or to (ii) the resistance of the solid-electrolyte interphase (SEI) layer [29, 160], or to (iii) the charge transfer resistance [26, 27, 56–60]. More conservatively, it has also been pointed out that "definitive assignment of each arc to a particular phenomenon is not possible given the probed data" [60]. Finally, the non-vertical line beyond point C (Figure 3.1) at low frequencies (if observed) has been assigned to (i) ion transport limitation in the electrolyte in porous electrode structures [51] or to (ii) ion transport limitation in the bulk electrolyte [56–58].

This chapter aims to provide a rigorous interpretation of Nyquist plots obtained by EIS for redox active electrodes. To do so, EIS measurements of redox active electrodes based on three-electrode configurations were numerically reproduced for a wide range of electrode conductivity, electrolyte thickness, redox reaction rate constant, and bias potential. Then, the physical interpretation of EIS measurements developed numerically was validated experimentally.

4.2 Numerical analysis

4.2.1 Schematic and assumptions

Figure 4.2 shows a one-dimensional (1D) simulated domain consisting of a planar current collector supporting a planar redox active working electrode of thickness L_P and an electrolyte domain of thickness L corresponding to a three-electrode configuration. Following assumptions were made: (1) the electrolyte was binary and symmetric, i.e., it consisted of two ion species of opposite valency $\pm z$ ($z > 0$). (2) The two ion species were also assumed to have identical diameter a and diffusion coefficient D. (3) The Stern layer contained no free charge and its thickness H was approximated as the radius of the ions, so that $H = a/2$ [8, 16, 151]. (4) The transport properties of the electrode and electrolyte were taken as constant. (5) Bulk motion of the electrolyte was negligible. (6) Ion intercalation in the

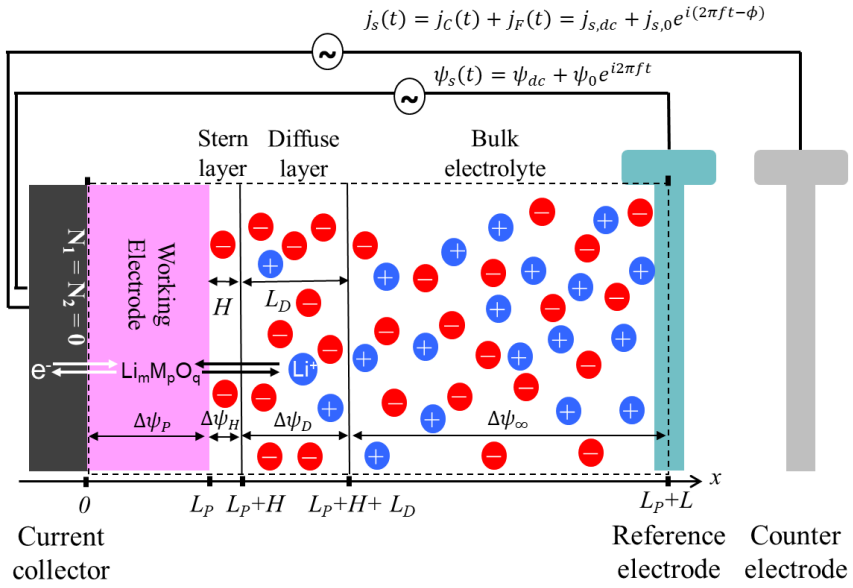

Figure 4.2: Schematics of the simulated one-dimensional pseudocapacitive electrode in a three-electrode setup. The dashed line encloses the computational domain simulated.

electrode was modeled as a diffusion process. (7) Heat generation was ignored and the temperature was uniform and constant in the electrode and electrolyte. (8) The contact resistance between the electrode and the current collector and the resistance of the current collector were negligible. (9) Self-discharge of the electrode or the device was ignored.

Simulations reported in this chapter were based on the modified Poisson-Nernst-Planck (MPNP) model for the spatiotemporal evolution of the potential $\psi(x,t)$ [Equation (2.1)] in the electrode and electrolyte as well as the ion concentrations $c_1(x,t)$ of cations and $c_2(x,t)$ of anions [Equations (2.2) and (2.4)] in the binary and symmetric electrolyte for redox active electrodes. In addition, the boundary conditions varied depending on whether EIS or cyclic voltammetry were simulated. EIS simulations imposed potential $\psi_s(t)$ at the current collector/electrode interface as a harmonic function of time t [Equation (1.3)]. For cyclic voltammetry, the potential $\psi_s(t)$ at the current collector/electrode inter-

face was imposed as a triangular wave with respect to cycle period [Equation (1.1)].

4.2.2 Constitutive relationships

In order to solve the coupled transient 1D equations as well as the initial and boundary conditions, a total of 21 parameters were necessary including (i) the electrode properties σ_P, k_0 $\Delta\psi_{eq}$, $c_{1,P,max}$, $c_{1,P,0}$, α, and $D_{1,P}$, (ii) the electrolyte properties c_∞, z, ϵ_r, a, and D, (iii) the dimensions of the simulated electrode and electrolyte domains L_P and L, along with (iv) the operating conditions ψ_{dc}, ψ_0, and f for EIS simulations and ψ_{min}, ψ_{max} and v for cyclic voltammetry, and (v) temperature T (in K).

The electrical conductivity σ_P of the electrode, the length of the electrolyte domain L, the redox reaction rate constant k_0, and the bias potential ψ_{dc} were treated as variables to achieve various resistances. Most parameters were taken from the literature. For electrodes consisting of transition metal oxides, the equilibrium potential difference $\Delta\psi_{eq}$ can be modeled as a linear function of the state-of-charge (SOC) defined ad $c_{1,P}/c_{1,P,max}$, where $c_{1,P,max}$ is the maximum intercalated lithium concentration in the pseudocapacitive electrode [82, 83, 161]. Note that for MnO_2 dense films of thickness 100 μm, $\Delta\psi_{eq}(t)$ (in V) was measured as [162]

$$\Delta\psi_{eq}(t) = 10.5[4 - c_{1,P}(t)/c_{1,P,max}] - 39.9. \tag{4.1}$$

Here, $c_{1,P,max}$ was taken as $c_{1,P,max} \approx 31.9$ mol/L, corresponding to fully lithiated metal oxide $LiMnO_2$ [163, 164]. The initial concentration of Li^+ in the electrode $c_{1,P,0}$ was chosen as the equilibrium concentration solution for electrode potential equal to ψ_{dc}. The transfer coefficient α was assumed to be 0.5, corresponding to identical energy barriers for forward and backward redox reactions [8]. The diffusion coefficient $D_{1,P}$ of the intercalated Li^+ in the transition metal oxides

Table 4.1: Value or range of electrode and electrolyte properties and dimensions used in the simulations reported in this study.

Parameter	**Symbol**	**Value**	**Unit**
Electrode conductivity	σ_P	10^{-5} - 5 x 10^{-4}	S/m
Maximum ion concentration in the electrode	$c_{1,P,max}$	31.9	mol/L
Initial ion concentration in the electrode	$c_{1,P,0}$	6.38 - 6.58	mol/L
Reaction rate constant	k_0	10^{-9} - 10^{-8}	$\mathrm{m}^{1+3\,\alpha}\mathrm{mol}^{-\alpha}\mathrm{s}^{-1}$
Transfer coefficient	α	0.5	
Diffusion coefficient in the electrode	$D_{1,P}$	10^{-14}	m^2/s
Bulk ion concentration	c_∞	1	mol/L
Valency	z	1	
Dielectric constant	ϵ_r	64.4	
Ion diameter	a	0.67	nm
Diffusion coefficient in the electrolyte	D	2.6 x 10^{-10}	m^2/s
Electrode thickness	L_P	100	nm
Electrolyte thickness	L	16 - 64	μm
Bias potential	ψ_{dc}	0.1 - 0.6	V
Amplitude of oscillating potential	ψ_0	5	mV
Frequency	f	0.1 - 5 x 10^4	Hz
Potential window	ψ_{min}	0	V
	ψ_{max}	0.5	V
Scan rate	v	0.001	mV/s
Temperature	T	298	K

typically ranges from 10^{-16} to 10^{-10} m^2/s [165]. Here, $D_{1,P}$ was chosen as 10^{-14} m^2/s.

As for the electrolyte, we considered 1M $LiClO_4$ salt in propylene carbonate (PC) solvent such that the bulk ion concentration $c_\infty = 1$ mol/L and valency $z = 1$. The dielectric constant was taken as that of PC, i.e., $\epsilon_r = 64.4$ [152]. The effective solvated ion diameter a and diffusion coefficient D were taken as those of solvated Li^+ ion in PC such that $a = 0.67$ nm and D = 2.6 x 10^{-10} m^2/s [166].

Finally, for EIS simulations, the oscillating potential amplitude was set as $\psi_0 = 5$ mV and the frequency f varied between 0.1 and 8 x 10^8 Hz. For cyclic voltammetry, the potential window was $\psi_{min} = 0$ V and $\psi_{max} = 0.5$ V and the scan rate v was very low, i.e., $v = 0.001$ mV/s, to reproduce conditions of no kinetic limitations. The temperature T was set as $T = 298$ K. Table 7.1 summarizes the values or ranges of these different parameters.

4.2.3 Data processing

4.2.3.1 Faradaic and capacitive current densities

The current density at the electrode/electrolyte interface $j_s(t)$ [Equation (1.3)] can be expressed as the sum of (i) the capacitive current density $j_C(t)$ resulting from the EDL formation and (ii) the faradaic current density $j_F(t)$ related to the redox reactions, i.e., $j_s(t) = j_C(t)+j_F(t)$. The capacitive current density $j_C(L_P, t)$ can be defined as [167]

$$j_C(L_P, t) = -\epsilon_0 \epsilon_r \frac{\partial^2 \psi}{\partial x \partial t}(L_P, t) \tag{4.2}$$

where $\epsilon_0 = 8.854 \times 10^{-12}$ F/m is the vacuum permittivity. The faradaic current density $j_F(L_P$,t) can be defined by the generalized Frumkin-Butler-Volmer model evaluated at the electrode/electrolyte interface and expressed as [8]

$$j_F(L_P, t) = j_{F,ex}(t)\left\{\exp\left[\frac{(1-\alpha)zF\eta(L_P, t)}{R_u T}\right] - \exp\left[\frac{-\alpha z F \eta(L_P, t)}{R_u T}\right]\right\} \tag{4.3}$$

where $j_{F,ex}(t)$ [Equtaion (2.7)] is the so-called exchange current density, $F = eN_A = 9.648 \times 10^4$ C/mol is the Faraday's constant, and $R_u = 8.314$ J mol^{-1} K^{-1} is the universal gas constant.

4.2.3.2 Electrical resistances

The electrical resistance R_P (in Ω m^2) per unit surface area of the planar electrode and the bulk electrolyte resistance R_∞ (in Ω m^2) depend on the thicknesses L_P and L and the electrical conductivities σ_P and σ_∞ of the electrode and electrolyte according to [7, 168]

$$R_P = L_P/\sigma_P \qquad \text{and} \tag{4.4}$$

$$R_\infty \approx L/\sigma_\infty \qquad \text{with} \qquad \sigma_\infty = (2z^2F^2Dc_\infty)/(R_uT). \tag{4.5}$$

Moreover, the so-called charge-transfer resistance R_{ct} (in Ω m^2) under EIS simulations can be expressed as [8]

$$R_{ct} = \frac{\eta - \eta_{dc}}{j_F - j_{F,dc}} \tag{4.6}$$

where η (in V) is the surface overpotential [Equation (2.8)], η_{dc} is the time-independent DC overpotential, j_F (in A/m^2) is the resulting faradaic current density, and $j_{F,dc}$ is the time-independent DC faradaic current density. Here, η and j_F can also be expressed in complex notation as

$$\eta(t) = \eta_{dc} + \eta_0 e^{i[2\pi f t - \phi_\eta(f)]} \quad \text{and} \quad j_F(t) = j_{F,dc} + j_{F,0} e^{i[2\pi f t - \phi_F(f)]} \tag{4.7}$$

where η_0 is the amplitude of the oscillating overpotential, $\phi_\eta(f)$ is the frequency-dependent phase angle between the imposed potential $\psi_s(t)$ and the overpotential $\eta(t)$, $j_{F,0}$ is the amplitude of the oscillating faradaic current density, and $\phi_F(f)$ is the frequency-dependent phase angle between the imposed potential $\psi_s(t)$ and the faradaic current density $j_F(t)$.

Similarly, the mass-transfer resistance R_{mt} (in Ω m^2) caused by ion transport in the diffuse layer can be expressed as [8]

$$R_{mt} = \frac{\Delta\psi_D - \Delta\psi_{D,dc}}{j_F - j_{F,dc}} \tag{4.8}$$

where $\Delta\psi_D$ (in V) is the potential drop across the diffuse layer of thickness L_D and located between $x = L_P + H$ and $x = L_P + H + L_D$ (Figure 7.1) while $\Delta\psi_{D,dc}$ is the time-independent DC potential drop across the diffuse layer. Similarly, using complex notations, $\Delta\psi_D$ can be expressed as

$$\Delta\psi_D = \Delta\psi_{D,dc} + \Delta\psi_{D,0} e^{i[2\pi f t - \phi_D(f)]} \tag{4.9}$$

where $\Delta\psi_{D,0}$ is the amplitude of the oscillating potential drop across the diffuse layer, and $\phi_D(f)$ is the frequency-dependent phase angle between the imposed potential $\psi_s(t)$ and the potential drop across the diffuse layer $\Delta\psi_D(t)$.

4.3 Experimental methods

In order to validate experimentally the physical interpretation of EIS obtained numerically, a redox active MoS_2 electrode was synthesized. First, a slurry was prepared by mixing 70 wt% MoS_2 nanoparticles, 10 wt% Super P (Alfa Aesar), 10 wt% multiwall carbon nanotubes (mwCNT, Sigma Aldrich), and 10 wt% polyvinylidene fluoride (PVDF, Kynar) in N-methyl-2-pyrrolidinone (NMP, Sigma Aldrich). The MoS_2 nanoparticles were synthesized through the sulfurization of MoO_2 nanoparticles according to a previously reported procedure [169]. Then, the slurry was drop-cast onto a 1x1 cm^2 carbon-coated aluminum current collector (MTI) with a weight loading of 0.4 mg MoS_2 nanoparticles. The electrode was dried in air overnight and under vacuum at 120^{o}C for at least 2 h. Finally, the electrode was placed in a three-neck half-cell with activated carbon counter and (i) Li/Li^+ or (ii) Na/Na^+ reference electrodes where each electrode was clipped to and immersed in (i) 1 M $LiClO_4$ (Sigma Aldrich) in ethylene carbonate:dimethyl carbonate (EC:DMC, 1:1 by volume) or (ii) 1 M $NaClO_4$ (Alfa Aesar) in EC/DMC (1:1 by volume) electrolyte. EIS measurements were performed on the MoS_2 electrode with potential amplitude ψ_0 of 10 mV, bias potential ψ_{dc} versus reference electrodes ranging between 1.8 and 2.2 V and frequency f ranging between 0.1 Hz and 2 x 10^5 Hz.

4.4 Results and discussion

Table 4.2 summarizes the 8 different cases considered to identify the electrode R_P, electrolyte R_∞, charge transfer R_{ct} and mass transfer R_{mt} resistances from

Table 4.2: Simulation parameters and corresponding resistances R_P, R_∞, R_{ct}, and R_{mt} values for 9 EIS simulations for pseudocapacitive electrodes.

Case number	$\boldsymbol{\sigma_P}$ **(S/m)**	$\boldsymbol{L}$ **(μm)**	$\boldsymbol{k_0}$ **($\mathbf{m^{1+3\,\alpha}mol^{-\alpha}s^{-1}}$)**	$\boldsymbol{\psi_{dc}}$ **(V)**	$\boldsymbol{R_P}$ **(Ω cm^2)**	$\boldsymbol{R_\infty}$ **(Ω cm^2)**	$\boldsymbol{R_{ct}}$ **(Ω cm^2)**	$\boldsymbol{R_{mt}}$ **(Ω cm^2)**
1	1 x 10^{-4}	64	10^{-9}	0.1	10	4.2	24.3	20.2
2	5 x 10^{-5}	64	10^{-9}	0.1	20	4.2	13.5	11.4
3	1 x 10^{-5}	64	10^{-9}	0.1	100	4.2	7.6	6.6
4	5 x 10^{-5}	32	10^{-9}	0.1	20	2.1	17.1	14.9
5	5 x 10^{-5}	16	10^{-9}	0.1	20	1.05	19.9	17.7
6	5 x 10^{-5}	32	5 x 10^{-9}	0.1	20	2.1	1.4	1.1
7	5 x 10^{-5}	32	10^{-8}	0.1	20	2.1	0.6	0.5
8	5 x 10^{-5}	8	10^{-8}	0.1	20	0.53	0.7	0.6
				0.2	20	0.53	0.7	0.6
				0.3	20	0.53	0.8	0.7
				0.4	20	0.53	0.9	0.7
				0.6	20	0.53	1.2	1.0
9	5 x 10^{-5}	8	0	0.1	20	0.53	-	-
				0.3	20	0.53	-	-
				0.6	20	0.53	-	-

the Nyquist plots of a pseudocapacitive electrode in a three-electrode setup.

4.4.1 Current densities and overpotentials

Figures 4.3(a)-4.3(c) show the (i) faradaic current density $j_F(t)$, (ii) capacitive current density $j_C(t)$, and (iii) total current density $j_s(t) = j_C(t) + j_F(t)$ as functions of the dimensionless time ft during one EIS cycle for Case 1 (Table 4.2) at frequency f equal to (a) 2 Hz, (b) 20 Hz, and (c) 2000 Hz. A phase shift between capacitive and faradaic current densities was observed at all frequencies. In addition, the faradaic current density $j_F(t)$ always dominated over the capacitive current density $j_C(t)$ (i.e., $j_{F,dc} > j_{C,dc}$) and their amplitudes were dependent on frequency. Figure 4.3(d) shows the amplitudes of oscillations of (i) the faradaic current density $j_{F,0}$, (ii) the capacitive current density $j_{C,0}$, and (iii) the total current density $j_{s,0}$ as functions of frequency f. It indicates that the amplitude of the faradaic current density $j_{F,0}$ was the largest at low frequencies while that of the capacitive current density $j_{C,0}$ was the largest at high frequencies. In other words, the major contribution to the impedance Z was the faradaic reactions at low frequencies and the EDL formation at high frequencies.

Moreover, Figure 4.3(e) shows the overpotential $\eta(t)$ and the faradaic current density $j_F(t)$ as functions of the dimensionless time ft for Case 1 (Table 4.2) at frequency f equal to 2, 20 and 2000 Hz. It indicates that η and j_F were in phase at all frequencies, i.e., $\phi_\eta(f) = \phi_F(f)$ [Equation (4.7)]. Figure 4.3(f) shows j_F as a function of η for EIS simulations for Case 1. It established a linear relationship between j_F and η for all frequencies considered. In addition, the amplitude η_0 of the overpotential oscillations were very small. Note that similar conclusions can be drawn from the plot of j_F as a function of $\Delta\psi_D$ (Figure S1 in supporting information). Thus, the charge transfer resistance and mass transfer resistance,

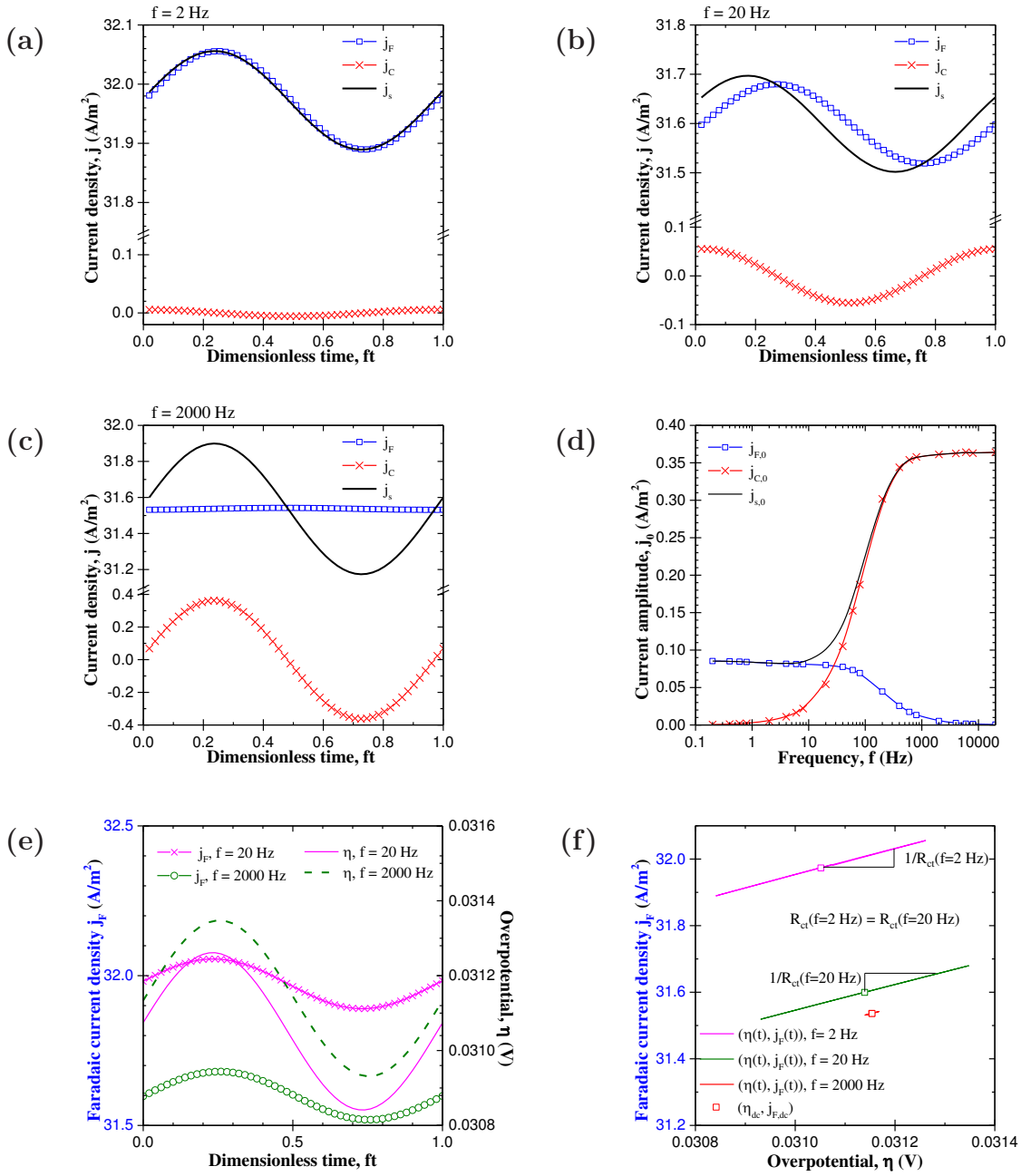

Figure 4.3: (a)-(c) Faradaic j_F, capacitive j_C, and total $j_s = j_C + j_F$ current densities as functions of the dimensionless time ft in one oscillating cycle for frequency of (a) 2 Hz, (b) 20 Hz, and (c) 2000 Hz. (d) Amplitudes of current density oscillations as functions of frequency. (e) Faradaic current density j_F and overpotential η as functions of dimensionless time ft and (f) j_F vs. η for frequencies f of 2, 20, and 2000 Hz under EIS simulations.

given by Equations (4.6) and (4.8), can be estimated as

$$\frac{1}{R_{ct}} = \frac{j_F(t) - j_{F,dc}}{\eta(t) - \eta_{dc}} \approx \left.\frac{\partial j_F}{\partial \eta}\right|_{\eta=\eta_{dc}} \tag{4.10}$$

$$\frac{1}{R_{mt}} = \frac{j_F(t) - j_{F,dc}}{\Delta\psi_D(t) - \Delta\psi_{D,dc}} \approx \left.\frac{\partial j_F}{\partial \Delta\psi_D}\right|_{\Delta\psi_D=\Delta\psi_{D,dc}} \tag{4.11}$$

In other words, $1/R_{ct}$ and $1/R_{mt}$ correspond, respectively, to the slope of j_F vs. η and j_F vs. $\Delta\psi_D$ near the DC operating points. Figure 4.3(f) also indicates that R_{ct} was independent of frequency. Similar observations can be made for the mass transfer resistance R_{mt} [Figure S1(b) in supporting information].

4.4.2 Interpretation of Nyquist plots

4.4.2.1 Electrode resistance R_P

Figure 4.4 shows the Nyquist plots for the electrodes of Cases 1-3 featuring electrode electrical conductivity σ_P equal to (a) 1 x 10^{-4} S/m, (b) 5 x 10^{-5} S/m, and (c) 1 x 10^{-5} S/m, corresponding to electrode resistance R_P [Equation (4.4)] equal to (a) 10 Ω cm^2, (b) 20 Ω cm^2, and (c) 100 Ω cm^2, respectively. All other parameters remained the same in these three cases (Table 4.2). Figure 4.4 indicates that the high-frequency intersection of the Nyquist plot with the Z_{re}-axis (corresponding to R_A in Figure 3.1) increased with decreasing conductivity σ_P and was systematically equal to the electrode resistance R_P. The same observations have already been made for simulations of EDLC electrodes [168].

Moreover, the diameter of the semi-circle at high frequencies (corresponding to $R_{AB} = R_B - R_A$ in Figure 3.1) was not affected by the electrode conductivity and was equal to 4.2 Ω cm^2 in all cases. By contrast, the diameter of the semi-circle at lower frequencies (corresponding to $R_{BC} = R_C - R_B$ in Figure 3.1) decreased with decreasing electrode conductivity σ_P.

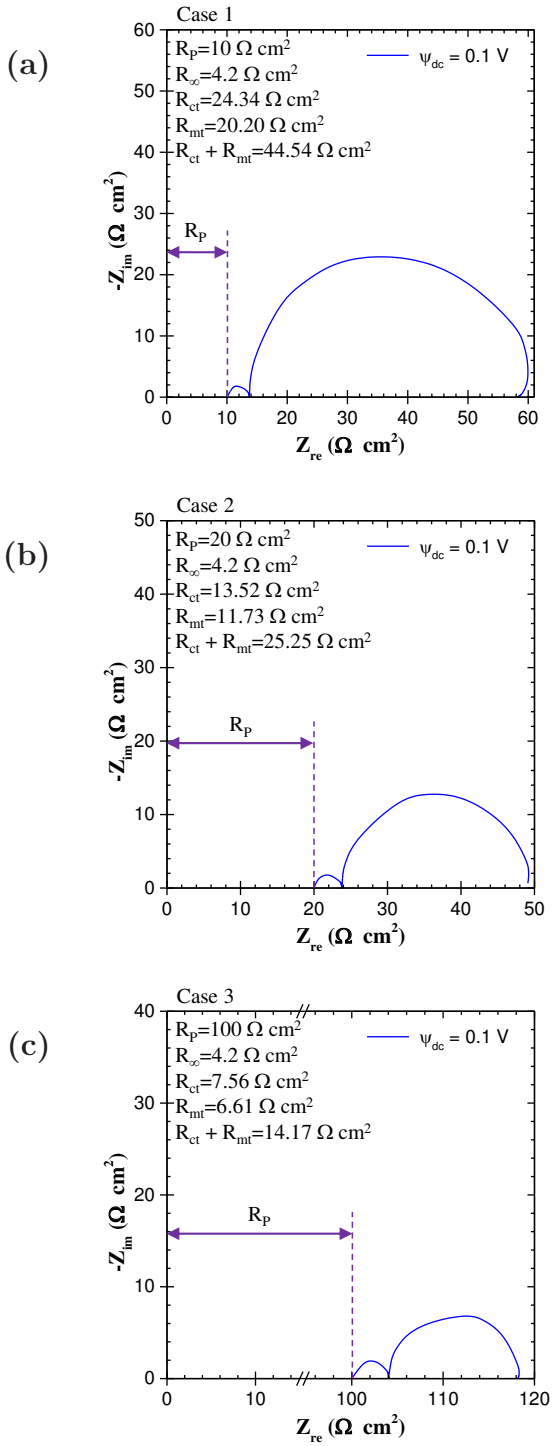

Figure 4.4: Nyquist plots for redox active electrodes for Cases 1-3 featuring electrode resistance R_P equals to (a) 10 Ω cm^2, (b) 20 Ω cm^2, and (c) 100 Ω cm^2.

4.4.2.2 Bulk electrolyte resistance R_∞

Figure 4.5 shows the Nyquist plots for electrodes of Cases 2, 4, and 5 featuring electrolyte thickness L equal to (a) 64 μm, (b) 32 μm, and (c) 16 μm, corresponding to bulk electrolyte resistance R_∞ [Equation (4.5)] equal to (a) 4.2 Ω cm^2, (b) 2.1 Ω cm^2, and (c) 1.05 Ω cm^2, respectively. All other parameters remained the same in these three cases. Here, the electrode resistance R_P was constant and equal to 20 Ω cm^2 for all three cases. Previous conclusion identifying $R_A = R_P$ was also valid for these cases. In addition, Figure 4.5 establishes that the diameter of the semi-circle at high frequencies (corresponding to $R_{AB} = R_B - R_A$ in Figure 3.1) was equal to the bulk electrolyte resistance, i.e., $R_{AB} = R_\infty$. In fact, the same observations were made for EDLC electrodes [168]. Moreover, increasing the electrolyte thickness L reduced the diameter of the semi-circle at lower frequencies, corresponding to $R_{BC} = R_C - R_B$ (Figure 3.1).

4.4.2.3 Charge transfer resistance R_{ct} and mass transfer resistance R_{mt}

To further explain the diameter of the semi-circle at intermediate frequencies (R_{BC} in Figure 4.1), charge transfer resistance R_{ct} and mass transfer resistance R_{mt} were varied by changing the reaction rate constant k_0. Figure 4.6 shows the Nyquist plots for electrodes for Cases 4, 6, and 7 featuring redox reaction rate constant k_0 equal to (a) 10^{-9} m$^{2.5}$mol$^{-0.5}$s^{-1}, (b) 5×10^{-9} m$^{2.5}$mol$^{-0.5}$s^{-1}, and (c) 10^{-8} m$^{2.5}$mol$^{-0.5}$s^{-1}. These cases corresponded to charge transfer R_{ct} [Equation (4.6)] and mass transfer R_{mt} [Equation (4.8)] resistances equal to (a) 24.3 Ω cm^2 and 20.2 Ω cm^2, (b) 13.5 Ω cm^2 and 11.7 Ω cm^2, and (c) 7.6 Ω cm^2 and 6.6 Ω cm^2, respectively. All other parameters remained the same in these three cases. In particular, R_P and R_∞ were equal to 20 Ω cm^2 and 2.1 Ω cm^2, respectively. Previous identifications of $R_A = R_P$ and $R_{AB} = R_\infty$ remained valid in these cases as well. Figure 4.6 establishes that the diameter of the semi-circle at

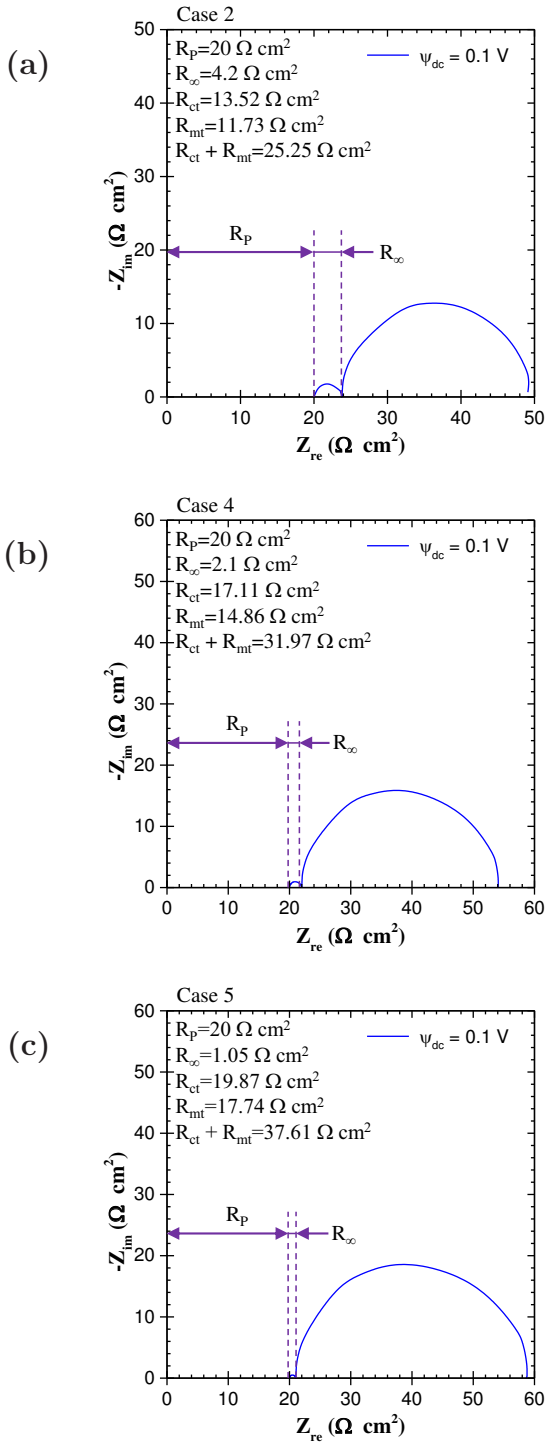

Figure 4.5: Nyquist plots for redox active electrodes for Cases 2, 4, and 5 featuring bulk electrolyte resistance R_∞ equals to (a) 4.2 Ω cm^2, (b) 2.1 Ω cm^2, and (c) 1.05 Ω cm^2.

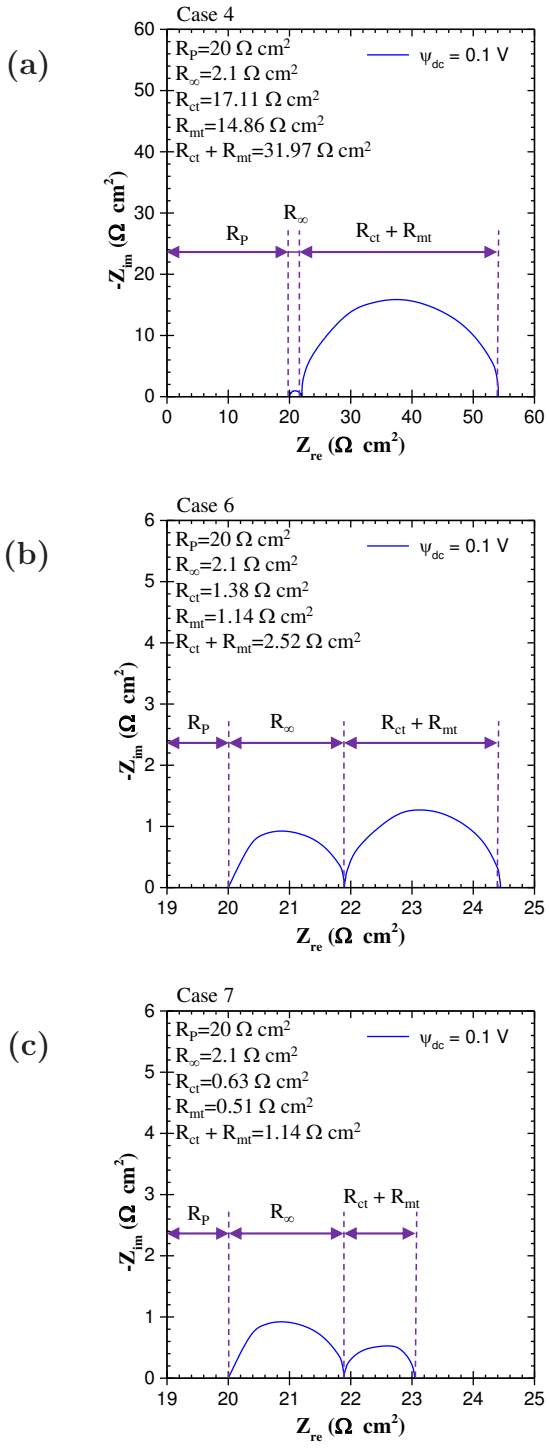

Figure 4.6: Nyquist plots for redox active electrodes for Cases 4, 6, and 7 featuring charge transfer R_{ct} and mass transfer R_{mt} resistances of (a) 24.3 Ω cm^2 and 20.2 Ω cm^2, (b) 13.5 Ω cm^2 and 11.7 Ω cm^2, and (c) 7.6 Ω cm^2 and 6.6 Ω cm^2, respectively.

lower frequencies R_{BC} (Figure 4.1) was systematically equal to the sum of charge transfer resistance R_{ct} and mass transfer resistance R_{mt} estimated using Equations (4.10) and (4.11), i.e., $R_{BC} = R_{ct} + R_{mt}$.

In addition, Figures 4.4 and 4.5 indicate that R_{ct} and/or R_{mt} decreased with (i) decreasing electrode conductivity σ_P and (ii) increasing electrolyte thickness L. To explain the trend in R_{ct}, Figures 4.7(a)-4.7(b) show (i) j_F versus η and j_F versus $\Delta\psi_D$ under cyclic voltammetry at very low scan rate ($v = 0.001$ mV/s) where there are no kinetic limitations and (ii) the points (η_{dc}, $j_{F,dc}$) and ($\Delta\psi_{D,dc}$, $j_{F,dc}$) obtained from EIS simulations and averaged from all frequencies considered for different values of (a) σ_P in Cases 1-3 and (b) L in Cases 2, 4, and 5. The figures indicate that the j_F-η curve remained nearly the same for different values of σ_P and L. In addition, the slope of the j_F-η curve at (η_{dc}, $j_{F,dc}$), corresponding to $1/R_{ct}$ [Equation (4.10)], decreased with increasing DC overpotential η_{dc} which increased with increasing σ_P and decreasing L. Similar observations were made for j_F-$\Delta\psi_D$ curve and $1/R_{mt}$.

To further explain the trend in the overpotential $\eta_{dc} = \Delta\psi_{H,dc} - \Delta\psi_{eq,dc}$ and potential drop across the diffuse layer $\Delta\psi_{D,dc}$, Figures 4.7(c)-4.7(d) shows the DC potential drops across (i) the electrode $\Delta\psi_{P,dc}$, (ii) the Stern layer $\Delta\psi_{H,dc}$, (iii) the diffuse layer $\Delta\psi_{D,dc}$, and (iv) the bulk electrolyte $\Delta\psi_{\infty,dc}$ for different values of (c) σ_P in Cases 1-2 and (d) L in Cases 2, 4, and 5. Note that the imposed DC potential ψ_{dc} at the current collector is such that

$$\psi_{dc} = \Delta\psi_{P,dc} + \Delta\psi_{H,dc} + \Delta\psi_{D,dc} + \Delta\psi_{\infty,dc}. \tag{4.12}$$

Figure 4.7(c) indicates that the potential drops $\Delta\psi_{H,dc}$, $\Delta\psi_{D,dc}$, and $\Delta\psi_{\infty,dc}$ increased with increasing σ_P to compensate for the decrease in the potential drop across the electrode $\Delta\psi_{P,dc}$ so as to maintain the imposed ψ_{dc}. Similarly, Figure 4.7(d) establishes that the potential drops $\Delta\psi_{P,dc}$, $\Delta\psi_{H,dc}$, and $\Delta\psi_{D,dc}$ decreased

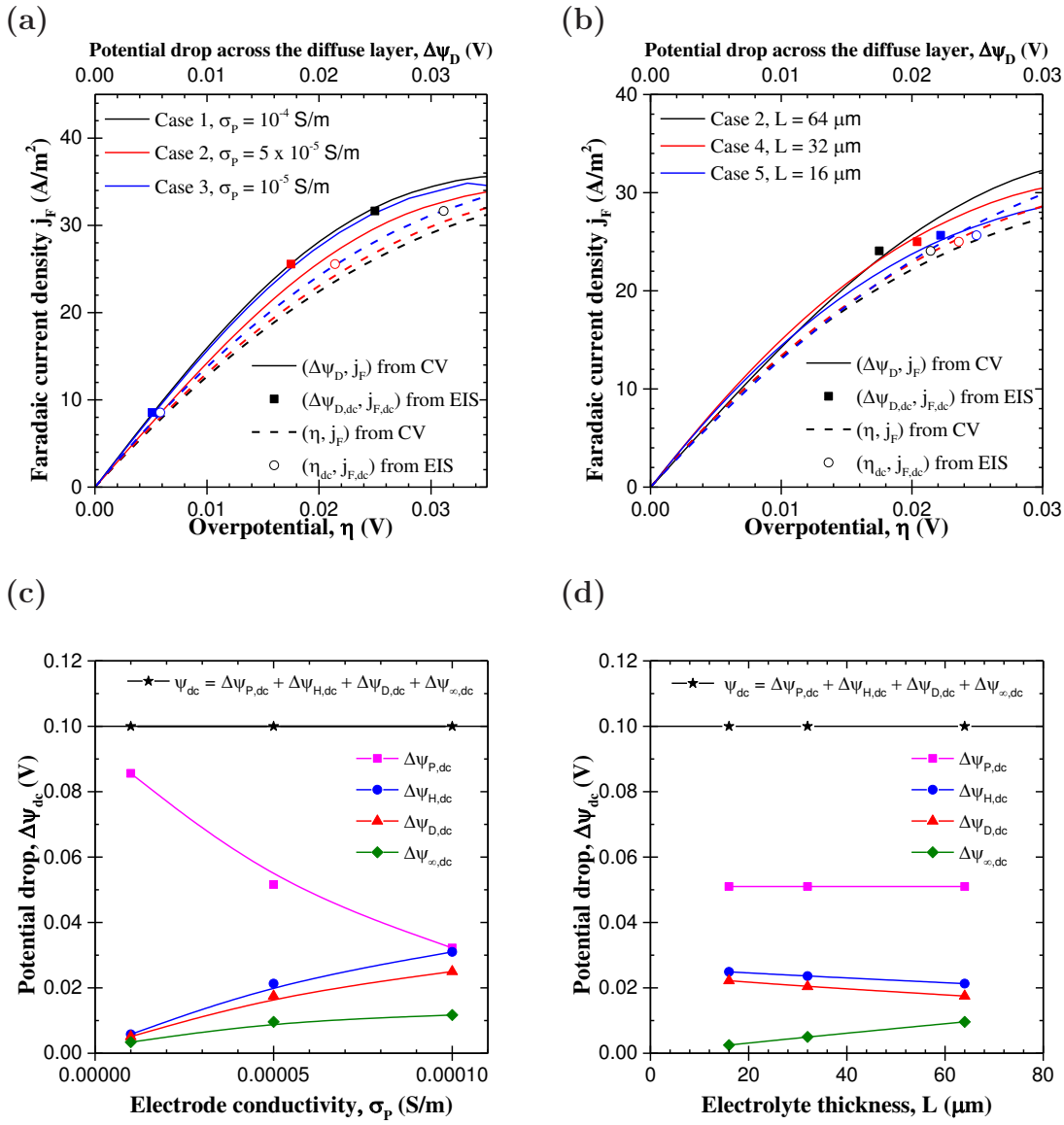

Figure 4.7: (a)(b) Faradaic current j_F as a function of overpotential η and of potential drop across the diffuse layer $\Delta\psi_D$ under cyclic voltammetry at very low scan rate (v = 0.001 mV/s) as well as (η_{dc}, $j_{F,dc}$) and ($\Delta\psi_{D,dc}$, $j_{F,dc}$) (averaged from all frequencies considered) from EIS simulations and (c)(d) DC potential drops from EIS simulations for different values of (a)(c) σ_P in Cases 1-3 and (b)(d) L in Cases 2, 4, and 5.

with increasing electrolyte thickness L to compensate for the increase in the potential drop across the bulk electrolyte $\Delta\psi_{\infty,dc}$ while ψ_{dc} remained constant. In other words, both potential drops $\Delta\psi_{H,dc}$ and $\Delta\psi_{D,dc}$ increased with increasing σ_P and decreasing L. In addition, under EIS simulations, the variation of state-of-charge of the electrode was negligible, resulting in nearly constant $\Delta\psi_{eq,dc}$. Thus, the DC overpotential $\eta_{dc} = \Delta\psi_{H,dc} - \Delta\psi_{eq,dc}$ and the charge transfer resistance R_{ct} varied like $\Delta\psi_{H,dc}$, i.e., they increased with increasing electrical conductivity σ_P and decreasing electrolyte thickness L. Note that the potential drop across the diffuse layer $\Delta\psi_{D,dc}$ and the potential drop across the Stern layer $\Delta\psi_{H,dc}$ were related [156] (see detailed derivation in supporting information). Therefore, the charge transfer resistance R_{ct} [Equation (4.6)] and the mass transfer resistance R_{mt} [Equation (4.8)] were coupled and could not be separated in the Nyquist plot.

4.4.2.4 Effect of bias potential ψ_{dc}

Figure 4.8(a) shows the Nyquist plot for Cases 8 and 9 with bias potential ψ_{dc} ranging from 0.1 to 0.6 V. All parameters were identical in Cases 8 and 9 except for k_0 equals to $k_0 = 10^{-8}$ $\mathrm{m^{2.5}mol^{-0.5}s^{-1}}$ in Case 8 (redox active) and $k_0 = 0$ in Case 9 (EDLC) (Table 4.2). Two semi-circles were observed for Case 8 while only one semi-circle and a nearly vertical line were observed for Case 9. It is important to note that the high frequency semi-circle AB for Cases 8 and 9 overlapped. In addition, the intercept of the Nyquist plot with the Z_{re} axis (point A) and the semi-circle AB at high frequency were independent of ψ_{dc}. Indeed, the resistances of the electrode R_P and bulk electrolyte R_∞ are properties of the electrode and electrolyte. They were both independent of redox reactions and of ψ_{dc}, as indicated in Equations (4.4) and (4.5). Moreover, the nearly vertical lines observed for Case 9 were also nearly independent of DC potential ψ_{dc}, as previously observed for EDLC electrodes [168]. The slope of the line indicated whether the charging

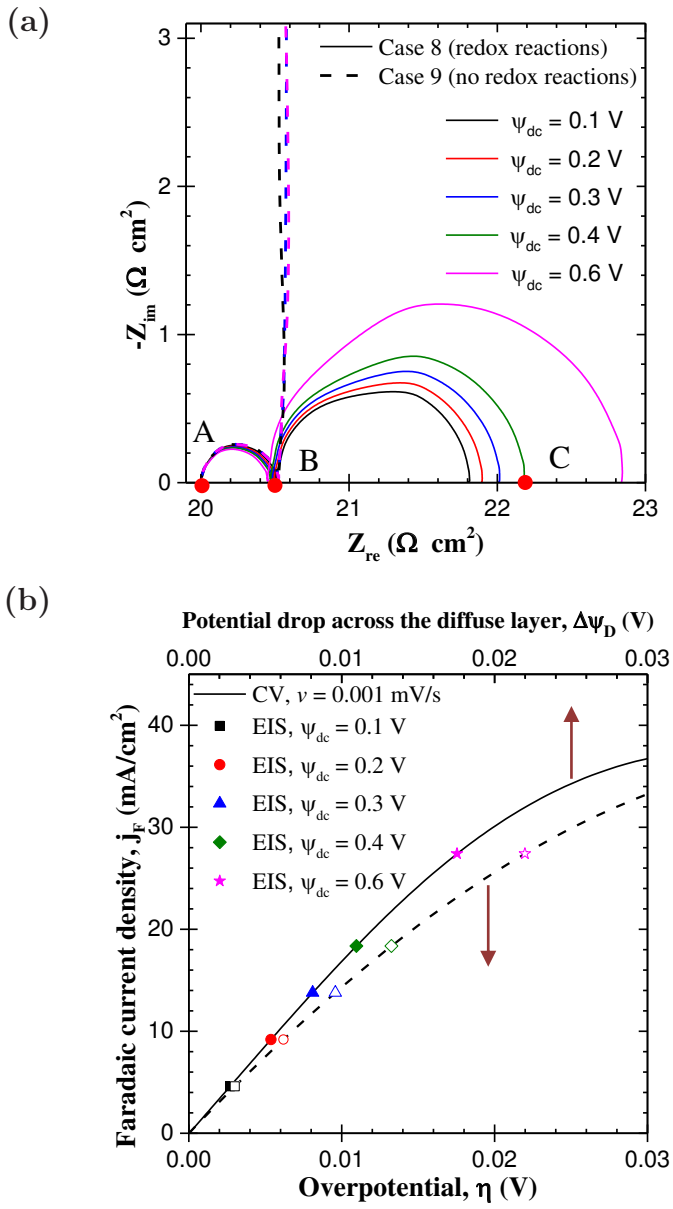

Figure 4.8: (a) Nyquist plot for Cases 8 (redox reactions) and 9 (no redox reactions) with bias potential ψ_{dc} of 0.1 - 0.6 V. (b) Corresponding faradaic current density j_F as a function of overpotential η and of potential drop across the diffuse layer $\Delta\psi_D$ under cyclic voltammetry at very low scan rate ($v = 0.001$ mV/s) as well as (η_{dc}, $j_{F,dc}$) and ($\Delta\psi_{D,dc}$, $j_{F,dc}$) (averaged from all frequencies considered) from EIS simulations for Case 8.

process was controlled by EDL formation (large slope) or limited by ion diffusion in the electrolyte (small slope) [168]. Here, the slope of the non-vertical line was very steep, indicating that the charging process was controlled by EDL formation in absence of faradaic reactions.

Furthermore, for Case 8, the diameter of the semi-circle BC at lower frequency, i.e., the charge and/or mass transfer resistances R_{ct} and R_{mt}, increased with increasing ψ_{dc}. Indeed, Figure 4.8(b) plots the faradaic current density j_F versus overpotential η and j_F versus potential drop across the diffuse layer $\Delta\psi_D$ under cyclic voltammetry at very low scan rate ($v = 0.001$ mV/s), i.e., without kinetic limitations. It also plots the corresponding points (η_{dc},$j_{F,dc}$) and ($\Delta\psi_{D,dc}$, $j_{F,dc}$) averaged from all frequencies under EIS simulations for the different bias potential ψ_{dc} considered. It indicates that (i) the DC overpotential η_{dc} increased with increasing bias potential ψ_{dc} and (ii) the slope of the j_F-η curve at point (η_{dc},$j_{F,dc}$), i.e., $1/R_{ct}$, decreased with increasing η_{dc}. Similar conclusion can be drawn for $\Delta\psi_D$ and thus for $1/R_{mt}$.

4.4.2.5 Comparison with experimental data

Figure 4.9(a) shows the Nyquist plots reported in the literature and obtained experimentally for $LiNi_{0.6}Co_{0.2}Mn_{0.2}O_2$ electrode in 1M $LiPF_6$ in ethylene carbonate and ethyl-methyl carbonate (EC/EMC, 3:7) electrolyte for bias potential ψ_{dc} of 3.7-4.2 V [6]. The experiment was performed in coin-type cells with lithium foil as the counter and reference electrode [6]. The Nyquist plots featured two semi-circles and closely resembled numerically-generated Nyquist plots illustrated in Figure 4.8(a). In addition, neither the high-frequency intersection of the Nyquist plot with the Z_{re}-axis R_A nor the diameter of the high frequency semi-circle R_{AB} was affected by ψ_{dc}. Similarly, the resistance R_{BC}, interpreted as the charge R_{ct} and/or mass R_{mt} transfer resistances, increased with increasing ψ_{dc}, as observed in the simulations.

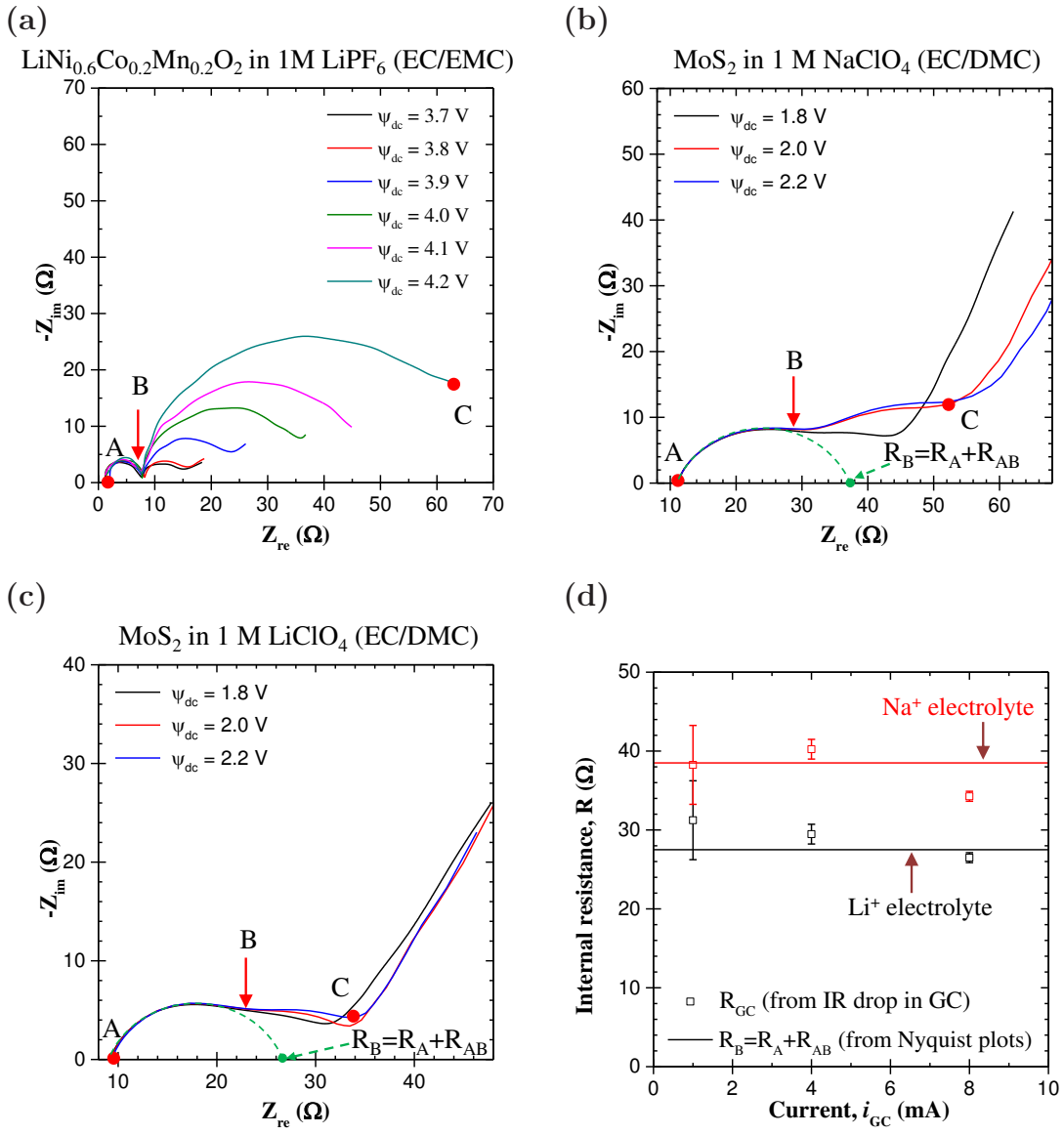

Figure 4.9: Nyquist plot obtained experimentally for (a) $LiNi_{0.6}Co_{0.2}Mn_{0.2}O_2$ in 1M $LiPF_6$ in EC/EMC(3:7) for bias potential ψ_{dc} of 3.7-4.2 V [6], (b,c) for MoS_2 mesoporous electrodes in (b) 1 M $NaClO_4$ in EC/DMC and (c) 1 M $LiClO_4$ in EC/DMC for bias potential ψ_{dc} of 1.8 - 2.2 V. (d) Internal resistance R_{GC} obtained experimentally from galvanostatic cycling as a function of current i_{GC} and R_B obtained from EIS measurement shown in (b,c) for MoS_2 electrodes.

Figures 4.9(b) and 4.9(c) show the Nyquist plots obtained experimentally for MoS_2 mesoporous electrodes in three-electrode configuration in (b) 1 M $NaClO_4$ (EC/DMC) and (c) 1 M $LiClO_4$ (EC/DMC) electrolytes for bias potential ψ_{dc} of 1.8 - 2.2 V. For both systems, Nyquist plots feature two partially overlapping semi-circles at high frequencies as well as a non-vertical line at low frequencies. The fact that the two semi-circles overlapped could be attributed to the fact that ion transport in the electrolyte (corresponding to R_∞) and ion intercalation into the MoS_2 electrode (related to R_{ct} and/or R_{mt}) took place simultaneously throughout the porous electrode. In addition, for both systems, the high-frequency intersection of the Nyquist plot with the Z_{re}-axis (point A) and the high frequency arc AB were not affected by ψ_{dc}. These experimental observations agreed with numerical simulations presented earlier. Moreover, the resistance R_A was identical in both experimental systems. This was consistent with the interpretation that R_A corresponded to the electrode resistance and the fact that both electrodes were nearly identical. In fact, the electrode resistance was equal to 10 Ω and similar to that of activated carbon electrodes (5-10 Ω) of similar dimensions reported in our previous study [168]. On the other hand, the resistance R_{AB} for the system with $NaClO_4$ electrolyte [Figure 4.9(b)] was larger than that for $LiClO_4$ electrolyte [Figure 4.9(c)]. This was in line with the fact that R_{AB} corresponded to the bulk electrolyte resistance and that $NaClO_4$ in EC/DMC feature lower ionic conductivity ($\sim$5 mS/cm) [170] than $LiClO_4$ in EC/DMC ($\sim$8.4 mS/cm) [171] at room temperature.

Furthermore, for both systems, the diameter of the second arc BC, i.e., the resistance R_{BC}, increased with increasing ψ_{dc}. This was consistent with numerical simulations in presence of redox reactions (Case 8, Figure 4.8). In addition, for any given bias potential, the resistance R_{BC} for $NaClO_4$ electrolyte was larger than that for $LiClO_4$ electrolyte. Note also that the pseudocapacitive charge storage mechanism for MoS_2 electrode is mainly due to ion intercalation [172]. However,

the kinetics of Na^+ intercalation into the MoS_2 electrode was slower than that of Li^+ due to the larger radius and heavier mass of Na^+ compared with Li^+ [172,173]. This resulted in larger charge and mass transfer resistances in the $NaClO_4$ than in the $LiClO_4$ electrolyte.

Moreover, the non-vertical line beyond point C could be assigned to ion transport limitation in the electrolyte in the porous electrodes or in the diffuse layer of the EDL. This feature was not observed (i) in numerical simulations for planar redox active electrodes [Case 8, Figure 4.8(a)] or (ii) in experiments for electrodes made of battery-type $LiNi_{0.6}Co_{0.2}Mn_{0.2}O_2$ material shown in Figure 4.9(a) [6]. The latter can be attributed to the dominance of faradaic reactions at low frequencies (beyond point C). However, similar non-vertical line was observed in numerically generated Nyquist plots for EDLC electrodes [Case 9, Figure 4.8(a)], as previously discussed. In fact, by contrast with planar pseudocapacitive electrodes or battery electrodes [6], the current contribution from EDL formation was likely large in the highly porous MoS_2 electrodes due to the large electrode surface area.

Finally, Figure 4.9(d) shows the internal resistance R_{GC} retrieved from the "IR drop" in galvanostatic cycling (see supporting information) as a function of the imposed current i_{GC} (1-8 mA) as well as $R_B = R_A + R_{AB}$ retrieved from the Nyquist plots for the two systems considered in Figures 4.9(b) and 4.9(c). It indicates that R_{GC} was nearly independent of the imposed current I_{GC} and was approximately equal to R_B. Note that R_{GC} has been attributed to the ohmic resistance of the system [154] and is equal to the sum of the electrical resistance of the electrode R_P and the ionic resistance of the electrolyte R_∞ [7,8,154,174,175]. This result confirms the physical interpretation developed from the numerical simulations establishing that $R_B = R_P + R_\infty$.

4.5 Chapter summary

This chapter presented physical interpretations of electrochemical impedance spectroscopy (EIS) results for redox active electrodes. The Nyquist plots presenting the imaginary and real parts of the complex impedance of individual electrodes were numerically reproduced based on the modified Poisson-Nernst-Planck model along with the generalized Frumkin-Butler-Volmer equation for redox reactions and closely resembled experimental measurements. It established that the electrode, bulk electrolyte, charge transfer, and mass transfer resistances could be identified from Nyquist plots. Furthermore, the electrode and bulk electrolyte resistances were independent of the bias potential. On the other hand, the charge and mass transfer resistance increased with increasing bias potential. Finally, these results and interpretations were confirmed experimentally for $LiNi_{0.6}Co_{0.2}Mn_{0.2}O_2$ and MoS_2 electrodes in organic electrolytes.

CHAPTER 5

Interfacial and Transport Phenomena in EDLC Electrodes Made of Ordered Carbon Spheres under Cyclic Voltammetry

Chapters 3-4 provided physical interpretations for EC electrodes based on one-dimensional numerical simulations. This chapter aims to extend our simulation tools to multidimensional systems and to investigate the effect of electrode nanoarchitecture on the performance of EDLC electrodes. The EDLC electrodes considered here consisted of highly-ordered monodisperse spherical carbon nanoparticles arranged in either simple cubic (SC) or face-centered cubic (FCC) packing structure. Cyclic voltammetry (CV) curves were numerically reproduced for a wide range of nanoparticle radius and electrode thickness. The integral capacitance (in μF/cm^2) obtained from cyclic voltammetry under different scan rates was the main performance metrics of the EDLC electrodes.

5.1 Analysis

5.1.1 Schematic and assumptions

Figure 6.1 shows schematics of the simulated EDLC electrodes consisting of (a) simple cubic (SC) or (b) face-centered cubic (FCC) packing of monodisperse carbon spheres of diameter d. By virtue of symmetry, a unit cell containing quarter-spheres was simulated. The current collector, electrode and electrolyte thicknesses were denoted by L_s, L_e, and L, respectively.

Following assumptions were made: (1) The electrolyte was binary and symmetric, i.e., it consisted of two ion species of opposite valency $\pm z$ ($z > 0$). The two ion species were further assumed to have identical diameter a and diffusion

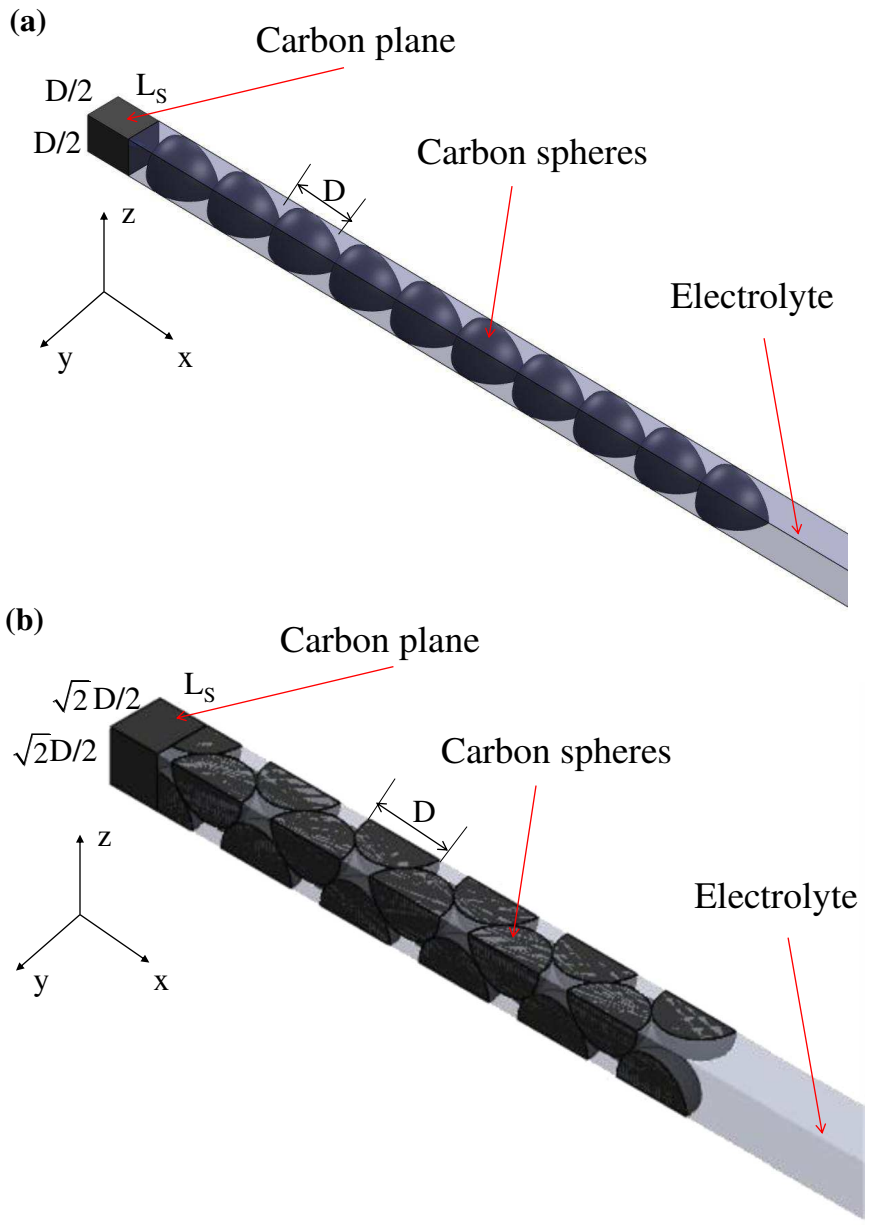

Figure 5.1: Schematics of the EDLC electrodes simulated made of ordered carbon spheres of diameter d in (a) SC packing and (b) FCC packing.

coefficient D. (2) The Stern layer contained no free charge and its thickness H was approximated as the radius of the ions, so that $H = a/2$ [8, 16, 151]. (3) The transport properties of the electrodes and electrolyte were taken as constant except for the electrolyte dielectric constant $\epsilon_r(E)$ which depended on the magnitude E of the local electric field vector. (4) Bulk motion of the electrolyte was negligible. (5) No redox reaction or ion intercalation took place within the electrode. (6) Heat generation was ignored and the EDLC was isothermal. (7) Electrical contact resistance between the carbon spheres was neglected.

5.1.2 Governing equations

Simulations reported in this chapter were based on the modified Poisson-Nernst-Planck (MPNP) model for the spatiotemporal evolution of the potential $\psi(x,t)$ [Equation (2.1)] in the electrode and electrolyte as well as the ion concentrations $c_1(x,t)$ of cations and $c_2(x,t)$ of anions [Equations (2.2) and (2.4)] in the binary and symmetric electrolyte.

5.1.3 Initial and boundary conditions

In order to solve Equations (2.5) to (2.8) for the time-dependent potential $\psi(\mathbf{r},t)$ and ion concentrations $c_i(\mathbf{r},t)$ in the three-dimensional space, one needs one initial condition and two boundary conditions in each direction for each variable. Zero electric potential and uniform ion concentrations equal to the bulk concentrations c_∞ were used as initial conditions for solving the MPNP model, i.e.,

$$\psi(\mathbf{r},0) = 0\,\mathrm{V} \quad \text{and} \quad c_i(\mathbf{r},0) = c_\infty, \qquad \text{for } i = 1{,}2 \tag{5.1}$$

The potential at the current collector/electrode interface was imposed as $\psi_s(t)$. During cyclic voltammetry measurements, $\psi_s(t)$ varied linearly with time [Equation (1.1)]. By virtue of symmetry in the two-electrode device, the boundary

condition in the device centerline, located at $\mathbf{r}_{cl} = (x = L_e + L, y, z)$, was given by

$$\psi(\mathbf{r}_{cl}, t) = 0 \quad \text{and} \quad c_i(\mathbf{r}_{cl}, t) = c_\infty. \tag{5.2}$$

Moreover, the electric potential and current density were continuous across the spherical electrode/electrolyte interface located at $\mathbf{r}_{E/E}$ and planar current collector/electrolyte interface located at $\mathbf{r}_{C/E}$ so that

$$\psi(\mathbf{r}_k^-, t) = \psi(\mathbf{r}_k^+, t) \text{ and } -\sigma_e \frac{\partial \psi}{\partial n}(\mathbf{r}_k^-, t) = -\epsilon_0 \epsilon_r \frac{\partial^2 \psi}{\partial n \partial t}(\mathbf{r}_k^+, t) \qquad \text{with k = E/E or C/E} \tag{5.3}$$

where $\partial/\partial n$ is the gradient normal to the electrode/electrolyte interface.

The electric potential varied linearly across the Stern layer so that the normal electric field at the planar and spherical Stern/diffuse layer interfaces, located at $\mathbf{r}_H$ satisfied [1, 16]

$$\frac{\partial \psi}{\partial n}(\mathbf{r}_H, t) = \frac{\psi(\mathbf{r}_{C/E}) - \psi(\mathbf{r}_H)}{H}, \quad \text{planar electrodes,} \tag{5.4}$$

$$-\epsilon_0 \epsilon_r \frac{\partial \psi}{\partial n}(\mathbf{r}_H, t) = C_s^{St} \left(\frac{d}{d + 2H} \right)^2 \left[\psi(\mathbf{r}_{E/E}, t) - \psi(\mathbf{r}_H, t) \right], \quad \text{spherical electrodes} \tag{5.5}$$

Here, the Stern layer capacitance for a sphere of diameter d is given by the Helmholtz model expressed as [176]

$$C_s^{St} = \frac{\epsilon_0 \epsilon_r}{H} (1 + \frac{2H}{d}) \tag{5.6}$$

These boundary conditions accounted for the presence of the Stern layers without explicitly simulating them in the computational domain thus reducing significantly the number of meshes and making possible the numerical solution of the strongly coupled equations considered [1].

Based on assumption (5), no ion intercalated into the electrodes. Thus, the ion mass flux vectors vanished at the electrode/electrolyte and current collec-

tor/electrolyte interfaces such that [16]

$$\mathbf{N}_i(\mathbf{r}_k, t) = \mathbf{0} \qquad \text{for i = 1, 2} \qquad \text{with k = E/E or C/E.} \tag{5.7}$$

By virtue of symmetry in the electrode packings, the normal electric field at the side walls of the simulated domain (Figure 6.1) and the ion flux across the side walls also vanished, i.e., $\partial\psi/\partial n = 0$, and $\mathbf{N}_i = \mathbf{0}$ $(i = 1, 2)$.

5.1.4 Constitutive relationships

In order to solve the transient 3D governing Equations (2.5) to (2.8) and their initial and boundary conditions, a total of 14 parameters were needed. These parameters include (i) the electrolyte properties ϵ_r, a, D, z, and c_∞, (ii) the electrode material conductivity σ_e, (iii) the electrode dimensions d, L_s, L_e, L, and (iv) the operating conditions ψ_{max}, ψ_{min}, T, and v.

The Booth model was used to account for the effect of the local electric field $\mathbf{E} = -\nabla\psi$ on the electrolyte dielectric constant expressed as [1, 177–180],

$$\epsilon_r(E) = \begin{cases} n^2 + (\epsilon_r(0) - n^2)\dfrac{3}{\beta E}\left[\coth(\beta E) - \dfrac{1}{\beta E}\right] & E \geq 10^7 \text{ V/m} \quad (5.8) \\ \epsilon_r(0) & E < 10^7 \text{ V/m} \quad (5.9) \end{cases}$$

where n is the refractive index of the electrolyte solution, $\epsilon_r(0)$ is the dielectric constant at zero electric field, and β is a semi-empirical constant. The electrolyte simulated was $(C_2H_5)_4NBF_4$ ($TEABF_4$) in propylene carbonate at room temperature featuring $n = 1.42$ [181], $\epsilon_r(0) = 64.4$ [152], and $\beta = 1.314$ x 10 $^{-8}$ m/V [177]. In addition, the bare ion diameter a of $(C_2H_5)_4N^+$ and BF_4^- were 0.68 nm and 0.33 nm [182]. However, as discussed in Refs. [141, 183], "Smaller bare ions tend to be more heavily solvated and therefore have larger effective diameters". Moreover, electrolyte ions are less solvated when the electrolyte concentration increases, resulting in smaller effective ion diameter [4, 184–187]. Considering the fact that

the solubility of $(C_2H_5)_4NBF_4$ in propylene carbonate at room temperature is 1 mol/L [188], the effective ion diameters of $(C_2H_5)_4N^+$ and BF_4^- were assumed to be identical and equal to 0.68 nm. Furthermore, the diffusion coefficient D of $(C_2H_5)_4N^+$ ions and BF_4^- in propylene carbonate at room temperature was taken as 3.17 x 10^{-10} m^2/s [189]. The ion valency was $z = 1$ and bulk concentration of the ion species was chosen as $c_\infty = 1$ mol/L, as commonly used experimentally [68]. In addition, the value was chosen as $\sigma_e = 5$ S/m based on the typical range of conductivity of carbon between 10^{-6} and 10^2 S/m [190, 191]. Moreover, the thickness of the planar current collector was taken as $L_s = 10$ nm and the length of the electrolyte domain simulated was $L = 100$ nm. The thickness of the porous carbon electrode L_e as well as the diameter of the carbon spheres d were treated as variables. Finally, the temperature was taken as room temperature, i.e. $T = 298$ K. The electrode was cycled between $\psi_{min} = 0$ V and $\psi_{max} = 1$ V. The scan rate varied from 1 to 10^5 V/s.

5.1.5 Method of solution

The governing equations along with the initial and boundary conditions were solved using COMSOL 4.4. Mesh element size was chosen to be the smallest at the electrode/electrolyte interface where ion concentration gradient and potential gradient were the largest. Moreover, the numerical convergence was considered to be reached when the local electric potential $\psi(\mathbf{r}, t)$ and the normal current density $j_n = \mathbf{j} \cdot \mathbf{n}$ at the electrode/electrolyte interface changed within 1% when reducing the minimum mesh element size and mesh growth rate in the boundary layer near the electrode/electrolyte interfaces by a factor of two. For example, the total number of finite elements was on the order of 10^7 for the simulations of electrodes made of 5 ordered carbon spheres shown in Figure 6.1. In addition, the adaptive time step was controlled by the relative and absolute tolerance set to be 0.01 and 0.001. This enabled the use of smaller time step when potential

and current density changed more rapidly. The simulations were run on Hoffman2 shared computing cluster of UCLA with 8 to 12 processors and 32 to 64 GB of RAM.

Finally, several cycles were simulated and an oscillatory steady state in $\psi(\mathbf{r}, t)$ and $j_n = \mathbf{j} \cdot \mathbf{n}$ was considered to be reached when the maximum relative error between the value of each variable at time t and its value at time $t - \tau_{CV}$ throughout the computational domain was less than 1%. These conditions were typically met by the third cycle for all conditions simulated. The CPU time for each simulation reported ranged between 1 and 4 days.

5.1.6 Data processing

Cyclic voltammetry simulations consist of imposing a triangular time-dependent potential $\psi_s(t)$ [Equation (1.1)] and predicting the current density to plot CV curves. The current density at the electrode/electrolyte and current collector/electrolyte interfaces arising from the formation and dissolution of electric double layer was expressed (in A/m^2) as [16, 30]

$$j_n(\mathbf{r}_k, t) = -\epsilon_0 \epsilon_r \frac{\partial}{\partial t} \frac{\partial \psi}{\partial n}(\mathbf{r}_k, t) \quad \text{with k = E/E or C/E.} \tag{5.10}$$

The current densities averaged over the footprint area, electrode/electrolyte interface area, and mass of the electrode respectively denoted by j_{fp} (in A/m^2), j_{BET} (in A/m^2), and j_g (in A/g) can be defined as

$$j_{fp}(t) = \frac{\iint_{A_{BET}} j_n(\mathbf{r}, t) dA_{BET}}{A_{fp}} \tag{5.11}$$

$$j_{BET}(t) = \frac{\iint_{A_{BET}} j_n(\mathbf{r}, t) dA_{BET}}{A_{BET}} \tag{5.12}$$

$$j_g(t) = \frac{\iint_{A_{BET}} j_n(\mathbf{r}, t) dA_{BET}}{m} \tag{5.13}$$

where A_{fp} is the footprint area of the electrode, corresponding to the area of the planar current collector, A_{BET} is the electrode/electrolyte interfacial area that can be measured experimentally by the Brunauer-Emmett-Teller (BET) method, and m is the total mass of all the carbon spheres constituting the electrode.

The corresponding capacitances can be estimated from the predicted CV curves according to [149]

$$C_k(v) = \frac{1}{\psi_{max} - \psi_{min}} \oint \frac{j_k(t)}{2v} d\psi_s \qquad \text{with } k = fp,\ BET, \text{ or } g. \tag{5.14}$$

where $j_k(t)$ is given by Equation (5.13), v is the scan rate, and ψ_s is the potential imposed at the current collector and given by Equation (1.1).

5.2 Results and discussion

5.2.1 Influence of carbon sphere number and diameter

CV curves of electrodes made of carbon spheres in SC packing were simulated under quasi-equilibrium conditions corresponding to situations when the capacitance was independent of scan rate [16]. Figures 5.2(a) and 5.2(b) show the footprint current density j_{fp} as a function of the imposed potential ψ_s, at scan rate $v = 1$ V/s, for electrodes made of N carbon spheres in SC packing with diameter d equals to either 15 nm ($1 \leq N \leq 9$) or 30 nm ($1 \leq N \leq 5$), corresponding to BET surface area of 200 m^2/g and 100 m^2/g, respectively. These figures indicate that for given sphere diameter and surface potential, the footprint current density increased with increasing sphere number. This can be attributed to the increasing electrode surface area with increasing carbon sphere number N while the footprint remained unchanged. In fact, Figures 5.2(c) and 5.2(d) plot the current density j_{BET} per unit surface area of electrode/electrolyte interface as a function of imposed potential ψ_s for d equals to 15 and 30 nm, respectively.

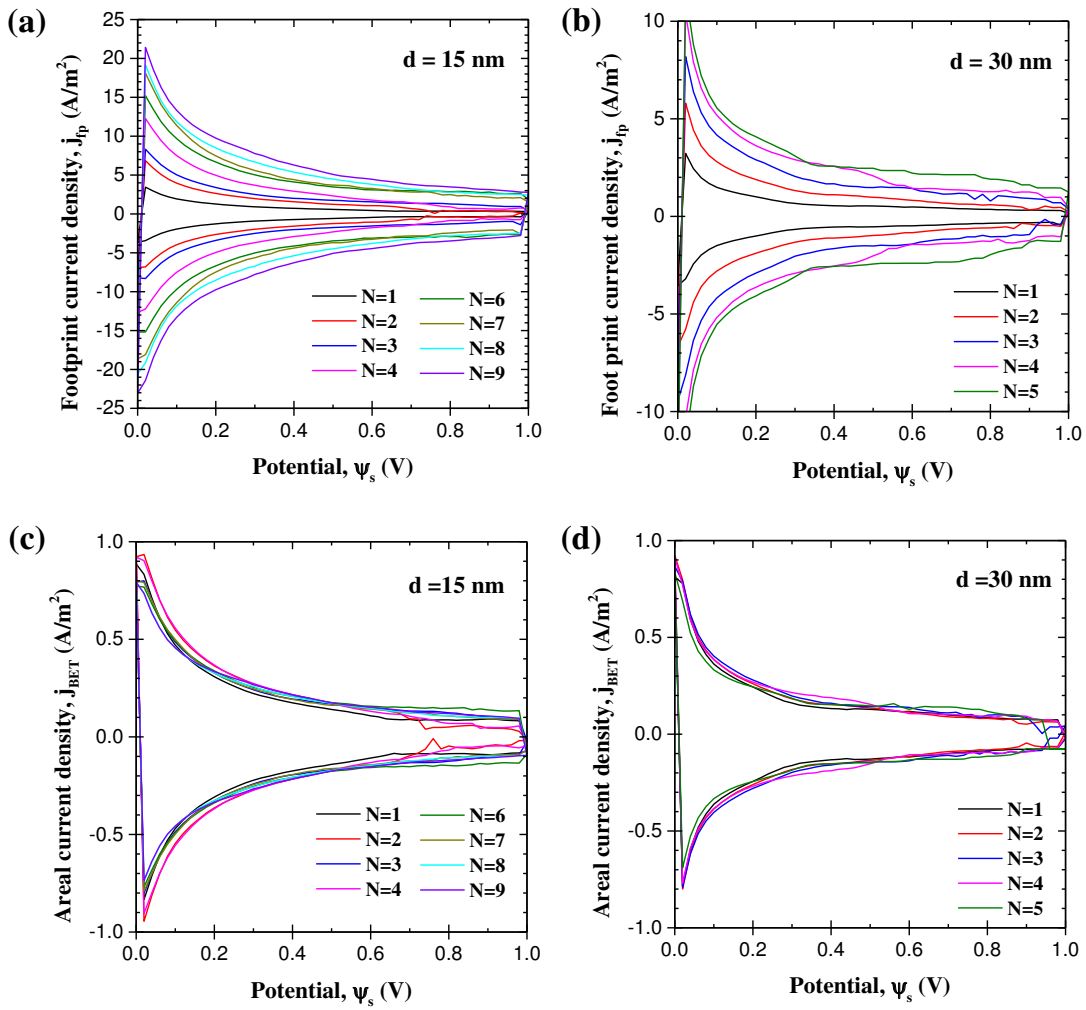

Figure 5.2: (a, b) Footprint current density j_{fp} and (c, d) areal current density j_{BET} as functions of surface potential ψ_s at scan rate $v = 1$ V/s for carbon spheres in SC packing with diameter d of (a, c) $d = 15$ nm, and (b, d) $d = 30$ nm.

These figures establish that the areal current density j_{BET} was weakly dependent of the number N of carbon spheres. In other words, the total current i (in A) was proportional to the BET surface area A_{BET}.

Moreover, Figure 5.3 shows (a) the footprint capacitance C_{fp}, (b) the areal capacitance C_{BET}, and (c) the gravimetric capacitance C_g of electrodes made of multiple carbon spheres in SC packing with diameter d of 15, 30, and 40 nm as functions of the electrode thickness $L_c(= Nd)$ under quasi-equilibrium conditions. It indicates that all three capacitances C_{fp}, C_{BET}, and C_g decreased with increasing sphere diameter d for a given electrode thickness L_c. On the other hand, for a given sphere diameter d, C_{fp} increased with increasing electrode thickness L_c. On the other hand, C_{BET} first increased with increasing electrode thickness L_c then reached a plateau for $L_C \geq 75$ nm. Finally, Cg remained nearly constant for all electrode thicknesses considered. Note that the capacitance C_{BET} ranged between 10 and 50 μF/cm^2 while C_g ranged between 20 and 100 F/g. These values were comparable with reported experimental measurements for electrodes with similar nanoarchitecture [4, 62, 65]. For example, areal capacitance C_{BET} was reported to be between 10 and 15 μF/cm^2 [4] and C_g between 60 and 110 F/g [4,65] for electrodes made of ordered mesoporous carbon spheres in non-aqueous electrolytes under cyclic voltammetry with potential window of 3 V [4] or 2 V [65]. In addition, Kim et al. [62] reported gravimetric capacitance C_g around 60 F/g for carbon electrodes with similar nanoarchitecture and potential windows in aqueous electrolytes under galvanostatic cycling with small current. To explain the trends in C_{fp}, C_{BET}, and C_g as functions of sphere diameter d and electrode thickness L_c, one needs to consider the normal electric field at the sphere surfaces.

Figure 5.4(a) shows the magnitude of the normal component E_n of the local electric field (i.e., $E_n = \mathbf{E} \cdot \mathbf{n} = -\partial\psi/\partial n$) at the electrode/electrolyte interface for $N = 3$ spheres in SC packing with diameter d of 15, 30, and 40 nm, at $t = 0.49\tau_{CV}$ corresponding to $\psi_s = 0.98$ V, i.e., near the end of the charging stage. Note that,

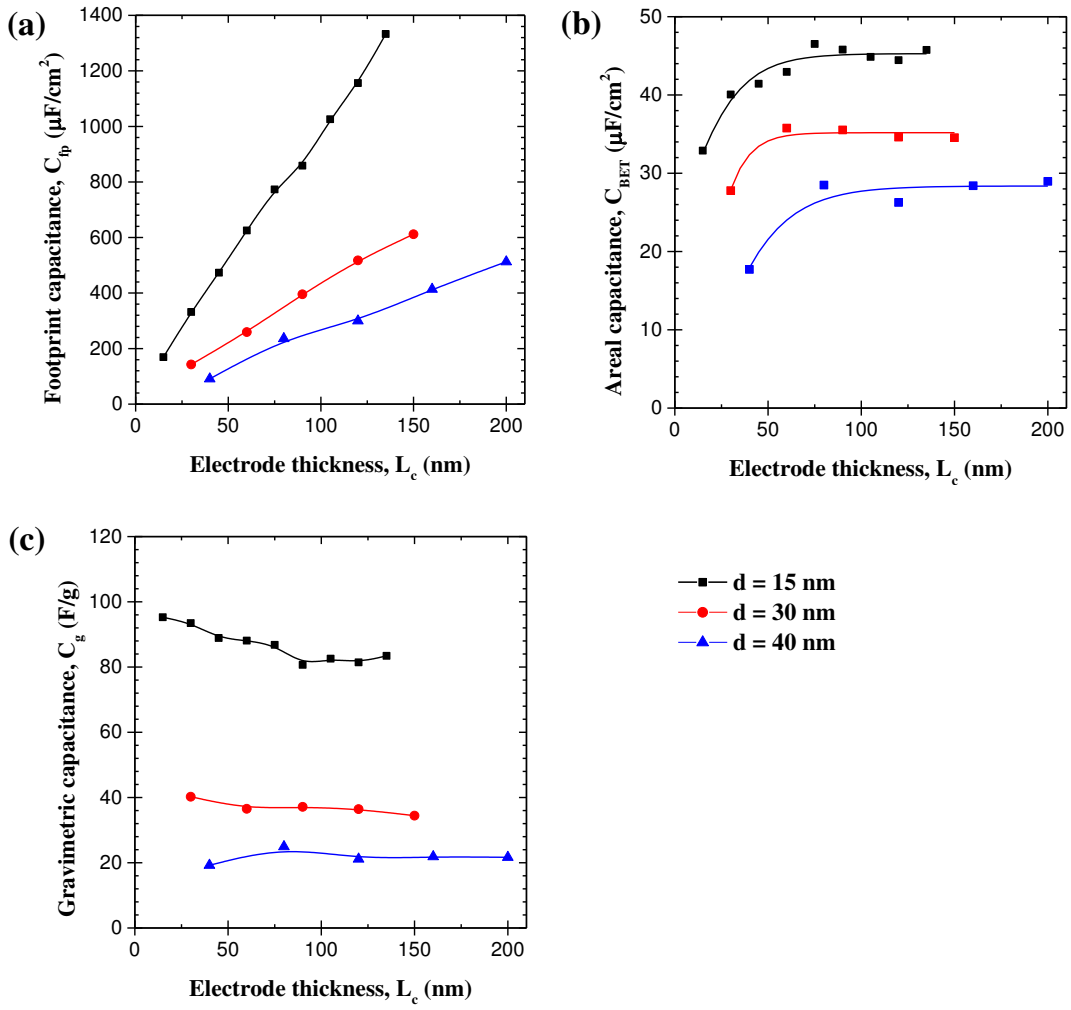

Figure 5.3: (a) Footprint capacitance C_{fp}, (b) areal capacitance C_{BET}, and (c) gravimetric capacitance C_g as functions of electrode thickness L_c under quasi-equilibrium conditions (low scan rates) for carbon spheres in SC packing with diameter $d = 15$, 30, and 40 nm.

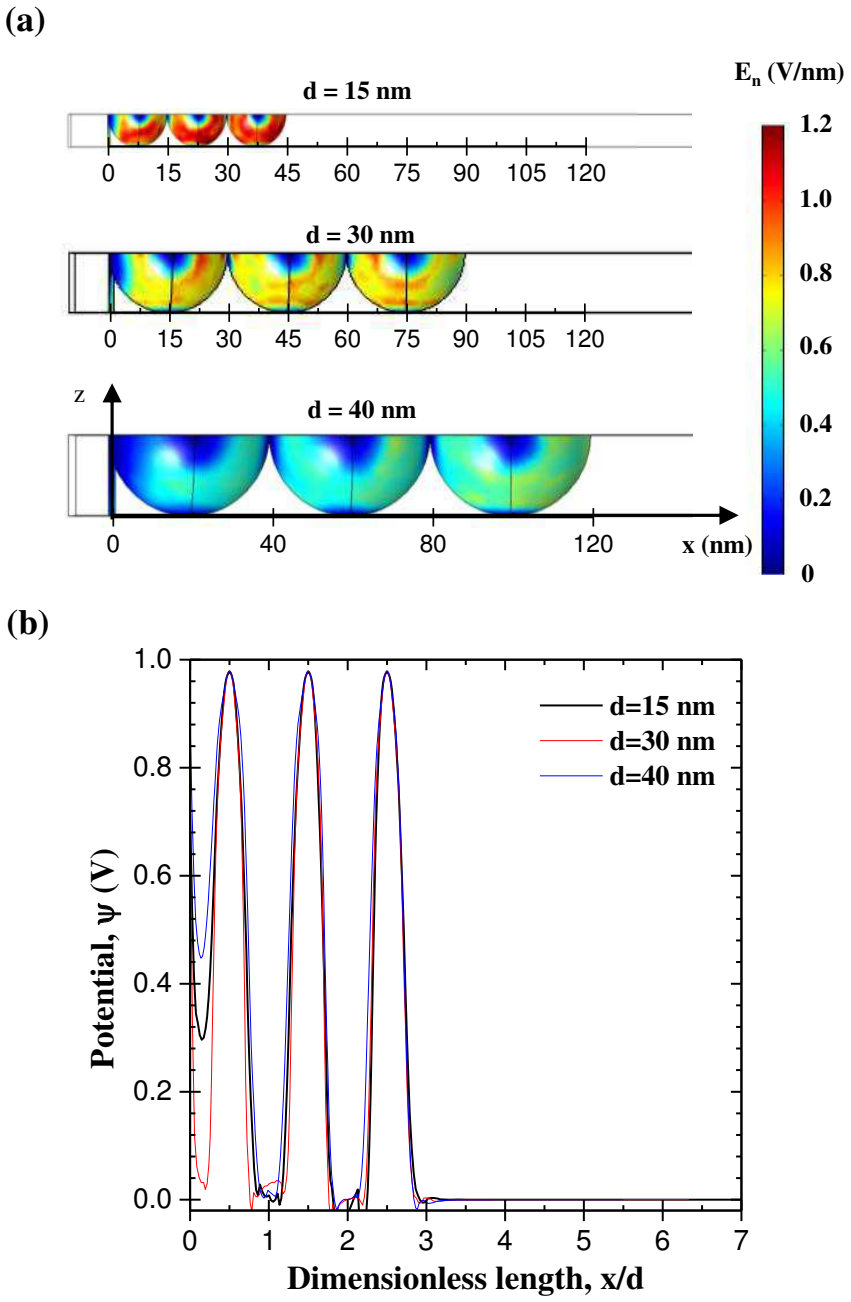

Figure 5.4: (a) Magnitude of the normal electric field E_n at the surface of carbon spheres for electrodes made of 3 carbon spheres in SC packing with diameter $d = 15$, 30, or 40 nm at $t = 0.49\tau_{CV}$ (or $\psi_s = 0.98$ V). (b) Corresponding electric potential $\psi(x/d)$ as a function of x/d along the x-direction given by ($0 \leq x \leq L$, $y = 0$, $z = d/2$).

during charging, the normal electric field increased everywhere at the electrode surface but the relative profile remained unchanged. Figure 5.4(a) indicates that the magnitude of the normal electric field E_n increased with decreasing sphere diameter d. This can be attributed to the fact that for smaller spheres, the electric potential decayed from $\psi(\mathbf{r}_{E/E}, t) \approx \psi_s(t)$ at the electrode surface to zero in the local bulk electrolyte within the porous electrode structure over a smaller distance. To further illustrate the effect of sphere diameter on the normal electric field, Figure 5.4(b) plots the electric potential along the x-direction as a function of the dimensionless position x/d at $t = 0.49\tau_{CV}$ for sphere diameter d equals to 15, 30, and 40 nm. It indicates that the electric potential profile scaled with x/d. In other words, the potential $\psi(x/d)$ and its derivative $\partial\psi/\partial(x/d)$ were independent of d, as were $\partial\psi/\partial(y/d)$ and $\partial\psi/\partial(z/d)$ (not shown). Therefore, the magnitude of the normal electric field $-\partial\psi/\partial n$ at the electrode surface was proportional to $1/d$. Thus, for a given potential, electrodes consisting of smaller carbon spheres attracted more ions to their surface resulting in larger areal or gravimetric charge densities (see Figure S1 in supplementary material). Consequently, the capacitances C_{fp}, C_{BET}, and C_g increased with decreasing sphere diameter d [Figure 5.3(a)].

Figure 5.5 shows the magnitude of the normal electric field E_n for electrodes made of 1 to 9 carbon spheres in SC packing for diameter d of 15 nm at $t = 0.49\tau_{CV}$. The systematically smaller value of E_n resulted in less charge storage on the surface of the first sphere facing the planar current collector (see Figure S2 in supplementary material). This was due to the fact that the planar current collector and the first sphere were at nearly the same potential $\psi_s(t)$ at all times t. On the other hand, the magnitude of the normal electric field E_n on other spheres remained unchanged with increasing sphere number N. Thus, the initial rise and the plateau in C_{BET} with increasing electrode thickness L_c or sphere number N [Figure 5.3(b)] can be attributed to the decreasing relative contribution of the

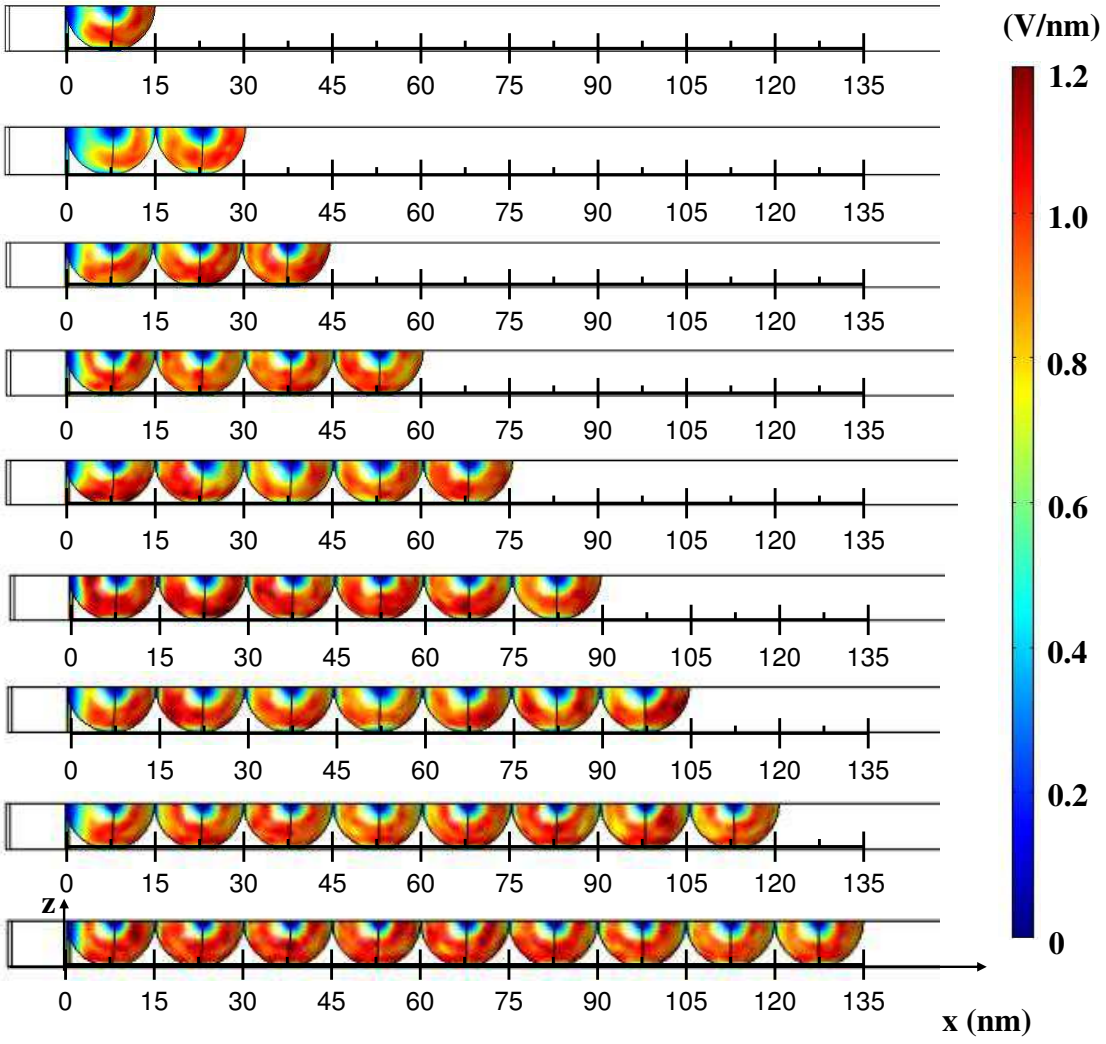

Figure 5.5: Magnitude of the normal electric field E_n at the surface of carbon spheres for electrodes made of 1 to 9 carbon spheres in SC packing with diameter $d = 15$ nm at $t = 0.49\tau_{CV}$ (or $\psi_s = 0.98$ V).

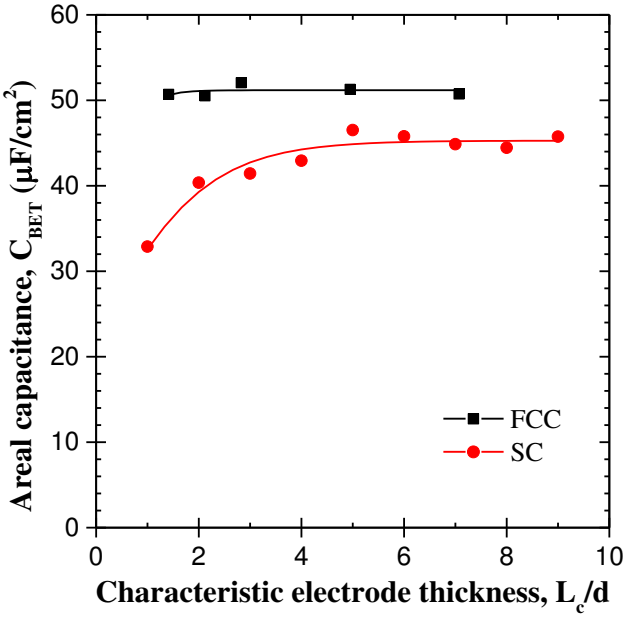

Figure 5.6: Areal capacitance C_{BET} as a function of the dimensionless electrode thickness L_c/d under quasi-equilibrium conditions (low scan rates) for carbon spheres in either FCC or SC packing with diameter $d = 15$ nm.

first sphere to the total charge storage.

5.2.2 Influence of electrode morphology

Figure 5.6 shows the areal capacitance C_{BET} as a function of the dimensionless electrode thickness L_c/d for the electrodes made of carbon spheres in either SC or FCC packings with diameter d of 15 nm under quasi-equilibrium conditions, i.e., low scan rate. It indicates that C_{BET} increased with increasing thickness for SC packing before reaching a plateau for $L_c/d \geq 5$. By contrast, C_{BET} for electrodes with FCC packing was independent of electrode thickness. Moreover, Figure 5.6 establishes that for any given electrode thickness, the areal capacitance of electrodes made of carbon spheres in FCC packing was systematically larger

than that in SC packing.

Figure 5.7 compares the magnitude of the normal electric field at the electrode/electrolyte interface for electrodes made of multiple carbon spheres in SC and FCC packings for diameter d of 15 nm, at $t = 0.49\tau_{CV}$ corresponding to $\psi_s = 0.98$ V. It indicates that for similar electrode thickness L_c, the magnitude of the normal electric field E_n at the carbon sphere surface was larger for FCC packing structure than for SC packing, resulting in larger capacitance C_{BET} (Figure 5.6). This can be attributed to the fact that the FCC structure was denser and featured less distance for the electric potential to decay from $\psi(\mathbf{r}_{E/E}, t) \approx \psi_s(t)$ at the carbon sphere surfaces to zero in the local bulk electrolyte within the porous electrode structure. Figure 5.8(a) shows the areal capacitance C_{BET} for the electrodes made of carbon spheres in FCC packing with 3 ($L_c = 2.12d$) and 10 ($L_c = 7.07d$) rows of spheres and in SC packing with 2 ($L_c = 2d$) and 7 ($L_c = 7d$) spheres as a function of scan rate v. It indicates that C_{BET} was independent of scan rate (quasi-equilibrium regime) for both FCC and SC packings at low scan rates. In addition, the electrodes made of carbon spheres in FCC packing had larger capacitance than that with SC packing, as previously observed (Figure 5.6). However, regardless of carbon sphere packing structure (SC or FCC), the capacitance C_{BET} dropped sharply at a critical scan rate which decreased with increasing electrode thickness. This could be due to ion diffusion limitation in the tortuous electrode structure and/or resistive losses in the potential propagation across the electrode at high scan rates.

Figure 5.8(b) shows the areal capacitance C_{BET} as a function of scan rate v for the electrodes made of 2 carbon spheres in SC packing with ion diffusion coefficient D equals to 3.17 x 10^{-9}, 3.317 x 10^{-10}, and 3.17 x 10^{-11} m^2/s. It indicates that the diffusion coefficient had no effect on the capacitance at any scan rate considered. In other words, the decrease in capacitance at high scan rates was not due to ion diffusion limitation through the porous electrode. On the

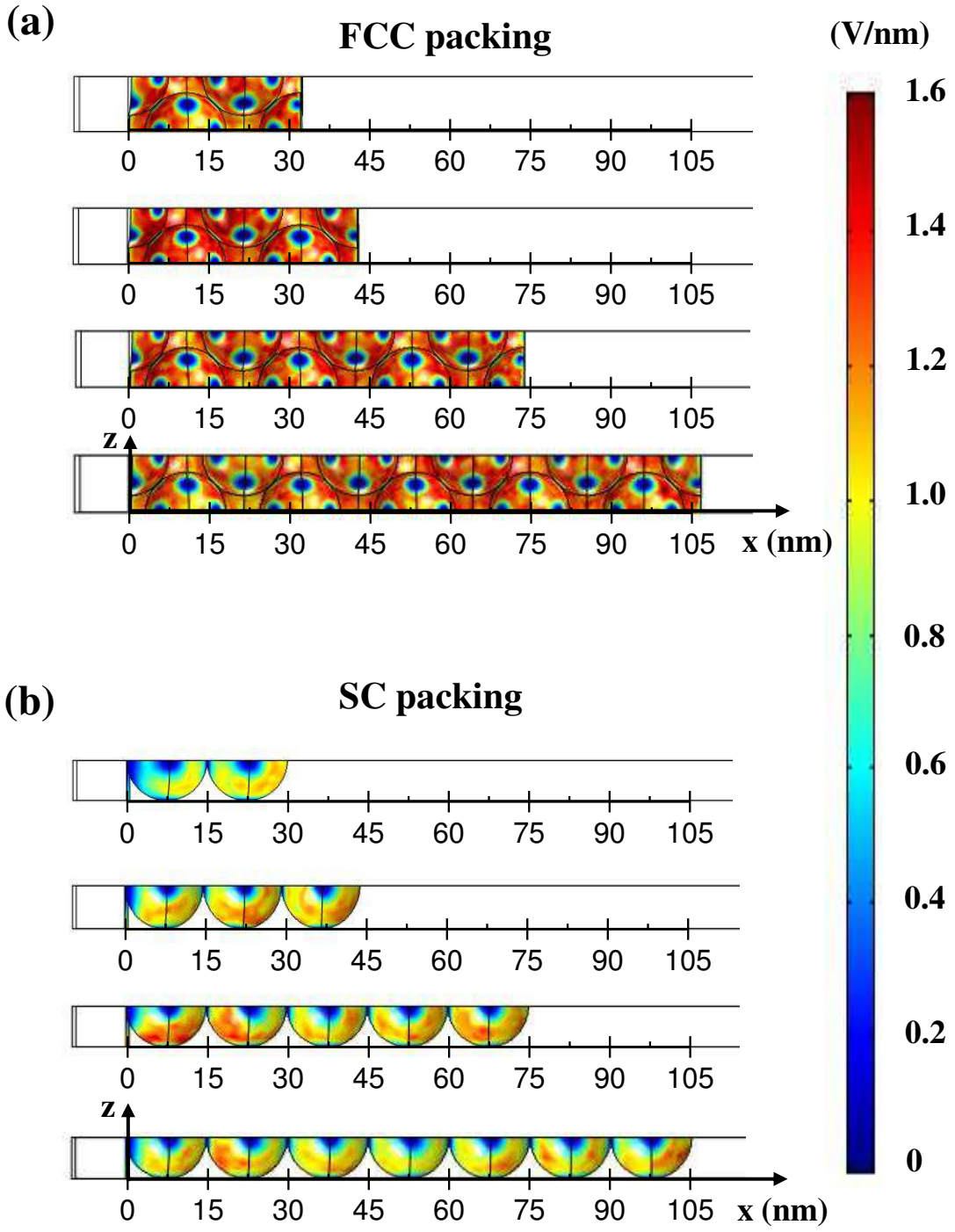

Figure 5.7: Magnitude of the normal electric field E_n at the surface of carbon spheres in (a) FCC packing and (b) SC packing with diameter $d = 15$ nm at $t = 0.98\tau_{CV}$ (or $\psi_s = 0.98$ V).

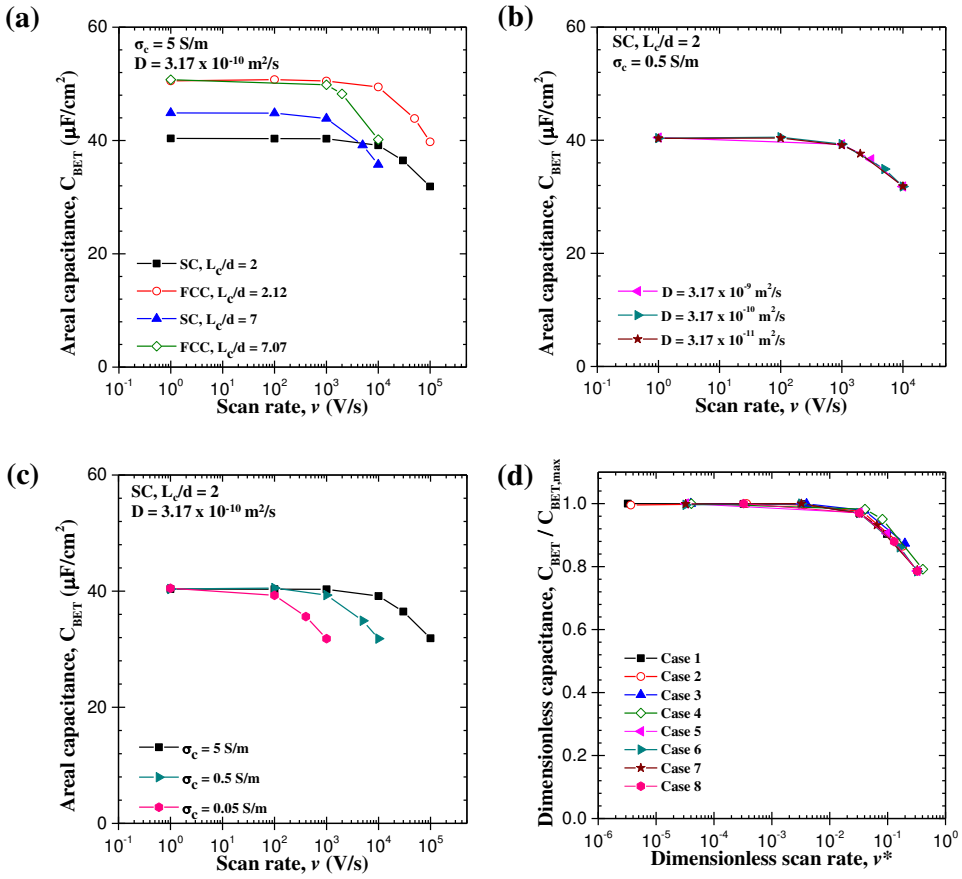

Figure 5.8: (a) Areal capacitance C_{BET} of electrodes made of FCC and SC packing of carbon spheres with diameter $d = 15$ nm as functions of scan rate v for different (a) electrode thicknesses, (b) diffusion coefficients, and (c) electrode conductivities. (b) Dimensionless areal capacitance $C_{BET}/C_{BET,max}$ of electrodes made of FCC and SC packing of carbon spheres with diameter $d = 15$ nm as functions of dimensionless scan rate v^* with parameters L_c/d, D, σ_c and morphology summarized in Table 5.1.

other hand, Figure 5.8(c) shows the areal capacitance C_{BET} as a function of scan rate v for electrodes made of 2 spheres with diameter $d = 15$ nm in SC packing and electrical conductivity σ_c of 5, 0.5, and 0.05 S/m. It indicates that the sharp drop in C_{BET} occurred at smaller critical scan rate as the electrical conductivity σ_c decreased. In fact, the potential propagation across the electrode was limiting the capacitance C_{BET} at high scan rates. Note that Wang and Pilon [30] previously observed ion diffusion limitation for planar (i.e., nonporous) electrodes resulting in the sharp drop in C_{BET} at high scan rates. However, the sharp drop in C_{BET} was observed at higher scan rate than in the present study. In the porous electrodes under consideration, resistive losses limited capacitance before ion diffusion at high scan rates.

Finally, Figure 5.8(d) shows the dimensionless capacitance $C_{BET}/C_{BET,max}$ as a function of dimensionless scan rate v^* for both FCC and SC packings with diameter $d = 15$ nm and for different values of electrical conductivity σ_c, ion diffusion coefficient D, and electrode thickness L_c, as summarized in Table 5.1.

Table 5.1: Parameters for eight cases of dimensionless capacitances reported in Figure 5.8(d)

Case number	$\boldsymbol{L_c/d}$	**Morphology**	$\boldsymbol{D}$ **(m^2/s)**	$\boldsymbol{\sigma_c}$ **(S/m)**
1	2	SC	3.17 x 10^{-10}	5
2	2.12	FCC	3.17 x 10^{-10}	5
3	7	SC	3.17 x 10^{-10}	5
4	7.07	FCC	3.17 x 10^{-10}	5
5	2	SC	3.17 x 10^{-9}	0.5
6	2	SC	3.17 x 10^{-10}	0.5
7	2	SC	3.17 x 10^{-11}	0.5
8	2	SC	3.17 x 10^{-10}	0.05

In addition, the dimensionless scan rate v^* was expressed as [30]

$$v^* = \frac{v\tau_e}{\psi_{max} - \psi_{min}} = \frac{\tau_e}{\tau_{CV}/2} \tag{5.15}$$

where τ_{CV} is the CV cycle period and the time scale τ_e is chosen to be the charac-

teristic time for potential propagation (i.e., for electron transport in the electrode material) instead of the diffusion time scale $\tau_D = L^2/D$ used by Wang and Pilon [30]. This time scale τ_e can be expressed as [192]

$$\tau_e = \frac{L_c}{u_e} = \frac{\rho_c n_e e L_c^2}{M_c(\psi_{max} - \psi_{min})\sigma_c}. \tag{5.16}$$

Here, L_c is the thickness of the porous carbon electrode, u_e is the so-called drift velocity, i.e., the average velocity of electrons under electric field $E = (\psi_{max} - \psi_{min})/L_c$, and expressed as $u_e = (M_c\sigma_c E)/(\rho_c n_e e)$, where ρ_c is the density of the electrode material, n_e is the number of free electrons per atom in the electrode material, M_c is the atomic mass (in u) of the electrode material and σ_c is the electrode material electrical conductivity. For carbon nanospheres, $\rho_c = 500$ kg/m^3 [191], $n_e = 1$, and $M_c = 12.01$ u. Figure 5.8(d) indicates that the capacitance ratio $C_{BET}/C_{BET,max}$ for electrodes with different electrical conductivity σ_c, ion diffusion coefficient D, electrode thickness L_c, and packing structures collapsed on the same curve when plotted as a function of dimensionless scan rate v^*. In addition, for dimensionless scan rate v^* smaller than 0.3, the areal capacitance was maximum and rate-independent, corresponding to $v \leq \alpha/[(\psi_{max} - \psi_{min})^2 L_c^2]$ where $\alpha = 0.3 M_c\sigma_c/\rho_c n_e e$ depends only on the electrode material. Thus, electrode materials with large values of α are desirable to achieve high rate performance. For example, $\alpha = 4.7$ for gold [193] while α ranges between 7.5 x $10^{-8} - 1.2$ x 10^{-3} for carbon nanoparticles [191] and between 4.1 x $10^{-13} - 1.5$ x 10^{-4} for activated carbon (porous) [190, 191] depending on their electrical conductivity and density.

5.3 Chapter summary

This chapter presented three-dimensional transient simulations of EDLC electrodes consisting of monodisperse carbon spheres with different diameters and ordered in FCC and SC packing structures under cyclic voltammetry. Simulations

were based on a continuum model accounting for interfacial and transport phenomena throughout the electrode and the electrolyte. For any given morphology, the areal capacitance increased with decreasing sphere diameter. In addition, FCC packing featured larger capacitance than SC packing. These results were explained by considering the magnitude of the electric field at the carbon spheres/electrolyte interfaces. Moreover, for all cases considered, the areal capacitance remained constant at low scan rate but decreased beyond a critical scan rate when potential propagation across the electrode could not follow the rapid changes in the potential imposed at the current collector. In fact, the rate-dependent regime of capacitance was reached at lower scan rates for thicker electrodes, regardless of the electrode morphology. Finally, dimensional analysis was performed to collapse capacitance versus scan rate plots, based on ratio of CV cycle period and the time scale for electron transport in the electrode. These results and the computational tools developed can be used to design and optimize EDLC electrodes to maximize energy and/or power densities.

CHAPTER 6

Interfacial and Transport Phenomena in Electrodes Consisting of MnO_2 Coated Carbon Nanorods under Cyclic Voltammetry

The previous chapter studied the effect of electrode morphology on the performance of EDLC electrodes using multi-dimensional simulations under cyclic voltammetry. This chapter aims to extend the study to pseudocapacitive electrodes. To do so, two-dimensional axis-symmetric numerical simulations of pseudocapacitive electrodes consisting of ordered conducting nanorods coated with a thin film of pseudocapacitive material were performed to identify an optimum pseudocapacitive layer thickness that maximizes total areal capacitance.

6.1 Background

6.1.1 Empirical characterization of pseudocapacitive electrodes

A semi-empirical approach for analyzing cyclic voltammetry (CV) measurements has been used extensively [172, 194–200] to determine whether the charge storage process involves (i) surface-controlled mechanism when the measured current density is proportional to scan rate or (ii) diffusion-controlled mechanism when the measured current density is proportional to the square root of scan rate [201]. This approach assumed linear summation of the two contributions to the measured current density j_T at low scan rates according to [201],

$$j_T(v,\psi_s) = k_1(\psi_s)v + k_2(\psi_s)v^{1/2} \quad \text{or} \quad \frac{j_T(v,\psi_s)}{v^{1/2}} = k_1(\psi_s)v^{1/2} + k_2(\psi_s). \tag{6.1}$$

Here, $k_1(\psi_s)$ and $k_2(\psi_s)$ are semi-empirical functions associated respectively with surface-controlled and diffusion-controlled mechanisms. They correspond to the slope and intercept in the plot of $j_T/v^{1/2}$ versus $v^{1/2}$ for a given potential $\psi_s(t)$. The functions $k_1(\psi_s)$ and $k_2(\psi_s)$ are independent of scan rate v but depend on the imposed potential ψ_s [201].

Another approach commonly used experimentally [31, 194, 198, 199, 202–207] assumed that the total current density obeys a power law with respect to the scan rate v according to [202]

$$j_T(v, \psi_s) = a_0(\psi_s)v^{b(\psi_s)} \tag{6.2}$$

where the so-called b-value was expected to vary between 1/2 (diffusion-controlled mechanism) and 1 (surface-controlled mechanism) [202]. A b-value of 1 across the potential window is highly desirable to achieve high charging rates [31]. Unfortunately, a dip in the b-value when plotted as a function of $\psi_s(t)$ has often been observed experimentally and attributed to the redox peak from faradaic reactions retrieved from CV curves [194, 198, 207]. However, recent modeling efforts have clarified the physical phenomena responsible for the dip in the b-value [31].

Finally, note that the above data analysis methods can be applied to the gravimetric (in A/g) or areal (in A/m^2) current densities, or the total current i_T (in A).

6.2 Analysis

6.2.1 Schematic and assumptions

Figure 6.1(a) shows the schematic of a pseudocapacitive electrode consisting of a planar current collector of thickness L_s supporting an array of electrically conducting nanorods coated by a layer of pseudocapacitive material. According to

(a)

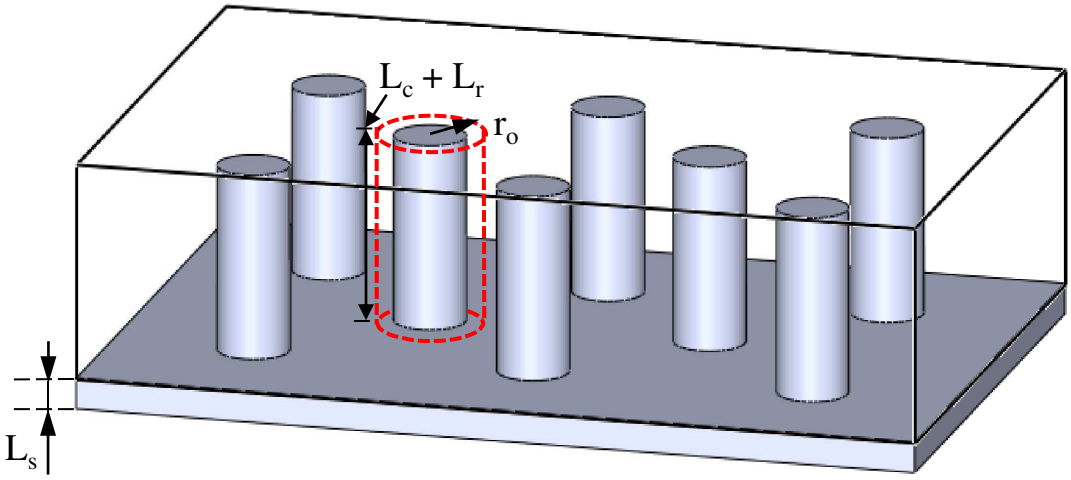

(b)

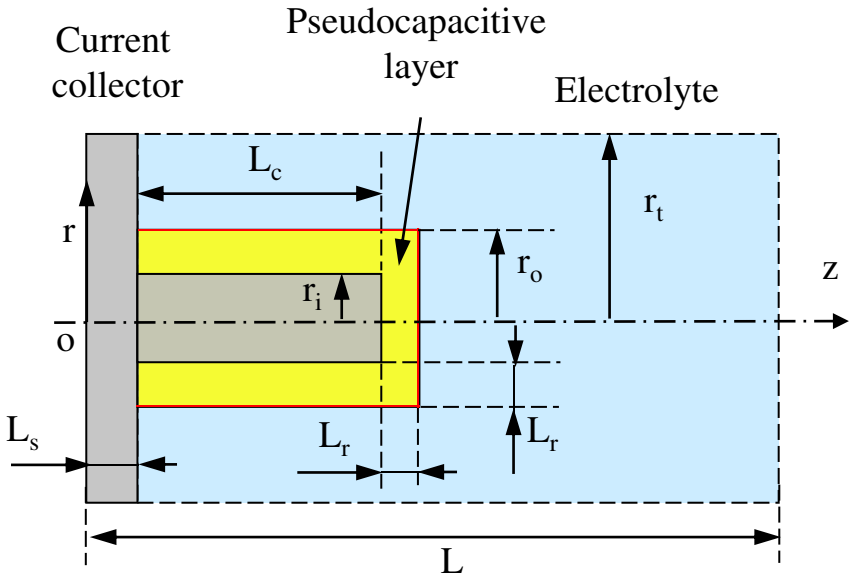

Figure 6.1: Schematics of (a) electrodes consisting of highly ordered conducting nanorods coated with pseudocapacitive material on a planar current collector(b) simulated 2D cross-section of one rod along with the cylindrical coordinate system.

preliminary simulations, charge storage on an individual nanorod was not affected by the presence of its neighbors if the distance between adjacent nanorods was larger than 10 nm. Indeed, under this condition, the electric double layers (EDLs) formed near two adjacent coated nanorods did not overlap. Thus, a single axially symmetric nanorod with a conducting nanorod of radius r_i and length L_c conformably coated by a pseudocapacitive layer of thickness L_r was simulated in cylindrical coordinates, as illustrated in Figure 6.1(b). This generic electrode was conceived as a representation of pseudocapacitive electrodes synthesized experimentally [71, 72, 125–127]. Similarly, the electrolyte consisted of $LiClO_4$ in propylene carbonate, as commonly used experimentally [208].

Following assumptions were made: (1) the electrolyte was binary and symmetric, i.e., two ion species were considered and featured the same ion diameter a, valency $\pm z$, and diffusion coefficient D. (2) The Stern layer contained no free charges and its thickness H was approximated as the radius of the ions, so that $H = a/2$ [8, 16, 151]. (3) The transport properties in the electrode and electrolyte were constant. (4) Bulk motion of the electrolyte was negligible. (5) The system was isothermal and its temperature remained constant.

6.2.2 Governing equations

Simulations reported in this chapter were based on the modified Poisson-Nernst-Planck (MPNP) model for the spatiotemporal evolution of the potential $\psi(x,t)$ [Equation (2.1)] in the electrode and electrolyte as well as the ion concentrations $c_1(x,t)$ of cations and $c_2(x,t)$ of anions [Equations (2.2) and (2.4)] in the binary and symmetric electrolyte for EDLC electrodes or devices.

The local electric potential $\psi(\mathbf{r},t)$ in the electrode consisting of a pseudocapacitive layer coated on conducting nanorods was governed by the Poisson equation

[Equation (2.1)]. expressed as [16, 146]

$$\nabla \cdot (\sigma_P \nabla \psi) = 0 \quad \text{in the pseudocapacitive layer} \tag{6.3}$$

$$\nabla \cdot (\sigma_C \nabla \psi) = 0 \quad \text{in the conducting nanorod} \tag{6.4}$$

where σ_P and σ_C are the electrical conductivities of the pseudocapacitive material and of the conducting nanorod, respectively.

The local molar concentration of the intercalated Li^+ (species 1) in the pseudocapacitive layer, denoted by $c_{1,P}(\mathbf{r}, t)$, was governed by the mass diffusion equation [Equation (2.9)].

Moreover, the modified Poisson-Nernst-Planck (MPNP) model governed the spatiotemporal evolutions of the electric potential $\psi(\mathbf{r}, t)$ [Equation (2.1)] and of the two ion concentrations $c_i(\mathbf{r}, t)$ [Equations (2.2) and (2.4)] in the electrolyte [141–143].

6.2.3 Initial and boundary conditions

The initial electric potential was assumed to be uniform across the simulated electrode and electrolyte and given by $\psi(\mathbf{r}, 0) = 0$ V. In addition, the initial cation (Li^+) and anion (ClO_4^-) concentrations in the electrolyte were taken as uniform and equal to their bulk concentrations according to $c_1(\mathbf{r}, 0) = c_2(\mathbf{r}, 0) = c_\infty$. Similarly, the initial concentration of intercalated Li^+ in the pseudocapacitive electrode was uniform and equal to $c_{1,P,0}$, i.e., $c_{1,P}(\mathbf{r}, 0) = c_{1,P,0}$.

The potential at the current collector surface $(r, z = 0)$ was imposed as $\psi_s(t)$. For cyclic voltammetry, $\psi_s(t)$ varied linearly with time [Equation (1.1)]. The corresponding boundary condition in the centerplane located at $\mathbf{r}_{cp} = (0 \leq r \leq r_t, z = L_s + L)$ was given, by virtue of symmetry, as

$$\psi(\mathbf{r}_{cp}, t) = 0. \tag{6.5}$$

The electric potential in the EDL varied linearly across the Stern layer so that the normal electric field at planar and cylindrical Stern/diffuse layer interfaces, located at $\mathbf{r}_H$ satisfied [1, 16]

$$\frac{\partial \psi}{\partial n}(\mathbf{r}_H, t) = \frac{\psi(\mathbf{r}_{S/E,pl}) - \psi(\mathbf{r}_H)}{H} \quad \text{for planar interfaces} \tag{6.6}$$

$$-\epsilon_0 \epsilon_r \frac{\partial \psi}{\partial n}(\mathbf{r}_H, t) = C_s^{St} \left(\frac{r_o}{r_o + H} \right) \left[\psi(\mathbf{r}_{S/E,cy}) - \psi(\mathbf{r}_H) \right] \quad \text{for cylindrical interfaces} \tag{6.7}$$

where $\mathbf{r}_{S/E,pl}$ and $\mathbf{r}_{S/E,cy}$ refer to the location of the planar electrode or current collector/electrolyte interfaces and to that of the cylindrical solid/electrolyte interfaces such that $\mathbf{r}_{S/E,pl} = (r_o \leq r \leq r_t, z = L_s) \cup (0 \leq r \leq r_o, z = L_s + L_c + L_r)$ and $\mathbf{r}_{S/E,cy} = (r = r_o, L_s \leq z \leq L_s + L_c + L_r)$, where r_o is the total radius of the coated nanorod, i.e., $r_o = r_i + L_r$. Here, the Stern layer capacitance C_s^{St} is given by Helmholtz model for cylindrical electrode expressed as [176]

$$C_s^{St} = \frac{\epsilon_0 \epsilon_r}{r_o \ln(1 + H/r_o)}. \tag{6.8}$$

These boundary conditions accounted for the presence of the Stern layer without explicitly simulating it in the computational domain. This approach significantly reduced the number of finite elements necessary to numerically solve the equations. In fact, it made possible the numerical solutions of the above coupled transient 2D governing equations [1].

Moreover, at the current collector/electrolyte interface located at $\mathbf{r}_{C/E} = (r_o \leq r \leq r_t, z = L_s)$, only the capacitive current due to the electric double layer formation contributed to the total current density so that

$$-\sigma_C \frac{\partial \psi}{\partial n}(\mathbf{r}_{C/E}, t) = j_C(\mathbf{r}_H, t) \tag{6.9}$$

where $\partial/\partial n$ corresponds to the gradient along the direction normal to the electrode/electrolyte interface. Here, $j_C(\mathbf{r}_H, t)$ is the capacitive current density at the

Stern/diffuse layer interface located at $\mathbf{r}_H$ and defined as [167]

$$j_C(\mathbf{r}_H, t) = -\epsilon_0 \epsilon_r \frac{\partial^2 \psi}{\partial n \partial t}(\mathbf{r}_H, t). \tag{6.10}$$

On the other hand, the current density at the pseudocapacitive layer/electrolyte interface, located at $\mathbf{r}_{P/E} = (r = r_o, L_s \leq z \leq L_s + L_c + L_r) \cup (0 \leq r \leq r_o, z = L_s + L_c + L_r)$ equaled to the sum of the capacitive current density $j_C(\mathbf{r}_H, t)$ (in $\mathrm{A/m^2}$) due to EDL formation and the faradaic current density $j_F(t)$ (in $\mathrm{A/m^2}$) due to redox reactions, so that [16, 145]

$$-\sigma_P \frac{\partial \psi(\mathbf{r}_{P/E}, t)}{\partial n} \quad = \quad j_C(\mathbf{r}_H, t) + j_F(\mathbf{r}_{P/E}, t). \tag{6.11}$$

The faradaic current density $j_F(\mathbf{r}_{P/E}$,t) can be defined by the generalized Frumkin-Butler-Volmer model evaluated at the pseudocapacitive layer/electrolyte interface and expressed as [8]

$$j_F(\mathbf{r}_{P/E}, t) = j_{F,ex}(t) \left\{ \exp\left[\frac{(1-\alpha) z F \eta(\mathbf{r}_{P/E}, t)}{R_u T} \right] - \exp\left[\frac{-\alpha z F \eta(\mathbf{r}_{P/E}, t)}{R_u T} \right] \right\} \tag{6.12}$$

where $j_{F,ex}(t)$ [Equation (2.7)] is the so-called exchange current density, α is the transfer coefficient, and $\eta(\mathbf{r}_{P/E}, t)$ is the surface overpotential.

Moreover, the mass flux of the intercalated $\mathrm{Li^+}$ vanished at the conducting nanorod/pseudocapacitive layer interface located at $\mathbf{r}_{N/P} = (0 \leq r \leq r_i, z = L_s + L_c) \cup (r = r_i, L_s \leq z \leq L_s + L_c)$ and at the current collector/pseudocapacitive layer interface located at $\mathbf{r}_{C/P} = (r_i \leq r \leq r_o, z = L_s)$ such that

$$\mathbf{N}_1(\mathbf{r}_{N/P}, t) = \mathbf{N}_1(\mathbf{r}_{C/P}, t) = \mathbf{0}. \tag{6.13}$$

The mass flux of $\mathrm{Li^+}$ intercalating or deintercalating through the pseudocapacitive layer/electrolyte interface was related to the faradaic current density $j_F(\mathbf{r}_{P/E}, t)$

based on stoichiometry as [7]

$$\mathbf{N}_1(\mathbf{r}_{P/E}, t) = \frac{j_F(\mathbf{r}_{P/E}, t)}{z\,F}\mathbf{n}_{P/E}. \tag{6.14}$$

Finally, both the current collector and the pseudocapacitive layer were impermeable to ClO_4^- ions ($i = 2$) so that

$$\mathbf{N}_2(\mathbf{r}_{P/E}, t) = \mathbf{N}_2(\mathbf{r}_{C/E}, t) = \mathbf{0}. \tag{6.15}$$

6.2.4 Constitutive relationships

A total of 23 input parameters were needed to solve the governing equations [Equations (2.5) to (2.8)] along with the initial and boundary conditions. These parameters include (i) the electrolyte properties ϵ_r, a, z, D, and c_∞, (ii) the pseudocapacitive layer properties $\Delta\psi_{eq}$, $c_{1,P,max}$, $c_{1,P,0}$, $D_{1,P}$, k_0, α, and σ_P, (iii) the electrical conductivity of the conducting nanorod and current collector σ_C, (iv) the electrode dimensions r_i, r_t, L, L_c, L_s, and L_r, and (v) the operating conditions T, ψ_{max}, ψ_{min}, and v. Typical values of these parameters were collected from the literature [82, 83, 145, 146, 152, 161–163, 165, 166, 190, 191, 209–211].

The binary and symmetric electrolyte simulated corresponded to 1 M $LiClO_4$ in propylene carbonate (PC) solvent, i.e., $c_\infty = 1$ M [208]. The dielectric constant of the electrolyte was taken as constant and equal to $\epsilon_r = 66.1$ corresponding to that of PC at zero electric field [152]. The effective solvated ion diameters a and diffusion coefficient D were taken as those of Li^+ ion ($z = 1$) in PC and equal to $a = 0.67$ nm and D = 2.6 x 10^{-10} m^2/s [166].

For electrode consisting of transition metal oxides, the equilibrium potential difference $\Delta\psi_{eq}$ is typically determined experimentally based on open-circuit potentials [145, 146]. It can be modeled as a linear function of the state-of-charge (SOC) expressed as $c_{1,P}/c_{1,P,max}$ [82, 83, 161]. For MnO_2 dense films of thickness

100 μm at low scan rates, $\Delta\psi_{eq}(t)$ (in V) was measured as [162]

$$\Delta\psi_{eq}(t) = 10.5[4 - c_{1,P}(t)/c_{1,P,max}] - 39.9. \tag{6.16}$$

This expression was used in the present study with the maximum intercalated lithium concentration in the pseudocapacitive layer $Li_mM_pO_q$ estimated as $c_{1,P,max} = m\rho/M$ where ρ and M are the density and molar mass of the fully intercalated metal oxide. For $LiMnO_2$, ρ and M were reported as $\rho \approx 3.0$ g/cm^3 and $M = 93.9$ g/mol [163] yielding $c_{1,P,max} \approx 31.9$ mol/L. Finally, the initial concentration of Li^+ in the electrode was chosen as $c_{1,P,0} \approx 6.38$ mol/L such that the initial equilibrium potential difference $\Delta\psi_{eq}(t = 0)$ was zero. In addition, the value of the diffusion coefficient $D_{1,P}$ of the intercalated Li^+ in the transition metal oxides was chosen as 10^{-12} m^2/s, based on the typical range from 10^{-16} to 10^{-10} m^2/s [165]. The reaction rate constant k_0 for transition metal oxides has been reported to range between 10^{-11} and 10^{-8} m$^{2.5}$mol$^{-0.5}$s^{-1} [145, 146, 165]. Here, it was taken as $k_0 = 10^{-8}$ m$^{2.5}$mol$^{-0.5}$s^{-1} to maximize contribution from redox reactions. The transfer coefficient α was assumed to be 0.5, corresponding to identical energy barriers for forward and backward redox reactions [8]. The electrical conductivity of metal oxides may vary with the intercalation of lithium as well as the structure of the material [209–211]. Here, a constant value $\sigma_P = 10^{-5}$ S/m was selected based on the range of electrical conductivity between 10^{-6} S/m and 10^{-3} S/m for Li_xMnO_2 ($0 \leq x \leq 1$) at room temperature [210]. On the other hand, the electrical conductivity of the conducting nanorod and current collector was taken as the same value of $\sigma_C = 5$ S/m based on the typical range of carbon conductivity between 10^{-6} and 10^2 S/m [190, 191].

Moreover, the thicknesses of the current collector L_s and height of the conducting nanorod L_c were taken as $L_s = 10$ nm and $L_c = 100$ nm. The radius of the conducting nanorod r_i and the thickness of the pseudocapacitive layer L_r

were treated as variables. The thickness of the computational domain was taken as $L = 0.5$ μm, corresponding to half the thickness of the device. The radius of the computational domain r_t was chosen as $r_t = r_i + L_r + 40$ nm.

Finally, the potential window was selected to be large enough to show all relevant phenomena occurring during charging and discharging. Consequently, the imposed potential $\psi_s(t)$ was cycled between $\psi_{min} = -0.2$ and $\psi_{max} = +0.85$ V. The scan rate v varied from 10^{-3} to 10^4 V/s while the temperature was uniform and constant at $T = 298$ K.

6.2.5 Method of solution

The governing equations along with the initial and boundary conditions were solved using COMSOL 4.4 in parallel computing mode. Mesh element size was chosen to be the smallest at the electrode/electrolyte interface, where the gradients of ion concentrations $c_1(\mathbf{r}, t)$ or $c_2(\mathbf{r}, t)$ and potential $\psi(\mathbf{r}, t)$ were the largest. Numerical convergence was considered to be reached when changes in the local electric potential $\psi(\mathbf{r}, t)$ and the normal component of current density $j_n = \mathbf{j} \cdot \mathbf{n}$ at the electrode/electrolyte interface were less than 1% when reducing the minimum mesh size by a factor of two. In addition, the adaptive time step was controlled by the relative and absolute tolerances set to be both 0.0004. This enabled the use of smaller time steps when potential and current density changed more rapidly with time. The total number of finite elements was on the order of 10^6. The simulations were run on Hoffman2 shared computing cluster of UCLA with 4 to 8 processors and 32 to 64 GB of RAM.

Finally, several cycles were simulated and an oscillatory steady state was considered to be reached when the maximum relative error in $\psi(\mathbf{r}, t)$ and $j_n = \mathbf{j} \cdot \mathbf{n}$ between two consecutive cycles, at time t and t$-\tau_{CV}$, was less than 1%. These conditions were typically met by the third cycle for all conditions simulated. It

took around 24 hours CPU time to obtain a numerically converged solution under oscillatory steady-state conditions.

6.2.6 Data processing

The interfacial area-averaged capacitive current density $j_{C,BET}$, due to EDL formation and dissolution, and faradaic current density $j_{F,BET}$, associated with faradaic reactions, (both in A/m^2) were estimated as

$$j_{k,BET}(t) = \frac{1}{A_{BET}} \iint_{A_{BET}} j_k(\mathbf{r}, t) \mathrm{d}A_{BET} \quad \text{with } k = C, \text{ or } F \tag{6.17}$$

where A_{BET} is the total surface area of the solid/electrolyte interface, equivalent to that measured experimentally by the Brunauer-Emmett-Teller (BET) method [212]. In addition, the total areal current density was estimated as $j_{T,BET} = j_{C,BET} + j_{F,BET}$.

Moreover, the associated areal integral capacitance $C_{k,BET}$ (in μF/cm^2) can be estimated from the predicted CV curves at scan rate v according to [149]

$$C_{k,BET}(v) = \frac{1}{\psi_{max} - \psi_{min}} \oint \frac{j_{k,BET}(t)}{2v} d\psi_s \quad \text{with } k = C, F, \text{ or } T. \tag{6.18}$$

Similarly, the gravimetric current density $j_{k,g}$ (in A/g) can be expressed as

$$j_{k,g} = j_{k,BET} A_{BET} / m_P \quad \text{with } k = C, F, \text{ or } T \tag{6.19}$$

where m_P is the total mass of the pseudocapacitive material coated on the conducting nanorod. Then, the gravimetric capacitance $C_{k,g}(v)$ (in F/g) can be expressed as

$$C_{k,g}(v) = \frac{1}{\psi_{max} - \psi_{min}} \oint \frac{j_{k,g}(t)}{2v} d\psi_s \quad \text{with } k = C, F, \text{ or } T. \tag{6.20}$$

6.3 Results and discussion

6.3.1 Physical interpretation

This section considers an electrode consisting of 35 nm thick pseudocapacitive material coated on a conducting nanorod with radius r_i of 5 nm and length L_c of 100 nm [Figure 6.1(b)]. This configuration was chosen based on experimentally synthesized electrodes consisting of multiple layers of MnO_2 nanocrystals, 10 nm in diameter, deposited on carbon nanotube with outer radius of 7.5 $\pm$ 2.5 nm [72]. Figure 6.2(a) shows the gravimetric (i) capacitive current density $j_{C,g}$, (ii) faradaic current density $j_{F,g}$, and (iii) total current density $j_{T,g}$ as functions of the imposed potential $\psi_s(t)$ at scan rate $v = 0.1$ V/s. It also shows (b) the corresponding concentrations $c_1(0, L_s + L_c + L_r, t)$ of the cation Li^+ and $c_2(0, L_s + L_c + L_r, t)$ of the anion ClO_4^-, (c) the concentration $c_{1,P}(t)$ of the intercalated Li^+ in the pseudocapacitive layer, and (d) the overpotential η as functions of the imposed potential $\psi_s(t)$. Note that the intercalated Li^+ concentration $c_{1,P}(\mathbf{r}, t)$ was uniform throughout the thin pseudocapacitive layer, i.e., $c_{1,P}(\mathbf{r}, t) = c_{1,P}(t)$.

Figure 6.2(a) indicates that the CV curves displayed two regimes namely (i) a faradaic regime in the lower portion of the potential window when contribution by the faradaic current density $j_F(t)$ dominated and (ii) a capacitive regime in the higher portion of the potential window when the capacitive current density $j_C(t)$ dominated. The transition between faradaic and capacitive regimes can be attributed to Li^+ ion starvation in the electrolyte at the pseudocapacitive layer/electrolyte interface during charging, represented by a blue square in of Figure 6.2. Indeed, the exchange current density $j_{F,ex}$ [Equation (2.7)] decayed to zero as Li^+ starvation occurred in the electrolyte, i.e., $c_1(\mathbf{r}_H, t) \to 0$. This was caused by faster Li^+ electrodiffusion in the electrolyte away from the electrode/electrolyte interface compared with Li^+ deintercalation from the electrode to the electrode/electrolyte interface due to faradaic reactions. In addi-

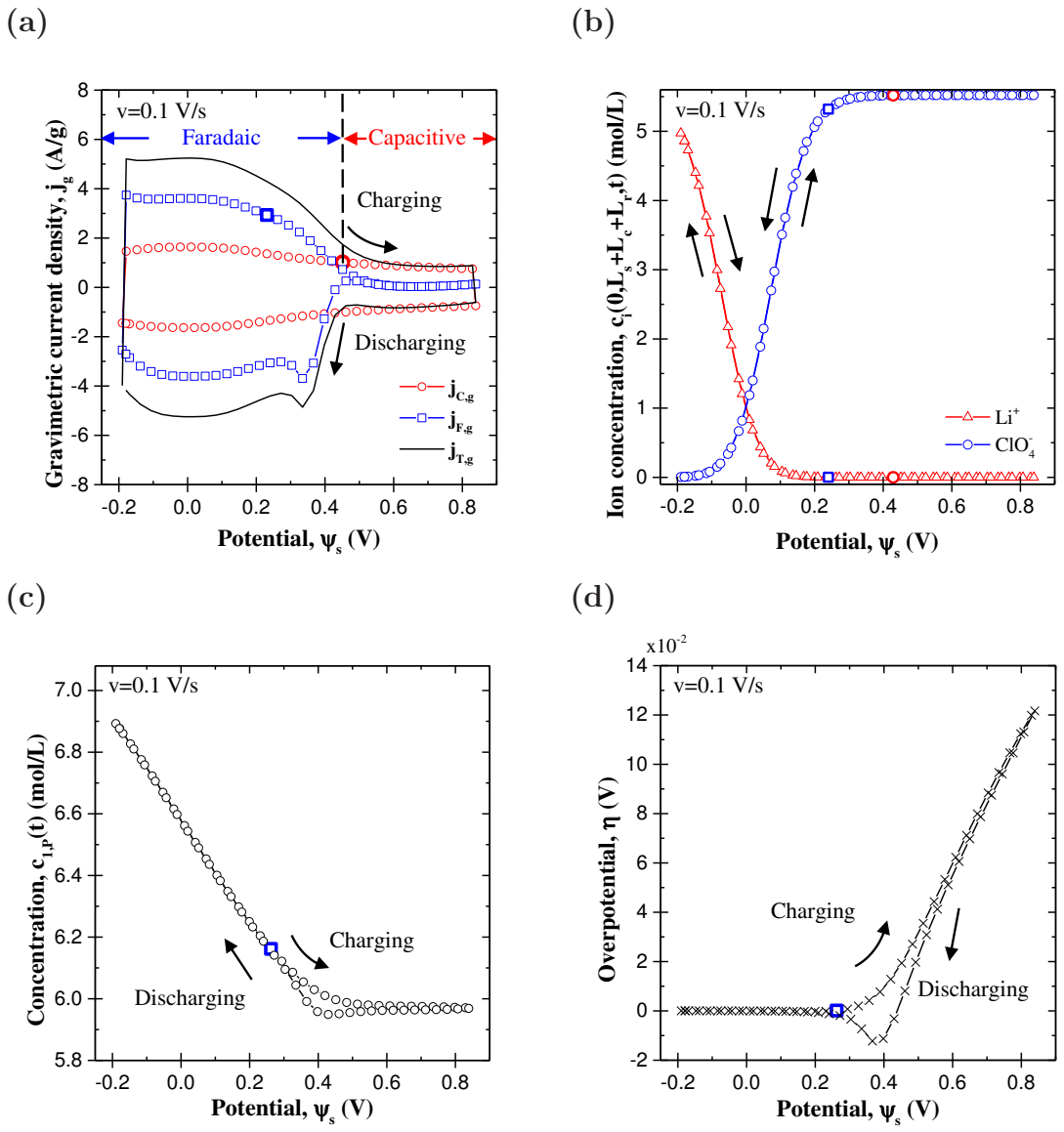

Figure 6.2: (a) Gravimetric capacitive $j_{C,g}$, faradaic $j_{F,g}$, and total $j_{T,g}$ current densities as functions of imposed potential $\psi_s(t)$ for an electrode consisting of conducting nanorod with radius r_i of 5 nm supporting pseudocapacitive material with thickness L_r of 35 nm, at scan rate $v = 0.1$ V/s. (b) Corresponding Li^+ ion concentration $c_1(0, L_s+L_c+L_r, t)$ and ClO_4^- ion concentration $c_2(0, L_s+L_c+L_r, t)$ at the electrode/electrolyte interface, (c) intercalated Li^+ concentration in the pseudocapacitive layer $c_{1,P}(t)$, and (d) overpotential η as functions of $\psi_s(t)$ at $v = 0.1$ V/s.

tion, Figure 6.2(b) indicates that ClO_4^- ions formed EDL at the pseudocapacitive layer/electrolyte interface while Li^+ ion concentration reached zero in the capacitive regime. In fact, the ClO_4^- at the pseudocapacitive layer/electrolyte interface reached saturation concentration soon after the onset of the capacitive regime, as indicated by a red circle.

Moreover, Figure 6.2(c) indicates that the Li^+ ion concentration $c_{1,P}(t)$ in the pseudocapacitive layer varied linearly with imposed potential in the faradaic regime but remained constant in the capacitive regime. Overall, Li^+ intercalation and deintercalation were fast and reversible despite a small hysteresis at the transition between faradaic and capacitive regimes. Finally, Figure 6.2(d) indicates that the overpotential $\eta(t)$ was nearly constant and close to zero in the faradaic regime. However, it was large and varied linearly with time in the capacitive regime, as theoretically explained previously for planar pseudocapacitive electrodes [31].

Further interpretation of the CV results was obtained by varying the scan rate v between 0.01 and 10^3 V/s. Figure 6.3(a) shows the log-log graph of the total gravimetric current density $j_{T,g}$ as a function of scan rate v in log scale for imposed potential $\psi_s(t)$ of 0.1, 0.3, 0.4, and 0.6 V. The slope of $j_{T,g}$ vs. v corresponds to the so-called b-value [Equation (6.2)]. Figure 6.3(b) shows the b-value for different values of $\psi_s(t)$ during charging. It indicates that the b-value approached unity in both the faradaic and capacitive regimes. However, it featured a dip at the transition from faradaic to capacitive regimes corresponding to the steep drop in the faradaic current density [Figure 6.2(a)] due to the ion starvation of Li^+ in the electrolyte at the electrode/electrolyte interface [Figure 6.2(b)]. Similar observations were made for planar pseudocapacitive electrodes [32].

Moreover, Figure 6.3(c) plots $j_{T,g}/v^{1/2}$ as a function of $v^{1/2}$ for the imposed potential $\psi_s(t)$ of 0.1, 0.3, 0.4, and 0.6 V for scan rate v less than 1 V/s. The slope and intercept corresponded to $k_1(\psi_s)$ and $k_2(\psi_s)$ in Equation (6.1), respectively. The coefficient of determination R^2 for linear fitting of $j_{T,g}/v^{1/2}$ and $v^{1/2}$ was

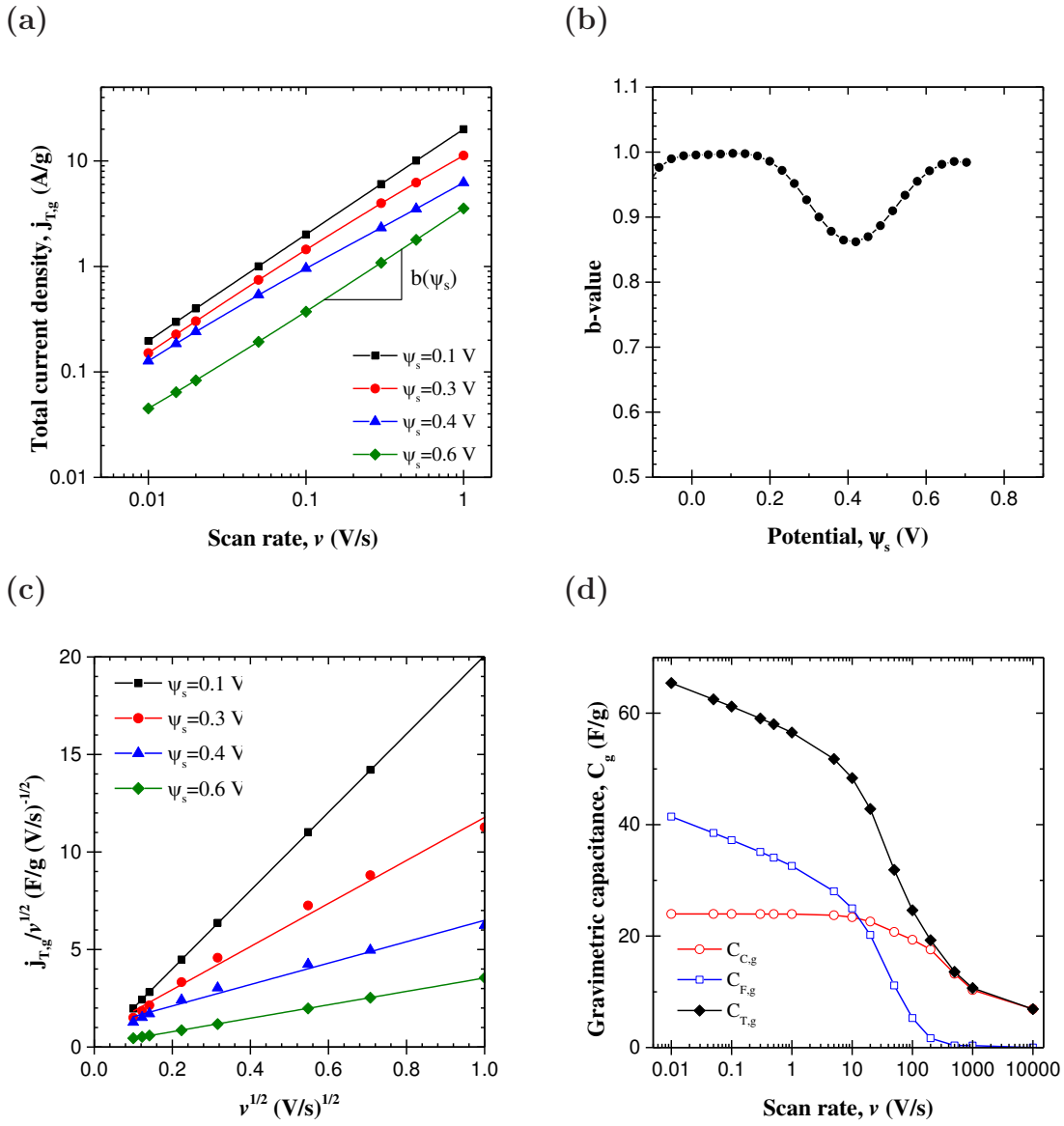

Figure 6.3: (a) Gravimetric current density $j_{T,g}$ as a function of scan rate v in log-log scale, (b) b-value as a function of the imposed potential $\psi_s(t)$, (c) $j_{T,g}/v^{1/2}$ as a function of $v^{1/2}$ for $v \leq 1$ V/s, and (d) gravimetric capacitive $C_{C,g}$, faradaic $C_{F,g}$, and total $C_{T,g}$ capacitances as functions of scan rate v for an electrode consisting of conducting nanorod with radius r_i of 5 nm supporting pseudocapacitive material with thickness L_r of 35 nm.

between 0.96 and 1. To the best of our knowledge, these results provides, for the first time, theoretical validations of the semi-empirical relationship $j_{T,g} = k_1 v + k_2 v^{1/2}$ commonly used experimentally [172,194–200], as previously discussed.

Furthermore, Figure 6.3(d) shows the gravimetric capacitances (i) $C_{C,g}(v)$ due to the formation of the EDL, (ii) $C_{F,g}(v)$ associated with faradaic reactions, and (iii) $C_{T,g}(v) = C_{F,g}(v) + C_{C,g}(v)$ as functions of scan rate v. It indicates that $C_{C,g}(v)$ was independent of scan rate for $v \leq 10$ V/s and decreased sharply with increasing scan rate for $v \geq 10$ V/s. This was also observed in simulations of planar and porous EDLC electrodes [16] and can be attributed to the fact that the potential propagation across the electrode and/or the ion transport in the electrolyte cannot follow the fast changes in the imposed potential $\psi_s(t)$ at high scan rates. On the other hand, $C_{F,g}$ decreased continuously with increasing scan rate. This was due to the fact that the intrinsically slow faradaic reactions cannot follow the increasingly rapid changes in the imposed potential $\psi_s(t)$. Consequently, the faradaic capacitance $C_{F,g}$ dominated at low scan rates but decreased faster than $C_{C,g}$ with increasing scan rate. Finally, the total capacitance values in Figure 6.3(d) at low scan rates (e.g., 65 F/g or 286 F/cm^3 at $v = 0.01$ V/s) were quantitatively comparable with experimentally measured capacitance of 175-250 F/cm^3 for similar electrode structures at the same scan rate [72]. Note that the scan rate in actual CV measurements for pseudocapacitive electrodes ranges typically from 10^{-3} to 1 V/s with no sharp decrease in the total capacitance with increasing scan rate observed [71, 72, 126, 127, 130]. Similar observations could be made in Figure 6.3(d). Here, however, the scan rate v was varied over a wider range to study the rate-dependent capacitance at very high scan rate.

6.3.2 Effect of conducting nanorod radius

Figure 6.4 shows (a) the areal capacitive current density $j_{C,BET}$ (in A/m^2) and (b) the gravimetric faradaic current density $j_{F,g}$ (in A/g) as functions of the imposed

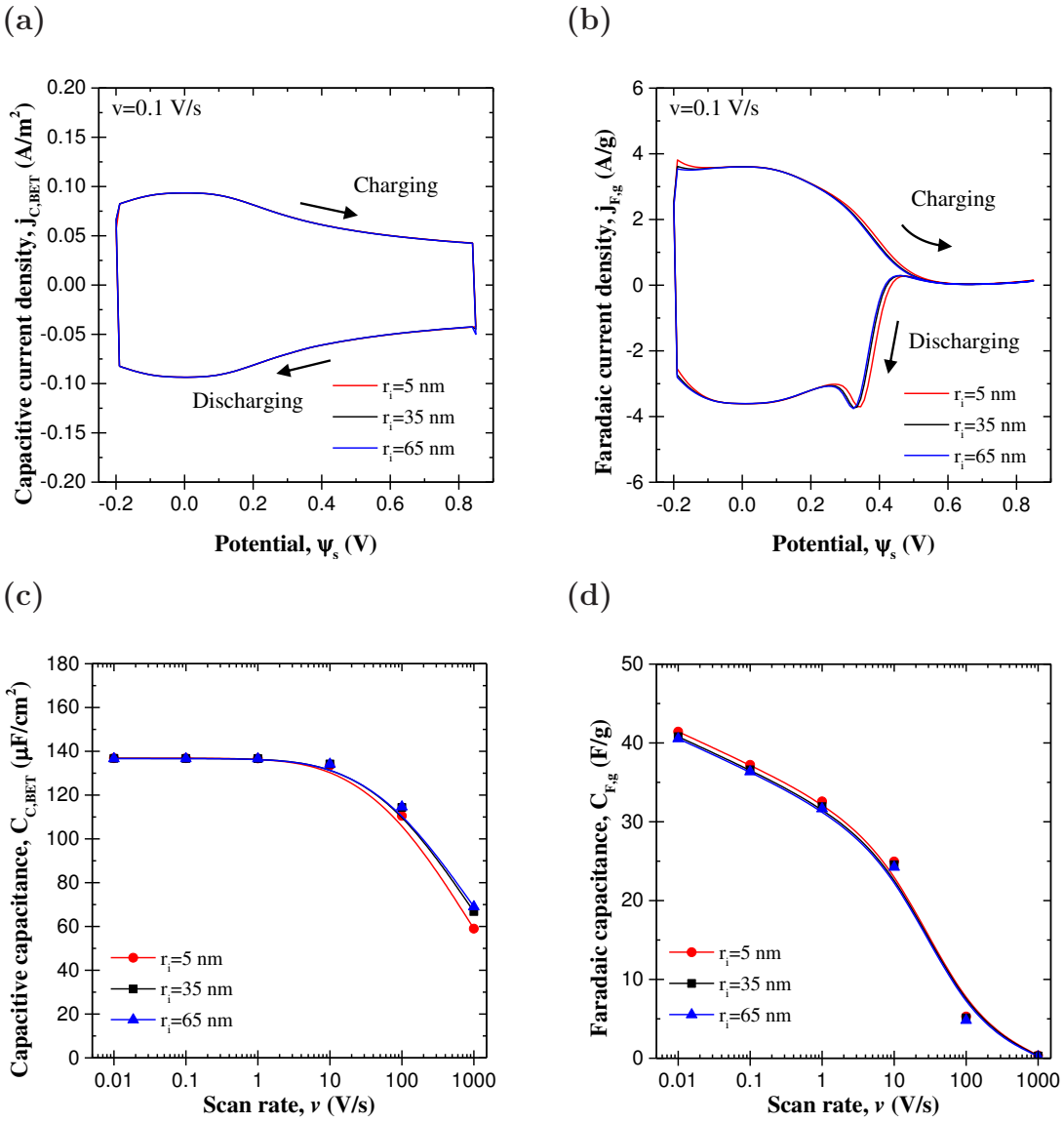

Figure 6.4: (a)(b) Areal capacitive current density $j_{C,BET}$ and gravimetric faradaic current density $j_{F,g}$ as functions of imposed potential $\psi_s(t)$ at scan rate v = 0.1 V/s, as well as (c)(d) areal capacitive capacitance $C_{C,BET}$ and gravimetric faradaic capacitance $C_{F,g}$ as functions of scan rates v for electrodes consisting of conducting nanorod with radius r_i of 5, 35, and 65 nm supporting pseudocapacitive material with thickness L_r of 35 nm.

potential $\psi_s(t)$ for electrodes consisting of conducting nanorod with radius r_i of 5, 35, and 65 nm supporting 35 nm thick pseudocapacitive layer, at scan rate $v =$ 0.1 V/s. Figure 6.4(a) indicates that the areal capacitive current density $j_{C,BET}$ was independent of r_i. In other words, the total capacitive current i_C (in A) was linearly proportional to the BET surface area A_{BET} such that $i_C \approx j_{C,BET} A_{BET}$, regardless of the radius of the conducting nanorod. Similarly, Figure 6.4(b) indicates that the gravimetric faradaic current density $j_{F,g}$ was also independent of r_i and the total faradaic current was linearly proportional to the mass of the pseudocapacitive layer, i.e., $i_F \approx j_{F,g} m_P$. This was attributed to the fast Li^+ intercalation/deintercalation within the volume of the pseudocapacitive layer.

Moreover, Figure 6.4 shows (c) the areal capacitive capacitance $C_{C,BET}$ and (d) the gravimetric faradaic capacitance $C_{F,g}$ as functions of scan rate v for different values of conducting nanorod radius r_i. These figures indicate that $C_{C,BET}$ was independent of r_i at low scan rates and decreased slightly with decreasing r_i at high scan rates. On the other hand, $C_{F,g}$ was independent of radius r_i at all scan rates considered. Thus, the gravimetric capacitive capacitance $C_{C,g} = C_{C,BET}/(m_P/A_{BET})$ decreased and the areal faradaic capacitance $C_{F,BET} = C_{F,g} m_P/A_{BET}$ increased with increasing mass loading of the pseudocapacitive material m_P/A_{BET} at low scan rates. This explains the fact that the total capacitance $C_T = C_C + C_F$ decreased with increasing m_P/A_{BET} when expressed per BET surface area but increased when expressed per unit mass of the pseudocapacitive layer, as observed experimentally [125]. To further interpret the behaviors of $C_{C,BET}$ and $C_{F,g}$ as functions of scan rate v, one needs to consider the potential propagation across the electrode, the ion transport in the electrolyte at different scan rates, and the Li^+ ion concentration intercalated in the pseudocapacitive layer.

Figures 6.5(a) and 6.5(b) show the potential $\psi_{tip}(t)$ at the tip of the coated nanorod, located at $(r, z) = (0,\ L_s + L_c + L_r)$, as a function of the dimension-

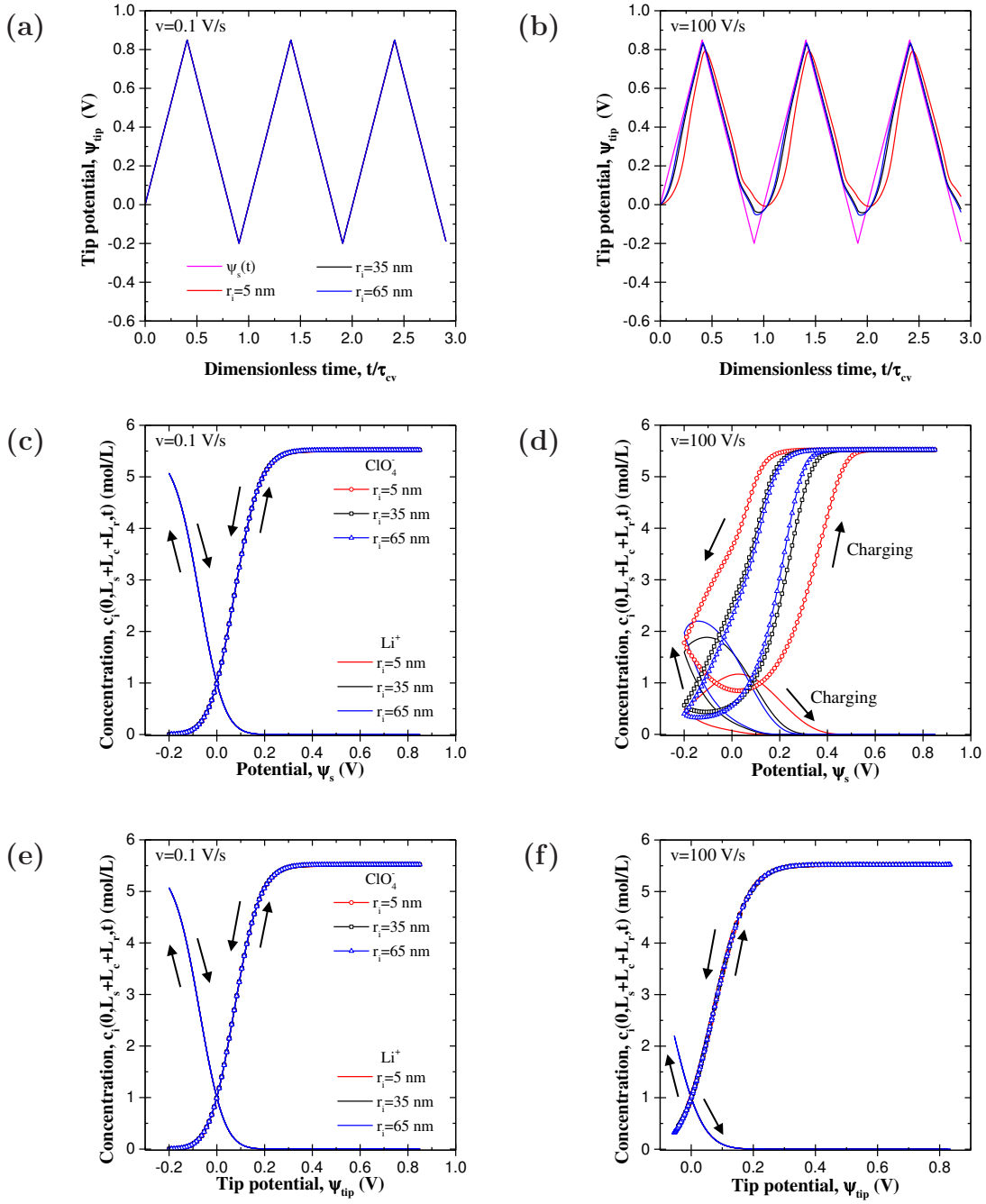

Figure 6.5: Tip potential $\psi_{tip}(t)$ as a function of the dimensionless time t/τ_{CV}, for electrodes consisting of conducting nanorod with radius r_i of 5, 35, and 65 nm supporting pseudocapacitive material with thickness L_r of 35 nm, at scan rate (a) $v = 0.1$ and (b) 100 V/s. Li^+ ion concentration $c_1(0, L_s + L_c + L_r, t)$ and ClO_4^- ion concentration $c_2(0, L_s + L_c + L_r, t)$ at the electrode/electrolyte interface (c)(d) as functions of the imposed potential ψ_s and (e)(f) as functions of the tip potential $\psi_{tip}(t)$ for the same electrodes at scan rates $v = 0.1$ and 100 V/s.

less time t/τ_{CV} at scan rates $v = 0.1$ and 100 V/s, respectively, for electrodes consisting of conducting nanorod with radius r_i of 5, 35, and 65 nm supporting 35 nm thick pseudocapacitive material layer. At low scan rates, the conducting nanorod radius r_i had no effect on $\psi_{tip}(t)$ which was identical to the imposed potential $\psi_s(t)$ [Figure 6.5(a)]. However, at high scan rates, a time lag and a reduction in amplitude in $\psi_{tip}(t)$ was increasingly apparent with decreasing nanorod radius [Figure 6.5(b)]. This was due to the fact that the electrical resistance R_C of the conducting nanorod increased with decreasing r_i according to $R_C = L_c/(\sigma_C \pi r_i^2)$. In addition, Figures 6.5(c) and 6.5(d) show the corresponding concentrations $c_1(0, L_s + L_c + L_r, t)$ of cations Li^+ and $c_2(0, L_s + L_c + L_r, t)$ of anions ClO_4^- at the electrode/electrolyte interface as functions of the imposed potential $\psi_s(t)$ at scan rates $v = 0.1$ and 100 V/s, respectively. Hysteresis in ion concentrations in the electrolyte were observed only at high scan rates. Moreover, Figures 6.5(e) and 6.5(f) show the same concentrations $c_1(0, L_s + L_c + L_r, t)$ and $c_2(0, L_s + L_c + L_r, t)$ but as functions of the potential $\psi_{tip}(t)$ at the tip of the coated nanorod, at scan rates $v = 0.1$ and 100 V/s, respectively. It is interesting to note that no hysteresis was observed for $c_1(0, L_s + L_c + L_r, t)$ and $c_2(0, L_s + L_c + L_r, t)$ when plotted versus $\psi_{tip}(t)$ at either scan rates. This indicates that the decrease in $C_{C,BET}$ at high scan rates was due to the slow potential propagation across the electrode. However, it was not due to ion diffusion limitation in the electrolyte. Similar behavior was observed and the same conclusions were reached for 3D simulations of porous EDLC electrodes made of ordered carbon spheres with various values of electrode electrical conductivity and ion diffusion coefficient in the electrolyte [150]. Furthermore, the hysteresis in the concentration $c_{1,P}$ of the Li^+ in the pseudocapacitive layer occurred at all scan rates but was independent of r_i. This led to a continuous decrease in the contribution of faradaic reactions to charge storage and to the decrease of $C_{F,g}$ with increasing scan rate v [Figure 6.4(d)].

6.3.3 Effect of pseudocapacitive layer thickness

Figures 6.6(a) and 6.6(b) show the areal capacitive current density $j_{C,BET}$ and the gravimetric faradaic current density $j_{F,g}$ as functions of the imposed potential $\psi_s(t)$ for electrodes consisting of conducting nanorod of radius r_i of 5 nm supporting pseudocapacitive layer of thickness L_r of 5, 20, 35, 50, and 100 nm, at scan rate $v =$ 0.1 V/s. Figure 6.6(a) indicates that the areal capacitive current density $j_{C,BET}$ was independent of L_r. This was also observed for other conducting nanorod radii r_i. In addition, Figure 6.6(b) indicates that the gravimetric faradaic current density $j_{F,g}$ was nearly independent of L_r in the lower portion of the faradaic regime ($\psi_s(t) \leq 0.2$ V). However, for larger potential $\psi_s(t)$, $j_{F,g}$ started decreasing sharply to zero faster with increasing L_r.

To further investigate the effect of L_r, the scan rate v was varied between 10^{-3} V/s and 10^4 V/s. Figure 6.6(c) shows the b-value as a function of the imposed potential $\psi_s(t)$ for different values of coating thickness L_r. It indicates that the dip in the b-value became more prominent with increasing pseudocapacitive layer thickness L_r due to a sharper decrease in the total current density $j_{T,g}$ during the transition between the faradaic and capacitive regimes [Figure 6.6(b)].

Moreover, Figures 6.6(e) and 6.6(f) show respectively the areal capacitive capacitance $C_{C,BET}$ and the gravimetric faradaic capacitance $C_{F,g}$ as functions of scan rate v for different values of thickness L_r. It indicates that $C_{C,BET}$ was independent of L_r at low scan rates, corresponding to the equilibrium capacitance, as observed previously for EDLC electrodes [30]. However, it started decreasing sharply and at lower scan rates as L_r increased. In addition, the gravimetric faradaic capacitance $C_{F,g}$ decreased continuously with increasing coating thickness L_r for any given scan rate. Here also, to explain these observations, one needs to consider the temporal evolution of the electrode tip potential, the ion concentrations in the electrolyte at the solid/electrolyte interfaces, as well as the

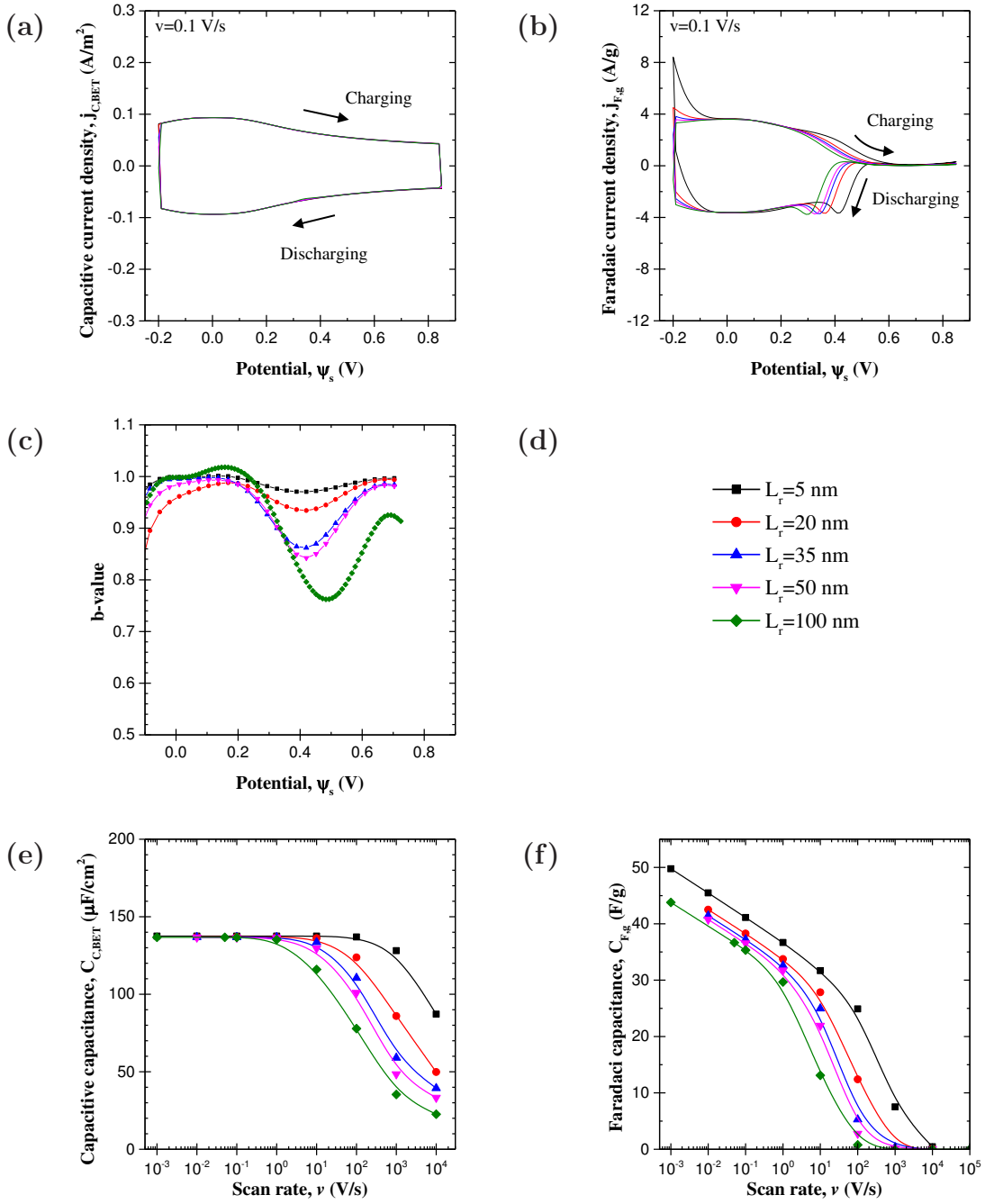

Figure 6.6: (a)(b) Areal capacitive current density $j_{C,BET}$ and gravimetric faradaic current density $j_{F,g}$ as functions of imposed potential $\psi_s(t)$ at scan rate $v = 0.1$ V/s, (c) b-value as a function of the imposed potential $\psi_s(t)$, and corresponding (e) areal capacitive capacitance $C_{C,BET}$ and (f) gravimetric faradaic capacitance $C_{F,g}$ as functions of scan rates v for electrodes consisting of conducting nanorod with radius r_i of 5 nm supporting pseudocapacitive material with thickness L_r of 5, 20, 35, 50, and 100 nm.

total changes in the state of charge (SOC) during charging.

Figures 6.7(a) and 6.7(b) show the potential $\psi_{tip}(t)$ at the tip of the electrode, located at $(r, z) = (0, L_s + L_c + L_r)$, as a function of the dimensionless time t/τ_{CV}, for the same electrodes as those simulated in Figure 6.6, at scan rates $v = 0.1$ and 100 V/s, respectively. Here also, a time lag in the tip potential was observed only at high scan rates associated with a reduction in amplitude in $\psi_{tip}(t)$ which became more apparent with increasing L_r. This was attributed to the increase in electrical resistance $R_P \approx L_r/[\sigma_P(\pi r_i^2 + 2\pi r_i L_c)]$ across the pseudocapacitive layer with increasing L_r at high scan rates. Note that, L_r had a significantly stronger effect on $\psi_{tip}(t)$ than r_i [Figure 6.5(b)]. This was due to the significantly smaller electrical conductivity of the pseudocapacitive layer σ_P compared with that of the conducting nanorod σ_C. Here also, Figures 6.7(c) and 6.7(d) show that the corresponding concentrations $c_1(0, L_s + L_c + L_r, t)$ of cations Li^+ and $c_2(0, L_s + L_c + L_r, t)$ of anions ClO_4^- at the electrode/electrolyte interface as functions of the potential $\psi_{tip}(t)$ at the tip of the coated nanorod did not feature any hysteresis, at scan rates $v = 0.1$ and 100 V/s, respectively. Therefore, the decrease in $C_{C,BET}$ at high scan rates, observed in Figure 6.6(e), was only due to slow potential propagation across the electrode and not to ion diffusion limitations in the electrolyte.

Moreover, Figures 6.7(e) and 6.7(f) show the total change in SOC, $\Delta c_{1,P}/c_{1,P,max}$, during charging as a function of pseudocapacitive layer thickness L_r, at scan rates $v = 0.1$ and 100 V/s. It indicates that the total change in SOC during charging decreased with increasing scan rate v and thickness L_r. This led to the continuous decrease in charge storage by faradaic reactions and thus to the continuous decrease in $C_{F,g}$ with increasing scan rate v and coating thickness L_r [Figure 6.6(f)].

Finally, Figure 6.8(a) shows the areal capacitive capacitance $C_{C,BET}$ shown in Figure 6.6(e), for different values of thickness L_r, but as a function of dimensionless

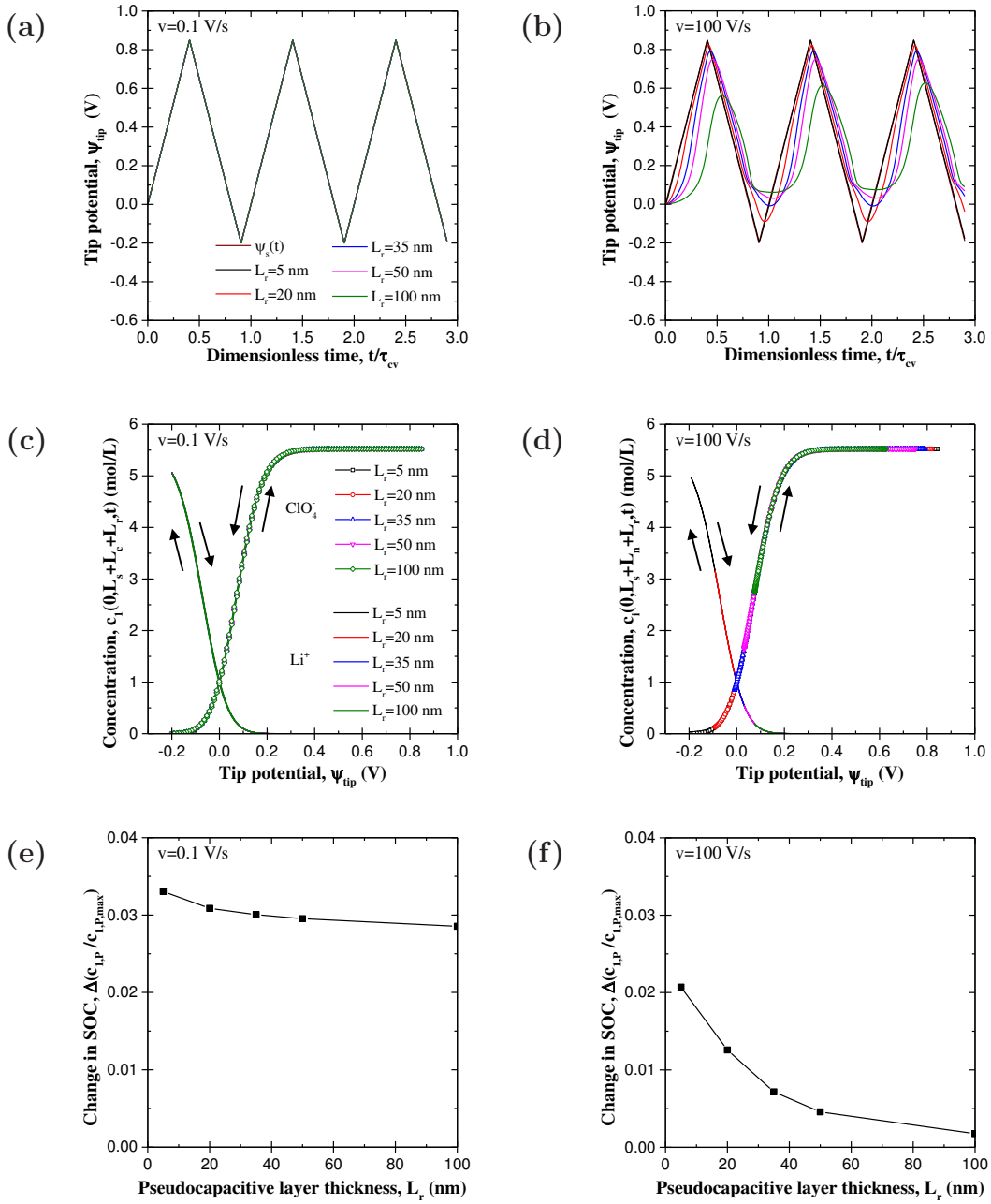

Figure 6.7: Tip potential $\psi_{tip}(t)$ as a function of dimensionless time t/τ_{CV}, for electrodes consisting of conducting nanorod 5 nm in radius r_i supporting pseudocapacitive material with thickness L_r of 5, 20, 35, 50, and 100 nm, at scan rate (a) $v = 0.1$ and (b) 100 V/s. Corresponding Li^+ ion concentration $c_1(0, L_s+L_c+L_r, t)$ and ClO_4^- ion concentration $c_2(0, L_s+L_c+L_r, t)$ at the electrode/electrolyte interface as functions of the tip potential $\psi_{tip}(t)$ for (c) $v = 0.1$ and (d) 100 V/s. SOC variation $\Delta(c_{1,P}/c_{1,P,max})$ as a function of the pseudocapacitive layer thickness for (e) $v = 0.1$ and (f) 100 V/s.

(a)

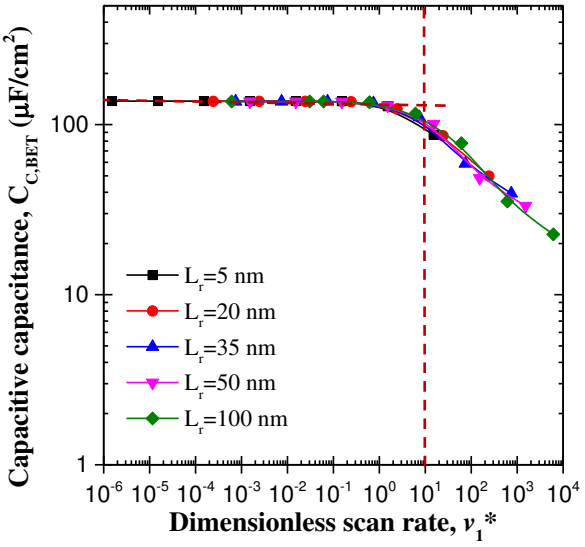

(B)

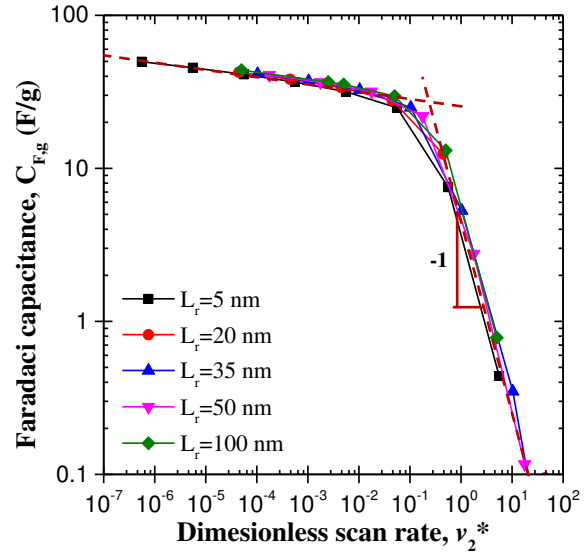

Figure 6.8: (a) Areal capacitive capacitance $C_{C,BET}$ as a function of dimensionless scan rates v_1^* and (e) gravimetric faradaic capacitance $C_{F,g}$ as a function of dimensionless scan rates v_2^* for electrodes consisting of conducting nanorod with radius r_i of 5 nm supporting pseudocapacitive material with thickness L_r of 5, 20, 35, 50, and 100 nm.

scan rate v_1^* expressed as [30]

$$v_1^* = \frac{\tau_e}{\tau_{CV}/2} = \frac{v\tau_e}{\psi_{max} - \psi_{min}}. \tag{6.21}$$

Here, the time scale τ_e was the characteristic time for electron transport across the pseudocapacitive layer expressed as [192]

$$\tau_e = \frac{L_r}{u_e} = \frac{\rho n_e e L_r^2}{M_u(\psi_{max} - \psi_{min})\sigma_P} \tag{6.22}$$

where u_e is the so-called drift velocity, i.e., the average velocity of electrons under electric field $E = (\psi_{max} - \psi_{min})/L_r$ expressed as $u_e = (M_u\sigma_P E)/(\rho n_e e)$, with n_e the number of free electrons per atom in the pseudocapacitive layer and M_u the atomic mass (in u) of the pseudocapacitive layer. For $LiMnO_2$, $n_e = 1$ and $M_u = 93.9$ u [193]. Figure 6.8(a) indicates that the areal capacitive capacitance $C_{C,BET}$, for different values of L_r, collapsed on a single curve and featured self-similar behavior when plotted as a function of dimensionless scan rates v_1^*. Note that Wang and Pilon [30] obtained similar results by scaling τ_{CV} by the ion diffusion time scale in the electrolyte $\tau_D = L^2/D$ instead of τ_e. However, unlike in Ref. [30], the present simulations established that limitations due to potential propagation in the electrode prevailed over ion diffusion limitations in the electrolyte. In addition, the areal capacitive capacitance $C_{C,BET}$ remained constant for $v_1^* \leq 10$.

Similarly, Figure 6.8(b) shows the gravimetric faradaic capacitance $C_{F,g}$, shown in Figure 6.6(f), but as a function of dimensionless scan rate v_2^* expressed as [30]

$$v_2^* = \frac{\tau_f}{\tau_{CV}/2} = \frac{v\tau_f}{\psi_{max} - \psi_{min}} \tag{6.23}$$

where the time scale τ_f associated with faradaic reactions and ion intercalation in

the pseudocapacitive layer can be expressed as

$$\tau_f = \sqrt{\tau_i \tau_r}. \tag{6.24}$$

Here, $\tau_i = L_r^2/D_{1,p}$ is the time scale for ion intercalation in the pseudocapacitive layer treated as a diffusion process [213]. On the other hand, τ_r is the effective time for faradaic reactions that can be expressed as [214]

$$\tau_r = \frac{\sqrt{K}}{k_0(A_{BET}/m)} \approx \frac{\sqrt{K}L_r}{k_0} \tag{6.25}$$

where K is the equilibrium constant for redox reactions $m\,\mathrm{Li}^+ + \mathrm{M}_p\mathrm{O}_q + m\,\mathrm{e}^- \rightleftharpoons \mathrm{Li}_m\mathrm{M}_p\mathrm{O}_q$ taking place at the pseudocapacitive layer/electrolyte interface. According to chemical thermodynamics, K can be expressed as $K = e^{zFE^0/R_uT}$ [215] where E^0 is the standard reduction potential for the above reaction reported relative to standard hydrogen electrode at 1 atm pressure, 298 K temperature, and for 1 M reactant ion (Li^+) concentration in the electrolyte [216]. For Li^+ reacting with MnO_2, $E^0 = -0.16$ V [217] and $K = 1.9 \times 10^{-3}$ at 298 K. Here also, Figure 6.8(b) establishes that the capacitance $C_{F,g}$ collapsed on a single curve when plotted as a function of v_2^*. In addition, $C_{F,g}$ was proportional to $(v_2^*)^{-1}$ at high scan rates such that $v_2^* > 0.2$.

6.3.4 Total capacitances and optimum dimensions

Figure 6.9 shows (a) the total gravimetric capacitance $C_{T,g}$ and (b) the total areal capacitance $C_{T,BET}$ as functions of pseudocapacitive layer thickness L_r for electrodes consisting of conducting nanorod with radius r_i of 5 nm for scan rate v = 1, 2.5, 5, 10, 30, and 100 V/s. Figures 6.9(a) and 6.9(b) also show $C_{T,g}$ and $C_{T,BET}$ as functions of L_r for a planar electrode with the same electrolyte and electrode properties for scan rate v = 1 V/s [32]. The predicted values of the total gravimetric capacitance $C_{T,g}$ ranged between 20 F/g and 200 F/g. These

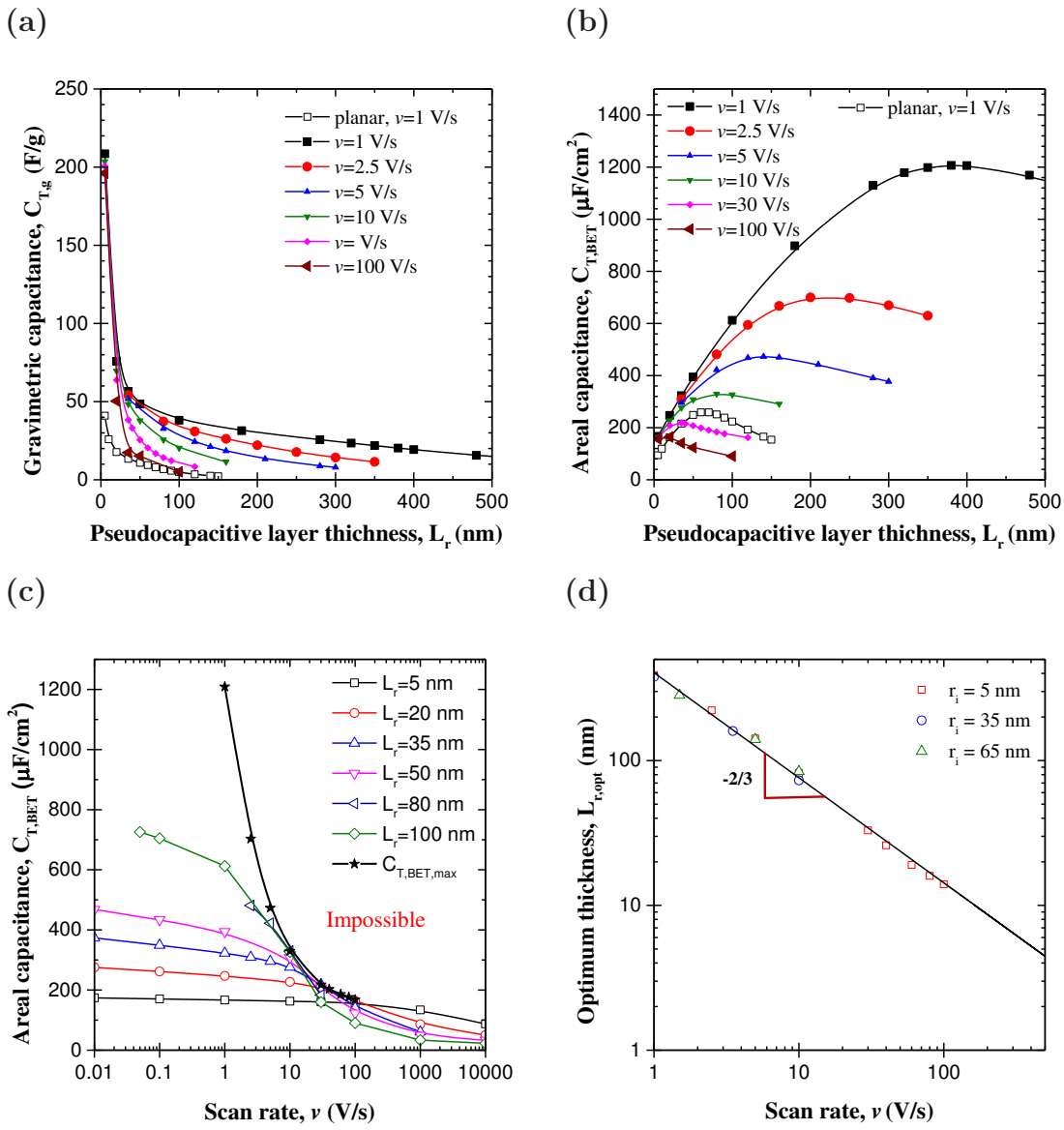

Figure 6.9: Total (a) gravimetric $C_{T,g}$ and (b) areal $C_{T,BET}$ capacitances as functions of the thickness L_r of pseudocapacitive layer for planar electrodes at scan rate $v = 1$ V/s and for electrodes consisting of conducting nanorod with radius r_i of 5 nm, at scan rates $v = 1$ to 100 V/s. (c) Total $C_{T,BET}$ and maximum possible $C_{T,BET,max}$ areal capacitances as functions of scan rate v for electrodes consisting of conducting nanorod with radius r_i of 5 nm. (d) The optimum thickness $L_{r,opt}$ as a function of the scan rate v for electrodes consisting of conducting nanorod with radius r_i of 5, 35, and 65 nm.

values were comparable with capacitances measured for electrodes with similar morphologies and ranging between 60 F/g and 800 F/g [71, 73, 74]. Note that the total gravimetric capacitance systematically increased with decreasing pseudocapacitive layer thickness for all scan rates considered. The same trend was also observed for other nanorod radii r_i (not shown). Note that for given electrode and electrolyte dimensions, the total capacitance $C_{T,g}$ or $C_{T,BET}$ for planar pseudocapacitive electrodes increased with increasing electrical conductivity σ_P and ion diffusion coefficient $D_{1,p}$ in the electrode [32]. Moreover, during charging, transport properties $D_{1,p}$ decreased [218] and σ_P increased [219–221] due to the presence of Li^+ intercalated in the metal oxide structure. The dependence of $D_{1,p}$ and σ_P on the local intercalated Li^+ concentration does not seem to be available in the literature and accounting for these processes falls outside the scope of the present simulations. Figure 6.9(b) indicates that the total areal capacitance reached a maximum $C_{T,BET,max}$ at an optimum pseudocapacitive layer thickness $L_{r,opt}(v)$, for a given scan rate v. The existence of $L_{r,opt}(v)$ can be attributed to the trade-off between offering large volume of pseudocapacitive layer for volumetric faradaic intercalation of Li^+ while maintaining acceptable potential drop across the electrode. Moreover, Figures 6.9(a) and 6.9(b) indicate that the total capacitances $C_{T,g}$ and $C_{T,BET}$ as well as the optimum thickness $L_{r,opt}$ for electrodes with conducting nanorod scaffold were much larger than those for planar electrodes [32] for a given scan rate (1 V/s). These observations confirm the positive effect of the conducting scaffold on the electrode performance.

Furthermore, Figure 6.9(c) shows the total capacitance $C_{T,BET}$ along with the maximum possible areal capacitance $C_{T,BET,max}$ as functions of scan rate v for pseudocapacitive layer thickness L_r from 5 to 100 nm. The curve for $C_{T,BET,max}$ represents the envelop of the $C_{T,BET}$ - v curves. Any pair (v, $C_{T,BET}$) on the right side of $C_{T,BET,max}(v)$ cannot be reached regardless of thickness L_r.

Finally, Figure 6.9(d) shows the optimum pseudocapacitive layer thickness

$L_{r,opt}$ as a function of scan rate v for electrodes consisting of conducting nanorod with radius r_i of 5, 35 and 65 nm. It indicates that r_i had a negligible effect on the optimum thickness $L_{r,opt}$ at all scan rates. In addition, the optimum pseudocapacitive layer thickness $L_{r,opt}$ was proportional to $v^{-2/3}$. The power law can be explained by considering the expression of the total capacitance $C_{T,BET}$ as the sum of capacitive and faradaic contributions, i.e., $C_{T,BET}(v, L_r) = C_{C,BET}[v_1^*(L_r)] + C_{F,g}[v_2^*(L_r)]m/A_{BET} \approx C_{C,BET}[v_1^*(L_r)] + C_{F,g}[v_2^*(L_r)]L_r$. In addition, the optimum thickness at any scan rate corresponded to $0.1 \leq v_1^* \leq 10$ and $v_2^* > 1$. Under these conditions, $C_{C,BET}(v_1^*)$ remained constant while $C_{F,g}(v_2^*)$ was proportional to $(v_2^*)^{-1}$, as discussed previously (Figure 6.8). Therefore,

$$\frac{\partial C_{T,BET}}{\partial L_r} \approx \frac{\partial C_{F,g}}{\partial v_2^*}\frac{\partial v_2^*}{\partial L_r}L_r + C_{F,g} \tag{6.26}$$

Substituting Equation (6.23) for $v_2^*(L_r)$ into Equation (6.26) and solving for the equation $\partial C_{T,BET}/\partial L_r(v, L_{r,opt}) = 0$ yielded $L_{r,opt} = C/v^{2/3}$, where C is a constant depending on the electrode and electrolyte properties as well as the working conditions discussed in Section 6.2.4.

6.4 Chapter summary

This chapter investigated the effect of nanoarchitecture on the performance of pseudocapacitive electrodes. It presented the first transient multidimensional simulations based on a physicochemical model derived from first-principles for pseudocapacitive electrodes consisting of a pseudocapacitive layer coated on conducting nanorods. First, two semi-empirical approaches commonly used in experiments relating the total current density to the scan rate were numerically reproduced and validated. The simulation tools were also used to determine the respective contributions of EDL formation and faradaic reactions to the total charge storage for different electrode dimensions and scan rates. The areal capacitive capaci-

tance, due to EDL formation, remained constant and independent of electrode dimensions at low scan rates. However, at high scan rates, it decreased more sharply with decreasing conducting nanorod radius and increasing pseudocapacitive layer thickness due to resistive losses. By contrast, the gravimetric faradaic capacitance, arising from reversible faradaic reactions, decreased continuously with increasing scan rate and coating thickness but remained independent of the conducting nanorod radius. Moreover, the predicted total gravimetric capacitance featured realistic values comparable with experimental measurements. Finally, an optimum pseudocapacitive layer thickness to maximize total areal capacitance (in $\mu F/cm^2$) was identified as a function of scan rate and corresponded to a trade-off between achieving large charge storage by using thick pseudocapacitive layer and minimizing resistive losses across the electrode.

CHAPTER 7

Critical Assessments of Methods Commonly Used to Generate Ragone Plots for Electrochemical Capacitors

Chapters 5-6 studied performance of EC electrodes with capacitance as the main criteria. However, the capacitance is not the main performance metrics for batteries or fuel cells. Thus, in order to compare the performance of EC devices with batteries and fuel cells, energy and power densities are commonly considered. This chapter aims to compare and evaluate commonly used methods for estimating the energy and power densities and producing Ragone charts of electrochemical capacitors (ECs).

7.1 Background

Increasing power requirements for modern applications such as electric vehicles [7, 45, 222] have resulted in increasing demand for electrical energy storage devices capable of delivering large power and energy densities. The energy density can be defined as the total energy released during discharging per unit volume (in J/m^3), mass (in J/kg), or surface area (in J/m^2) of the electrode of the energy storage device. For example, the energy density E_D per unit surface area of the electrode (in J/m^2) can be expressed as [92, 223]

$$E_D = -\int_{t_0+t_c}^{t_0+t_c+t_d} j_s(t)\psi_s(t)\mathrm{d}t \tag{7.1}$$

where t_0 is the starting time of a cycle, t_c and t_d are the durations of charging and discharging, $j_s(t)$ is the current density (in A/m^2) at the current collector/electrode interface, and $\psi_s(t)$ is the cell potential (in V). The product

$-j_s(t)\psi_s(t)$ represents the instantaneous output power density at time t during discharging. Similarly, the time-averaged power density P_D (in W/m^2) released during discharging can be expressed as [92, 223]

$$P_D = -\frac{1}{t_d}\int_{t_0+t_c}^{t_0+t_c+t_d} j_s(t)\psi_s(t)\mathrm{d}t = \frac{E_D}{t_d}. \tag{7.2}$$

7.1.1 Direct integration method

The energy and power densities under either galvanostatic cycling or cyclic voltammetry can be calculated directly using Equations (7.1) and (7.2), respectively [37, 87, 88]. For galvanostatic cycling, the current density $j_s(t)$ is imposed to be constant and of opposite sign ,i.e., $j_s(t) = \pm j_{GC}$ ($j_{GC} > 0$) during charging and discharging while the cell potential $\psi_s(t)$ is measured or computed. For cyclic voltammetry, the imposed cell potential $\psi_s(t)$ varies linearly with time at constant scan rate $v = |\mathrm{d}\psi_s/\mathrm{d}t|$ within the bounds of the potential window [ψ_{min}, ψ_{max}] while the current density $j_s(t)$ is measured or computed. Note that the integration method for energy and power densities may be mathematically involved and simpler methods such as RC circuit and integral capacitance methods are more straightforward and have been used extensively [35, 92–109].

7.1.2 RC circuit method

The electrical RC circuit method assumes that an EC device consists of an ideal capacitor of capacitance C (in μF/cm^2) in series with an ideal resistor of resistance R (in Ω m^2). Here, the capacitance and resistance are assumed to remain constant during charging and discharging. Then, the cell potential $\psi_s(t)$ and the current density $j_s(t)$ are related by the expression [92, 93]

$$\psi_s(t) = \frac{q_s(t)}{C} + j_s(t)R \tag{7.3}$$

where $q_s(t)$ is the surface charge density of the capacitor's electrode (in C/m^2) such that $\mathrm{d}q_s(t)/\mathrm{d}t = j_s(t)$ [9]. The resistance R (in Ω m^2) responsible for the ohmic potential drop across the cell can be retrieved from the sharp potential drop $\Delta\psi_{GC}$, also called "IR drop", observed at the transition between charging and discharging in galvanostatic cycling at constant current density j_{GC} as [153, 154]

$$R = \Delta\psi_{GC}/(2j_{GC}). \tag{7.4}$$

Equation (7.3) indicates that the cell potential $\psi_s(t)$ varied linearly with time during charging or discharging at constant current density j_{GC}. Thus, the expressions for energy and power densities in Equations (7.1) and (7.2) simplify as [93]

$$E_D = \frac{1}{2} j_{GC} t_d (\psi_{max} - \psi_{min} - j_{GC}R) \quad \text{and} \quad P_D = E_D/t_d \tag{7.5}$$

where ψ_{min} and ψ_{max} are, respectively, the minimum and maximum values of the measured or computed cell potential $\psi_s(t)$. Note that $j_{GC}t_d$ corresponds to the total charge released during constant current discharging.

7.1.3 Integral capacitance method

Another simplified method for estimating energy E_D and power P_D densities assumes that an EC device behaves as a conventional dielectric capacitor. In other words, the differential capacitance $C_{diff} = \mathrm{d}q_s/\mathrm{d}\psi_s$ [7] of the EC remains constant during charging and discharging and is equal to the integral capacitance C_{int} (in μF/cm^2) expressed as [94]

$$C_{int} = (j_{GC}t_d)/(\psi_1 - \psi_{min}) \quad \text{for galvanostatic cycling} \tag{7.6}$$

$$\text{and} \quad C_{int} = \frac{1}{\psi_{max} - \psi_{min}} \oint \frac{j_s(t)}{2v} d\psi_s \quad \text{for cyclic voltammetry} \tag{7.7}$$

where $\psi_1 = \psi_{max} - \Delta\psi_{GC}$ is the cell potential immediately after the IR drop at the transition from constant current charging to discharging and v is the scan rate of cyclic voltammetry. Note that assuming C_{diff} to be constant implies that (i) the potential $\psi_s(t)$ varies linearly with time under galvanostatic cycling, i.e., $\mathrm{d}\psi_s/\mathrm{d}t = j_{GC}/C_{diff}$ and (ii) the current density j_s remains constant under cyclic voltammetry $j_s = \mathrm{d}q_s/\mathrm{d}t = C_{diff}\mathrm{d}\psi_s/\mathrm{d}t = C_{diff}v$. In addition, assuming $C_{diff} = C_{int}$ implies that the current density can be expressed in terms of the cell potential as [224]

$$j_s(t) = C_{int}\frac{\mathrm{d}\psi_s(t)}{\mathrm{d}t} \tag{7.8}$$

Substituting Equation (7.8) into Equations (7.1) and (7.2) yields the following commonly used expressions for the energy and power densities of EC devices [35, 94–114, 224]

$$E_D = \frac{1}{2}C_{int}(\psi_1 - \psi_{min})^2 \qquad \text{and} \quad P_D = \frac{1}{2}C_{int}(\psi_1 - \psi_{min})^2/t_d \tag{7.9}$$

7.2 Analysis

7.2.1 Schematics and Assumptions

Figure 7.1 illustrates the one-dimensional (a) EDLC device and (b) hybrid pseudocapacitor simulated in the present study along with the associated coordinate system. The simulated EDLC consisted of two parallel planar carbon electrodes separated by an electrolyte solution. The hybrid pseudocapacitor consisted of a planar carbon electrode and a planar pseudocapacitive electrode separated by an electrolyte solution. Following assumptions were made: (1) The electrolyte was binary and symmetric, i.e., it consisted of two ion species of opposite valency $\pm z$ ($z > 0$). (2) The electrolyte properties were assumed to be constant and independent of electrolyte concentration. (3) The Stern layer thickness H was assumed to be half of the larger ion effective diameter, i.e., $H = \max(a_1/2, a_2/2)$ [16]. (4)

(a)

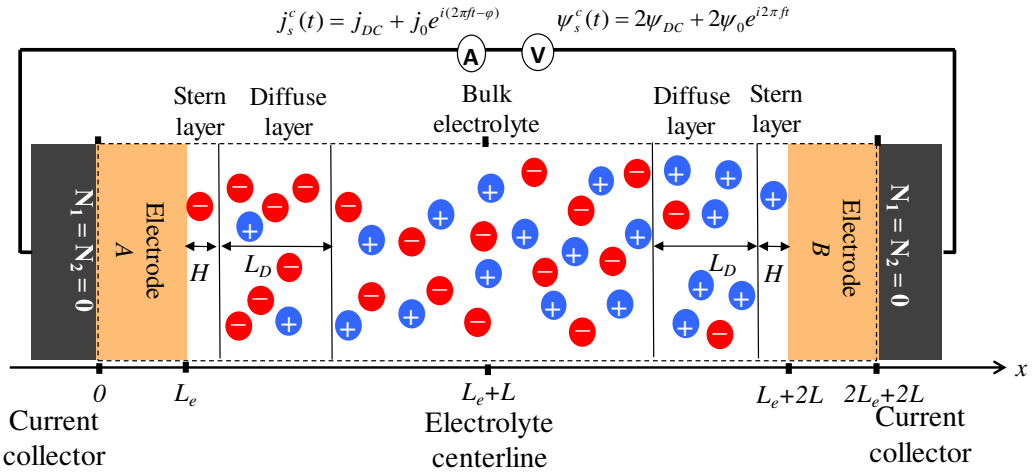

(b)

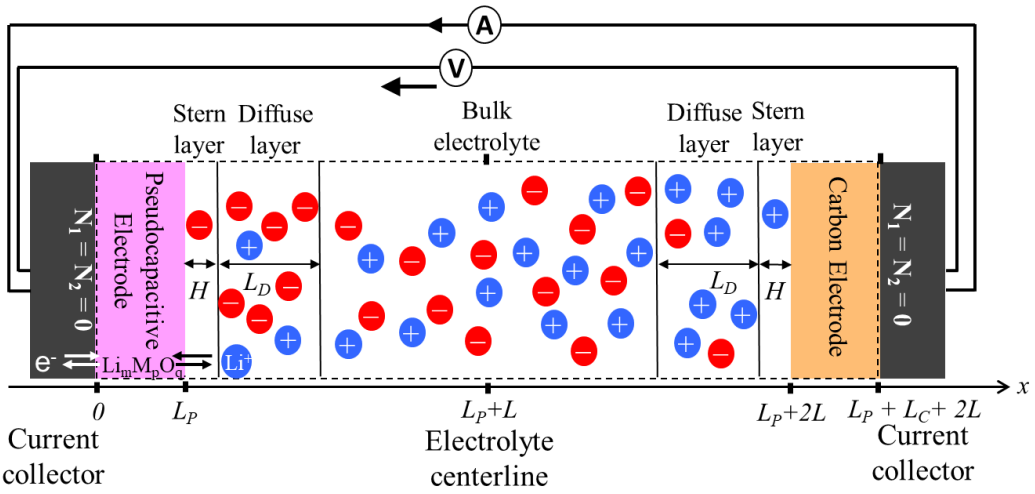

Figure 7.1: Schematics of the simulated 1D (a) EDLC and (b) pseudocapacitor device.

The ion intercalation in the pseudocapacitive electrode was modeled as a diffusion process. (5) The temperature of the EC device was constant and uniform. (6) Advection of the electrolyte was assumed to be negligible.

Simulations reported in this chapter were based on the generalized modified Poisson-Nernst-Planck (GMPNP) model for the spatiotemporal evolution of the potential $\psi(x,t)$ [Equation (2.1)] in the electrode and electrolyte as well as the ion concentrations $c_1(x,t)$ of cations and $c_2(x,t)$ of anions [Equations (2.2) and (2.5)] in the electrolyte for EDLC devices and hybrid pseudocapacitors. In addition, the boundary conditions varied depending on whether galvanostatic cycling or cyclic voltammetry were simulated. EIS simulations imposed potential $\psi_s(t)$ at the current collector/electrode interface as a harmonic function of time t [Equation (1.3)]. For galvanostatic cycling, the current density $j_s(t)$ imposed at the current collector/electrode interface or across the cell was a square wave of magnitude j_{GC} with respect to the cycle period [Equation (1.2)]. For cyclic voltammetry, the potential $\psi_s(t)$ at the current collector/electrode interface was imposed as a triangular wave with respect to cycle period [Equation (1.1)]. Other boundary conditions remained the same as described in Chapter 3 for device simulations.

7.2.2 Constitutive relationships

In order to solve the coupled transient 1D equations as well as the initial and boundary conditions, a total of 24 parameters were necessary, including (i) the electrolyte properties ϵ_r, z, a_1, a_2, D_1, D_2, $c_{\infty,1}$ and $c_{\infty,2}$, (ii) the electrical conductivity σ_c of the carbon electrode, (iii) the pseudocapacitive electrode properties $\Delta\psi_{eq}$, $c_{1,P,max}$, $c_{1,P,0}$, $D_{1,P}$, k_0, α, and σ_P, (iv) the dimensions of the simulated electrode and electrolyte domains L_c, L_P and L, along with (v) the operating conditions including the potential window ψ_{min}, ψ_{max}, the scan rate v for cyclic voltammetry or the imposed current density j_{GC} for galvanostatic cycling, and (vi) temperature T (in K).

Table 7.1: Value or range of electrode and electrolyte properties and dimensions used in the simulations reported in this study.

Parameters		**Electric double layer capacitors**			**Pseudocapacitors**	
		Case 1	**Case 2**	**Case 3**	**Case 4**	**Case 5**
Carbon electrode conductivity	σ_e (S/m)	0.5	0.5	0.5	0.5	0.5
Dielectric constant	ϵ_r	64.4	64.4	64.4	64.4	64.4
Valency	z	1	1	1	1	1
Ion diameter	a_1 (nm)	0.41	0.83	0.41	0.41	0.83
	a_2 (nm)	0.41	0.83	0.51	0.41	0.83
Diffusion coefficient	D_1 (m^2/s)	1 x 10^{-10}	1 x 10^{-10}	0.69 x 10^{-10}	1 x 10^{-10}	1 x 10^{-10}
	D_2 (m^2/s)	1 x 10^{-10}	1 x 10^{-10}	1.31 x 10^{-10}	1 x 10^{-10}	1 x 10^{-10}
Bulk ion concentration	$c_{\infty,1}$ (mol/L)	1	1	1	1	1
	$c_{\infty,2}$ (mol/L)	1	1	1	1	1
Carbon electrode thickness	L_c (nm)	100	100	100	100	100
Pseudocapacitive electrode thickness	L_P (nm)	-	-	-	100	100
Electrolyte thickness	$2L$ (μm)	20	20	20	20	20
Potential window	ψ_{min} (V)	0	0	0	0	0
	ψ_{max} (V)	1	1	1	1	1
Imposed current density	j_{GC} (mA/cm^2)	2 - 2000	2 - 2000	2 - 2000	2 - 2000	2 - 2000
Scan rate	v (V/s)	50 - 5000	50 - 5000	50 - 5000	50 - 5000	50 - 5000
Temperature	T	298	298	298	298	298
Maximum concentration in pseudocapacitive electrode	$c_{1,P,max}$ (mol/L)	-	-	-	6.38	6.38
Initial concentration in pseudocapacitive electrode	$c_{1,P,0}$ (mol/L)	-	-	-	31.9	31.9
Reaction rate constant	k_0 (m$^{2.5}$mol$^{-0.5}$s^{-1})	-	-	-	10^{-8}	10^{-8}
Transfer coefficient	α	-	-	-	0.5	0.5
Diffusion coefficient in pseudocapacitive electrode	$D_{1,P}$ (m^2/s)	-	-	-	1 x 10^{-12}	1 x 10^{-12}
Pseudocapacitive electrode conductivity	σ_P (S/m)	-	-	-	0.5	0.5

Table 7.1 summarizes the values or range of the 24 parameters for the five cases considered in the present study. Cases 1-3 correspond to simulations of EDLC devices and Cases 4 and 5 to simulations of hybrid pseudocapacitors. Cases 1 and 2 assumed that the two ion species had the same diameter and diffusion coefficient with $a_1 = a_2 = 0.41$ nm and $D_1 = D_2 = 10^{-10}$ m^2/s for Case 1 and $a_1 = a_2 = 0.83$ nm and $D_1 = D_2 = 10^{-10}$ m^2/s for Case 2. Case 3 corresponds to the more realistic situation of asymmetric effective ion diameter and diffusion coefficient in the electrolyte such that $a_1 = 0.41$ nm, $a_2 = 0.51$ nm [225,226], $D_1 = 0.69 \times 10^{-10}$ m^2/s, and $D_2 = 1.31 \times 10^{-10}$ m^2/s [227]. Note that all other properties of the electrolyte in all cases were evaluated at approximately $T = 293$ K for $LiPF_6$ in propylene carbonate (PC) [68, 152, 225–228]. In all three cases, the valency of the ion species were $\pm z$ with $z = 1$ [68]. The dielectric constant was estimated as $\epsilon_r = 64.4$ for PC [152]. The bulk ion concentrations were taken as $c_{\infty,1} = c_{\infty,2} = 1$ mol/L, as often used experimentally [208]. Moreover, the two electrodes simulated were separated by a distance of $2L = 40$ μm and had thickness $L_c = 100$ nm with electrode electrical conductivity $\sigma_c = 0.5$ S/m, based on the range of conductivity of carbon reported between 10^{-6} and 10^2 S/m [190, 191].

Cases 4 and 5 use the same properties of carbon electrode and electrolyte as Cases 1 and 2, respectively. For pseudocapacitive electrode consisting of transition metal oxides, the equilibrium potential difference $\Delta\psi_{eq}$ was modeled as a linear function of the state-of-charge (SOC) $c_{1,P}/c_{1,P,max}$ [82, 83, 161]. For MnO_2 dense films of thickness 100 μm at low scan rates, $\Delta\psi_{eq}(t)$ (in V) was measured as [162]

$$\Delta\psi_{eq}(t) = 10.5[4 - c_{1,P}(t)/c_{1,P,max}] - 39.9. \tag{7.10}$$

Here, $c_{1,P,max} \approx 31.9$ mol/L is the maximum intercalated lithium concentration in the pseudocapacitive electrode, corresponding to fully lithiated metal oxide MnO_2 [163,164]. The initial concentration of Li^+ in the electrode was $c_{1,P,0} \approx 6.38$ mol/L

such that the equilibrium potential was zero initially [164]. The reaction rate constant k_0 was taken as $k_0 = 10^{-8}$ $m^{2.5}mol^{-0.5}s^{-1}$ to maximize contribution from redox reactions, based on the range of k_0 for transition metal oxides between 10^{-11} and 10^{-8} $m^{2.5}mol^{-0.5}s^{-1}$ [145,146,165]. The transfer coefficient α was assumed to be 0.5, corresponding to identical energy barriers for forward and backward redox reactions [8]. The value of the diffusion coefficient $D_{1,P}$ of the intercalated Li^+ in the pseudocapacitive electrode was taken as $D_{1,p} = 10^{-12}$ m^2/s, based on the typical range from 10^{-16} to 10^{-10} m^2/s [165]. Moreover, the thickness and the electrical conductivity of the pseudocapacitive electrode were chosen to be the same as the carbon electrode to facilitate comparison among cases, i.e., $L_P = 100$ nm and $\sigma_P = 0.5$ S/m.

Finally, the potential window was set as $\psi_{min} = 0$ V and $\psi_{max} = 1$ V for both galvanostatic cycling and cyclic voltammetry. The magnitude of the imposed current density j_{GC} for galvanostatic cycling ranged between 2 and 200 mA/cm^2. The scan rate v in cyclic voltammetry ranged between 50 V/s and 5000 V/s. The governing equations along with the initial and boundary conditions were solved using COMSOL 5.2. Mesh and time-step selections to achieve numerical convergence and oscillatory steady state conditions were discussed in detail in Refs. [1,148] and need not be repeated.

7.2.3 Data processing

First, the energy E_D and power P_D densities were estimated using Equations (7.1) and (7.2) from the predicted current density $j_s(t)$ and cell potential $\psi_s(t)$ for galvanostatic cycling and cyclic voltammetry. Similarly, the resistance R and integral capacitance C_{int} were computed from galvanostatic cycling simulations according to Equations (7.4) and (7.6), respectively. They were then used to estimate E_D and P_D by the RC circuit [Equation (7.5)] and integral capacitance [Equation (7.9)] methods.

Furthermore, the energy provided to an EC during charging (in J/m^2) can be expressed as [92, 223]

$$E_C = \int_{t_0}^{t_0+t_c} j_s(t)\psi_s(t)dt \tag{7.11}$$

It cannot be entirely retrieved during discharging because of irreversible heat generation [5, 7, 229, 230]. In fact, over one cycle period, the energy conservation equation for electrochemical capacitor can be written as [7]

$$E_C = Q_{irr} + E_D \tag{7.12}$$

where Q_{irr} (in J/m^2) is the irreversible thermal energy generated over the entire cycle per unit electrode surface area [33]. For EDLC devices (Cases 1-3), the heat generation for an entire cycle period t_{cd} is equal to Joule heating Q_J (in J/m^2), i.e., $Q_{irr} = Q_J$ where Q_J is expressed as [231]

$$Q_J = \int_{t_0}^{t_0+t_{cd}} R j_s^2(t)\mathrm{d}t \tag{7.13}$$

where t_{cd} is the cycle period, i.e., $t_{cd} = t_c + t_d$. On the other hand, for hybrid pseudocapacitors (Cases 4-5), the faradaic reactions also contributes to the irreversible heat generation such that $Q_{irr} = Q_J + Q_F$ where the heat generation associated with faradaic reactions over a cycle period t_{cd} can be expressed as [33]

$$Q_F = \int_{t_0}^{t_0+t_{cd}} j_F(t)\eta(t)\mathrm{d}t. \tag{7.14}$$

Here, $j_F(t)$ (in A/m^2) is the faradaic current density, given by the generalized Frumkin-Butler-Volmer model [Equation (S.15)]. In addition, $\eta(t) = \Delta\psi_H(t) - \Delta\psi_{eq}(t)$ is the overpotential, $\Delta\psi_H$ is the potential drop across the Stern layer and $\Delta\psi_{eq}(t)$ is the equilibrium potential given by Equation (7.10) [8]. For each case, we assessed whether each of the four methods used to estimate energy and power densities satisfies the energy conservation principle given by Equation (7.12).

7.3 Experiments

The four different methods of estimating E_D and P_D were also compared experimentally on EDLC and hybrid pseudocapacitive devices. An EDLC device with footprint surface area of 1 cm^2 consisted of two identical electrodes separated by a 350 μm glass fiber separator (GF85 filter, Advantec MFS Inc.) immersed in 1 M $LiPF_6$ in EC:DMC (1:1) as electrolyte. The activated carbon electrode was prepared by making a slurry consisting of (i) 70 wt% YP-50F activated carbon (Kuraray), (ii) 20 wt% Super P, and (iii) 10 wt% PVDF as a binder in N-Methyl-2-pyrrolidone (NMP). The resulting slurries were drop casted onto a 1x1 cm^2 Ni foil, serving as the current collector. The mass loading of each electrode was 2.3 mg activated carbon per cm^2. The electrodes were dried under vacuum at 120^{o}C for at least 2 hr. Then, the EDLC device was assembled, installed, and cycled between $\psi_{min} = 0$ V and $\psi_{max} = 1$ V under (i) galvanostatic cycling with constant current i_{CC} ranging between 0.05 and 8 mA and (ii) cyclic voltammetry with scan rate v ranging between 0.5 and 100 mV/s.

A hybrid pseudocapacitor with footprint surface area of 1 cm^2 was also assembled and consisted of a pseudocapacitive MnO_2-graphene electrode and an activated carbon (AC) electrode separated by a 350 μm glass fiber separator (GF85 filter, Advantec MFS Inc.) immersed in 0.5 M Na_2SO_4 in DI water. To prepare the pseudocapacitive MnO_2 electrode, first, MnO_2-graphene composite were synthesized using a microwave synthesis adapted from a previously reported procedure [127]. In a typical synthesis, 90 mg of KS6 synthetic graphite (Imerys) was added to 50 mL of DI water and sonicated until a stable suspension was obtained (1 hr). Then, 450 mg of $KMnO_4$ (Sigma Aldrich) was added to the graphene suspension and stirred for 5 min and sonicated for another 30 min. The suspension was then heated to 185^{o}C for 1 hr using a microwave oven (CEM Discover SP Microwave Synthesizer). The MnO_2-graphene composite was washed and centrifuged

with DI water five times before it was dried overnight in an oven at 100^{o}C. Then, a slurry was prepared by mixing 70 wt% of active material (85:15 MnO_2:graphene composite), 20 wt% of Super P (Alfa Aesar) as conductor, and 10 wt% polyvinylidene fluoride (PVDF, Kynar) as a binder in N-Methyl-2-pyrrolidone (NMP, Sigma Aldrich). Activated carbon electrode was synthesized as described previously. The mass loading was 1.2 mg for MnO_2 and 2.3 mg for activated carbon per cm^2. The electrodes were dried under vacuum at 120^{o}C for at least 2 hr. Then, the hybrid device was assembled, installed, and cycled between $\psi_{min} = 0$ V and $\psi_{max} = 1.25$ V under (i) galvanostatic cycling with constant current i_{CC} ranging between 0.1 and 8 mA and (ii) cyclic voltammetry with scan rate v ranging between 5 and 200 mV/s.

7.4 Results and discussion

7.4.1 EDLC devices

7.4.1.1 Ragone plots

Figure 7.2 shows the Ragone plots of energy E_D versus power P_D densities for EDLC devices numerically predicted for (a) Case 1, (b) Case 2, (c) Case 3, and (d) experimentally measured using (1) the direct integration method under galvanostatic cycling, (2) the direct integration method under cyclic voltammetry, (3) the RC circuit method, and (4) the integral capacitance method. The power density P_D was varied by changing the current density j_{GC} for galvanostatic cycling or the scan rate v for cyclic voltammetry. All four plots show the typical "hook" shape characteristic of Ragone plots [92]. The large decrease in energy density at high charging/discharging rates, i.e., at high power density, indicates the upper bound of the suitable range of charging/discharging rates [93]. In addition, Figures 7.2(a) and 7.2(b) indicate that the RC circuit method and the integral capacitance method agreed with the direct integration methods for elec-

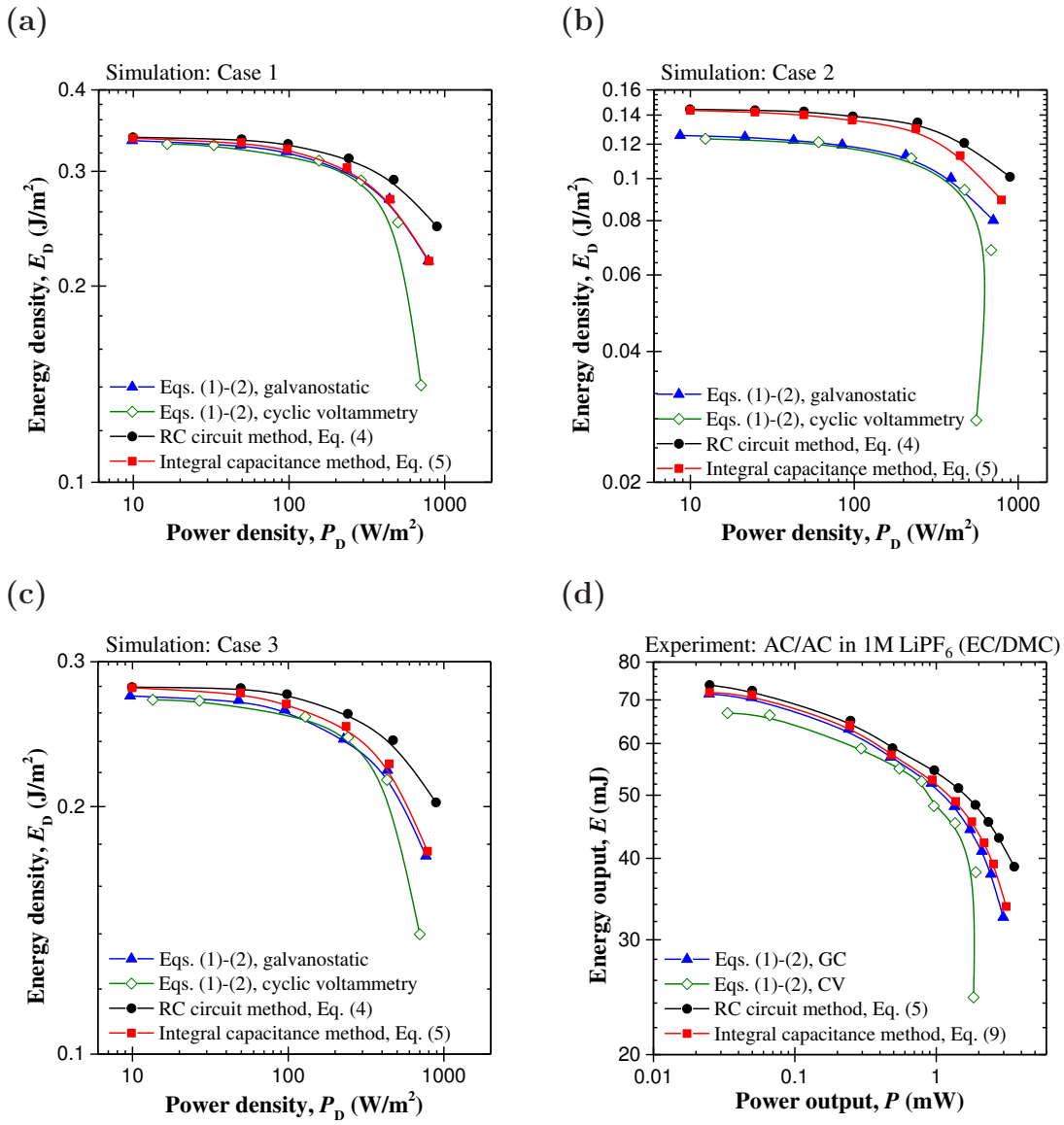

Figure 7.2: Energy density E_D as a function of power density P_D for EDLC devices generated from four different methods (a)-(c) numerically for (a) Case 1, (b) Case 2, (c) Case 3, and (d) experimentally.

trolyte with small ions (Case 1) at low charging/discharging rates, i.e., at low power density P_D. However, for electrolyte with large ions (Case 2), these two methods systematically predicted a larger energy density than that obtained by the direct integration methods. On the other hand, Figures 7.2(a) and 7.2(c) establish that asymmetry in the effective ion diameter and diffusion coefficient in the electrolyte had negligible effect on the energy and power densities. Furthermore, the experimentally obtained Ragone plot [Figure 7.2(d)] qualitatively agreed with the simulation results for Case 3 corresponding to carbon electrodes in 1 M $LiPF_6$ in PC as electrolyte. Finally, for all numerical simulations and experiments considered, the direct integration method under cyclic voltammetry predicted lower energy and power densities at high rates than under galvanostatic cycling.

To explain the discrepancies in the Ragone plots obtained from the four different methods considered, Figures 7.3(a) and 7.3(b) show the cell potential ψ_s as a function of the dimensionless time t/t_{cd} for relatively low imposed current density $j_{GC} = 2$ mA/cm^2 for (a) $a_1 = a_2 = 0.83$ nm (Case 1) and for (b) $a_1 = a_2 = 0.41$ nm (Case 2). Results assuming point charge ions ($a_1 = a_2 = 0$) are also presented as a reference while all other parameters remained the same as those of (a) Case 1 and (b) Case 2. The figures indicate that when ions were treated as point charge, the potential systematically varied linearly with time. By contrast, for ions of finite size (Cases 1 and 2), the temporal evolution of cell potential fell under the linear temporal evolution during both charging and discharging. In addition, Figures 7.3(c) and 7.3(d) show the corresponding anion concentration $c_2(L_c, t)$ at the positive electrode/electrolyte interface ($x = L_c$) as a function of dimensionless time t/t_{cd}. Note that the cation concentration $c_1(L_c + 2L, t)$ at the negative electrode/electrolyte interface ($x = L_c + 2L$) had the same behavior by virtue of symmetry. Figures 7.3(c) and 7.3(d) indicate that the temporal evolution of ion concentrations in Case 2 ($a_1 = a_2 = 0.83$ nm) deviated significantly from that

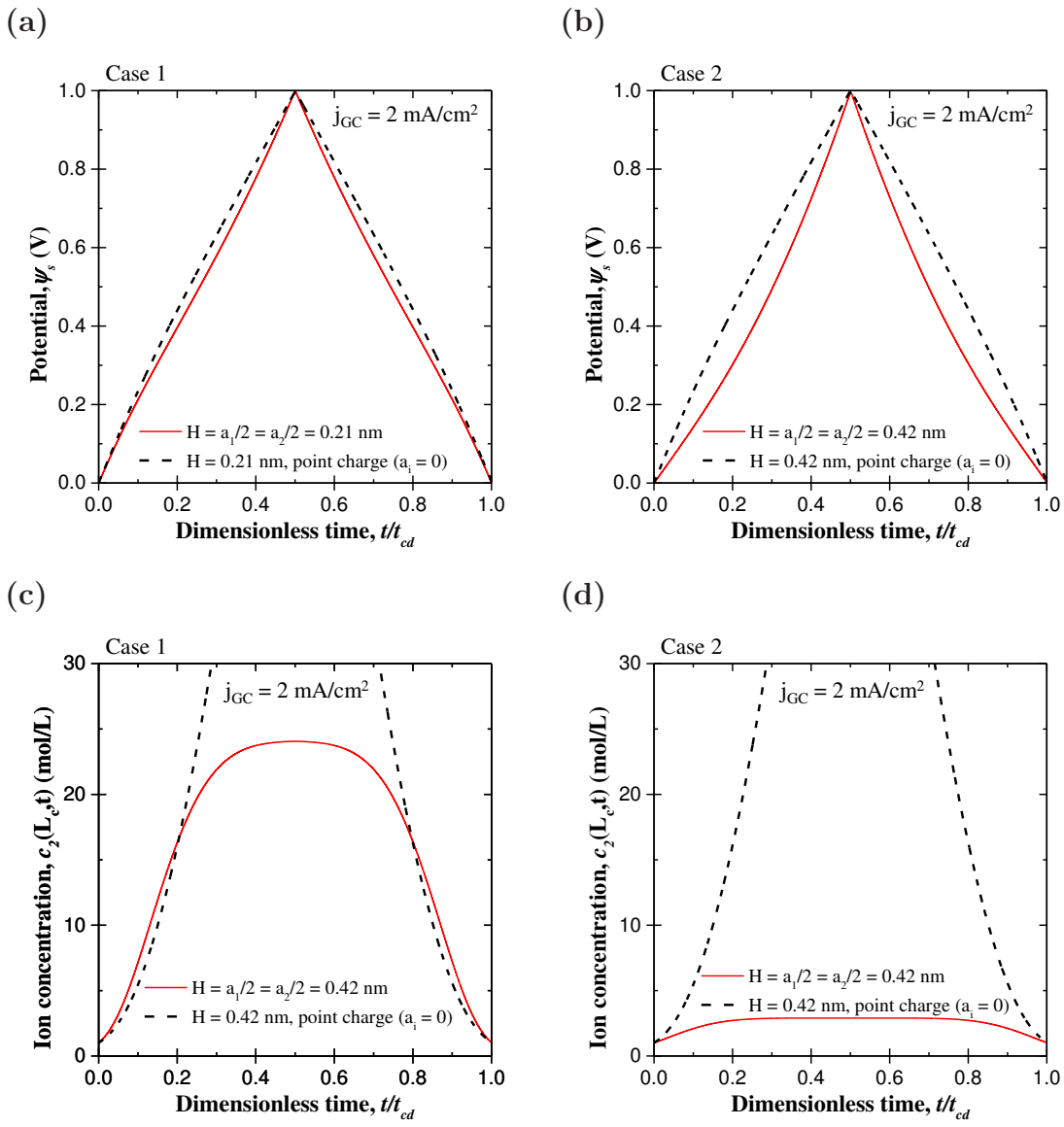

Figure 7.3: (a)(b) Electrical potential $\psi_s(t)$ and (c)(d) anion concentration $c_2(L_c, t)$ at the positive electrode/electrolyte interface as functions of dimensionless time t/t_{cd} for low current density $j_{GC} = 2$ mA/cm^2 for (a)(c) Case 1, (b)(d) Case 2, compared with the corresponding cases where ions were treated as point charge.

obtained when treating ions as point charges. The deviation was less pronounced in Case 1 featuring smaller ions ($a_1 = a_2 = 0.41$ nm). Therefore, the effect of finite ion size on the ion concentrations at the electrode surface was responsible for the non-linear temporal evolution of cell potential. This was true for all imposed current densities considered. Note also that the RC circuit [Equation (7.3)] and integral capacitance [Equation (7.8)] methods are based on the assumption that the capacitance is constant and thus the cell potential varies linearly with time during discharging. Unfortunately, this assumption was not valid for finite ion size (both numerically and experimentally) and led to overestimation of energy and power densities by the RC and integral capacitance methods [Figure 7.2(a)]. This was particularly true for electrolyte consisting of large ion species (Case 2).

Furthermore, Figure 7.4 shows (a,b) the CV curves and (c,d) the corresponding instant (input) power $P(t) = i_s(t)\psi_s(t)$ as functions of dimensionless time t/t_{cd} for experimental results of EDLC devices under cyclic voltammetry with scan rate v of (a,c) 0.5 mV/s and (b,d) 80 mV/s, respectively. Similar behavior was observed for numerical results (see Appendix C). At high scan rates, the current remained positive even after switching from charging to discharging. Consequently, the instant input power density $P(t) = i_s(t)\psi_s(t)$ was also positive at the beginning of discharging instead of being negative, as observed at low scan rates. On the other hand, Figures 7.4(e)-7.4(f) show the instant (input) power $P(t) = i_s(t)\psi_s(t)$ as functions of dimensionless time t/t_{cd} for experimental results of EDLC devices under galvanostatic cycling with imposed current i_{GC} of (e) 0.5 mA and (f) 8 mA, respectively. They indicate that the instant input power $P(t)$ was always negative throughout the discharging process under galvanostatic cycling. This resulted in the systematic discrepancy between cyclic voltammetry and galvanostatic cycling (Figure 7.2) in estimating the energy density using Equation (7.1) at high charging/discharging rates.

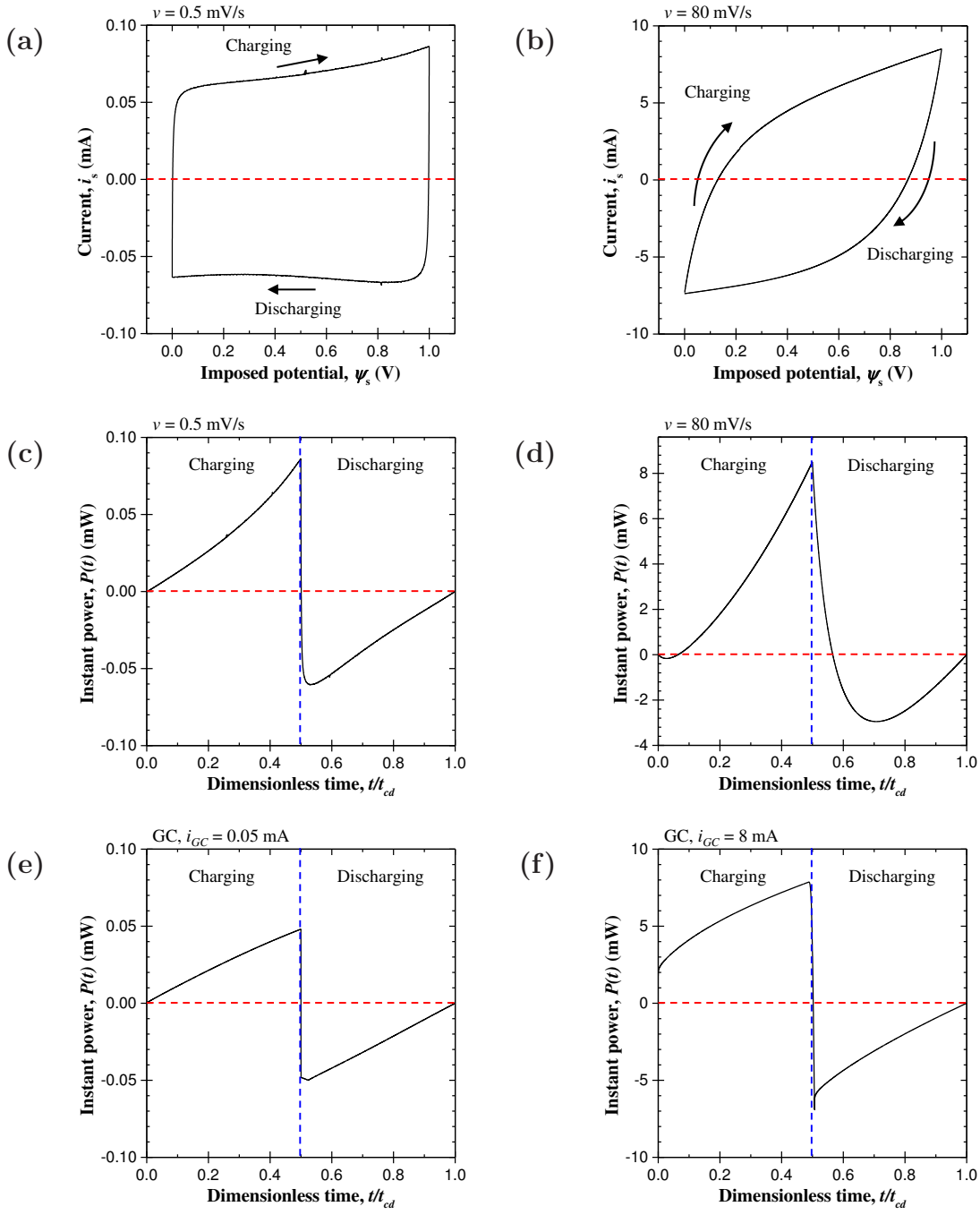

Figure 7.4: Experimentally measured (a)(b) CV curves and (c)-(f) instant power $P(t)$ as functions of dimensionless time t/t_{cd} for EDLC devices under (a)-(d) cyclic voltammetry at scan rates (a)(c) $v = 0.5$ mV/s and (b)(d) $v = 80$ mV/s and (e)(f) galvanostatic cycling at imposed current (e) $i_{GC} = 0.05$ mA and (f) $i_{GC} = 8$ mA.

7.4.1.2 Energy balance

Figure 7.5 shows the energy losses $E_C - E_D$ predicted by the four methods under consideration versus the irreversible heat generation $Q_{irr} = Q_J$ [Equation (7.13)] for (a) Case 1, (b) Case 2, and (c) Case 3. It indicates that, in all cases, the direct integration methods under galvanostatic cycling and cyclic voltammetry both satisfied energy conservation principle expressed by Equation (7.12). These observations were despite the difference in predicting E_D at high rates (Figure 7.2). In other words, underestimation of E_D by the direct integration method under cyclic voltammetry at high rates (Figure 7.2) was compensated by the same underestimation of E_C, possibly due to the symmetric charging/discharging behavior of EDLC devices (Figure 7.3). By contrast, the RC circuit method violated the first law of thermodynamics for the three cases considered for EDLC devices. Similarly, the integral capacitance method did not satisfy the energy conservation principle for electrolyte with large ions (Case 2).

Finally, energy balance for experimental measurements was not performed here due to the fact that the experimental uncertainty of heat generation measurement (2-4 mJ) over one cycle was on the same order of magnitude as the difference in estimating energy densities using different methods (1-4 mJ). Thus, it was impossible to distinguish the four methods by performing energy conservation principle on experimental results.

7.4.2 Hybrid pseudocapacitors

7.4.2.1 Ragone plots

Figure 7.6 shows the Ragone plots for hybrid pseudocapacitors numerically predicted for (a) Case 4 and (b) Case 5 and (c) experimentally measured for MnO_2-graphene/AC device using the four methods under consideration. It indicates that the experimental Ragone plot [Figure 7.6(c)] qualitatively agreed with the simula-

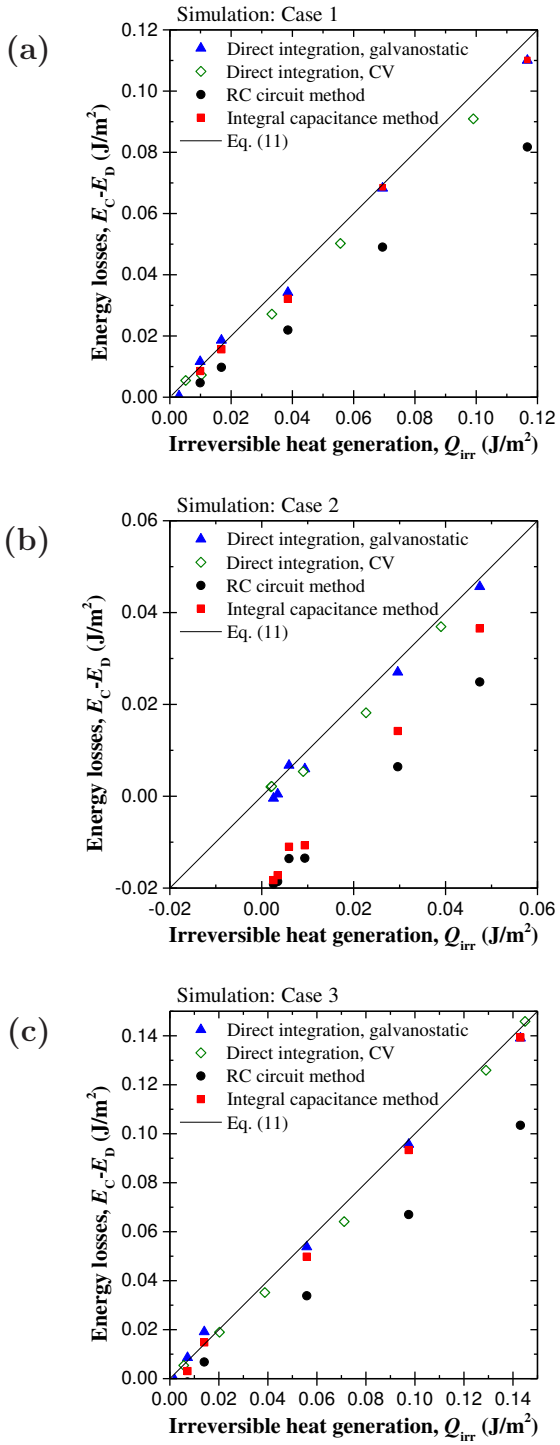

Figure 7.5: Energy losses $E_C - E_D$ as a function of irreversible heat generation Q_{irr} for EDLC devices of (a) Case 1, (b) Case 2, and (c) Case 3. Energy conservation principle requires that $E_C - E_D = Q_{irr}$, as expressed by Equation (7.12).

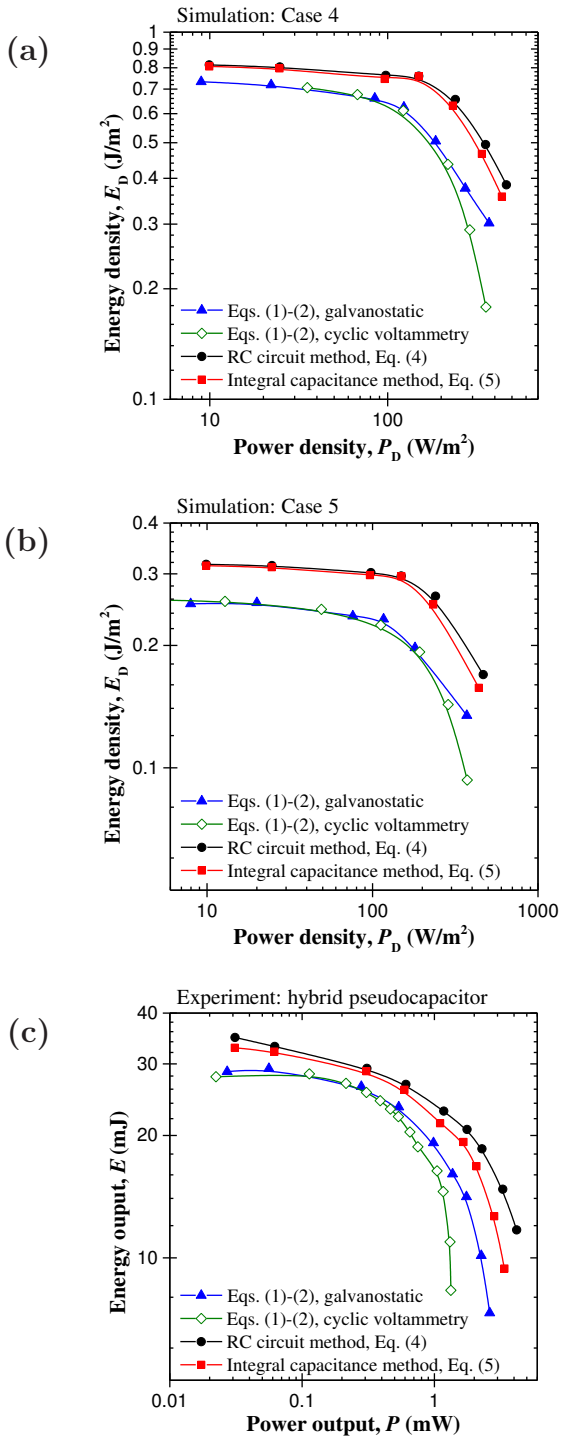

Figure 7.6: Energy density E_D as a function of power density P_D obtained from the four different methods considered for numerically simulated hybrid pseudocapacitors of (a) Case 4 and (b) Case 5 and (c) experimentally for MnO_2-graphene/AC with aqueous Na_2SO_4 device.

tion results. In all cases, the direct integration method under cyclic voltammetry underestimated the energy and power densities at high rates compared with those predicted under galvanostatic cycling, as previously observed for EDLCs (Figure 7.2). Here also, this can be attributed to the fact that the instant power density $P(t) = i_s(t)\psi_s(t)$ was positive at the beginning of discharging at high scan rates under cyclic voltammetry but remained negative throughout the discharging process under galvanostatic cycling both experimentally and in numerical simulations (see Appendix C).

Moreover, the RC circuit and the integral capacitance methods systematically predicted larger energy density than the direct integration methods both numerically and experimentally. To explain this trend, one needs to consider the potential evolution for hybrid pseudocapacitors. Figure 7.7(a) shows the cell potential $\psi_s(t)$ as a function of the dimensionless time t/t_{cd} numerically predicted for Cases 1 (EDLC) and 4 (hybrid pseudocapacitor) with $j_{GC} = 50$ mA/cm^2. Note that all parameters were the same in both cases except for those associated with the redox reactions. Unlike for EDLCs, the potential evolution in hybrid pseudocapacitors during charging and discharging was asymmetric. At the beginning of the charging step, the time rate of change $|\mathrm{d}\psi_s/\mathrm{d}t|$ was relatively large for a short period of time, after which $|\mathrm{d}\psi_s/\mathrm{d}t|$ sharply decreased, resulting in a distinct "kink" in $\psi_s(t)$. In addition, the potential evolution during discharging of hybrid pseudocapacitors fell below that of EDLCs. Similar comparison can be made between Cases 2 (EDLC) and 5 (hybrid pseudocapacitor) (see Appendix C). In addition, Figures 7.7(b)-7.7(c) show the cell potential $\psi_s(t)$ as a function of dimensionless time t/t_{cd} for galvanostatic cycling (b) numerically predicted for Case 4 with j_{GC} varying between 20 and 200 mA/cm^2 and (c) experimentally obtained with current i_{GC} between 0.1 and 8 mA. Figure 7.7(b) indicates that the "kink" during charging and the convex potential evolution during discharging were observed for all current densities. Figure 7.7(c) establishes that experimental

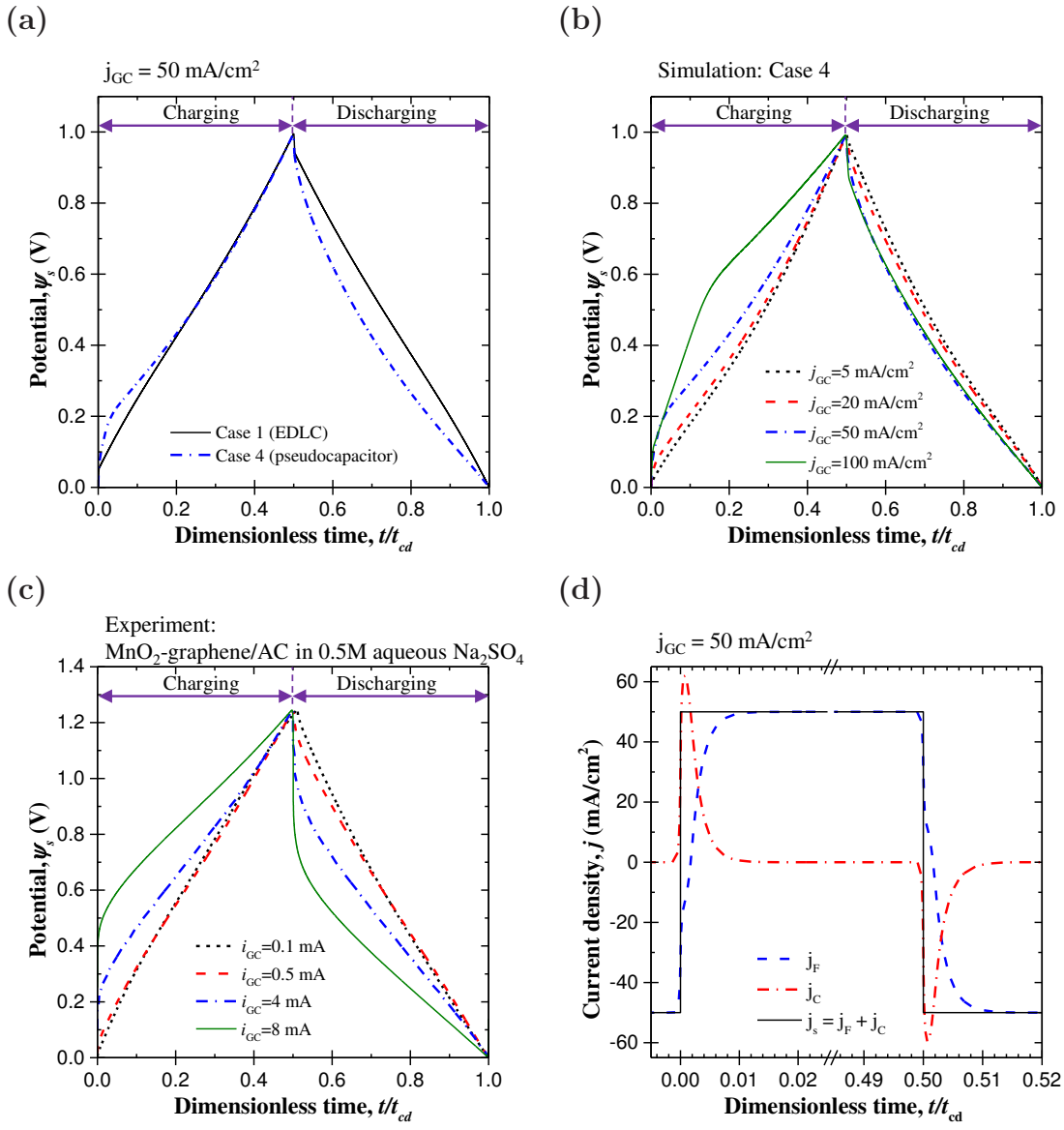

Figure 7.7: (a)-(c) Electrical potential $\psi_s(t)$ as a function of dimensionless time t/t_{cd} (a) for Cases 1 and 4 under galvanostatic cycling with current density $j_{GC} = 50$ mA/cm^2, (b) for Case 4 under galvanostatic cycling with imposed current density varying from 5 mA/cm^2 to 100 mA/cm^2, and (c) for experimental results with imposed current varying from 0.5 mA to 8 mA. (d) Faradaic j_F, capacitive j_C, and imposed $j_{GC} = j_F + j_C$ current densities as functions of dimensionless time t/t_{cd} for Case 4 under galvanostatic cycling with current density $j_{GC} = 50$ mA/cm^2.

data were very similar to numerical simulations of Case 4 [Figure 7.7(b)] with a sharper "kink" with increasing current.

Furthermore, Figure 7.7(d) shows the faradaic j_F, capacitive j_C, and total $j_s = j_F + j_C$ current densities as functions of dimensionless time t/t_{cd} numerically predicted for Case 4 with $j_{GC} = 50$ mA/cm^2. It establishes that a spike in the capacitive current density occurred at the transition between charging and discharging resulting in a relatively small differential capacitance C_{diff} and thus a large slope $|\mathrm{d}\psi_s/\mathrm{d}t| = j_{GC}/C_{diff}$ of the potential evolution [Figure 7.7(a)] [33]. This can be attributed to the fact that the relatively slow faradaic reactions cannot follow the rapid current reversal between charging and discharging. However, the faradaic current density j_F dominated later in the charging/discharging process, resulting in a relatively larger differential capacitance C_{diff} and thus a smaller slope $|\mathrm{d}\psi_s/\mathrm{d}t|$ [Figure 7.7(a)] [33]. This shift between the dominance of capacitive and faradaic current densities contributed to the change in slope and thus the non-linear and asymmetric cell potential $\psi_s(t)$ in hybrid pseudocapacitors. However, the RC circuit [Equation (7.3)] and integral capacitance [Equation (7.8)] methods both assume that the cell potential varies linearly with time during discharging, as previously discussed. Unfortunately, this assumption was not valid in presence of faradaic reactions and led to the overestimation of energy and power densities of hybrid pseudocapacitors by the RC and integral capacitance methods (Figure 7.6).

7.4.2.2 Energy balance

Figure 7.8 shows the energy losses $E_C - E_D$ for hybrid pseudocapacitors predicted by the four different methods under consideration versus the irreversible heat generation $Q_{irr} = Q_J + Q_F$ [Equations (7.13) and (7.14)] for (a) Case 4 and (b) Case 5. It indicates that, unlike other methods, the direct integration method under galvanostatic cycling satisfied the energy conservation principle expressed

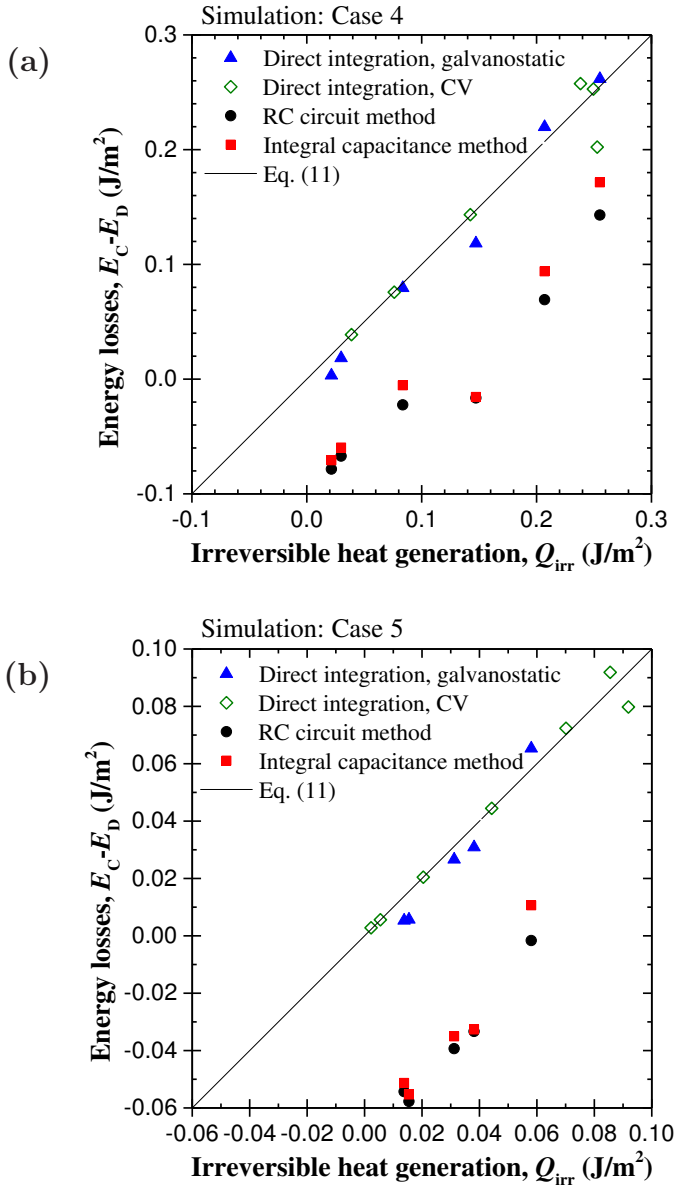

Figure 7.8: Energy losses $E_C - E_D$ as a function of irreversible heat generation Q_{irr} for hybrid capacitors of (a) Case 4 and (b) Case 5.

by Equation (7.12) under all conditions. Therefore, the direct integration method under galvanostatic cycling was the most appropriate method to evaluate energy and power densities in order to generate Ragone plots for hybrid pseudocapacitors. By contrast, the direct integration method under cyclic voltammetry did not satisfy the energy conservation principle at high scan rates, corresponding to large irreversible heat generation. In addition, the RC circuit and integral capacitance methods systematically violated the energy conservation principle. Here also, energy balance for experimental results was not performed due to the fact that the uncertainty of heat generation measurements was on the same order of magnitude as the difference in estimating energy densities using different methods. Thus, it was impossible to distinguish the four methods by performing energy conservation principle on experimental results.

7.5 Chapter summary

This chapter compared four different methods commonly used to generate Ragone charts for EDLCs and hybrid pseudocapacitors namely (i) the direct integration method under galvanostatic cycling, (ii) the direct integration method under cyclic voltammetry, (iii) the RC circuit method, and (iv) the integral capacitance method. The numerically generated Ragone plots were qualitatively comparable with experimental results for both EDLCs and hybrid pseudocapacitors. In addition, the direct integration under galvanostatic cycling was found to be the most appropriate method not only conceptually but also because it intrinsically satisfies that first law of thermodynamics. By contrast, the direct integration method under cyclic voltammetry underestimated the energy density at high scan rates, i.e., at high power densities. The RC circuit and integral capacitance methods systematically overestimated the energy and power densities for electrolyte with large ions and/or in presence of redox reactions. Finally, the above observations were confirmed by experimental measurements on EDLCs made of activated car-

bon electrodes and organic electrolyte and on hybrid pseudocapacitors made of MnO_2-graphene and activated carbon electrodes in aqueous electrolyte.

CHAPTER 8

Conclusions and Future Work

8.1 Conclusions

The objectives of the study were as follows (i) to provide rigorous physical interpretations of EIS results for EDLC and pseudocapacitive electrodes, (ii) to develop design rules for the 3D morphology of EDLC and pseudocapacitive electrodes and the associated electrolyte, and (iii) to compare and evaluate the commonly used methods to estimate energy and power densities for EDLC devices and hybrid pseudocapacitors.

The first objective was achieved by performing 1D physicochemical modeling based on the modified Poisson-Nernst-Planck model along with the generalized Frumkin-Butler-Volmer equation for redox reactions under electrochemical impedance spectroscopy for EDLC electrodes and redox active electrodes. For EDLC electrodes and devices, the electrode resistance, bulk electrolyte resistance, diffuse layer resistance, and equilibrium differential capacitance can be retrieved directly from Nyquist plots. In addition, the internal resistance retrieved from the sum of electrode and bulk electrolyte resistances in EIS simulations showed good agreement with the internal resistance retrieved from the so-called "IR drop" in galvanostatic cycling. Finally, the physical interpretation was confirmed experimentally for EDLC devices with electrodes made of activated carbon in various electrolytes. In addition, for redox active electrodes, the electrode, bulk electrolyte, charge transfer, and mass transfer resistances could be identified from Nyquist plots. These results and interpretations were confirmed experimentally for $LiNi_{0.6}Co_{0.2}Mn_{0.2}O_2$ and MoS_2 electrodes in organic electrolytes.

The second objective was met by multidimensional modeling of EDLC and pseudocapacitive electrodes. Experimental cyclic voltammograms were reproduced numerically for EDLC electrodes of different thicknesses consisting of spherical nanoparticles arranged in either simple cubic (SC) or face-centered cubic (FCC) packing structure. For any given morphology, the areal capacitance increased with decreasing sphere diameter. FCC packing featured larger capacitance than SC packing. These results were explained by considering the magnitude of the electric field at the carbon spheres/electrolyte interfaces. For all cases considered, the areal capacitance remained constant at low scan rate but decreased beyond a critical scan rate when potential propagation across the electrode could not follow the rapid changes in the potential imposed at the current collector. In fact, a dimensional analysis was performed to collapse capacitance versus scan rate plots, based on ratio of CV cycle period and the time scale for electron transport in the electrode. Moreover, a similar approach was followed for pseudocapacitive electrodes consisting of a pseudocapacitive layer coated on conducting nanorods. First, two semi-empirical approaches commonly used in experiments relating the total current density to the scan rate were numerically reproduced and validated. Then, the respective contributions of EDL formation and faradaic reactions to the total charge storage were discriminated for different electrode dimensions and scan rates. Finally, an optimum pseudocapacitive layer thickness to maximize total areal capacitance (in $\mu F/cm^2$) was identified as a function of scan rate and corresponded to a trade-off between achieving large charge storage by using thick pseudocapacitive layer and minimizing resistive losses across the electrode.

The third objective was achieved by comparing four different methods commonly used to generate Ragone charts for EDLCs and hybrid pseudocapacitors namely (i) the direct integration method under galvanostatic cycling, (ii) the direct integration method under cyclic voltammetry, (iii) the RC circuit method, and (iv) the integral capacitance method. The numerically generated Ragone plots

were qualitatively comparable with experimental results for both EDLCs and hybrid pseudocapacitors. In addition, the direct integration under galvanostatic cycling was found to be the most appropriate method not only conceptually but also because it intrinsically satisfies that first law of thermodynamics, i.e., energy conservation principle. The direct integration method under cyclic voltammetry underestimated the energy density at high scan rates, i.e., high power densities. By contrast, the RC circuit and integral capacitance methods systematically overestimated the energy and power densities for electrolyte with large ions and/or in presence of redox reactions.

8.2 Future work

8.2.1 Realistic transport properties of ECs

Currently, a major challenge for continuum modeling of ECs lies in the difficulty of finding accurate and realistic transport properties of the electrodes and of the electrolytes. Several phenomena could occur during charging/discharging of ECs that are not currently accounted for in the assumptions of constant properties in the current model, namely, (i) variation of effective ion diameter a due to partial desolvation of ion species during charging along with the EDL formation and/or within the confinement in porous electrode, (ii) nonuniform ion diffusion coefficient in the electrolyte D_i and in the pseudocapacitive electrode $D_{1,P}$ due to the nonuniform ion concentration, (iii) variation of the equilibrium potential $\Delta\psi_{eq}$ for redox reactions due to the change in state-of-charge, and (iv) variation of the reaction rate constant k_0 during the charging and discharging processes, and (v) material-dependent open-circuit potential $\Delta\psi_{eq}$.

The effective ion size of an electrolyte solution can be evaluated either experimentally or theoretically. Experimentally, X-ray scattering was usually applied to measure the distance between ions in the system [185]. However, the results were

in the form of a distance distribution [185] and the local ion desolvation cannot be easily captured experimentally. Thus, alternatives such as MD simulations based on inter-atom forces can be helpful to identify the local ion desolvation occurring in the electric double layer. In fact, cation species as well as the electrode confinement have significant effect on the ion desolvation occurring near the electrode/electrolyte interface [232]. Therefore, it would be helpful to study the extend of desolvation for the ion species commonly used in ECs. Moreover, this extend of desolvation can be related to the effective ion diameter and can be combined with the current GMPNP model accounting for the variation of effective ion size locally near the electrodes during charging/discharging cycles. In addition, the diffusion coefficient of ion species have been measured in dilute solutions using dispersion techniques [233]. However, isolating the diffusion coefficient of each ion species for concentrated solutions is challenging due to the electrical forces among ions tending to keep the local concentrations of both ion species the same. Thus, it would be helpful to perform molecular dynamic simulations to gain insight into the concentration-dependent diffusion coefficient. Moreover, the SOC dependent equilibrium potential of Li_xMnO_2 was reported in literature [162]. It would be helpful to extend similar measurements to other pseudocapacitive materials and different electrode thickness.

8.2.2 Multidimensional thermal modeling of EC devices

Chapter 7 established that the energy losses of EC devices during one charging/discharging cycle is equal to the irreversible heat generation. Thus, it is important to study the thermal behavior of ECs and to optimize working conditions so as to minimize the irreversible heat generation. In fact, heat generation measurements for EDLCs and hybrid devices are currently underway in our laboratory [5]. However, many experimental observations can only be explained using intuition. On the other hand, previous thermal modeling for ECs based on first

principles developed in UCLA [229, 230] have been restricted to 1D geometries. It is necessary to extend the thermal models to account for realistic morphologies of electrodes. This could account for (i) the non-uniform current density in electrode/electrolyte interface for porous electrodes that may result in non-uniform local irreversible Joule heating, (ii) the geometry confinement of electrode structures resulting in local ion starvation, partially ion desolvation, or "overscreening" effect, which may result in the decreasing heat generation due to diffusion, entropy changes of ions, or redox reaction, (iii) the increasing EDL surface for porous electrodes that may cause the polarization (non-Ohmic) behavior of the electrolyte at the electrode/electrolyte interface to be significant, and (iv) the usage of oversize carbon electrode in hybrid devices to exceed the limitation of carbon electrode in hybrid devices.

Note that the multidimensional simulations of EC electrodes or devices are very costly in terms of computing time and resources. Coupling heat generation to 3D interfacial and transport phenomena would add significantly computational complexity. Thus, it would be recommended to simulate highly ordered and symmetric electrode morphologies. Such simulations could be used to compare with experimental heat generation measurements [5].

8.2.3 Experimental thermal characterizations of EC devices

Thermal behavior of EC devices are important to EC devices, as previously discussed. It would be interesting to perform thermal characterization methods such as electrothermal impedance spectroscopy (ETIS) on EC devices to gain insights into the thermal properties EC devices including the thermal resistance and heat capacity. ETIS consists of imposing a sinusoidal oscillating heat flux of small amplitude and measure the resulting temperature oscillations. Using complex notation, the thermal impedance can be expressed in terms of temperature and heat flux oscillations, similar to electrical impedance in EIS measurement. Then,

thermal resistance and heat capacity of the cell can be identified from the electrothermal impedance spectra. In fact, the ETIS measurement can be carried out at different state-of charge (SOC) to investigate the temporal evolution of the thermal properties of EC devices during charging and discharging. These thermal properties could serve as performance indicators for life time comparison among different electrical energy storage systems.

APPENDIX A

Supplementary Materials for Chapter 4

A.1 Current density and potential drop across the diffuse layer

Figure A.1(a) shows the faradaic current density j_F and potential drop across the diffuse layer $\Delta\psi_D$ as functions of the dimensionless time ft for Case 1 (Table 2) at frequency f of 2, 20 and 2000 Hz. It indicates that $\Delta\psi_D$ and j_F were in phase. This was true for all frequencies considered. Figure A.1(b) shows j_F as a function of $\Delta\psi_D$ for EIS simulations for Case 1. It established a linear relationship between j_F and $\Delta\psi_D$ for all frequencies considered. In addition, the amplitude $\Delta\psi_{D,0}$ of the oscillation of the potential drop across the diffuse layer was very small. Thus, the mass transfer resistance $1/R_{mt}$ [Equation (12)] can be estimated as the slope of the vs. $\Delta\psi_D$ plots near the DC operating points [Equation (15)]. Moreover, Figure A.1(b) also indicates that R_{mt} was independent of frequency.

A.2 Experimental potential evolution under galvanostatic cycling

Figure A.2 shows the potential $\psi_s(t)$ as a function of time t under galvanostatic cycling for imposed current i_{GC} of 1, 4, and 8 mA obtained experimentally for MoS_2 mesoporous electrodes in (a) 1 M $NaClO_4$ in EC/DMC and (b) 1 M $LiClO_4$ in EC/DMC. For both systems, the electrical potential experienced a rapid initial change $\Delta\psi_{GC}$ (the so-called "IR drop") at the beginning of discharging. The internal resistance R_{GC} [Figure 9(d)] can be calculated from the IR drop according to

$$R_{GC} = \frac{\Delta\psi_{GC}}{2i_{GC}} \tag{A.1}$$

(a)

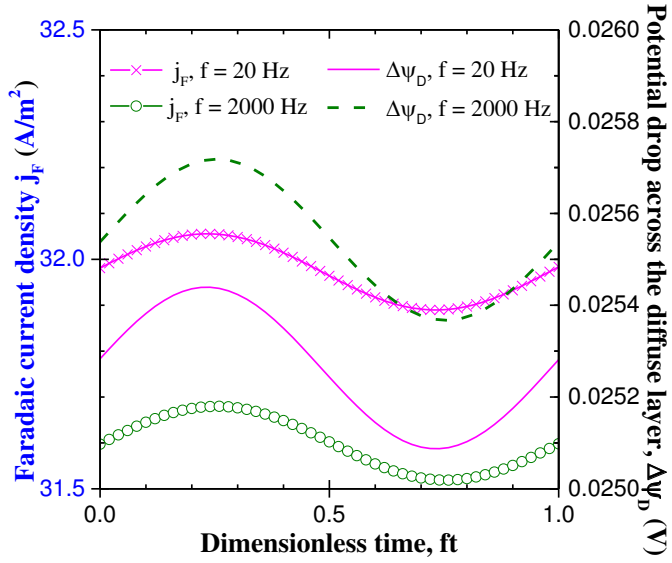

(b)

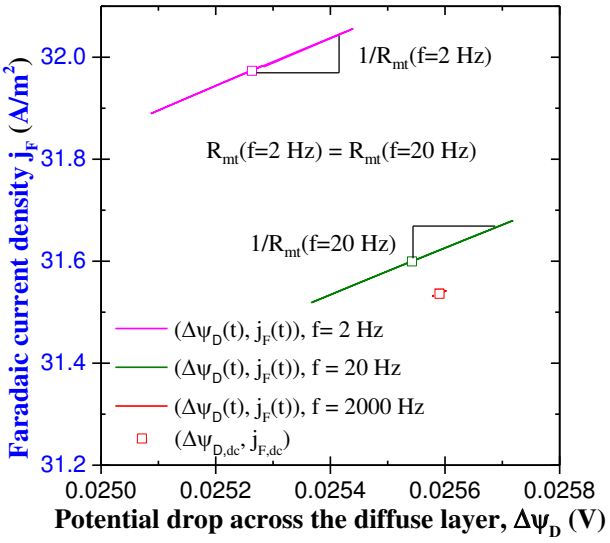

Figure A.1: (a) Faradaic current density j_F and potential drop across the diffuse layer $\Delta\psi_D$ as functions of the dimensionless time ft and (b) j_F vs. $\Delta\psi_D$ for frequencies f of 2, 20, and 2000 Hz under EIS simulations.

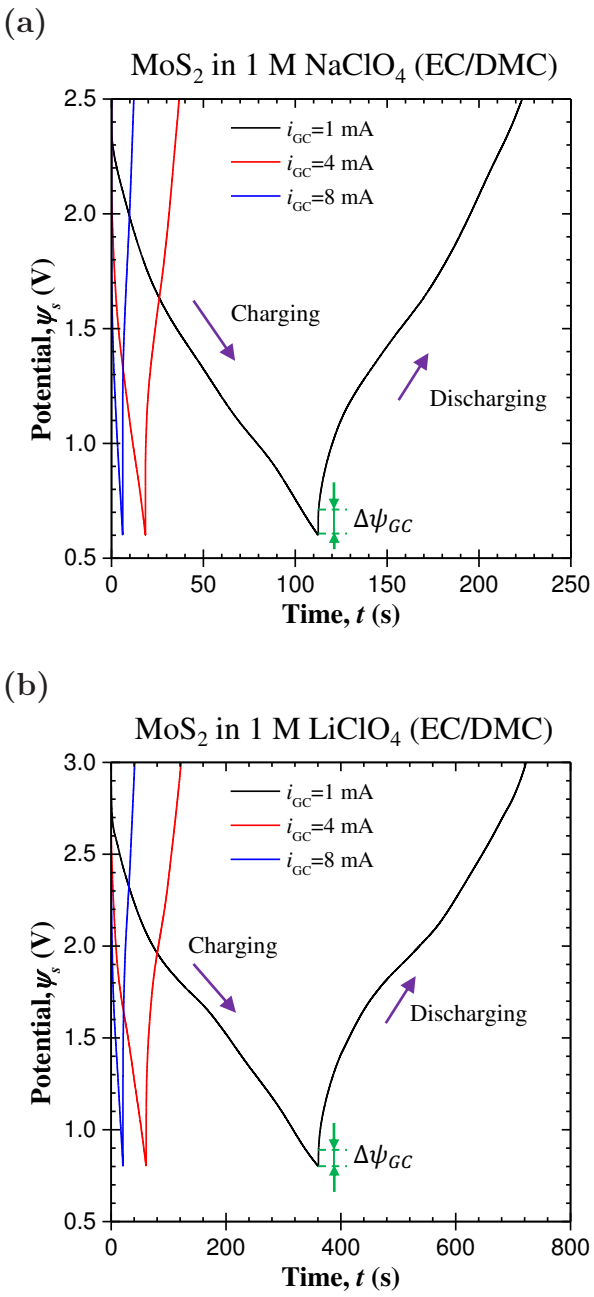

Figure A.2: Potential $\psi_s(t)$ as a function of time t under galvanostatic cycling for imposed current i_{GC} of 1, 4, and 8 mA obtained experimentally for MoS_2 mesoporous electrodes in (a) 1 M $NaClO_4$ in EC/DMC and (b) 1 M $LiClO_4$ in EC/DMC.

APPENDIX B

Supplementary Materials for Chapter 5

B.1 Charge densities

Figure B.1 shows the charge stored (a) per unit footprint surface area Q_{fp}, (b) per unit BET surface area Q_{BET}, and (c) per unit mass of the electrode Q_g as functions of electrode thickness L_c for sphere diameter d of 15, 30, and 40 nm at $t = 0.49\tau_{CV}$ corresponding to $\psi_s = 0.98$ V, i.e., near the end of the charging stage. For a given electrode thickness, all three charge densities increased with decreasing sphere diameter due to the larger normal electric field E_n attracting the ions to the electrode surface.

B.2 Charge stored on each sphere

Figure B.2 shows the charge Q_i on each sphere ($1 \leq i \leq N$) for electrodes made of multiple carbon spheres in SC packing with diameter d of (a) 15, (b) 30, and (c) 40 nm at $t = 0.49\tau_{CV}$ corresponding to $\psi_s = 0.98$ V, i.e., near the end of the charging stage. For a given number N of carbon spheres, the first sphere facing the planar current collector stored less charge than other spheres due to the systematically smaller value of normal electric field E_n.

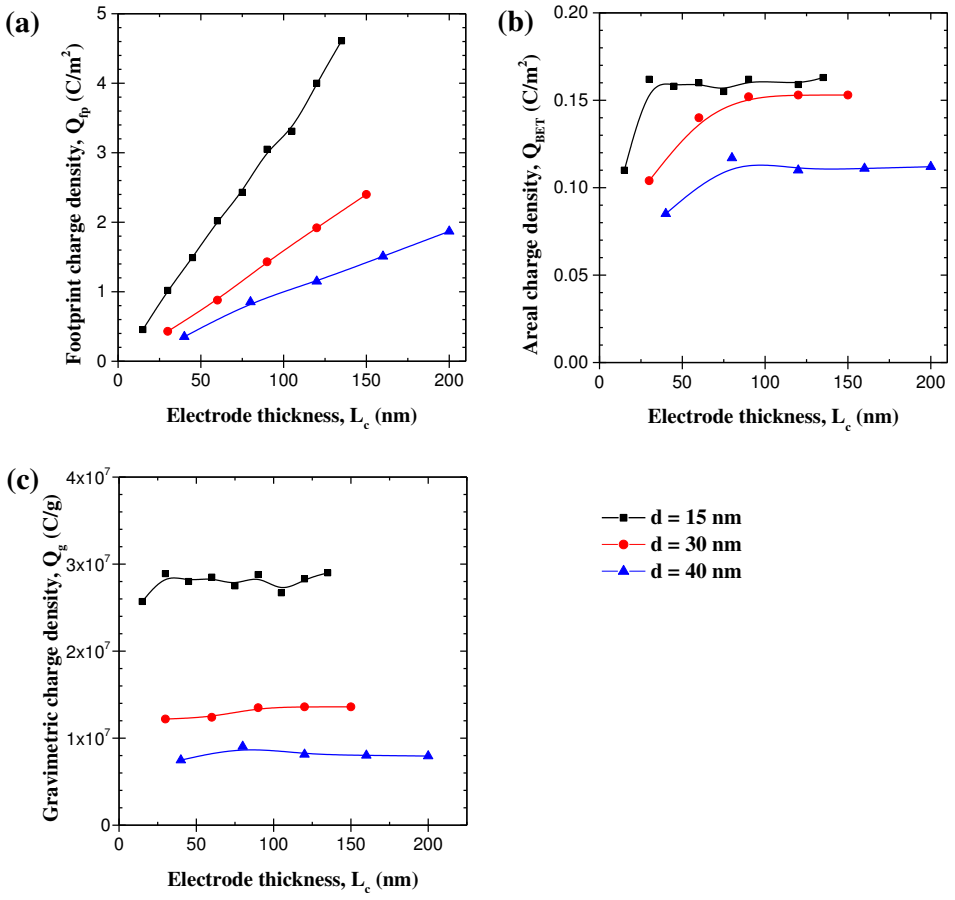

Figure B.1: Charge stored at the end of charging (a) per unit footprint surface area Q_{fp}, (b) per unit BET surface area Q_{BET}, and (c) per unit mass of the electrode Q_g as functions of electrode thickness L_c for sphere diameter d of 15, 30, and 40 nm.

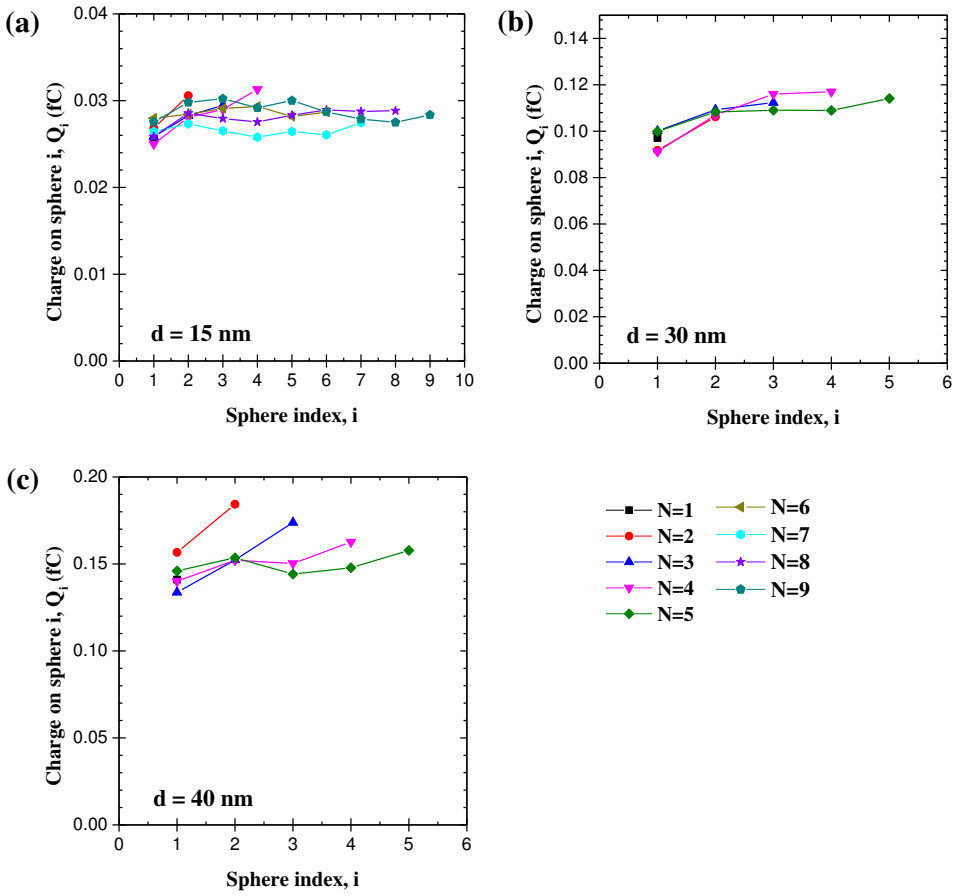

Figure B.2: Charge on each sphere Q_i at $t = 0.49\tau_{CV}$ ($\psi_s = 0.98$ V) as a function of sphere index i for electrodes made of multiple carbon spheres in SC packing with diameter d of (a) $d = 15$ nm, (b) $d = 30$ nm and (c) $d = 40$ nm.

APPENDIX C

Supplementary Materials for Chapter 7

C.1 EDLC devices

C.1.1 CV curves

Figure C.1 shows (a), (b) the CV curves and (c), (d) the corresponding instant (input) power $P(t) = j_s(t)\psi_s(t)$ as functions of dimensionless time t/t_{cd} for Case 1 obtained numerically under cyclic voltammetry with scan rate v of (a), (c) 50 V/s and (b), (d) 5000 V/s, respectively. Like experimental results, at high scan rates, the current density remained positive even after switching from charging to discharging. Consequently, the instant input power density $P(t) = j_s(t)\psi_s(t)$ was also positive at the beginning of discharging instead of being negative, as observed at low scan rates. On the other hand, Figures C.1(e)-C.1(f) show the instant (input) power $P(t) = j_s(t)\psi_s(t)$ as functions of dimensionless time t/t_{cd} for Case 1 obtained numerically under galvanostatic cycling with imposed current density j_{GC} of (e) 20 mA/cm^2 and (f) 200 mA/cm^2, respectively. The figures indicate that the instant input power $P(t)$ was always negative throughout the discharging process under galvanostatic cycling. Similar observations could be made for Cases 2 and 3. This resulted in the systematic discrepancy between cyclic voltammetry and galvanostatic cycling (Figure 2) in estimating the energy density using Equation (1).

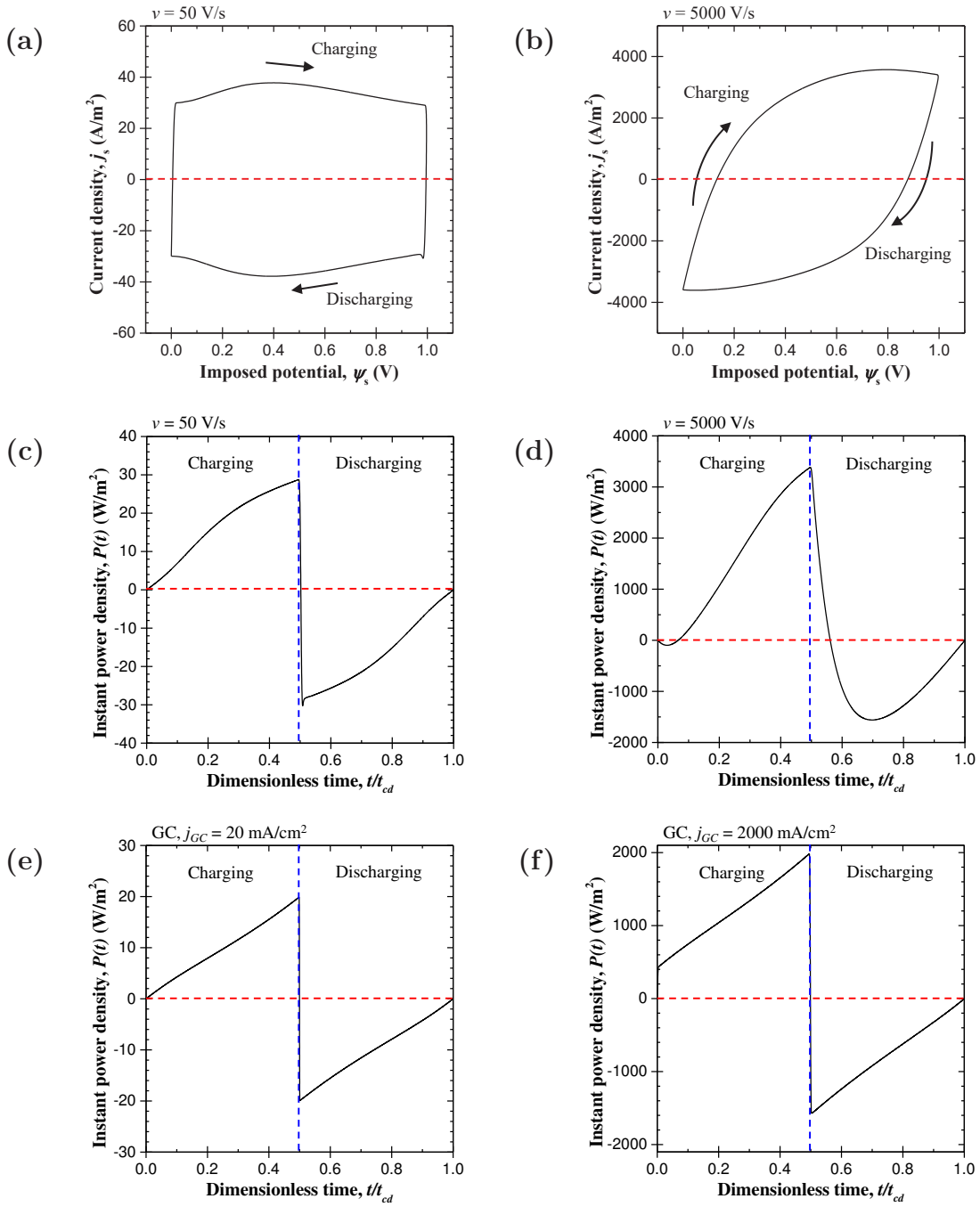

Figure C.1: Numerically predicted (a)(b) CV curves and (c)-(f) instant power $P(t)$ as functions of dimensionless time t/t_{cd} for Case 1 under (a)-(d) cyclic voltammetry at scan rates (a)(c) $v = 50$ V/s and (b)(d) $v = 5000$ V/s and (e)(f) galvanostatic cycling at imposed current density (e) $j_{GC} = 20$ mA/cm^2 and (f) $j_{GC} = 2000$ mA/cm^2.

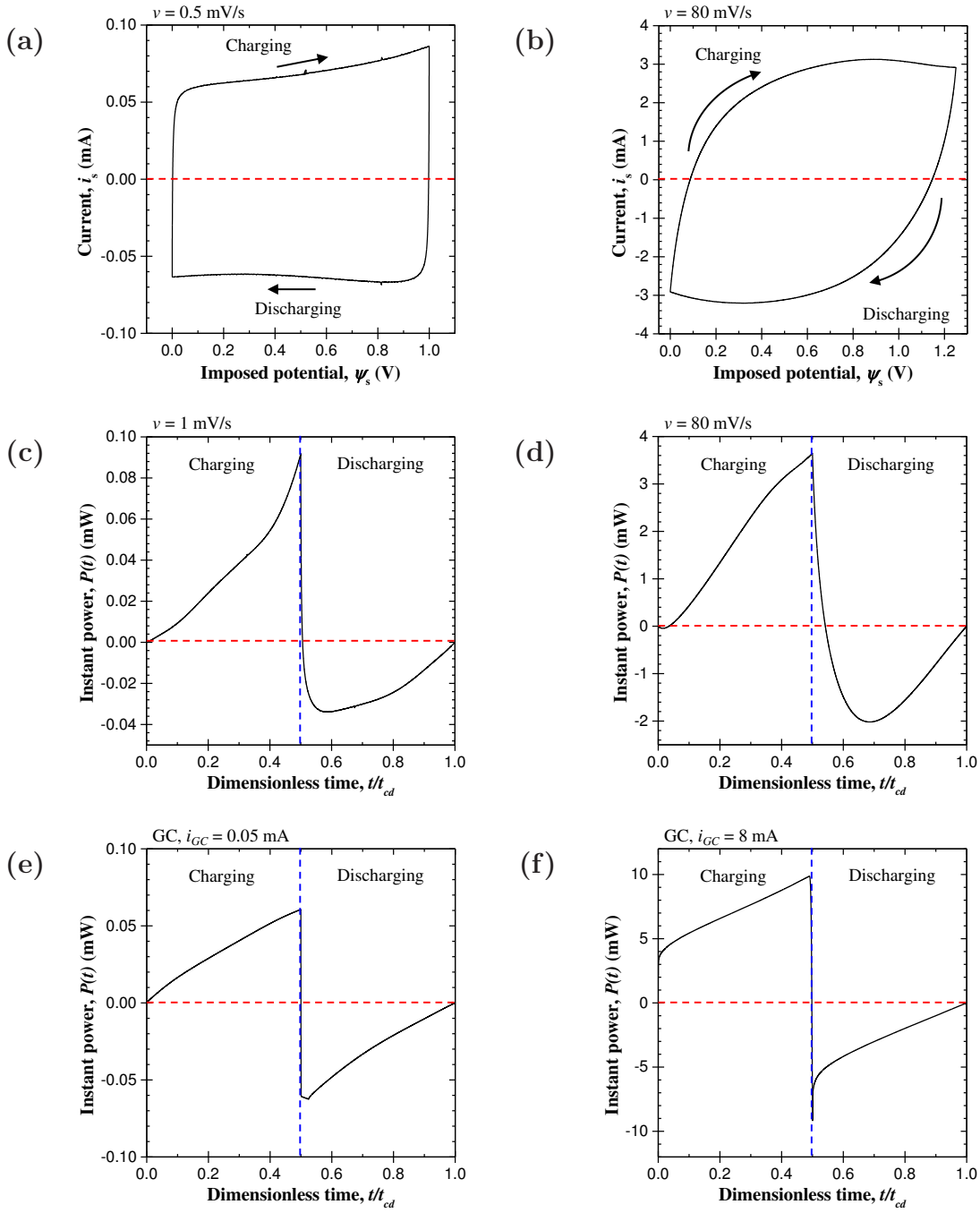

Figure C.2: Experimentally measured (a)(b) CV curves and (c)-(f) instant power $P(t)$ as functions of dimensionless time t/t_{cd} for hybrid pseudocapacitors under (a)-(d) cyclic voltammetry at scan rates (a)(c) $v = 1$ mV/s and (b)(d) $v = 80$ mV/s and (e)(f) galvanostatic cycling at imposed current (e) $i_{GC} = 0.05$ mA and (f) $i_{GC} = 8$ mA.

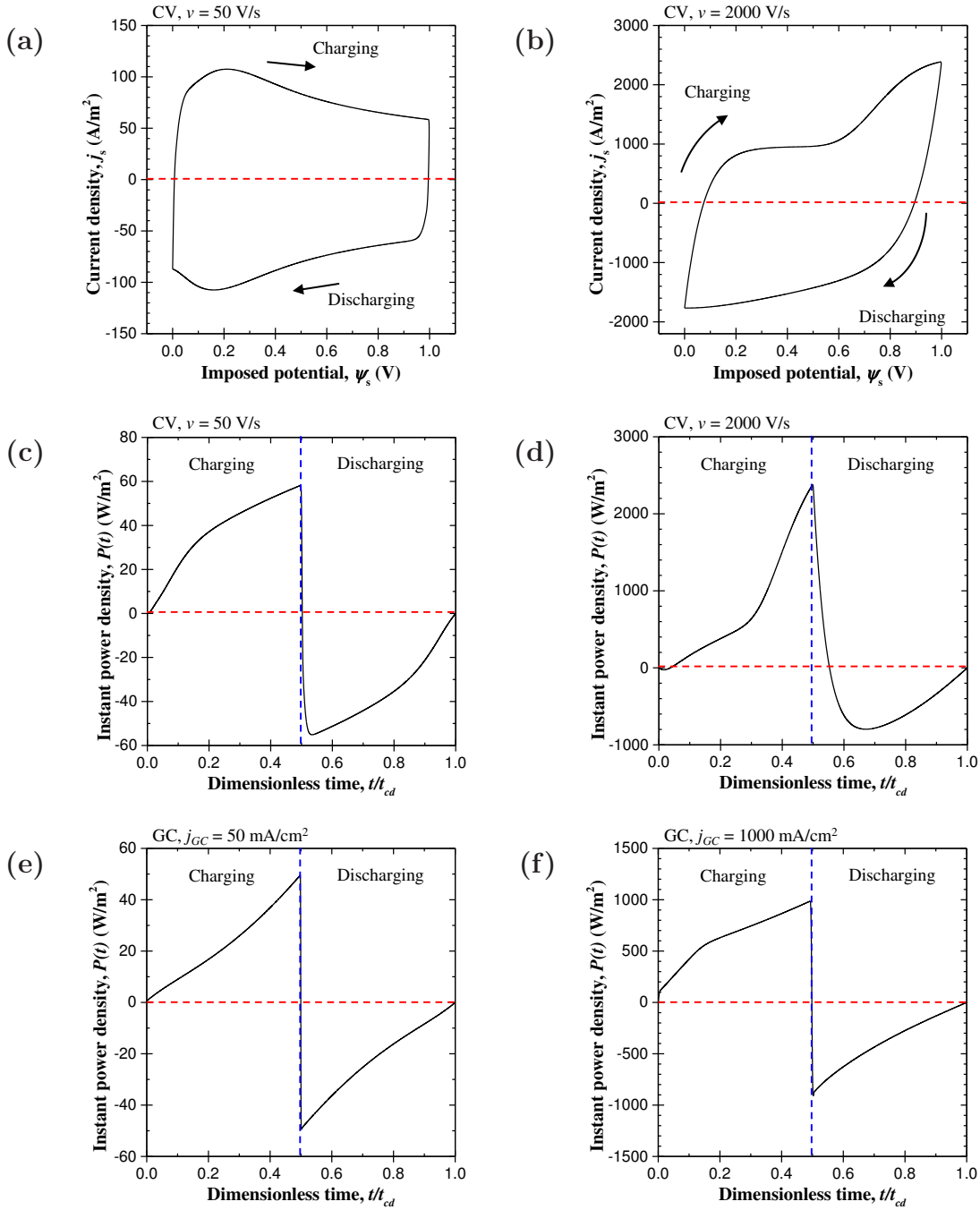

Figure C.3: Numerically predicted (a)(b) CV curves and (c)-(f) instant power $P(t)$ as functions of dimensionless time t/t_{cd} for Case 1 under (a)-(d) cyclic voltammetry at scan rates (a)(c) $v = 50$ V/s and (b)(d) $v = 2000$ V/s and (e)(f) galvanostatic cycling at imposed current density (e) $j_{GC} = 50$ mA/cm^2 and (f) $j_{GC} = 1000$ mA/cm^2.

C.2 Hybrid pseudocapacitors

C.2.1 CV curves

Figure C.2 shows (a), (b) the CV curves and (c), (d) the corresponding instant (input) power $P(t) = i_s(t)\psi_s(t)$ as functions of dimensionless time t/t_{cd} for experimental results of hybrid pseudocapacitors under cyclic voltammetry with scan rate v of (a), (c) 1 mV/s and (b), (d) 80 mV/s, respectively. At high scan rates, the current remained positive even after switching from charging to discharging. Consequently, the instant input power density $P(t) = i_s(t)\psi_s(t)$ was also positive at the beginning of discharging instead of being negative, as observed at low scan rates. On the other hand, Figures C.2(e)-C.2(f) show the instant (input) power $P(t) = i_s(t)\psi_s(t)$ as functions of dimensionless time t/t_{cd} for experimental results under galvanostatic cycling with imposed current i_{GC} of (e) 0.5 mA and (f) 8 mA, respectively. The figures indicate that the instant input power $P(t)$ was always negative throughout the discharging process under galvanostatic cycling. Similar behavior was observed for numerical results in Cases 4 [Figure C.3] and 5 (not shown). This resulted in the systematic discrepancy between cyclic voltammetry and galvanostatic cycling (Figure 6) in estimating the energy density using Equation (1).

C.2.2 Potential evolution under galvanostatic cycling

Figure C.4(a) shows the cell potential $\psi_s(t)$ as a function of dimensionless time t/t_{cd} numerically predicted for Cases 2 (EDLC) and 5 (hybrid pseudocapacitor) with $j_{GC} = 50$ mA/cm^2. Note that all other parameters did not vary. Unlike for EDLCs, the potential evolution in hybrid pseudocapacitors during charging and discharging was asymmetric. A distinct "kink" in $\psi_s(t)$ was observed during charging and the potential evolution during discharging of hybrid pseudocapacitors fell below that of EDLCs. In addition, Figure C.4(b) show the cell potential

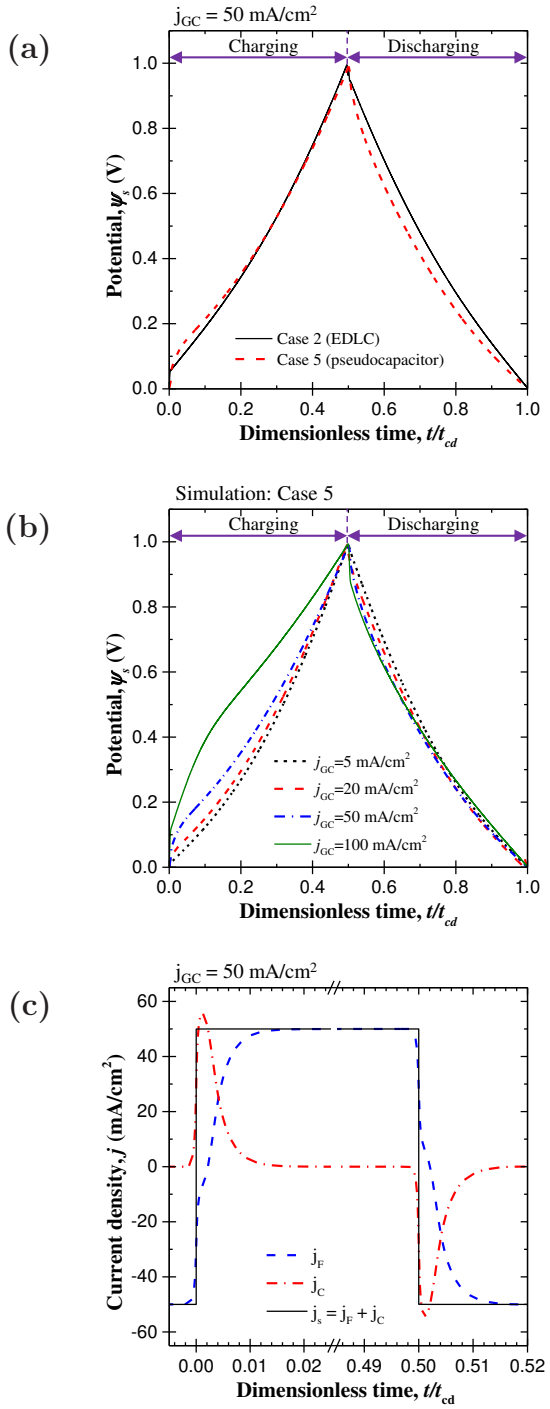

Figure C.4: (a)-(b) Electrical potential $\psi_s(t)$ as a function of dimensionless time t/t_{cd} (a) for Cases 2 and 5 under galvanostatic cycling with current density $j_{GC} = 50$ mA/cm^2 and (b) for Case 5 under galvanostatic cycling with imposed current density varying from 5 mA/cm^2 to 100 mA/cm^2. (c) Faradaic j_F, capacitive j_C, and imposed $j_{GC} = j_F + j_C$ current densities as functions of dimensionless time t/t_{cd} for Case 5 with imposed current density $j_{GC} = 50$ mA/cm^2.

$\psi_s(t)$ as a function of dimensionless time t/t_{cd} for galvanostatic cycling numerically predicted for Case 5 with j_{GC} varying between 20 and 200 mA/cm^2. It indicates that the "kink" during charging and the convex potential evolution during discharging were observed for all current densities. Furthermore, Figure C.4(c) shows the corresponding faradaic j_F, capacitive j_C, and the total $j_s = j_F + j_C$ current densities as functions of dimensionless time t/t_{cd} numerically predicted for Case 5. Similarly, a peak of the capacitive current density occurred at the transition between charging and discharging resulting in a relatively small differential capacitance C_{diff} and thus a large slope $|\mathrm{d}\psi_s/\mathrm{d}t| = j_{GC}/C_{diff}$ of the potential evolution [Figure C.4(a)].

References

[1] H. Wang and L. Pilon, "Mesoscale modeling of electric double layer capacitors with three-dimensional ordered structures", *Journal of Power Sources*, vol. 221, pp. 252–260, 2013.

[2] US Department of Energy, "Basic Research Needs for Electrical Energy Storage: Report of the Basic Energy Sciences Workshop for Electrical Energy Storage", Tech. Rep., Office of Basic Energy Sciences, DOE, 2007.

[3] Z. Zhao, S. Hao, P. Hao, Y. Sang, A. Manivannan, N. Wu, and H. Liu, "Lignosulphonate-cellulose derived porous activated carbon for supercapacitor electrode", *Journal of Materials Chemistry A*, vol. 3, no. 29, pp. 15049–15056, 2015.

[4] H.-J. Liu, W.-J. Cui, L.-H. Jin, C.-X. Wang, and Y.-Y. Xia, "Preparation of three-dimensional ordered mesoporous carbon sphere arrays by a two-step templating route and their application for supercapacitors", *Journal of Materials Chemistry*, vol. 19, no. 22, pp. 3661–3667, 2009.

[5] O. Munteshari, J. Lau, A. Krishnan, B. Dunn, and L. Pilon, "Isothermal calorimeter for measurements of time-dependent heat generation rate in individual supercapacitor electrodes", *Journal of Power Sources*, vol. 374, pp. 257–268, 2018.

[6] F. Schipper, M. Dixit, D. Kovacheva, M. Talianker, O. Haik, J. Grinblat, E. M. Erickson, C. Ghanty, D. T. Major, B. Markovsky, and D. Aurbach, "Stabilizing nickel-rich layered cathode materials by a high-charge cation doping strategy: zirconium-doped $LiNi_{0.6}Co_{0.2}Mn_{0.2}O_2$", *Journal of Materials Chemistry A*, vol. 4, no. 41, pp. 16073–16084, 2016.

[7] B. E. Conway, *Electrochemical Supercapacitors: Scientific Fundamentals and Technological Applications*, Kluwer Academic/Plenum Publishers, New York, NY, 1999.

[8] A. J. Bard, L. R. Faulkner, J. Leddy, and C. G. Zoski, *Electrochemical Methods: Fundamentals and Applications*, vol. 2, John Wiley & Sons, Hoboken, NJ, 1980.

[9] V. S. Bagotsky, *Fundamentals of Electrochemistry*, John Wiley & Sons, Hoboken, NJ, 2nd edition, 2006.

[10] P. Simon and Y. Gogotsi, "Materials for electrochemical capacitors", *Nature Materials*, vol. 7, no. 11, pp. 845–854, 2008.

[11] M. Brain, "How lithium-ion batteries work", HowStuffWorks.com, 14 November 2006, Accessed February 25, 2013.

[12] M. S. Halper and J. C. Ellenbogen, "Supercapacitors: A brief overview", Tech. Rep. No. MP 05W0000272, The MITRE Corporation, McLean, VA, 2006.

[13] Y. Zhang, H. Feng, X. Wu, L. Wang, A. Zhang, T. Xia, H. Dong, X. Li, and L. Zhang, "Progress of electrochemical capacitor electrode materials: A review", *International Journal of Hydrogen Energy*, vol. 34, no. 11, pp. 4889–4899, 2009.

[14] G. Wang, L. Zhang, and J. Zhang, "A review of electrode materials for electrochemical supercapacitors", *Chemical Society Reviews*, vol. 41, no. 2, pp. 797–828, 2012.

[15] Z.-S. Wu, G. Zhou, L.-C. Yin, W. Ren, F. Li, and H.-M. Cheng, "Graphene/metal oxide composite electrode materials for energy storage", *Nano Energy*, vol. 1, no. 1, pp. 107–131, 2012.

[16] H. Wang, A. Thiele, and L. Pilon, "Simulations of cyclic voltammetry for electric double layers in asymmetric electrolytes: A generalized modified Poisson-Nernst-Planck model", *Journal of Physical Chemistry C*, vol. 117, no. 36, pp. 18286– 18297, 2013.

[17] P. Simon, Y. Gogotsi, and B. Dunn, "Where do batteries end and supercapacitors begin?", *Science*, vol. 343, no. 6176, pp. 1210–1211, 2014.

[18] X. Z. Yuan, C. Song, H. Wang, and J. Zhang, *Electrochemical Impedance Spectroscopy in PEM Fuel Cells: Fundamentals and Applications*, Springer-Verlag, London, UK, 2010.

[19] M. Pech, D.and Brunet, P. Durou, H.and Huang, V. Mochalin, Y. Gogotsi, P. Taberna, and P. Simon, "Ultrahigh-power micrometre-sized supercapacitors based on onion-like carbon", *Nature Nanotechnology*, vol. 5, no. 9, pp. 651–654, 2010.

[20] H. Itoi, H. Nishihara, T. Kogure, and T. Kyotani, "Three-dimensionally arrayed and mutually connected 1.2-nm nanopores for high-performance electric double layer capacitor", *Journal of the American Chemical Society*, vol. 133, no. 5, pp. 1165–1167, 2011.

[21] A. Lasia, "Electrochemical impedance spectroscopy and its applications", in *Modern Aspects of Electrochemistry, No. 32*, B. E. Conway, J. O. M. Bockris, and R. E. White, Eds., chapter 2, pp. 143–248. Kluwer Academic Publishers, New York, NY, 2002.

[22] M. E. Orazem and B. Tribollet, *Electrochemical Impedance Spectroscopy*, John Wiley & Sons, Hoboken, NJ, 2008.

[23] G.-Q. Han, Y.-R. Liu, W.-H. Hu, B. Dong, X. Li, X. Shang, Y.-M. Chai, Y.-Q. Liu, and C.-G. Liu, "Crystallographic structure and morphology transformation of MnO_2 nanorods as efficient electrocatalysts for oxygen evolution reaction", *Journal of The Electrochemical Society*, vol. 163, no. 2, pp. H67–H73, 2016.

[24] P. Jin, X. Zhang, M. Zhen, and J. Wang, "MnO_2 nanotubes with graphene-assistance as low-cost counter-electrode materials in dye-sensitized solar cells", *RSC Advances*, vol. 6, no. 13, pp. 10938–10942, 2016.

[25] R. Thangappan, S. Kalaiselvam, A. Elayaperumal, R. Jayavel, M. Arivanandhan, R. Karthikeyan, and Y. Hayakawa, "Graphene decorated with MoS_2 nanosheets: a synergetic energy storage composite electrode for supercapacitor applications", *Dalton transactions*, vol. 45, no. 6, pp. 2637–2646, 2016.

[26] Y. Xiao, G. Han, H. Zhou, Y. Li, and J.-Y. Lin, "Nickel sulfide counter electrodes enhanced by hydrosulphuric acid hydrothermal treatments for use in Pt-free dye-sensitized solar cells", *Electrochimica Acta*, vol. 155, pp. 103–109, 2015.

[27] Z.-G. Ye, H.-M. Meng, and D.-B. Sun, "Electrochemical impedance spectroscopic (EIS) investigation of the oxygen evolution reaction mechanism of Ti/IrO_2+ MnO_2 electrodes in 0.5 M H_2SO_4 solution", *Journal of Electroanalytical Chemistry*, vol. 621, no. 1, pp. 49–54, 2008.

[28] C.-H. Lin, C.-H. Tsai, F.-G. Tseng, C.-C. M. Ma, H.-C. Wu, and C.-K. Hsieh, "Three-dimensional vertically aligned hybrid nanoarchitecture of two-dimensional molybdenum disulfide nanosheets anchored on directly grown one-dimensional carbon nanotubes for use as a counter electrode in dye-sensitized solar cells", *Journal of Alloys and Compounds*, vol. 692, pp. 941–949, 2017.

[29] Z. Quan, E. Ni, Y. Ogasawara, and N. Sonoyama, "Nano-size multiple metal oxide anode electrodes synthesized from layered double hydroxides−electrochemical reaction mechanism and surface morphology change during reaction with lithium ion", *Solid State Ionics*, vol. 268, pp. 268–272, 2014.

[30] H. Wang and L. Pilon, "Physical interpretation of cyclic voltammetry for measuring electric double layer capacitances", *Electrochimica Acta*, vol. 64, pp. 130–139, 2012.

[31] H.-L. Girard, H. Wang, A. L. d'Entremont, and L. Pilon, "Physical interpretation of cyclic voltammetry for hybrid pseudocapacitors", *The Journal of Physical Chemistry C*, vol. 119, no. 21, pp. 11349–11361, 2015.

[32] H.-L. Girard, B. Dunn, and L. Pilon, "Simulations and interpretation of three-electrode cyclic voltammograms of pseudocapacitive electrodes", *Electrochimica Acta*, vol. 211, pp. 420–429, 2016.

[33] A. L. d'Entremont, H.-L. Girard, H. Wang, and L. Pilon, "Electrochemical transport phenomena in hybrid pseudocapacitors under galvanostatic cycling", *Journal of the Electrochemical Society*, vol. 163, no. 2, pp. A229–A243, 2016.

[34] I. Yang, S.-G. Kim, S. H. Kwon, M.-S. Kim, and J. C. Jung, "Relationships between pore size and charge transfer resistance of carbon aerogels for organic electric double-layer capacitor electrodes", *Electrochimica Acta*, vol. 223, pp. 21–30, 2017.

[35] H. M. Coromina, B. Adeniran, R. Mokaya, and D. A. Walsh, "Bridging the performance gap between electric double-layer capacitors and batteries with high-energy/high-power carbon nanotube-based electrodes", *Journal of Materials Chemistry A*, vol. 4, no. 38, pp. 14586–14594, 2016.

[36] H. D. Yoo, J. H. Jang, J. H. Ryu, Y. Park, and S. M. Oh, "Impedance analysis of porous carbon electrodes to predict rate capability of electric double-layer capacitors", *Journal of Power Sources*, vol. 267, pp. 411–420, 2014.

[37] C. Lei, F. Markoulidis, Z. Ashitaka, and C. Lekakou, "Reduction of porous carbon/Al contact resistance for an electric double-layer capacitor (EDLC)", *Electrochimica Acta*, vol. 92, pp. 183–187, 2013.

[38] B. Fang and L. Binder, "A modified activated carbon aerogel for high-energy storage in electric double layer capacitors", *Journal of Power Sources*, vol. 163, no. 1, pp. 616–622, 2006.

[39] K. H. An, W. S. Kim, Y. S. Park, J.-M. Moon, D. J. Bae, S. C. Lim, Y. S. Lee, and Y. H. Lee, "Electrochemical properties of high-power supercapacitors using single-walled carbon nanotube electrodes", *Advanced Functional Materials*, vol. 11, no. 5, pp. 387–392, 2001.

[40] M. Arulepp, L. Permann, J. Leis, A. Perkson, K. Rumma, A. Jänes, and E. Lust, "Influence of the solvent properties on the characteristics of a double layer capacitor", *Journal of Power Sources*, vol. 133, no. 2, pp. 320–328, 2004.

[41] C.-L. Liu, W.-S. Dong, G.-P. Cao, J.-R. Song, L. Liu, and Y.-S. Yang, "Influence of KOH followed by oxidation pretreatment on the electrochemical performance of phenolic based activated carbon fibers", *Journal of Electroanalytical Chemistry*, vol. 611, no. 1, pp. 225–231, 2007.

[42] J. Gamby, P. Taberna, P. Simon, J. Fauvarque, and M. Chesneau, "Studies and characterisations of various activated carbons used for carbon/carbon supercapacitors", *Journal of Power Sources*, vol. 101, no. 1, pp. 109–116, 2001.

[43] C. Portet, G. Yushin, and Y. Gogotsi, "Electrochemical performance of carbon onions, nanodiamonds, carbon black and multiwalled nanotubes in electrical double layer capacitors", *Carbon*, vol. 45, no. 13, pp. 2511–2518, 2007.

[44] F. Lufrano, P. Staiti, and M. Minutoli, "Evaluation of nafion based double layer capacitors by electrochemical impedance spectroscopy", *Journal of Power Sources*, vol. 124, no. 1, pp. 314–320, 2003.

[45] R. Kötz and M. Carlen, "Principles and applications of electrochemical capacitors", *Electrochimica Acta*, vol. 45, no. 15, pp. 2483–2498, 2000.

[46] Y.-R. Nian and H. Teng, "Influence of surface oxides on the impedance behavior of carbon-based electrochemical capacitors", *Journal of Electroanalytical Chemistry*, vol. 540, pp. 119–127, 2003.

[47] J. Kang, S. H. Jayaram, J. Rawlins, and J. Wen, "Characterization of thermal behaviors of electrochemical double layer capacitors (EDLCs) with aqueous and organic electrolytes", *Electrochimica Acta*, vol. 144, pp. 200–210, 2014.

[48] J. Kang, S. Atashin, S. H. Jayaram, and J. Z. Wen, "Frequency and temperature dependent electrochemical characteristics of carbon-based electrodes made of commercialized activated carbon, graphene and single-walled carbon nanotube", *Carbon*, vol. 111, pp. 338–349, 2017.

[49] Y. He, W. Chen, X. Li, Z. Zhang, J. Fu, C. Zhao, and E. Xie, "Freestanding three-dimensional graphene/MnO_2 composite networks as ultralight and flexible supercapacitor electrodes", *ACS Nano*, vol. 7, no. 1, pp. 174–182, 2012.

[50] B. Vidhyadharan, I. I. Misnon, R. A. Aziz, K. Padmasree, M. M. Yusoff, and R. Jose, "Superior supercapacitive performance in electrospun copper oxide nanowire electrodes", *Journal of Materials Chemistry A*, vol. 2, no. 18, pp. 6578–6588, 2014.

[51] Y. Huang, Y. Li, Z. Hu, G. Wei, J. Guo, and J. Liu, "A carbon modified MnO_2 nanosheet array as a stable high-capacitance supercapacitor electrode", *Journal of Materials Chemistry A*, vol. 1, no. 34, pp. 9809–9813, 2013.

[52] K. Krishnamoorthy, G. K. Veerasubramani, P. Pazhamalai, and S. J. Kim, "Designing two dimensional nanoarchitectured MoS_2 sheets grown on Mo foil as a binder free electrode for supercapacitors", *Electrochimica Acta*, vol. 190, pp. 305–312, 2016.

[53] Q. Qu, P. Zhang, B. Wang, Y. Chen, S. Tian, Y. Wu, and R. Holze, "Electrochemical performance of MnO_2 nanorods in neutral aqueous electrolytes as a cathode for asymmetric supercapacitors", *The Journal of Physical Chemistry C*, vol. 113, no. 31, pp. 14020–14027, 2009.

[54] K. V. Sankar and R. K. Selvan, "The preparation of $MnFe_2O_4$ decorated flexible graphene wrapped with PANI and its electrochemical performances for hybrid supercapacitors", *RSC Advances*, vol. 4, no. 34, pp. 17555–17566, 2014.

[55] V. Subramanian, H. Zhu, and B. Wei, "Synthesis and electrochemical characterizations of amorphous manganese oxide and single walled carbon nanotube composites as supercapacitor electrode materials", *Electrochemistry Communications*, vol. 8, no. 5, pp. 827–832, 2006.

[56] D. Maheswari and P. Venkatachalam, "Enhanced performance of bi-layer Nb_2O_5 coated TiO_2 nanoparticles/nanowires composite photoanode in dye-sensitized solar cells", *Photonics and Nanostructures-Fundamentals and Applications*, vol. 12, no. 5, pp. 515–526, 2014.

[57] S. K. Meher, P. Justin, and G. R. Rao, "Nanoscale morphology dependent pseudocapacitance of NiO: Influence of intercalating anions during synthesis", *Nanoscale*, vol. 3, no. 2, pp. 683–692, 2011.

[58] Q. Pang, Y. Zhao, X. Bian, Y. Ju, X. Wang, Y. Wei, B. Liu, F. Du, C. Wang, and G. Chen, "Hybrid graphene @MoS_2@TiO_2 microspheres for use as a high performance negative electrode material for lithium ion batteries", *Journal of Materials Chemistry A*, vol. 5, no. 7, pp. 3667–3674, 2017.

[59] T. S. Sahu and S. Mitra, "Exfoliated MoS_2 sheets and reduced graphene oxide-an excellent and fast anode for sodium-ion battery", *Scientific reports*, vol. 5, pp. 12571, 2015.

[60] S. Wang, B. Hsia, C. Carraro, and R. Maboudian, "High-performance all solid-state micro-supercapacitor based on patterned photoresist-derived porous carbon electrodes and an ionogel electrolyte", *Journal of Materials Chemistry A*, vol. 2, no. 21, pp. 7997–8002, 2014.

[61] E. Frackowiak, "Carbon materials for supercapacitor application", *Physical Chemistry Chemical Physics*, vol. 9, no. 15, pp. 1774–1785, 2007.

[62] S.-K. Kim, E. Jung, M. D. Goodman, K. S. Schweizer, N. Tatsuda, K. Yano, and P. V. Braun, "Self-assembly of monodisperse starburst carbon spheres into hierarchically organized nanostructured supercapacitor electrodes", *ACS Applied Materials & Interfaces*, vol. 7, no. 17, pp. 9128–9133, 2015.

[63] D.-D. Zhou, H.-J. Liu, Y.-G. Wang, C.-X. Wang, and Y.-Y. Xia, "Ordered mesoporous/microporous carbon sphere arrays derived from chlorination of mesoporous TiC/C composite and their application for supercapacitors", *Journal of Materials Chemistry*, vol. 22, no. 5, pp. 1937–1943, 2012.

[64] H. Zhou, S. Zhu, M. Hibino, and I. Honma, "Electrochemical capacitance of self-ordered mesoporous carbon", *Journal of Power Sources*, vol. 122, no. 2, pp. 219–223, 2003.

[65] C. Vix-Guterl, S. Saadallah, K. Jurewicz, E. Frackowiak, M. Reda, J. Parmentier, J. Patarin, and F. Béguin, "Supercapacitor electrodes from new ordered porous carbon materials obtained by a templating procedure", *Materials Science and Engineering B*, vol. 108, no. 1-2, pp. 148–155, 2004.

[66] D. W. Wang, F. Li, H. T. Fang, M. Liu, G. Q. Lu, and H. M. Cheng, "Effect of pore packing defects in 2-D ordered mesoporous carbons on ionic transport", *Journal of Physical Chemistry B*, vol. 110, no. 17, pp. 8570–8575, 2006.

[67] H. Yamada, H. Nakamur, F. Nakahara, I. Moriguchi, and T. Kudo, "Electrochemical study of high electrochemical double layer capacitance of ordered porous carbons with both meso/macropores and micropores", *Journal of Physical Chemistry C*, vol. 111, no. 1, pp. 227–233, 2007.

[68] S. W. Woo, K. Dokko, H. Nakano, and K. Kanamura, "Preparation of three dimensionally ordered macroporous carbon with mesoporous walls for electric double-layer capacitors", *Journal of Materials Chemistry*, vol. 18, no. 14, pp. 1674–1680, 2008.

[69] H. J. Liu, X. M. Wang, W. J. Cui, Y. Q. Dou, D. Y. Zhao, and Y. Y. Xia, "Highly ordered mesoporous carbon nanofiber arrays from a crab shell biological template and its application in supercapacitors and fuel cells", *Journal of Materials Chemistry*, vol. 20, no. 20, pp. 4223–4230, 2010.

[70] G. Sun, J. Wang, X. Liu, D. Long, W. Qiao, and L. Ling, "Ion transport behavior in triblock copolymer-templated ordered mesoporous carbons with different pore symmetries", *Journal of Physical Chemistry C*, vol. 114, no. 43, pp. 18745–18751, 2010.

[71] Q. Li, X.-F. Lu, H. Xu, Y.-X. Tong, and G.-R. Li, "Carbon/MnO_2 double-walled nanotube arrays with fast ion and electron transmission for high-performance supercapacitors", *ACS Applied Materials & Interfaces*, vol. 6, no. 4, pp. 2726–2733, 2014.

[72] S. W. Lee, J. Kim, S. Chen, P. T. Hammond, and Y. Shao-Horn, "Carbon nanotube/manganese oxide ultrathin film electrodes for electrochemical capacitors", *ACS Nano*, vol. 4, no. 7, pp. 3889–3896, 2010.

[73] Z. Lei, F. Shi, and L. Lu, "Incorporation of MnO_2-coated carbon nanotubes between graphene sheets as supercapacitor electrode", *ACS Applied Materials & Interfaces*, vol. 4, no. 2, pp. 1058–1064, 2012.

[74] P. Yang, Y. Ding, Z. Lin, Z. Chen, Y. Li, P. Qiang, M. Ebrahimi, W. Mai, C. P. Wong, and Z. L. Wang, "Low-cost high-performance solid-state asymmetric supercapacitors based on MnO_2 nanowires and Fe_2O_3 nanotubes", *Nano Letters*, vol. 14, no. 2, pp. 731–736, 2014.

[75] A. M. Johnson and J. Newman, "Desalting by means of porous carbon electrodes", *Journal of The Electrochemical Society*, vol. 118, no. 3, pp. 510–517, 1971.

[76] B. Pillay and J. Newman, "The influence of side reactions on the performance of electrochemical double-layer capacitors", *Journal of The Electrochemical Society*, vol. 143, no. 6, pp. 1806–1814, 1996.

[77] I. J. Ong and J. Newman, "Double-layer capacitance in a dual lithium ion insertion cell", *Journal of The Electrochemical Society*, vol. 146, no. 12, pp. 4360–4365, 1999.

[78] V. Srinivasan and J. W. Weidner, "Mathematical modeling of electrochemical capacitors", *Journal of the Electrochemical Society*, vol. 146, no. 5, pp. 1650–1658, 1999.

[79] C. Lin, J. A. Ritter, B. N. Popov, and R. E. White, "A mathematical model of an electrochemical capacitor with double-layer and faradaic processes", *Journal of the Electrochemical Society*, vol. 146, no. 9, pp. 3168–3175, 1999.

[80] C. Lin, B. N. Popov, and H. J. Ploehn, "Modeling the effects of electrode composition and pore structure on the performance of electrochemical capacitors", *Journal of The Electrochemical Society*, vol. 149, no. 2, pp. 167–175, 2002.

[81] D. Dunn and J. Newman, "Predictions of specific energies and specific powers of double-layer capacitors using a simplified model", *Journal of The Electrochemical Society*, vol. 147, no. 3, pp. 820–830, 2000.

[82] H. Kim and B. N. Popov, "A mathematical model of oxide, carbon composite electrode for supercapacitors", *Journal of the Electrochemical Society*, vol. 150, no. 9, pp. 1153–1160, 2003.

[83] G. Sikha, R. E. White, and B. N. Popov, "A mathematical model for a lithium-ion battery/electrochemical capacitor hybrid system", *Journal of the Electrochemical Society*, vol. 152, no. 8, pp. 1682–1693, 2005.

[84] M. W. Verbrugge and P. Liu, "Microstructural analysis and mathematical modeling of electric double-layer supercapacitors", *Journal of The Electrochemical Society*, vol. 152, no. 5, pp. 79–87, 2005.

[85] S. Kazaryan, S. Razumov, S. Litvinenko, G. Kharisov, and V. Kogan, "Mathematical model of heterogeneous electrochemical capacitors and calculation of their parameters", *Journal of The Electrochemical Society*, vol. 153, no. 9, pp. 1655–1671, 2006.

[86] S. K. Griffiths and R. H. Nilson, "Optimum interparticle porosity for charge storage in a packed bed of nanoporous particles", *Journal of The Electrochemical Society*, vol. 157, no. 4, pp. 469–479, 2010.

[87] J. Dong, Y. Jiang, Q. Li, Q. Wei, W. Yang, S. Tan, X. Xu, Q. An, and L. Mai, "Pseudocapacitive titanium oxynitride mesoporous nanowires with iso-oriented nanocrystals for ultrahigh-rate sodium ion hybrid capacitors", *Journal of Materials Chemistry A*, vol. 5, no. 22, pp. 10827–10835, 2017.

[88] E. Senokos, V. Reguero, J. Palma, J. Vilatela, and R. Marcilla, "Macroscopic fibres of CNTs as electrodes for multifunctional electric double layer capacitors: from quantum capacitance to device performance", *Nanoscale*, vol. 8, no. 6, pp. 3620–3628, 2016.

[89] Z. Qin, Z. J. Li, G. Q. Yun, K. Shi, K. Li, and B. C. Yang, "ZnO nanorods inserted graphene sheets with improved supercapacitive performance", *Applied Surface Science*, vol. 292, pp. 544–550, 2014.

[90] X. Liu and P. G. Pickup, "Ru oxide supercapacitors with high loadings and high power and energy densities", *Journal of Power Sources*, vol. 176, no. 1, pp. 410–416, 2008.

[91] Z.-S. Wu, K. Parvez, X. Feng, and K. Müllen, "Graphene-based in-plane micro-supercapacitors with high power and energy densities", *Nature Communications*, vol. 4, pp. 2487, 2013.

[92] T. Christen and M. W. Carlen, "Theory of Ragone plots", *Journal of Power Sources*, vol. 91, no. 2, pp. 210–216, 2000.

[93] W. G. Pell and B. E. Conway, "Quantitative modeling of factors determining Ragone plots for batteries and electrochemical capacitors", *Journal of Power Sources*, vol. 63, no. 2, pp. 255–266, 1996.

[94] X. Y. Chen, C. Chen, Z. J. Zhang, D. Xie, X. Deng, and J. W. Liu, "Nitrogen-doped porous carbon for supercapacitor with long-term electrochemical stability", *Journal of Power Sources*, vol. 230, pp. 50–58, 2013.

[95] Y. Cai, Y. Luo, H. Dong, X. Zhao, Y. Xiao, Y. Liang, H. Hu, Y. Liu, and M. Zheng, "Hierarchically porous carbon nanosheets derived from Moringa oleifera stems as electrode material for high-performance electric double-layer capacitors", *Journal of Power Sources*, vol. 353, pp. 260–269, 2017.

[96] X. Du, L. Wang, W. Zhao, Y. Wang, T. Qi, and C. M. Li, "Preparation of hierarchical porous carbon from waste printed circuit boards for high performance electric double-layer capacitors", *Journal of Power Sources*, vol. 323, pp. 166–173, 2016.

[97] S. Gao, K. Wang, Z. Du, Y. Wang, A. Yuan, W. Lu, and L. Chen, "High power density electric double-layer capacitor based on a porous multi-walled carbon nanotube microsphere as a local electrolyte micro-reservoir", *Carbon*, vol. 92, pp. 254–261, 2015.

[98] Y. Guo, Z.-Q. Shi, M.-M. Chen, and C.-Y. Wang, "Hierarchical porous carbon derived from sulfonated pitch for electrical double layer capacitors", *Journal of Power Sources*, vol. 252, pp. 235–243, 2014.

[99] Z.-Q. Hao, J.-P. Cao, Y. Wu, X.-Y. Zhao, L. Zhou, X. Fan, Y.-P. Zhao, and X.-Y. Wei, "Preparation of porous carbons from waste sugar residue for high performance electric double-layer capacitor", *Fuel Processing Technology*, vol. 162, pp. 45–54, 2017.

[100] M. Kim, I. Oh, and J. Kim, "Superior electric double layer capacitors using micro- and mesoporous silicon carbide sphere", *Journal of Materials Chemistry A*, vol. 3, no. 7, pp. 3944–3951, 2015.

[101] C. Lei, N. Amini, F. Markoulidis, P. Wilson, S. Tennison, and C. Lekakou, "Activated carbon from phenolic resin with controlled mesoporosity for an electric double-layer capacitor (EDLC)", *Journal of Materials Chemistry A*, vol. 1, no. 19, pp. 6037–6042, 2013.

[102] A. C. Nwanya, D. Obi, K. I. Ozoemena, R. U. Osuji, C. Awada, A. Ruediger, M. Maaza, F. Rosei, and F. I. Ezema, "Facile synthesis of nanosheet-like CuO film and its potential application as a high-performance pseudocapacitor electrode", *Electrochimica Acta*, vol. 198, pp. 220–230, 2016.

[103] D. Puthusseri, V. Aravindan, S. Madhavi, and S. Ogale, "3D micro-porous conducting carbon beehive by single step polymer carbonization for high performance supercapacitors: the magic of in situ porogen formation", *Energy & Environmental Science*, vol. 7, no. 2, pp. 728–735, 2014.

[104] M. K. Singh, M. Suleman, Y. Kumar, and S. Hashmi, "A novel configuration of electrical double layer capacitor with plastic crystal based gel polymer electrolyte and graphene nano-platelets as electrodes: a high rate performance", *Energy*, vol. 80, pp. 465–473, 2015.

[105] M. Suleman, Y. Kumar, and S. Hashmi, "Flexible electric double-layer capacitors fabricated with micro-/mesoporous carbon electrodes and plastic crystal incorporated gel polymer electrolytes containing room temperature ionic liquids", *Journal of Solid State Electrochemistry*, vol. 19, no. 5, pp. 1347–1357, 2015.

[106] Y. Wang, H. Dou, B. Ding, J. Wang, Z. Chang, Y. Xu, and X. Hao, "Nanospace-confined synthesis of oriented porous carbon nanosheets for high-performance electrical double layer capacitors", *Journal of Materials Chemistry A*, vol. 4, no. 43, pp. 16879–16885, 2016.

[107] X. Yu, D. Ruan, C. Wu, J. Wang, and Z. Shi, "Spiro-(1, 1)-bipyrrolidinium tetrafluoroborate salt as high voltage electrolyte for electric double layer capacitors", *Journal of Power Sources*, vol. 265, pp. 309–316, 2014.

[108] X. Zeng, B. Yang, X. Li, and R. Yu, "Three-dimensional hollow CoS_2 nanoframes fabricated by anion replacement and their enhanced pseudocapacitive performances", *Electrochimica Acta*, vol. 240, pp. 341–349, 2017.

[109] H. Zhang, L. Zhang, J. Chen, H. Su, F. Liu, and W. Yang, "One-step synthesis of hierarchically porous carbons for high-performance electric double layer supercapacitors", *Journal of Power Sources*, vol. 315, pp. 120–126, 2016.

[110] Z. Liu, P. Ma, J. Ulstrup, Q. Chi, K. Zhu, and X. Zhou, "New class of two-dimensional bimetallic nanoplatelets for high energy density and electrochemically stable hybrid supercapacitors", *Nano Research*, vol. 10, no. 9, pp. 3018–3034, 2017.

[111] N. Mahmood, M. Tahir, A. Mahmood, J. Zhu, C. Cao, and Y. Hou, "Chlorine-doped carbonated cobalt hydroxide for supercapacitors with enormously high pseudocapacitive performance and energy density", *Nano Energy*, vol. 11, pp. 267–276, 2015.

[112] Z. Wu, X. Pu, X. Ji, Y. Zhu, M. Jing, Q. Chen, and F. Jiao, "High energy density asymmetric supercapacitors from mesoporous $NiCo_2S_4$ nanosheets", *Electrochimica Acta*, vol. 174, pp. 238–245, 2015.

[113] Y.-Z. Su, K. Xiao, N. Li, Z.-Q. Liu, and S.-Z. Qiao, "Amorphous Ni $(OH)_2$@ three-dimensional Ni core–shell nanostructures for high capacitance pseudocapacitors and asymmetric supercapacitors", *Journal of Materials Chemistry A*, vol. 2, no. 34, pp. 13845–13853, 2014.

[114] R. Li, S. Wang, J. Wang, and Z. Huang, "Ni_3S_2@ CoS core–shell nanotriangular pyramid arrays on Ni foam for high-performance supercapacitors", *Physical Chemistry Chemical Physics*, vol. 17, no. 25, pp. 16434–16442, 2015.

[115] J. Y. Hwang, M. Li, M. F. El-Kady, and R. B. Kaner, "Next-generation activated carbon supercapacitors: A simple step in electrode processing leads to remarkable gains in energy density", *Advanced Functional Materials*, vol. 27, no. 15, 2017.

[116] J. Wei, D. Zhou, Z. Sun, Y. Deng, Y. Xia, and D. Zhao, "A controllable synthesis of rich nitrogen-doped ordered mesoporous carbon for CO_2 capture and supercapacitors", *Advanced Functional Materials*, vol. 23, no. 18, pp. 2322–2328, 2013.

[117] J. Zhi, W. Zhao, X. Liu, A. Chen, Z. Liu, and F. Huang, "Highly conductive ordered mesoporous carbon based electrodes decorated by 3D graphene and 1D silver nanowire for flexible supercapacitor", *Advanced Functional Materials*, vol. 24, no. 14, pp. 2013–2019, 2014.

[118] B. Zhang, J. Liang, C. Xu, B. Wei, D. Ruan, and D. Wu, "Electric double-layer capacitors using carbon nanotube electrodes and organic electrolyte", *Materials Letters*, vol. 51, no. 6, pp. 539–542, 2001.

[119] D. N. Futaba, K. Hata, T. Yamada, T. Hiraoka, Y. Hayamizu, Y. Kakudate, O. Tanaike, H. Hatori, M. Yumura, and S. Iijima, "Shape-engineerable and highly densely packed single-walled carbon nanotubes and their application as super-capacitor electrodes", *Nature materials*, vol. 5, no. 12, pp. 987, 2006.

[120] G. Xiong, P. He, B. Huang, T. Chen, Z. Bo, and T. S. Fisher, "Graphene nanopetal wire supercapacitors with high energy density and thermal durability", *Nano energy*, vol. 38, pp. 127–136, 2017.

[121] Y. Shao, M. F. El-Kady, L. J. Wang, Q. Zhang, Y. Li, H. Wang, M. F. Mousavi, and R. B. Kaner, "Graphene-based materials for flexible supercapacitors", *Chemical Society Reviews*, vol. 44, no. 11, pp. 3639–3665, 2015.

[122] M. F. El-Kady, Y. Shao, and R. B. Kaner, "Graphene for batteries, supercapacitors and beyond", *Nature Reviews Materials*, vol. 1, no. 7, pp. 16033, 2016.

[123] V. Augustyn, P. Simon, and B. Dunn, "Pseudocapacitive oxide materials for high-rate electrochemical energy storage", *Energy & Environmental Science*, vol. 7, no. 5, pp. 1597–1614, 2014.

[124] W. Wei, X. Cui, W. Chen, and D. G. Ivey, "Manganese oxide-based materials as electrochemical supercapacitor electrodes", *Chemical Society Reviews*, vol. 40, no. 3, pp. 1697–1721, 2011.

[125] Z. Fan, J. Chen, M. Wang, K. Cui, H. Zhou, and Y. Kuang, "Preparation and characterization of manganese oxide/CNT composites as supercapacitive materials", *Diamond and Related Materials*, vol. 15, no. 9, pp. 1478–1483, 2006.

[126] C. Y. Lee, H. M. Tsai, H. J. Chuang, S. Y. Li, P. Lin, and T. Y. Tseng, "Characteristics and electrochemical performance of supercapacitors with manganese oxide-carbon nanotube nanocomposite electrodes", *Journal of the Electrochemical Society*, vol. 152, no. 4, pp. A716–A720, 2005.

[127] J. Yan, Z. Fan, T. Wei, W. Qian, M. Zhang, and F. Wei, "Fast and reversible surface redox reaction of graphene–MnO_2 composites as supercapacitor electrodes", *Carbon*, vol. 48, no. 13, pp. 3825–3833, 2010.

[128] A. E. Fischer, K. A. Pettigrew, D. R. Rolison, R. M. Stroud, and J. W. Long, "Incorporation of homogeneous, nanoscale MnO_2 within ultraporous carbon structures via self-limiting electroless deposition: implications for electrochemical capacitors", *Nano Letters*, vol. 7, no. 2, pp. 281–286, 2007.

[129] H. Zhou, X. Wang, E. Sheridan, H. Gao, J. Du, J. Yang, and D. Chen, "Boosting the energy density of 3D dual-manganese oxides-based Li-ion supercabattery by controlled mass ratio and charge injection", *Journal of The Electrochemical Society*, vol. 163, no. 13, pp. A2618–A2622, 2016.

[130] J. W. Lee, A. S. Hall, J.-D. Kim, and T. E. Mallouk, "A facile and template-free hydrothermal synthesis of Mn_3O_4 nanorods on graphene sheets for supercapacitor electrodes with long cycle stability", *Chemistry of Materials*, vol. 24, no. 6, pp. 1158–1164, 2012.

[131] Y. Chen, C. G. Liu, C. Liu, G. Q. Lu, and H. M. Cheng, "Growth of single-crystal α-MnO_2 nanorods on multi-walled carbon nanotubes", *Materials Research Bulletin*, vol. 42, no. 11, pp. 1935–1941, 2007.

[132] G.-X. Wang, B.-L. Zhang, Z.-L. Yu, and M.-Z. Qu, "Manganese oxide/MWNTs composite electrodes for supercapacitors", *Solid State Ionics*, vol. 176, no. 11, pp. 1169–1174, 2005.

[133] E. Raymundo-Pinero, V. Khomenko, E. Frackowiak, and F. Beguin, "Performance of manganese oxide/CNTs composites as electrode materials for

electrochemical capacitors", *Journal of the Electrochemical Society*, vol. 152, no. 1, pp. A229–A235, 2005.

[134] T. Cottineau, M. Toupin, T. Delahaye, T. Brousse, and D. Belanger, "Nanostructured transition metal oxides for aqueous hybrid electrochemical supercapacitors", *Applied Physics A*, vol. 82, no. 4, pp. 599–606, 2006.

[135] J. Xiao, L. Wan, S. Yang, F. Xiao, and S. Wang, "Design hierarchical electrodes with highly conductive $NiCo_2S_4$ nanotube arrays grown on carbon fiber paper for high-performance pseudocapacitors", *Nano Letters*, vol. 14, no. 2, pp. 831–838, 2014.

[136] L. Wan, J. Xiao, F. Xiao, and S. Wang, "Nanostructured (Co, Ni)-based compounds coated on a highly conductive three dimensional hollow carbon nanorod array (HCNA) scaffold for high performance pseudocapacitors", *ACS Applied Materials & Interfaces*, vol. 6, no. 10, pp. 7735–7742, 2014.

[137] Z. Ma, X. Huang, S. Dou, J. Wu, and S. Wang, "One-pot synthesis of Fe_2O_3 nanoparticles on nitrogen-doped graphene as advanced supercapacitor electrode materials", *The Journal of Physical Chemistry C*, vol. 118, no. 31, pp. 17231–17239, 2014.

[138] J. Eskusson, P. Rauwel, J. Nerut, and A. Jänes, "A hybrid capacitor based on Fe_3O_4-graphene nanocomposite/few-layer graphene in different aqueous electrolytes", *Journal of The Electrochemical Society*, vol. 163, no. 13, pp. A2768–A2775, 2016.

[139] C. Zhong, Y. Deng, W. Hu, J. Qiao, L. Zhang, and J. Zhang, "A review of electrolyte materials and compositions for electrochemical supercapacitors", *Chemical Society Reviews*, vol. 44, no. 21, pp. 7484–7539, 2015.

[140] K. Fic, G. Lota, M. Meller, and E. Frackowiak, "Novel insight into neutral medium as electrolyte for high-voltage supercapacitors", *Energy & Environmental Science*, vol. 5, no. 2, pp. 5842–5850, 2012.

[141] M. Z. Bazant, M. S. Kilic, B. D. Storey, and A. Ajdari, "Towards an understanding of induced-charge electrokinetics at large applied voltages in concentrated solutions", *Advances in Colloid and Interface Science*, vol. 152, no. 1-2, pp. 48–88, 2009.

[142] M. S. Kilic, M. Z. Bazant, and A. Ajdari, "Steric effects in the dynamics of electrolytes at large applied voltages. II. Modified Poisson-Nernst-Planck equations", *Physical Review E*, vol. 75, no. 2, pp. 021503, 2007.

[143] L. H. Olesen, M. Z. Bazant, and H. Bruus, "Strongly nonlinear dynamics of electrolytes in large AC voltages", *Physical Review E*, vol. 82, no. 1, pp. 011501, 2010.

[144] M. S. Kilic, M. Z. Bazant, and A. Ajdari, "Steric effects in the dynamics of electrolytes at large applied voltages. I. Double-layer charging", *Physical Review E*, vol. 75, no. 2, pp. 021502, 2007.

[145] V. R. Subramanian, V. Boovaragavan, V. Ramadesigan, and M. Arabandi, "Mathematical model reformulation for lithium-ion battery simulations: Galvanostatic boundary conditions", *Journal of The Electrochemical Society*, vol. 156, no. 4, pp. A260–A271, 2009.

[146] G. M. Goldin, A. M. Colclasure, A. H. Wiedemann, and R. J. Kee, "Three-dimensional particle-resolved models of Li-ion batteries to assist the evaluation of empirical parameters in one-dimensional models", *Electrochimica Acta*, vol. 64, pp. 118–129, 2012.

[147] C.-W. Wang and A. M. Sastry, "Mesoscale modeling of a Li-ion polymer cell", *Journal of the Electrochemical Society*, vol. 154, no. 11, pp. A1035–A1047, 2007.

[148] H. Wang and L. Pilon, "Intrinsic limitations of impedance measurements in determining electric double layer capacitances", *Electrochimica Acta*, vol. 63, pp. 55–63, 2012.

[149] H. Wang and L. Pilon, "Reply to comments on "Intrinsic limitations of impedance measurements in determining electric double layer capacitances"by H. Wang and L. Pilon [Electrochimica Acta 63 (2012) 55]", *Electrochimica Acta*, vol. 76, no. 0, pp. 529 – 531, 2012.

[150] B.-A. Mei and L. Pilon, "Three-dimensional cyclic voltammetry simulations of EDLC electrodes made of ordered carbon spheres", *Electrochimica Acta*, vol. 255, pp. 168–178, 2017.

[151] J. H. Masliyah and S. Bhattacharjee, *Electrokinetic and Colloid Transport Phenomena*, John Wiley & Sons, Hoboken, NJ, 2006.

[152] G. J. Janz and R. P. T. Tomkins, *Nonaqueous Electrolytes Handbook*, vol. I, Academic Press, New York, NY, 1972.

[153] A. Burke and M. Miller, "Testing of electrochemical capacitors: Capacitance, resistance, energy density, and power capability", *Electrochimica Acta*, vol. 55, no. 25, pp. 7538–7548, 2010.

[154] S. Zhao, F. Wu, L. Yang, L. Gao, and A. F. Burke, "A measurement method for determination of DC internal resistance of batteries and supercapacitors", *Electrochemistry Communications*, vol. 12, no. 2, pp. 242–245, 2010.

[155] A. A. Kornyshev, "Double-layer in ionic liquids: paradigm change?", 2007.

[156] H. Wang, J. Fang, and L. Pilon, "Scaling laws for carbon-based electric double layer capacitors", *Electrochimica Acta*, vol. 109, pp. 316–321, 2013.

[157] Q. Wang, J. Yan, Y. Wang, T. Wei, M. Zhang, X. Jing, and Z. Fan, "Three-dimensional flower-like and hierarchical porous carbon materials as high-rate performance electrodes for supercapacitors", *Carbon*, vol. 67, pp. 119–127, 2014.

[158] R. Farma, M. Deraman, A. Awitdrus, I. Talib, E. Taer, N. Basri, J. Manjunatha, M. Ishak, B. Dollah, and S. Hashmi, "Preparation of highly porous binderless activated carbon electrodes from fibres of oil palm empty fruit bunches for application in supercapacitors", *Bioresource Technology*, vol. 132, pp. 254–261, 2013.

[159] I. I. G. Inal, S. M. Holmes, A. Banford, and Z. Aktas, "The performance of supercapacitor electrodes developed from chemically activated carbon produced from waste tea", *Applied Surface Science*, vol. 357, pp. 696–703, 2015.

[160] N. Li, R. An, Y. Su, F. Wu, L. Bao, L. Chen, Y. Zheng, H. Shou, and S. Chen, "The role of yttrium content in improving electrochemical performance of layered lithium-rich cathode materials for Li-ion batteries", *J. Mater. Chem. A*, vol. 1, no. 34, pp. 9760–9767, 2013.

[161] T. Jow and J. Zheng, "Electrochemical capacitors using hydrous ruthenium oxide and hydrogen inserted ruthenium oxide", *Journal of the Electrochemical Society*, vol. 145, no. 1, pp. 49–52, 1998.

[162] P. Guillemet, T. Brousse, O. Crosnier, Y. Dandeville, L. Athouel, and Y. Scudeller, "Modeling pseudocapacitance of manganese dioxide", *Electrochimica Acta*, vol. 67, pp. 41–49, 2012.

[163] Q. Zhong, B. Huang, J. Ma, and H. Li, "Experimental study on relationship between SOC and OCV of lithium-ion batteries", *International Journal of Smart Grid and Clean Energy*, vol. 3, no. 2, pp. 149–153, 2014.

[164] B.-A. Mei, B. Li, J. Lin, and L. Pilon, "Multidimensional cyclic voltammetry simulations of pseudocapacitive electrodes with a conducting nanorod scaffold", *Journal of The Electrochemical Society*, vol. 164, no. 13, pp. A3237–A3252, 2017.

[165] A. M. Colclasure and R. J. Kee, "Thermodynamically consistent modeling of elementary electrochemistry in lithium-ion batteries", *Electrochimica Acta*, vol. 55, no. 28, pp. 8960–8973, 2010.

[166] K. Nishikawa, Y. Fukunaka, T. Sakka, Y. Ogata, and J. Selman, "Measurement of $LiClO_4$ diffusion coefficient in propylene carbonate by moiré

pattern", *Journal of the Electrochemical Society*, vol. 153, no. 5, pp. A830–A834, 2006.

[167] H. Cohen and J. W. Cooley, "The numerical solution of the time-dependent Nernst-Planck equations", *Biophysical Journal*, vol. 5, no. 2, pp. 145–162, 1965.

[168] B.-A. Mei, O. Munteshari, J. Lau, B. Dunn, and L. Pilon, "Physical interpretations of Nyquist plots for EDLC electrodes and devices", *The Journal of Physical Chemistry C*, vol. 122, no. 1, pp. 194–206, 2017.

[169] J. B. Cook, H.-S. Kim, T. C. Lin, C.-H. Lai, B. Dunn, and S. H. Tolbert, "Pseudocapacitive charge storage in thick composite MoS_2 nanocrystal-based electrodes", *Advanced Energy Materials*, vol. 7, no. 2, pp. 1601283, 2017.

[170] A. Bhide, J. Hofmann, A. K. Dürr, J. Janek, and P. Adelhelm, "Electrochemical stability of non-aqueous electrolytes for sodium-ion batteries and their compatibility with $Na_{0.7}$ CoO_2", *Physical Chemistry Chemical Physics*, vol. 16, no. 5, pp. 1987–1998, 2014.

[171] K. Xu, "Nonaqueous liquid electrolytes for lithium-based rechargeable batteries", *Chemical reviews*, vol. 104, no. 10, pp. 4303–4418, 2004.

[172] J. B. Cook, H.-S. Kim, Y. Yan, J. S. Ko, S. Robbennolt, B. Dunn, and S. H. Tolbert, "Mesoporous MoS_2 as a transition metal dichalcogenide exhibiting pseudocapacitive Li and Na-ion charge storage", *Advanced Energy Materials*, vol. 6, no. 9, pp. 1501937, 2016.

[173] C. M. Burba and R. Frech, "Vibrational spectroscopic investigation of structurally-related $LiFePO_4$, $NaFePO_4$, and $FePO_4$ compounds", *Spectrochimica Acta Part A: Molecular and Biomolecular Spectroscopy*, vol. 65, no. 1, pp. 44–50, 2006.

[174] L. Bai, L. Gao, and B. E. Conway, "Problem of in situ real-area determination in evaluation of performance of rough or porous, gas-evolving electrocatalysts. Part 1.Basis for distinction between capacitance of the double layer and the pseudocapacitance due to adsorbed H in the H_2 evolution reaction at Pt", *Journal of the Chemical Society, Faraday Transactions*, vol. 89, no. 2, pp. 235–242, 1993.

[175] A. Burke, "R&D considerations for the performance and application of electrochemical capacitors", *Electrochimica Acta*, vol. 53, no. 3, pp. 1083–1091, 2007.

[176] D. Halliday, R. Resnick, and J. Walker, *Fundamentals of Physics*, John Wiley & Sons, Hoboken, NJ, 9th edition, 2010.

[177] H. Wang, J. Varghese, and L. Pilon, "Simulation of electric double layer capacitors with mesoporous electrodes: Effects of morphology and electrolyte permittivity", *Electrochimica Acta*, vol. 56, no. 17, pp. 6189–6197, 2011.

[178] H. Wang and L. Pilon, "Accurate simulation of electric double layer capacitance for ultramicroelectrodes", *Journal of Physical Chemistry C*, vol. 115, no. 33, pp. 16711–16719, 2011.

[179] F. Booth, "The dielectric constant of water and the saturation effect", *Journal of Chemical Physics*, vol. 19, no. 4, pp. 391–394, 1951.

[180] A. J. Appleby, "Electron transfer reactions with and without ion transfer", in *Modern Aspects of Electrochemistry, No. 38*, B. Conway, C. Vayenas, R. White, and M. Gamboa-Adelco, Eds., pp. 175–301. Kluwer Academic/Plenum Publishers, New York, NY, 2005.

[181] G. Moumouzias and G. Ritzoulis, "Relative permittivities and refractive indices of propylene carbonate + toluene mixtures from 283.15 K to 313.15 K", *Journal of Chemical & Engineering Data*, vol. 42, no. 4, pp. 710–713, 1997.

[182] J. Chmiola, G. Yushin, Y. Gogotsi, C. Portet, P. Simon, and P. L. Taberna, "Anomalous increase in carbon capacitance at pore sizes less than 1 nanometer", *Science*, vol. 313, no. 5794, pp. 1760–1763, 2006.

[183] J. N. Israelachvili, *Intermolecular and Surface Forces*, Academic Press, San Diego, CA, 2nd edition, 1992.

[184] B. Conway, "Electrolyte solutions: Solvation and structural aspects", *Annual Review of Physical Chemistry*, vol. 17, no. 1, pp. 481–528, 1966.

[185] Y. Marcus, "Ionic radii in aqueous solutions", *Chemical Reviews*, vol. 88, no. 8, pp. 1475–1498, 1988.

[186] V. Afanasev and A. Ustinov, "Adiabatic compressibility of hydrated complexes of electrolytes", *Electrochimica Acta*, vol. 54, no. 26, pp. 6455–6463, 2009.

[187] M. Noked, E. Avraham, A. Soffer, and D. Aurbach, "Assessing the concentration effect on hydration radii in aqueous solutions by electroadsorption on a carbon molecular sieve electrode", *The Journal of Physical Chemistry C*, vol. 114, no. 31, pp. 13354–13361, 2010.

[188] N. Nanbu, T. Ebina, H. Uno, S. Ishizawa, and Y. Sasaki, "Physical and electrochemical properties of quaternary ammonium bis (oxalato) borates and their application to electric double-layer capacitors", *Electrochimica acta*, vol. 52, no. 4, pp. 1763–1770, 2006.

[189] S. Porada, G. Feng, M. Suss, and V. Presser, "Capacitive deionization in organic solutions: case study using propylene carbonate", *RSC Advances*, vol. 6, no. 7, pp. 5865–5870, 2016.

[190] J. Sánchez-González, F. Stoeckli, and T. A. Centeno, "The role of the electric conductivity of carbons in the electrochemical capacitor performance", *Journal of Electroanalytical Chemistry*, vol. 657, no. 1, pp. 176–180, 2011.

[191] L. L. Zhang, R. Zhou, and X. Zhao, "Graphene-based materials as supercapacitor electrodes", *Journal of Materials Chemistry*, vol. 20, no. 29, pp. 5983–5992, 2010.

[192] D. J. Griffiths, *Introduction to electrodynamics*, Prentice Hall, 1962.

[193] A. S. for Metals, *Metals handbook*, vol. 3, The Society, 1967.

[194] J. Wang, J. Polleux, J. Lim, and B. Dunn, "Pseudocapacitive contributions to electrochemical energy storage in TiO_2 (anatase) nanoparticles", *The Journal of Physical Chemistry C*, vol. 111, no. 40, pp. 14925–14931, 2007.

[195] T. Brezesinski, J. Wang, S. H. Tolbert, and B. Dunn, "Ordered mesoporous α-MoO_3 with iso-oriented nanocrystalline walls for thin-film pseudocapacitors", *Nature Materials*, vol. 9, no. 2, pp. 146–151, 2010.

[196] Z. Chen, V. Augustyn, X. Jia, Q. Xiao, B. Dunn, and Y. Lu, "High-performance sodium-ion pseudocapacitors based on hierarchically porous nanowire composites", *ACS nano*, vol. 6, no. 5, pp. 4319–4327, 2012.

[197] B. Laskova, M. Zukalova, A. Zukal, M. Bousa, and L. Kavan, "Capacitive contribution to Li-storage in TiO_2 (B) and TiO_2 (anatase)", *Journal of Power Sources*, vol. 246, pp. 103–109, 2014.

[198] M. C. Lopez, G. F. Ortiz, P. Lavela, R. Alcantara, and J. L. Tirado, "Improved energy storage solution based on hybrid oxide materials", *ACS Sustainable Chemistry & Engineering*, vol. 1, no. 1, pp. 46–56, 2012.

[199] B. Zhao and Z. Shao, "From paper to paper-like hierarchical anatase TiO_2 film electrode for high-performance lithium-ion batteries", *The Journal of Physical Chemistry C*, vol. 116, no. 33, pp. 17440–17447, 2012.

[200] J.-H. Kim, K. Zhu, J. Y. Kim, and A. J. Frank, "Tailoring oriented TiO_2 nanotube morphology for improved Li storage kinetics", *Electrochimica Acta*, vol. 88, pp. 123–128, 2013.

[201] T.-C. Liu, W. Pell, B. Conway, and S. Roberson, "Behavior of molybdenum nitrides as materials for electrochemical capacitors comparison with ruthenium oxide", *Journal of the Electrochemical Society*, vol. 145, no. 6, pp. 1882–1888, 1998.

[202] H. Lindström, S. Södergren, A. Solbrand, H. Rensmo, J. Hjelm, A. Hagfeldt, and S.-E. Lindquist, "Li^+ ion insertion in TiO_2 (anatase). 2. voltammetry on nanoporous films", *The Journal of Physical Chemistry B*, vol. 101, no. 39, pp. 7717–7722, 1997.

[203] L. Kong, C. Zhang, S. Zhang, J. Wang, R. Cai, C. Lv, W. Qiao, L. Ling, and D. Long, "High-power and high-energy asymmetric supercapacitors based on Li^+-intercalation into a T-Nb_2O_5/graphene pseudocapacitive electrode", *Journal of Materials Chemistry A*, vol. 2, no. 42, pp. 17962–17970, 2014.

[204] J. Li, Z. Tang, and Z. Zhang, "Pseudocapacitive characteristic of lithium ion storage in hydrogen titanate nanotubes", *Chemical Physics Letters*, vol. 418, no. 4, pp. 506–510, 2006.

[205] E. Lim, H. Kim, C. Jo, J. Chun, K. Ku, S. Kim, H. I. Lee, I.-S. Nam, S. Yoon, K. Kang, et al., "Advanced hybrid supercapacitor based on a mesoporous niobium pentoxide/carbon as high-performance anode", *ACS nano*, vol. 8, no. 9, pp. 8968–8978, 2014.

[206] Y.-M. Lin, P. R. Abel, D. W. Flaherty, J. Wu, K. J. Stevenson, A. Heller, and C. B. Mullins, "Morphology dependence of the lithium storage capability and rate performance of amorphous TiO_2 electrodes", *The Journal of Physical Chemistry C*, vol. 115, no. 5, pp. 2585–2591, 2010.

[207] L. Shao, J.-W. Jeon, and J. L. Lutkenhaus, "Porous polyaniline nanofiber/vanadium pentoxide layer-by-layer electrodes for energy storage", *Journal of Materials Chemistry A*, vol. 1, no. 26, pp. 7648–7656, 2013.

[208] S.-B. Ma, K.-W. Nam, W.-S. Yoon, X.-Q. Yang, K.-Y. Ahn, K.-H. Oh, and K.-B. Kim, "A novel concept of hybrid capacitor based on manganese oxide materials", *Electrochemistry Communications*, vol. 9, no. 12, pp. 2807–2811, 2007.

[209] A. Bosman and C. Crevecoeur, "Mechanism of the electrical conduction in Li-doped NiO", *Physical Review*, vol. 144, no. 2, pp. 763, 1966.

[210] J. Molenda, M. Ziemnicki, M. Molenda, M. Bućko, and J. Marzec, "Transport and electrochemical properties of orthorhombic $LiMnO_2$ cathode material for Li-ion batteries", *Materials Science-Poland*, vol. 24, no. 1, pp. 75–83, 2006.

[211] C. Meneses, M. Macedo, and F. Vicentin, "$Li_xMn_2O_4$ thin films characterization by X-ray, electrical conductivity and XANES", *Microelectronics Journal*, vol. 34, no. 5, pp. 561–563, 2003.

[212] S. Brunauer, P. H. Emmett, and E. Teller, "Adsorption of gases in multimolecular layers", *Journal of the American Chemical Society*, vol. 60, no. 2, pp. 309–319, 1938.

[213] R. J. Borg and G. J. Dienes, *An introduction to solid state diffusion*, Elsevier, 2012.

[214] X. Sanchez-Vila, M. Dentz, and L. D. Donado, "Transport-controlled reaction rates under local non-equilibrium conditions", *Geophysical research letters*, vol. 34, no. 10, 2007.

[215] J. D. Hem, "Chemical equilibria and rates of manganese oxidation", Tech. Rep., USGPO,, 1963.

[216] W. M. Haynes, *CRC handbook of chemistry and physics*, CRC press, 2014.

[217] C. Daniel and J. O. Besenhard, *Handbook of battery materials*, John Wiley & Sons, 2012.

[218] A. Van der Ven, G. Ceder, M. Asta, and P. Tepesch, "First-principles theory of ionic diffusion with nondilute carriers", *Physical Review B*, vol. 64, no. 18, pp. 184307, 2001.

[219] J. W. Kim, V. Augustyn, and B. Dunn, "The effect of crystallinity on the rapid pseudocapacitive response of Nb_2O_5", *Advanced Energy Materials*, vol. 2, no. 1, pp. 141–148, 2012.

[220] B. Orel, M. Maček, J. Grdadolnik, and A. Meden, "In situ UV-Vis and ex situ IR spectroelectrochemical investigations of amorphous and crystalline electrochromic Nb_2O_5 films in charged/discharged states", *Journal of Solid State Electrochemistry*, vol. 2, no. 4, pp. 221–236, 1998.

[221] M. Maček, B. Orel, and U. O. Krašovec, "The effect of lithiation on the electrochromism of sol-gel derived niobium oxide films", *Journal of the Electrochemical Society*, vol. 144, no. 9, pp. 3002–3010, 1997.

[222] J. R. Miller and P. Simon, "Electrochemical capacitors for energy management", *Science*, vol. 321, no. 5889, pp. 651–652, 2008.

[223] H. Farsi and F. Gobal, "A mathematical model of nanoparticulate mixed oxide pseudocapacitors; Part I: model description and particle size effects", *Journal of Solid State Electrochemistry*, vol. 13, no. 3, pp. 433–443, 2009.

[224] F. T. Ulaby, U. Ravaioli, and E. Michielssen, *Fundamentals of Applied Electromagnetics*, Prentice Hall, Upper Saddle River, NJ, 2014.

[225] S. H. Lapidus, N. N. Rajput, X. Qu, K. W. Chapman, K. A. Persson, and P. J. Chupas, "Solvation structure and energetics of electrolytes for multivalent energy storage", *Physical Chemistry Chemical Physics*, vol. 16, no. 40, pp. 21941–21945, 2014.

[226] S. Miyoshi, T. Akbay, T. Kurihara, T. Fukuda, A. T. Staykov, S. Ida, and T. Ishihara, "Fast diffusivity of PF_6^- anions in graphitic carbon for a dual-carbon rechargeable battery with superior rate property", *The Journal of Physical Chemistry C*, vol. 120, no. 40, pp. 22887–22894, 2016.

[227] K. Hayamizu, "Temperature dependence of self-diffusion coefficients of ions and solvents in ethylene carbonate, propylene carbonate, and diethyl carbonate single solutions and ethylene carbonate + diethyl carbonate binary solutions of $LiPF_6$ studied by NMR", *Journal of Chemical & Engineering Data*, vol. 57, no. 7, pp. 2012–2017, 2012.

[228] M. T. Ong, O. Verners, E. W. Draeger, A. C. Van Duin, V. Lordi, and J. E. Pask, "Lithium ion solvation and diffusion in bulk organic electrolytes from first-principles and classical reactive molecular dynamics", *The Journal of Physical Chemistry B*, vol. 119, no. 4, pp. 1535–1545, 2015.

[229] A. d'Entremont and L. Pilon, "First-principles thermal modeling of electric double layer capacitors under constant-current cycling", *Journal of Power Sources*, vol. 246, pp. 887 – 898, 2014.

[230] A. L. dEntremont and L. Pilon, "First-principles thermal modeling of hybrid pseudocapacitors under galvanostatic cycling", *Journal of Power Sources*, vol. 335, pp. 172–188, 2016.

[231] J. P. Joule, "XXXVIII. On the heat evolved by metallic conductors of electricity, and in the cells of a battery during electrolysis", *Philosophical Magazine Series 3*, vol. 19, no. 124, pp. 260–277, 1841.

[232] A. E. Hofmann, I. C. Bourg, and D. J. DePaolo, "Ion desolvation as a mechanism for kinetic isotope fractionation in aqueous systems", *Proceedings of the National Academy of Sciences*, vol. 109, no. 46, pp. 18689–18694, 2012.

[233] A. Alizadeh, C. N. De Castro, and W. Wakeham, "The theory of the taylor dispersion technique for liquid diffusivity measurements", *International Journal of thermophysics*, vol. 1, no. 3, pp. 243–284, 1980.